CONTROLLED DIFFUSION BLADE AXIAL FAN: FLUID MECHANICAL MECHANISTIC EFFECTS ON FAN PERFORMANCE

By

David Jennings Barrent

A THESIS

Submitted to
Michigan State University
in partial fulfillment of the requirements
for the degree of

Mechanical Engineering – Master of Science

2015

ABSTRACT

CONTROLLED DIFFUSION BLADE AXIAL FAN: FLUID MECHANICAL MECHANISTIC EFFECTS ON FAN PERFORMANCE

By

David Jennings Barrent

Axial fan configurations, with three-to-nine controlled diffusion (CD) blades, have been examined using experimental methods. The initial measurements: pressure rise/flow rate, revealed distinct and opposite patterns: discontinuous pressure ”jumps” for the 3-4 and 6-9 blade fans. The three, five and nine blade fans were selected for detailed examination using: i) time-mean surface pressure data from which the net lift force could be obtained and ii) X array hot-wire data (stationary probe) in the near wakes of the rotating blades. These data were processed to provide ensemble statistics. These data, plus the input shaft power were interpreted using the First Law of Thermodynamics in its control volume form. The results indicate that increasing the number of blades installed on the fan suppresses turbulent fluctuations in the wake of the fan. Additionally, similar phenomena in the flow field are observed at lower flow coefficient as the number of blades on the fan is increased.

Dedicated to my Mother and Father for supporting me when I have needed it the most.

ACKNOWLEDGMENTS

I would like to thank Dr. John Foss for hiring me as an undergraduate research assistant starting in 2012. I did not have graduate school on my radar before the experiences I was exposed to in my first months within the lab. I have learned quite a bit the past few years in the TSFL and I am honored to call Dr. Foss my mentor.

This research work would not be possible without students that have used the facility and fan assembly before me. Andrew Cawood, Douglas Neal, and Behdad Davoudi have always been available when I have questions concerning my research and their previous research work. As my fluids lab TA Andrew told me about a research opportunity over the summer and I am happy that I took him up on the offer. I am thankful for him getting me into the lab that summer and sparking my interest in fluid mechanics during spring with his enthusiasm in the classroom. The time spent working under him as he finished his research work provided me a great foundation for the onset of my Master's Research. A special thanks to Doug for developing the experiment itself and providing me with guidance to get the hot-wire wake velocity measurements up and running for this research. The second half of this research effort would have been painful without his help getting that experiment up and running. I have spent many hours processing and interpreting data this semester and I am thankful to have had Behdad around to bounce ideas off of when I process something new. I also greatly appreciate his guidance to some of the aspects of his experiment as they pertain to mine.

Many thanks are necessary for the rest of the current group working with me in the Turbulent Shear Flows Laboratory. Al, thank you for all of the work you have done to help me finish this research work. I have truly enjoyed our political banter and lunches

over the years. Although, lunch has never been the same since Kyle Bade's departure. Miss having you around Kyle. Brian and Tyler, thanks for your help over the years with various projects and I have enjoyed getting to know you in your time at the lab. Megan, I am grateful for all of your help with my experiments the past two semesters. Running the fan for pressure measurements and helping me make figures have been a tremendous help to me the past two semesters.

The past semester has been a stressful whirlwind of finishing classes, running experiments, processing data and writing. To combat the stress I started practicing yoga this semester and it has worked wonders on keeping me focused and level in these stressful times. I would like to thank Jen Hayes of Yoga State for helping me on my journey to reducing stress in my life, and all my friends I have made along the way at the studio. Especially, Lyndsay, for getting on me every week asking how this document was going and helping me fine tune diet this semester.

I am blessed to have made it this far and owe it to all of those who have supported me. My family has been my rock for my entire life. I would not be writing this document without the support from my Mother, Father, and Sister during my time in graduate school; Thank you. Enjoy the read!

TABLE OF CONTENTS

LIST OF TABLES

LIST OF FIGURES

KEY TO SYMBOLS AND ABBREVIATIONS

Abbreviations	**Description**
AFRD	Axial Fan Research and Development Facility
CD	Controlled Diffusion Blade
RCDB	Rotating Controlled Diffusion Blade
X-probe	Axial Fan Research and Development Facility

Coordinates	**Description**
r–θ–z	Spherical coordinate system
$\hat{\boldsymbol{r}},\ \hat{\boldsymbol{\theta}},\ \hat{\boldsymbol{z}}$	Unit vectors in cylindrical coordinates

Greek Symbols	**Description**
α_o	Measured velocity angle with respect to the probe axis
α_{AoI}	Angle of incidence between incoming velocity and tangent to the leading edge of the fan blade
η	Spanwise position that ranges from [0,1] from hub to tip
κ	Non dimensional kinetic energy at the exit of the fan defined by $\int_{c.s.} 1/2\ \rho(\boldsymbol{V}\cdot\boldsymbol{V})\ \boldsymbol{V}\cdot\hat{\boldsymbol{n}}\, dA\ [1/(r_{tip}\times\rho V_{tip}{}^2 r_{tip}{}^2)]$
λ	Axial velocity wake minimum centered azimuthal position of hot-wire probe in fan wake
μ	Dynamic viscosity of air
ν	Kinematic viscosity of air
ξ	Energy losses in the control volume due to dissipation and viscous effects
ρ	Density of air
Σ	Representative comparison of azimuthal velocity defined by $\int V_\theta(\theta)\ d\theta$ for the different fan configurations

Φ	Flow coefficient $\overline{V}/V_{tip}$
χ	Non dimensional flow work rate term defined by $\int_{c.s.} P/\rho\ \rho \cdot \boldsymbol{V} \cdot \hat{\boldsymbol{n}}\ dA\ [1/(r_{tip} \times \rho {V_{tip}}^2 {r_{tip}}^2)]$
Ψ	Head rise coefficient $\Delta P/(\rho * {V_{tip}}^2)$
$\boldsymbol{\Omega}$	Angular velocity vector of the fan

Roman Symbols	**Description**
A	Flow area in r-θ – plane of the fan
A_i, B_i, n_i	Hotwire calibration constants
c	Chord length of the RCDB (133.9 mm)
$c.s.$	Control Surface of Control Volume
$\mathrm{C_p}$	Pressure coefficient $(P_{tap} - P_{atm})/(\frac{1}{2}\rho \mathrm{w}_\infty$
I-V	Operating conditions selected for further study from performance data (I, II, III, IV, V)
$\dot{m}$	Mass flow rate through the fan plane
$\hat{\boldsymbol{n}}$	Outward facing normal of control volume surfaces
P_{shaft}	Shaft power into the control volume
P_{atm}	Atmospheric pressure in the laboratory
P_{rec}	Receiver pressure
P_{ref}	Common reference pressure for all pressure transducers
P_{tap}	Pressure at the blade surface
q	Turbulence kinetic energy
Q_o	Measured velocity magnitude of processed X-probe
$\hat{\boldsymbol{r}}$	Position vector in the radial direction

Re_c	Reynolds number based on airfoil chord length $\mathrm{Re}_c = (\vec{W}(r_{center})c)/\nu$
r_{sensor}	Radial distance to pressure transducer
r_{tap}	Radial distance to surface pressure tap on an instrumented blade
r_{tip}	Tip radius of the fan (0.366 meters)
s_i^j	Phase averaged sample for revolution: i and "Bin": j
T	Input shaft torque measurement
t	Time during experimental measurement
$\boldsymbol{V}$, V_i, $\vec{V}$	Velocity vector $\vec{V} = \boldsymbol{V} = V_i = V_r + V_\theta + V_z$
V_r, V_θ, V_z	Velocity components in cylindrical coordinates V_r, V_θ measured in in the wake of the fan $f = f(t)$
V_r', V_θ', V_z'	Velocity fluctuation components in cylindrical coordinates V_r', V_θ' measured in the wake of the fan $f = f(t)$
V_{tip}	Tangential velocity at r_{tip} of the fan
V_z^*, V_θ^*	Phase averaged wake velocity in the axial and azimuthal directions $f = f(\theta)$
$\widetilde{V}_z$, $\widetilde{V}_z$	Phase averaged root mean square (RMS) of turbulence intensity in the axial and azimuthal directions $f = f(\theta)$
$\overline{V_z' V_\theta'}$	Phase averaged Reynolds stress in the θ-z–plane $f = f(\theta)$
$\vec{W}$	Apparent approach velocity which stagnates on the leading edge of the blade. $\vec{W} = \vec{W}(r)$

Chapter 1

INTRODUCTION

1.1 Overview for this Thesis

1.1.1 Motivation

This experimental investigation explored fundamental fluid mechanical phenomena in an axial fan flow field. More specifically, these experiments focused on how the flow field changes for different operating conditions of the fan. In addition to providing insight within the academic community, these results will be utilized by companies in industry to improve axial fan design. Currently, members of the industrial community are challenged with regulations and standards regarding noise pollution and mechanical efficiencies. A Consortium was formed by a group of these companies to fund research that will advance the field through fundamental investigations of axial fan flow fields. The axial fan used in the present investigation has been examined in previous investigations in the Turbulent Shear Flows Laboratory (TSFL) at Michigan State University. These experimental investigations provide a diverse validation database for the computational community. This database, to which the present investigation contributes, will support to development of more accurate computational models for axial fans and improve fan designs.

1.1.2 Previous Investigations

1.1.2.1 Ph.D. Dissertation – Douglas Neal (2010)

The axial fan used in this investigation was developed to detail the effects of rotation in a flow field from a stationary reference frame to an equivalent rotating reference frame. The original experiment, in the stationary reference frame, examined the development of the boundary layer on a controlled diffusion (CD) airfoil. Controlled diffusion airfoils have their camber and thickness distributions tailored to avoid boundary layer separation on the suction surface by controlling diffusion (deceleration) from the peak velocity point to the trailing edge [Gelder, T.F. *et. al.* (1987)] and [Johnson (1998)]. This airfoil shape has been extensively studied in wind tunnel experiments and computational simulations in a stationary reference frame and was selected for comparison in the rotating reference frame.

A fan was designed with blades that have similar flow fields to the stationary experiment. The blade twist of the rotating controlled diffusion blade (RCDB) was designed to ensure an identical angle of attack along the span of the blade for the selected design operating condition. Changing the number of blades installed on the fan effected blade loading and was compared with the blade loading of the CD blade in the stationary reference frame. Time averaged surface pressure measurements were collected and analyzed in both experiments for this comparison. The three blade fan blade loading matched closely with that of the CD blade in the wind tunnel experiment. Experimental and computational results suggested that the solidity of the fan in the rotating experiment was analogous to the jet width of the incoming flow to the stationary blade [Neal (2010)]. Additionally, Neal performed velocity hot-wire measurements in the wake of the fan, obtaining three components of the velocity vector, with a four wire method developed for in his investigation. These data suggested that the radial velocity was small in the wake region. Therefore, velocity measurements in the wake of the fan can be resolved in the axial and azimuthal directions neglecting the radial velocity component. The present investigation used the surface pressure and hot-wire wake velocity experimental techniques to explore the fan flow field.

1.1.2.2 M.S. Thesis – Andrew Cawood (2012)

This investigation developed a technique to measure the unsteady surface pressure on the CD airfoil and RCDB. These measurements examined the development of the suction side boundary layer these blades. Additionally, this investigation conducted experiments at an off design operating condition with no pressure difference across the inlet and outlet of the control volume considered for the fan. The original design operating condition experienced a pressure drop across this control volume.

1.1.2.3 M.S. Thesis – Behdad Davoudi (2014)

This investigation examined the propagated far field aeroacoustic noise upstream of the fan. A microphone array was mounted above the fan to record, isolate, and characterize the fan noise. This investigation was conducted with the three and nine blade fan configurations. Operating conditions studied in this investigation were restricted to a pressure rise across the fan. Noise pollution from the downstream helper fan in the experiment created this restriction. This investigation also obtained velocity magnitude hot-wire data in the wake of the fan. These data were obtained at five different radial locations and they were correlated with the turbulence intensity in the wake, propagated far field noise, and operating condition of the fan.

1.1.3 The Present Investigation — Areas of Contributions

Fan performance and mechanical efficiency were the two main motivations of the present investigation. The axial fan of this investigation can be assembled with two to nine blades installed. The three to nine blade fan configurations were selected for study in the present investigation. Fan integral data were obtained for all seven of these fan configurations to provide a population of operating conditions to select from for further investigation. Fan integral measurements include the pressure rise across the fan, mass flow rate though the fan, and the fan shaft torque supplied by the driving motor. These measurements were collected and analyzed. As a result, the three, five, and nine blade fan configurations were selected for further/detailed investigations.

Time averaged surface pressure measurements and hot-wire velocity measurements in the wake of the fan were two additional experimental methods utilized for this investigation. Previous investigations have studied surface pressure measurements on the RCDB; however, this study expands these measurements to include different radial positions. Four additional radial locations were available for study. Two component velocity hot-wire measurements were also collected downstream in the near-wake of the fan. These measurements were obtained at the center of the blade span to minimize tip and hub flow effects. Examination of these data detailed the effect of blade loading on fan efficiency. All of these measurements supplement the substantial experimental database for this fan; they are made available as validation data to create more accurate computational simulations of axial fans.

1.2 Basic Fluid Mechanical Principals

Three subject areas have been selected for this discussion: control volume analysis for this axial fan; fan performance characteristic curves; characteristic lengths and velocities of this investigation.

1.2.1 Control Volume Definition

A control volume approach was used to evaluate the global quantities including the mechanical efficiency of this fan. Figure 1.1 presents the formulation of two control volumes used to evaluate this fan. The red dashed line displays the boundaries of Control Volume (1). The black double dot dashed line displays the boundaries of Control Volume

(2). The differences of inlet for these control volumes allow the fan to be considered in two separate types of application. Control Volume (1) considers the fan in an environment where atmospheric, negligible kinetic energy air is readily available to be moved through the system. Control Volume (2) is similar to examining a fan in a duct where there will be kinetic energy at the inlet control surface due to the fan bringing air into the duct further upstream or supplied by an upstream fan within the duct.

Figure 1.1 also indicated various parameters important for the flow and each control volume. A cylindrical coordinate system was used for the present investigation when in the inertial reference frame with $+z$ along the flow path through the fan. The fan rotates in the $-\theta$ direction with a constant azimuthal velocity of 450 revolutions per minute or 7.5 Hertz. The pressure at the inlet control surface for Control Volume (2) is found by calculating the dynamic pressure from the incoming flow velocity $\overline{V}$. $\overline{V}$ is the average incoming velocity in the contracted portion of the shroud from the mass flow rate of the fan and assumed to be constant radially with thin boundary layers on either wall.

Equation 1.1 provides the work rate equation from the First Law of Thermodynamics for these control volumes. Table 1.1 indicates the physical significance of each term in the equation and provides the symbol each will be represented by in this document. The research performed for this investigation produced representative values for (A), (B), and (C) and allowed for quantitative comparison of the efficiency between fan configurations and operating conditions. The input torque contributing to the shaft power, $\mathrm{P}_{shaft} = Torque|\mathbf{\Omega}|$, was evaluated at the indicated location in Figure 1.1 by means of a torque meter mounted on the shaft. κ will be evaluated as a surrogate quantity at the fan plane exit surface because the velocity measurements were limited to one radial location

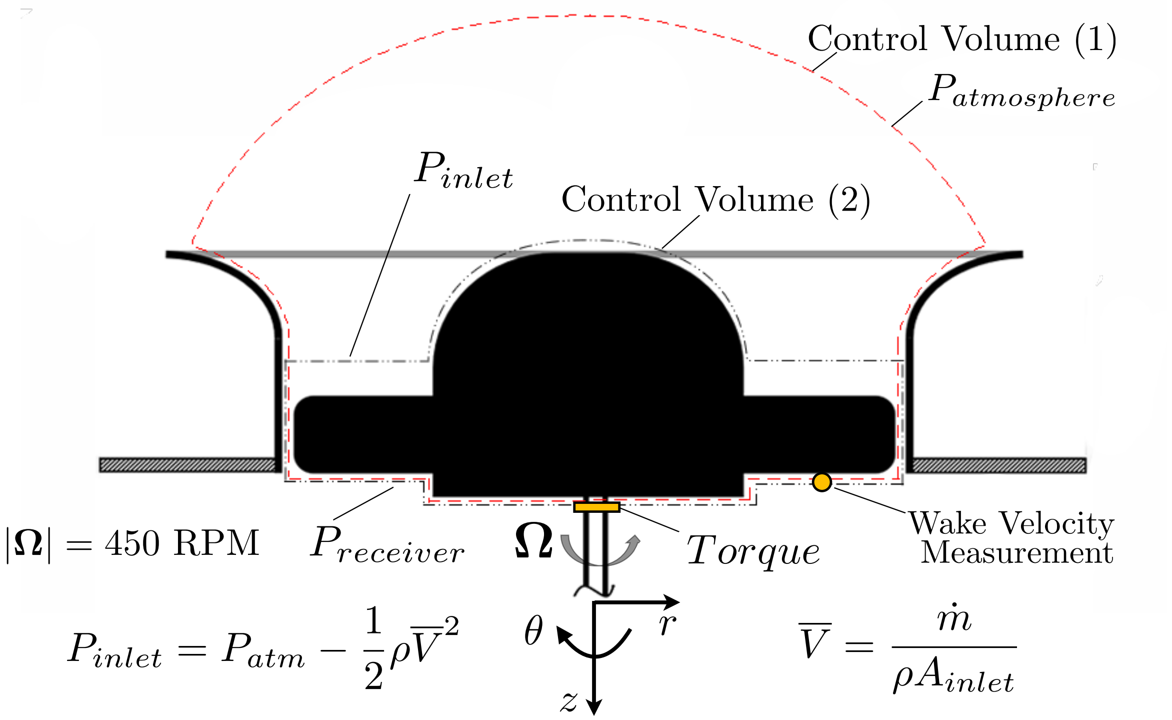

Figure 1.1 Control volumes for the present investigation

Table 1.1 Work rate equation terms

Term	Physical Meaning	Notation
(A)	Input shaft power from motor	P_{shaft}
(B)	Kinetic energy of fluid at bottom control surface	κ
(C)	Flow work rate from pressure	χ
(D)	Dissipative losses	ξ

indicated in Figure 1.1.

$$\underbrace{\mathrm{P}_{shaft}}_{(\mathrm{A})} = \underbrace{\int_{c.s.} (\frac{1}{2}\ \rho(\boldsymbol{V}\cdot\boldsymbol{V})\ \ \boldsymbol{V}\cdot\hat{\boldsymbol{n}}\ dA}_{(\mathrm{B})} + \underbrace{\int_{c.s.} \frac{P}{\rho}\ \rho\cdot\boldsymbol{V}\cdot\hat{\boldsymbol{n}}\ dA}_{(\mathrm{C})} + \underbrace{Losses}_{(\mathrm{D})} \tag{1.1}$$

1.2.2 Fan Characteristic Curve Introduction

Characteristic curves of fan performance display the relationship between the pressure increase across and the mass flux through the fan plane . An ideal fan would have a linear

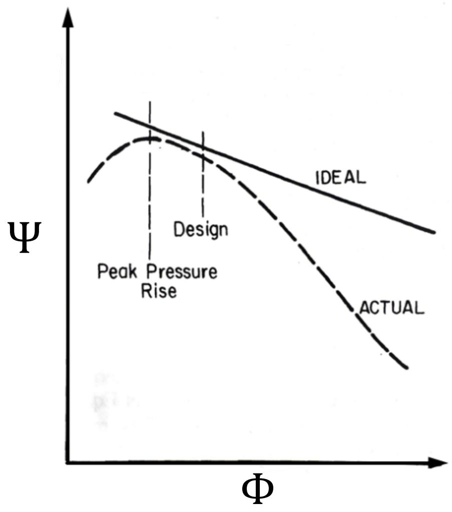

Figure 1.2 Sample axial fan characteristic curve [Lakshminarayana, B. (1996)]

relationship between these two parameters. Figure 1.2 [Lakshminarayana, B. (1996)] plots the actual and ideal performance curves for a typical axial fan. The abscissa and ordinate represent the flow coefficient, Φ, and the head rise coefficient, Ψ, respectively. Φ is a non-dimensional representation of the average upstream axial velocity, $\overline{V} = \dot{m}/\rho A_{inlet}$. It is made non-dimensional by the tangential speed at the fan blade tip: $\vec{V}_{tip} = \boldsymbol{\hat{r}_{tip}} \times \boldsymbol{\Omega}$; $V_{tip} = |\vec{V}_{tip}|$. $\boldsymbol{\Omega}$ is the angular velocity vector of the fan and $\boldsymbol{r_{\hat{tip}}}$ represents the position vector to the tip of the blade. Ψ is a non-dimensional representation of the pressure difference control volume inlet and outlet: ΔP. It is made non-dimensional by: ρV_{tip}^2. In Figure 1.2 the actual curve reaches its max efficiency around the indicated design point. Lakshminarayana notes the following two points about Figure 1.2: When the fan is operated at lower flow coefficient than its design condition it will reach a maximum head rise coefficient indicating the onset of blade stall; Blade stall will cause uncontrolled flow separation along the blade surface and decreased efficiency. [Lakshminarayana, B. (1996)] The present investigation examined various operating conditions along the characteristic curve for the three, five, and nine blade fan configurations.

1.2.3 Characteristic Scales of the Subject Flow

The characteristic scales used in the present investigation are determined by the reference frame in which the measurements are obtained. Measurements obtained in the inertial reference frame, integral data and hot-wire wake measurements, use the following characteristic scales. The tangential velocity at the tip of the blade, V_{tip}, was used as the characteristic velocity magnitude. The tip radius $r_{tip} = |\boldsymbol{\hat{r}_{tip}}|$ was selected as the characteristic length. These scales were selected because they appropriately represent the physical problem (i.e., they are independent variables). As added benefit, they remained constant between all operating conditions and blade configurations of the fan. Measurements obtained in the rotating reference frame, time averaged surface pressure measurements, used difference characteristic scales. The apparent velocity magnitude of the approach flow at the leading edge of the blade, $|\vec{W}| = w_\infty = w_\infty(r)$, as a characteristic velocity magnitude that is a function of radial position. The length scale of this reference frame is the chord length of the blade, $c = 133.9$ mm. This length and velocity magnitude (at the center of the span of the blade) are used in the definition of a chord based Reynolds number, $\mathrm{Re}_c = (\vec{W}(r_{center})c)/\nu$, for the flow over the fan. The Reynolds number for these experiments was of the order $\sim O(10^5)$

Chapter 2

EXPERIMENTAL CONSIDERATIONS

2.1 Axial Flow Research and Development Facility (AFRD)

2.1.1 Overview

The present investigation was conducted using the Axial Fan Research and Development (AFRD) Facility within the TSFL at Michigan State University. This facility was developed to obtain detailed velocity and performance data for axial fans. The inlet of this flow facility was designed to accommodate various fans to be used in a variety of research studies. Previous investigations of axial fans within this facility include: [Morris, S.C. *et. al.* (2001)], [Dusel (2005)], [Neal, D.R. and Foss, J.F. (2007)], [Neal (2010)], [Cawood (2012)], [Davoudi (2014)].

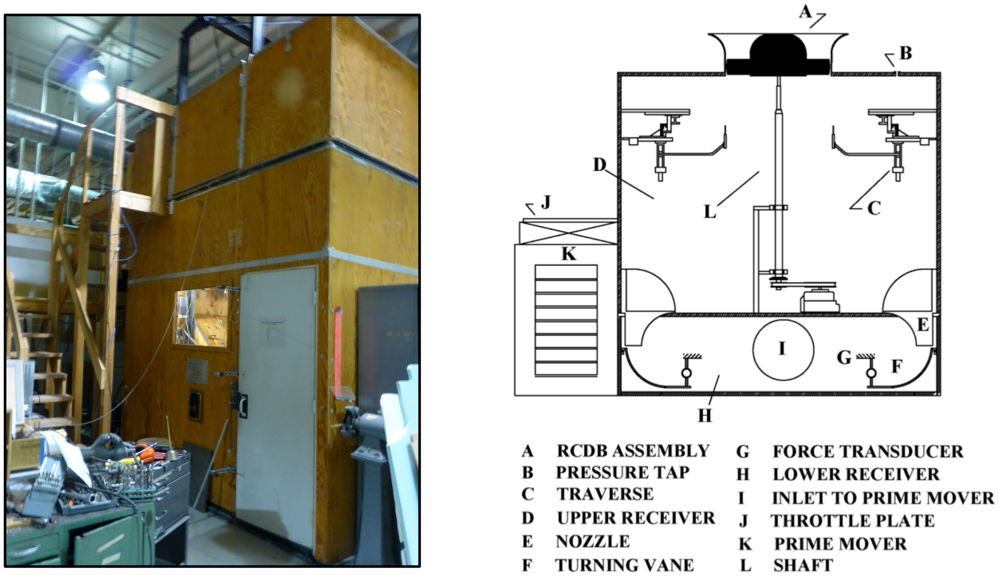

(a) (b)

Figure 2.1 Axial Fan Research and Development Facility: (a) Facility Exterior, (b) Schematic of Facility [Neal (2010)]

Features of the AFRD are labeled in the schematic: Figure 2.1(b). This vertical wind tunnel transported atmospheric air from above the facility into the upper receiver (D) by the action of the fan assembly (A). (See Section 2.2) The prime mover (K) delivered the air from (D) to the atmosphere. The shaft of the test fan was driven by a Reliance Electric 11.2 kW (15 HP) electric D.C. motor with controlled angular velocity. Air entering the facility at (A) is directed to the exit nozzles (E on either side of the facility) into the lower receiver (H). Turning vanes (F) direct those flows, to the inlet of the prime mover (I). These turning vanes measure the "net moment of momentum flux" via a force transducer (G). That magnitude is proportional to the mass flow rate [Morris, S.C. *et. al.* (2001)]. The "net moment of momentum flux" was measured by the moment of the force transducer output about a pivot point. Previous investigations with this fan utilized one turning vane and force transducer to measure the mass flow rate. Due to the higher mass flow rates produced by the nine blade fan both turning vanes and force transducers were used in the present investigation. The throttle plate (J) at the exit of the facility was mechanically driven to adjust the mass flow rate of the system.

2.1.2 Fan Integral Data Experimental Features

Integral fan data were acquired within the AFRD for the present investigation. These data include pressure rise across the fan, mass flow rate through the fan, input shaft torque to the fan, and the angular velocity of the fan. The pressure difference between the upper receiver and atmospheric pressure in the laboratory environment was measured using a wall pressure tap (B) in Figure 2.1(b). The mass flow rate measurement was made with the force transducer in the scheme detailed above (Section 2.1.1). A Himmelstein torque meter, Figure 2.2, was installed on the fan shaft (L) to measure the input shaft torque to the fan from the driving motor. An optical encoder was installed on the shaft of

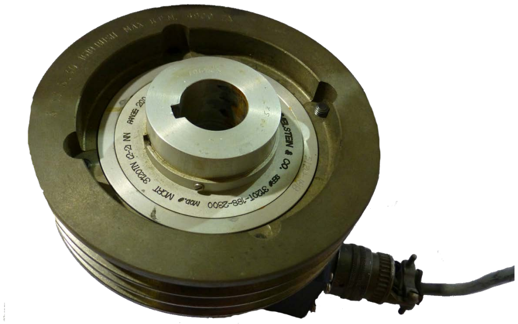

Figure 2.2 Hammelstiein Torque Sensor

the fan to measure its angular position and the angular velocity of the fan. It records the position once per revolution. All of these integral data were recorded using an IOTech Inc. Wave-Book/516E analog to digital acquisition board. This data acquisition board can sample at 1 MHz over 16 separate 16-bit channels.

2.1.3 Near-Wake Velocity Measurements

Downstream velocity measurements in the near-wake of the fan were obtained using the traverse system (C) from Figure 2.1(b). A hot-wire probe was mounted in a stationary position within the wake of the fan to obtain two velocity components as the fan rotated. These data are referenced to azimuthal positions: θ, for a given radial location: r, and downstream location: z. A two wire hot-wire probe, (X-probe), was utilized to obtain these velocity measurements. Figure 2.3 displays a Computer Aided Design drawing of an X-probe. This probe obtains two components of velocity with accuracy in time. An approximate frequency response of 5000 Hz was used in this study.

The present investigation obtained measurements with the X-probe component of a four wire hot-wire (Mitchell) probe, Figure 2.4. The X-probe components of this probe are indicated by the red lines at the sensor location for visual aid. The Mitchell probes used for the present investigation were designed and fabricated at the TSFL. They have

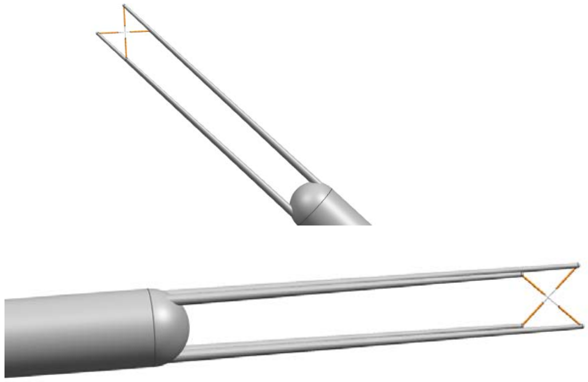

Figure 2.3 Drawing of X-probe

four 5μm diameter 1 mm active length tungsten sensors. Two of these sensors were mounted at opposing 45° angles to the axis along the probe. The tungsten wire was copper plated to assist in mounting the wire to the broaches and to provide aerodynamic isolation of the active sensor. The entire length of each sensor is 3 mm. Two additional wires were mounted normal to the plane made by the X-probe. (that were parallel to each another) All four of these wires in tandem can measure the transverse vorticity in the flow. Further detail in this experimental capability by this type of probe can be found in [Wallace, J.M. and Foss, J.F. (1995)]. The probe used for these measurements will be referred to interchangeably as a X-probe and hot-wire probe for the remainder of this document.

2.1.3.1 Hot-Wire Calibration and Operating Procedure

A TSI IFA-300 constant temperature hot-wire anemometer was utilized for these measurements. Operating hot-wires with this method maintains the tungsten sensor at a (nominally) constant temperature and obtains velocity from the convection caused by the oncoming flow. Therefore, a X-probe must be calibrated in order to be utilized for experimental measurements to know the relationship between velocity and these volt-

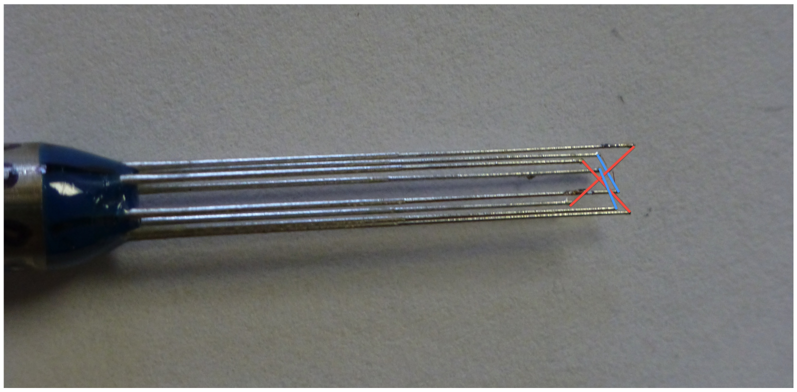

Figure 2.4 Sample Mitchell probe utilized for measurements

age fluctuations. The calibration procedure used in the present investigation has been developed from [Tropea and Foss (2007)]: see Section 5.2.8.

The velocity: Q_i, and incoming angle of the flow: α_i, are related to the output voltage by Equation (2.1) where: E_i is the voltage from the sensor; α_i is the angle of the known calibration flow with respect to the probe axis; Q_i is the velocity magnitude of the incoming flow; and A_i, B_i, and n_i are the calibration constants that relate the anemometer output voltage to the flow velocity for each wire. A single wire probe will evaluate this relationship for $i = 1$ $\alpha_i = 0^\circ$ only and not consider variations in α only obtaining the magnitude of incoming velocity. The X-probe was calibrated at thirteen angles $i = 1$–13 (-36°, -30°, -24°, -18°, -12°, -6°, -0°, 6°, 12°, 18°, 24°, 30°, 36°) in order to accurately resolve all incoming velocities between the two bounding angles. Corresponding A_i, B_i, and n_i values are found for all of the different incoming angles for each wire. These data are used to determine the incoming velocity magnitude and angle with respect to the probe during the experiment.

$$E_i{}^2(\alpha_i) = A_i(\alpha_i) + B_i(\alpha_i){Q_i}^{n_i(\alpha_i)} \tag{2.1}$$

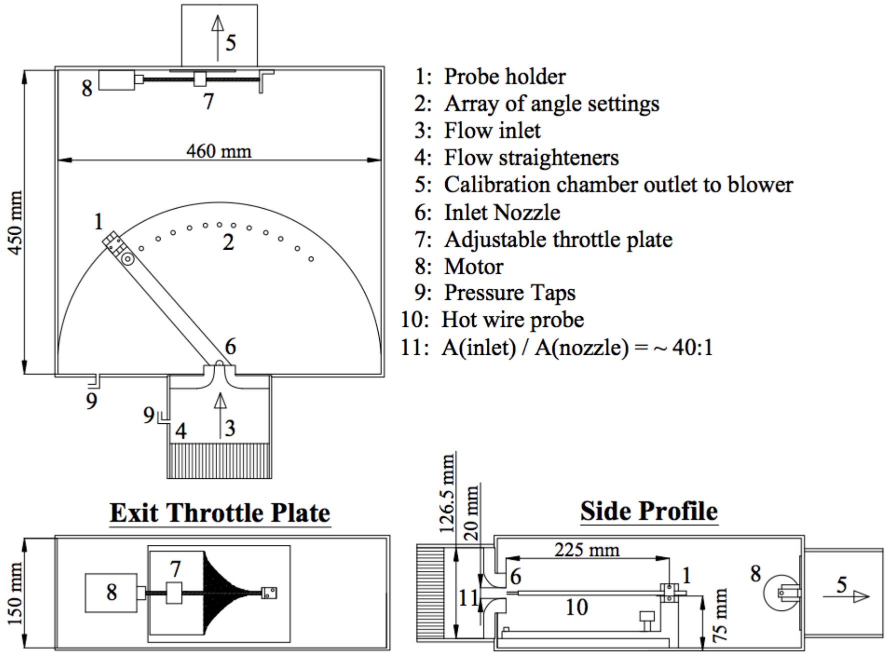

Figure 2.5 Hot-wire calibration facility [Neal (2010)]

Figure 2.5 displays the calibration facility that was used to calibrate the X-probe before and after experimental use. The probe was mounted in the probeholder: 1, with the plane of the X (made by the two wires) parallel to the bottom of the calibration facility. Pressure taps: 9, are used to calculate the velocity of the air exiting the inlet nozzle: 6, by the Bernoulli Equation. The inlet velocity to the probe was (slowly) reduced by closing the exit throttle plate: 7, to allow for a quasi-steady state calibration. In this investigation the calibration data were sampled for 60 second intervals at 20 kiloHertz for each calibration angle. These thirteen data files were then processed to obtain the corresponding A_i, B_i, and n_i from Equation (2.1) for each wire.

Figure 2.6 displays the method that was used to determine the velocity magnitude and angle for any given instantaneous output voltages from each hot-wire. Each voltage is processed in Equation (2.1), with the appropriate constants for each wire. These velocities and angles for the voltages are plotted. The intersection between the two curves made

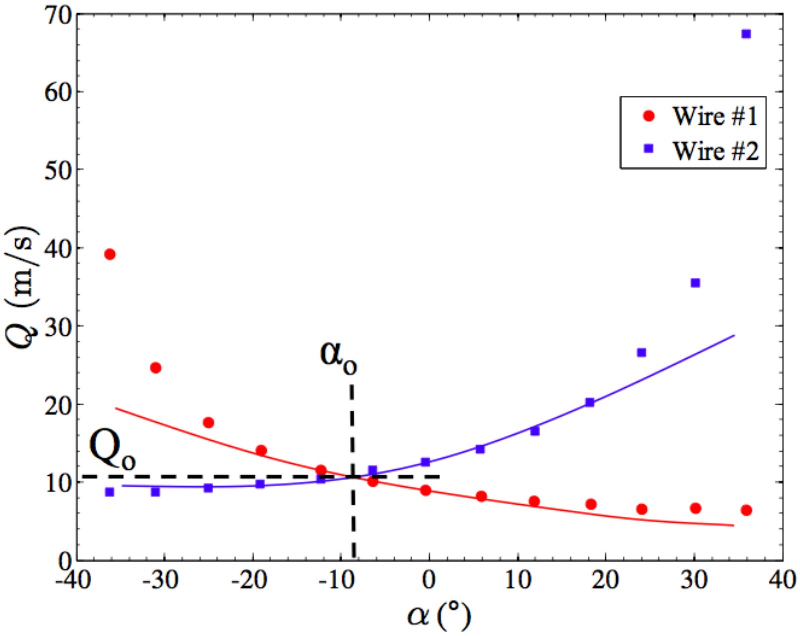

Figure 2.6 Example of how the magnitude Q_o and angle α_o of the velocity are found relative to the probe from the output voltages [Neal (2010)]

from the processed data give the velocity magnitude and angle of the oncoming flow with respect to the probe axis. Further details regarding calibration methods for a X-probe can be found in [Tropea and Foss (2007)]: see Section 5.2.8.

Proper experimental technique requires calibration of the probe before and after obtaining measurements in the wake of the fan. This ensures that the probe response did not drift significantly over the course of the experiment. Typically a calibration is accurate for three hours. The validity of the two calibrations was confirmed by processing a set of calibration data with A_i, B_i, and n_i from both calibrations and comparing the difference in velocity magnitude and angle ensuring that they were within 5% of each other. A histogram of the angles obtained by the probe during each experimental measurement was analyzed for each data set to ensure that maximum percentage of pitch angles: α_i, at the probe did not exceed the calibration range. The extremes of the calibration angles bound

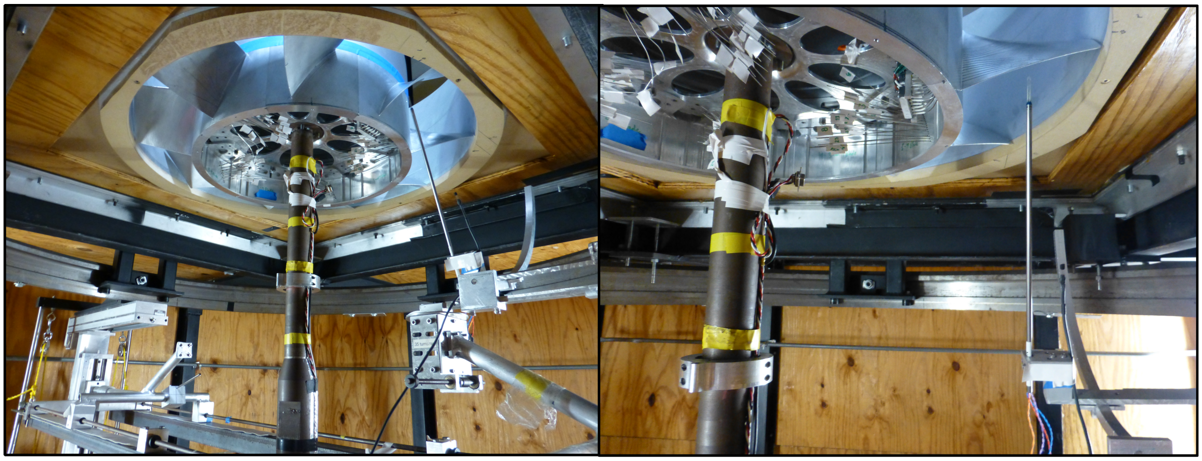
(a) (b)

Figure 2.7 Mounted X-probe in fan wake

the measurement capability of this device. Maximizing the measurement capability of the probe in this regard was accounted for in these measurements.

2.1.3.2 Stationary Mount

Once calibrated, the X-probe was mounted on the traverse system in the wake of the fan, Figure2.1(b)(C). Figure 2.7 displays the X-probe mounted in the wake of the fan from two different perspectives. Figure 2.8 provides a close up of the probe mounted downstream of the fan. The measurement portion of the X-probe was mounted 6 millimeters below the fan in z and at mid-span of the blade to minimize hub and tip flow effects. Small variations in fabrication of the fan blades caused the distance in z to vary slightly from blade to blade. Due to the fast response of the X-probe an accurate time history of the velocity in the wake was obtained. These data were phase averaged to calculate the means and statistics of the velocity in the wake for all θ using the optical encoder signal on the shaft indicating fan position.

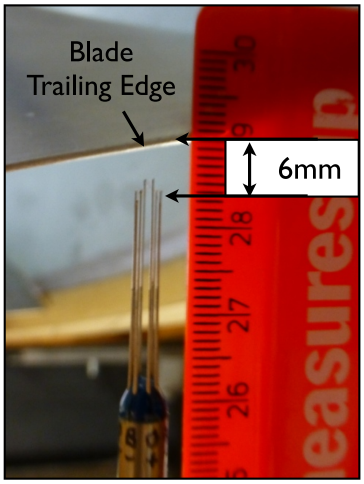

Figure 2.8 Close up of probe in fan wake

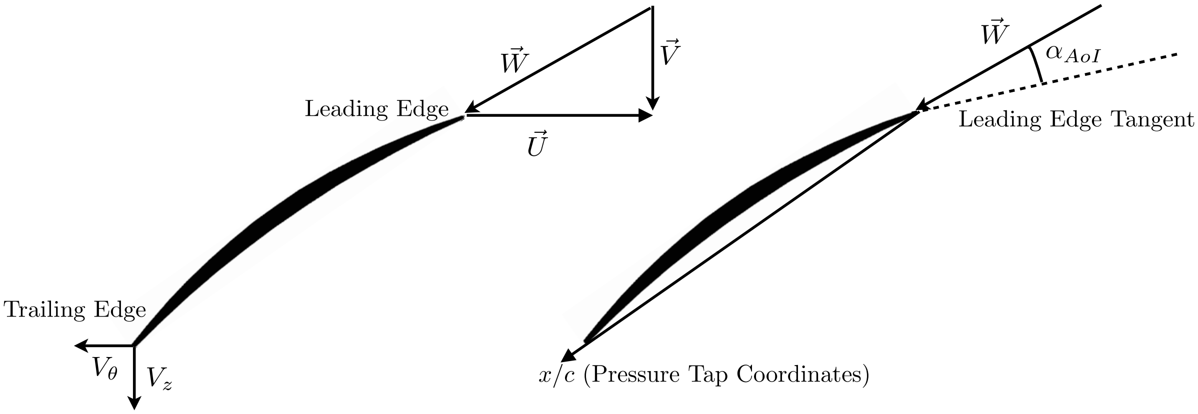

Figure 2.9 Incoming velocity profile

2.2 Controlled Diffusion Blade Axial Fan

2.2.1 Incoming Velocity

The apparent velocity to an observer on the leading edge of the fan blade can be represented by Equation (2.2). The velocity of the air with respect to the blade: $\vec{V}_{a/b}$, is the vector sum of the velocity of the air with respect to the ground: $\vec{V}_{a/g}$, and the velocity of the ground with respect to the blade: $\vec{V}_{g/b}$.

$$\vec{V}_{a/b} = \vec{V}_{a/g} + \vec{V}_{g/b} \tag{2.2}$$

This description is equivalent to Equation (2.3) presented with traditional turbomachinery nomenclature. Where: $\vec{W}$ represents the apparent incoming velocity to the blade given by the vector sum of the axial inlet velocity $\vec{V}$ and tangential velocity at the tip $\vec{U}$. The definitions of $\vec{V}$ and $\vec{U}$ are provided in Equation (2.4).

$$\vec{W} = \vec{V} - \vec{U} \tag{2.3}$$

$$\vec{U} = \vec{U}(r) = \hat{\boldsymbol{r}} \times \boldsymbol{\Omega} \; ; \; \overline{V} = \frac{\dot{m}}{\rho A_{inlet}} \tag{2.4}$$

The incoming velocity to a blade on the fan is displayed in Figure 2.9 in traditional turbomachinery nomenclature. The angle of incidence α_{AoI} is also noted in Figure 2.9 and is positive as indicated. α_{AoI} is the angle between the apparent incoming velocity $\vec{W}$ and the tangent to the leading edge of the blade.

2.2.2 Fan Assembly

This modular fan has nine blades available for installation and can be assembled with two to nine blades. Figure 2.10(a) displays the five blade fan mid-assembly. Figure 2.10(b) displays the inner and outer shroud of the fan while the five blade fan is mounted.

2.2.3 Experimental Features

2.2.3.1 Instrumented Blades

Five of the nine available blades for the fan have pressure taps installed on both surfaces of the airfoil. These blades have the same stream wise distribution of pressure taps. There are eighteen pressure taps along this chord line at a given span position for each blade and an additional three span wise taps located near the trailing edge of the blade. A photo indicating the locations of the pressure taps on the suction and pressure

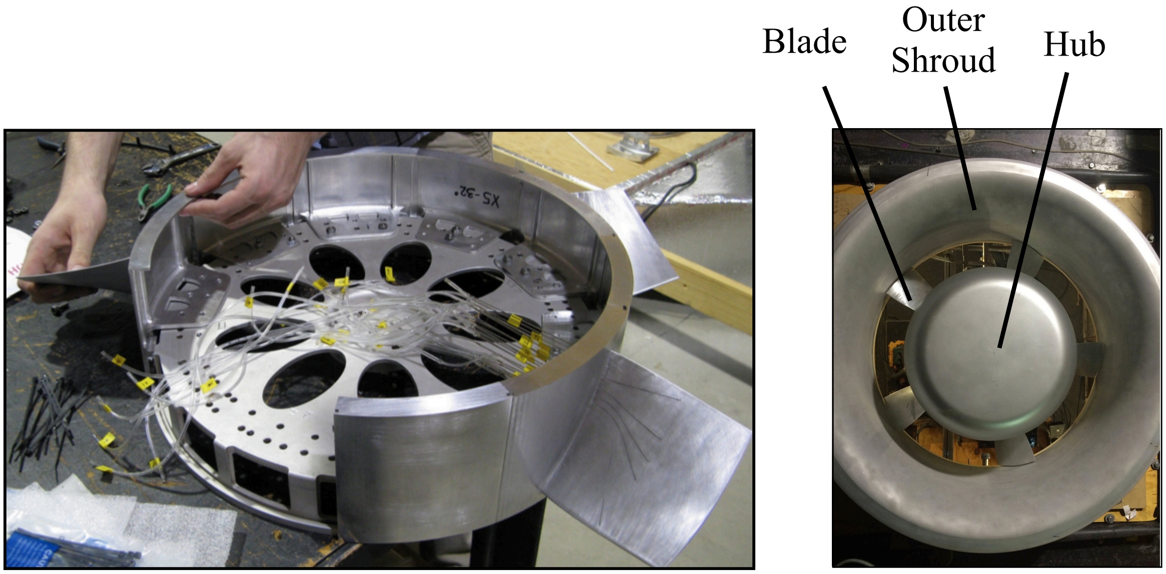

(a)

(b)

Figure 2.10 Fan Assembly: (a) five blade fan mid-assemby [Neal (2010)], (b) five blade fan mounted and shroud

Table 2.1 Pressure tap locations on the suction side of the blade

Tap	1	2	3	5	6	7	9	11	21	22	23	24	25
x/c	.013	.030	.052	.087	.149	.403	.534	.679	.858	.881	.899	.922	.978

side of the center span instrumented blade is provided in Figure 2.11.

The leading and trailing edge regions of the suction side of the blade have higher concentrations of pressure taps to examine the boundary layer behavior in those regions of the blade. The leading edge region will indicate the transition from a laminar to a turbulent boundary layer. The trailing edge region indicates if the flow is still attached leaving the trailing edge.

Tables 2.1 and 2.2 provide the chord position, x/c, of the eighteen stream wise pressure

Table 2.2 Pressure tap locations on the pressure side of the blade

Tap	4	8	10	12	29
x/c	.067	.400	.530	.675	.929

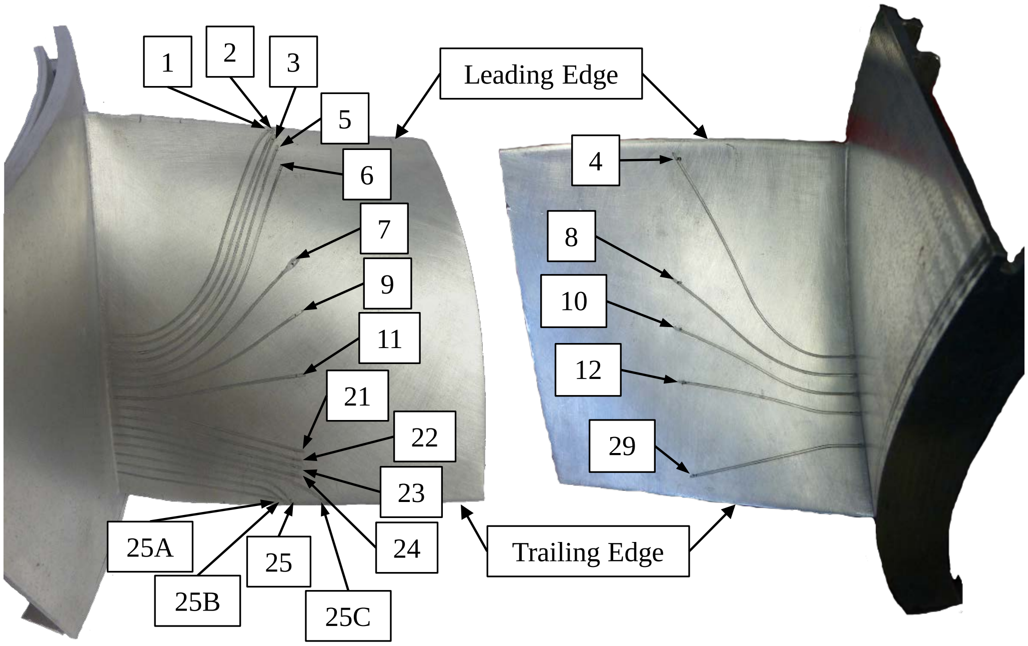

Figure 2.11 Suction and pressure side, left and right respectively, pressure taps indicated x/c distances corresponding to Tables 2.1 and 2.2

Table 2.3 Pressure tap locations on the suction side of the blade along the trailing edge

Tap	25A	25B	25	25C
Blade Color	η			
Red	.073	.096	.119	.196
Blue	.264	.287	.310	.387
Green	.454	.477	.500	.577
Black	.724	.747	.770	.847
Yellow	.827	.850	.873	.950

taps. Table 2.3 provides the radial position of the pressure taps that are represented non-dimensionally as η defined by Equation (2.5). Note that η ranges from 0–1 from *hub–tip*.

$$\eta = \frac{r_{tap} - r_{hub}}{r_{tip} - r_{hub}} \tag{2.5}$$

Figure 2.12 provides the five different radial locations that pressure measurements can be collected with this equipment. The color of the line indicating each radial location will be used to distinguish the different radial locations in plots of the experimental results.

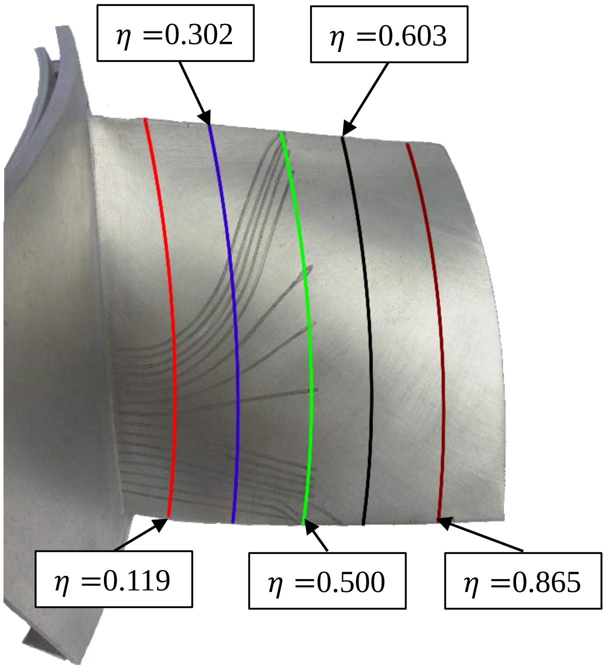

Figure 2.12 Streamwise distribution of pressure taps and η locations

2.2.3.2 Instrumentation in the Rotating Environment

An instrument cluster was developed to mount within the hub of the fan to obtain various experimental data. Figure 2.13 displays the instrument cluster indicating the features of interest for the present investigation. The measurement capabilities of this instrument cluster will be detailed in the following subsections.

2.2.3.2.1 Mean Surface Pressure

Time averaged pressure measurements were obtained in the rotating reference frame utilizing 21 pressure transducers. Figure 2.14 displays the scale of the All Sensors model D2-4V-MINI pressure transducers that were installed in the instrument cluster. Seven of these transducers have ±5 inch H_2O measurement ranges and the other fourteen transducers have ±1 inch H_2O measurement ranges. To operate a pressure transducer, a known reference pressure must be connected on one side of the measurement diaphragm.

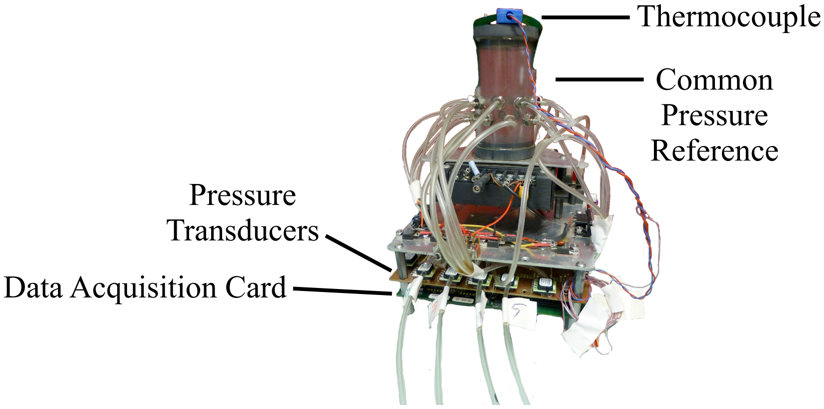

Figure 2.13 Instrument cluster

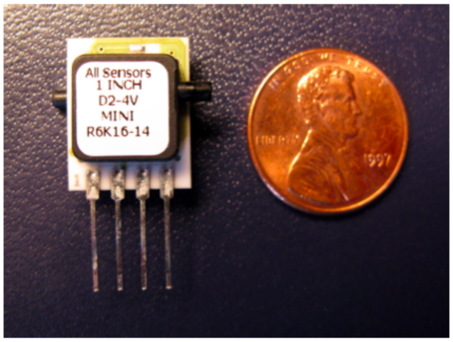

Figure 2.14 Pressure transducer scale [Neal (2010)]

The instrument cluster is equipped with a common reservoir for all of the pressure transducers; see Figure 2.13. This chamber is open to the environment inside of the hub which is the pressure inside the receiver: P_{rec}. The pressure differential measurement between the atmosphere and the upper receiver detailed in Section 2.1.2 allows for the common reference to be brought to atmospheric pressure: P_{atm}.

Centrifugal forces from the rotating environment act on the air within the connecting tubes from the pressure tap (hypodermic tubing) to the pressure transducer. A method was developed [Neal (2010)] to account for these effects given in Equation (2.6). ΔP_{corr1} and ΔP_{corr2} are the centrifugal corrections for each tube on either side of the diagram

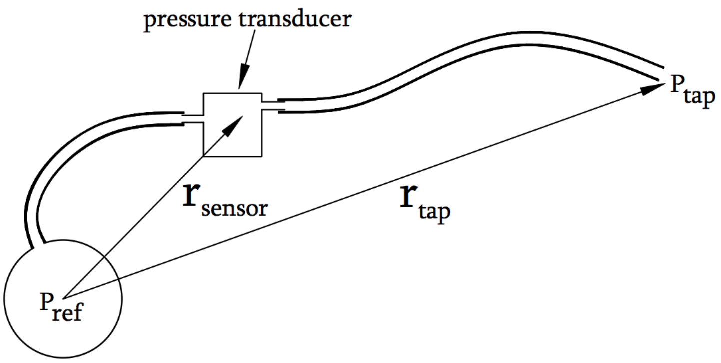

Figure 2.15 Pressure measurement schematic [Neal (2010)]

of the pressure transducer.

$$\Delta P_{corr1} = \frac{\rho|\mathbf{\Omega}|^2(r_{tap}^2 - r_{sensor}^2)}{2} \ ; \ \Delta P_{corr2} = \frac{\rho|\mathbf{\Omega}|^2(r_{sensor}^2 - r_{ref}^2)}{2} \tag{2.6}$$

$$\Delta P_{actual} = \Delta P_{measured} + \Delta P_{corr1} + \Delta P_{corr2} \tag{2.7}$$

Figure 2.15 indicates the radial locations of the pressure taps and sensors respectively. Equation (2.7) provides the formulation for the actual pressure difference between the pressure tap and common reference chamber, $\Delta P_{actual} = P_{tap} - P_{ref}$. This equation can be simplified to Equation (2.8) because the common reference chamber was installed at the axis of rotation, $r_{ref} = 0$.

$$\Delta P_{actual} = \Delta P_{measured} + \frac{\rho|\mathbf{\Omega}|^2 r_{tap}^2}{2} \tag{2.8}$$

$$P_{tap(gage)} = \Delta P_{measured} + \frac{\rho|\mathbf{\Omega}|^2 r_{tap}^2}{2} + (P_{rec} - P_{atm}) \tag{2.9}$$

The pressure difference can be further adjusted to gage pressure by adding the pressure difference between the upper receiver pressure and atmosphere, $P_{rec} - P_{atm}$, to the right hand side of Equation (2.8) provided in Equation (2.9). The gage pressures at the taps was used in the calculation of pressure coefficients for the present investigation.

2.2.3.2.2 Fluctuating Surface Pressure

Cawood (2012) developed a method using microphones to obtain the unsteady surface pressure measurements at each pressure tap for the $\eta = 0.5$ instrumented blade. These measurements were used to characterize the behavior of the boundary layer on the suction surface of the blade for two different operating conditions. This capability was not utilized for the present investigation. The details of the development, use and results of this measurement capability are found in *Surface Pressure Measurments on a Rotating Controlled Diffusion Blade* [Cawood (2012)].

2.2.3.2.3 Rotating Hot-Wire Wake Velocity

Neal (2010) and Cawood (2012) both obtained hot-wire data in the wake of a fan blade with the probe moving with the fan. Similar measurements were not obtained for any of the cases within the present investigation. The details of the development, use, and results of this measurement capability are found in *The Effects of Rotation on the Flow Field Over a Controlled Diffusion Airfoil* [Neal (2010)] and *Surface Pressure Measurments on a Rotating Controlled Diffusion Blade* [Cawood (2012)].

2.2.3.2.4 Data Acquisition

Measurements within the hub assembly are obtained with the IOTech Inc. DaqBoard/ 3035USB data acquisition board. This data acquisition board sampled at 1 MegaHertz over 64 separate 16-bit channels. The position of this data acquisition board is indicated in Figure 2.13. In order for this board to be controlled and its obtained data stored, signals were transmitted to and from the instrument cluster via a slip ring (Figure 2.16) installed on the shaft. Electrical connections on the rotating and stationary side of the slip ring connected the power signal to the instrument cluster along with a data USB connection. The digital signal minimized data loss using the slip ring assembly. This is in contrast to an analogue signal that would be degraded from the electrical noise produced by the slip ring assembly. USB cable length limits forced the computer controlling the DaqBoard to be placed inside the AFRD. It was controlled remotely outside of the facility via ethernet connection.

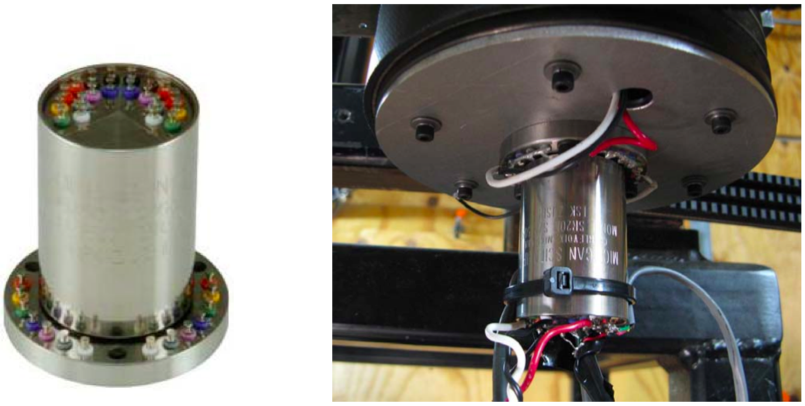

Figure 2.16 Slip ring assembly at the base of the fan shaft [Neal (2010)]

Chapter 3

RESULTS AND DISCUSSION

3.1 Fan Integral Measurements

Initial experiments for the present investigation focused on obtaining integral data for a variety of fan configurations. The seven separate configurations with three to nine blades were selected for this comparison. Obtained integral data measurements consisted of the pressure rise across the fan plane, the mass flow rate though the fan plane, and the input shaft torque to the fan supplied by the driving motor, as discussed in Section 2.1.2.

3.1.1 Characteristic and Torque Curves

The characteristic curve examines the behavior of the pressure rise from inlet to exit of the selected control volume of interest via the head rise coefficient: Ψ, as a function of the flow coefficient: Φ. Control Volume (1) was selected to compare the the head rise coefficient and flow coefficient for the selected fans. Ψ_1 and Φ are defined in Equation (3.1). The data collected from the three to nine blade fans with Control Volume (1) is displayed in Figure 3.1. These data were collected for a low flow coefficient up to the zero head rise coefficient operating condition.

$$\Psi_1 = \frac{P_{rec} - P_{atm}}{\rho V_{tip}^2} \ ; \ \Phi = \frac{\overline{V}}{V_{tip}} \tag{3.1}$$

Each of the fans exhibit similar behavior as the flow coefficient is decreased from the zero head rise coefficient (right to left on Figure 3.1). The trajectory of these curves is different between fan configurations and corresponds to higher magnitude slope as the number of blades is increased moving from left to right. One major difference occurs midway

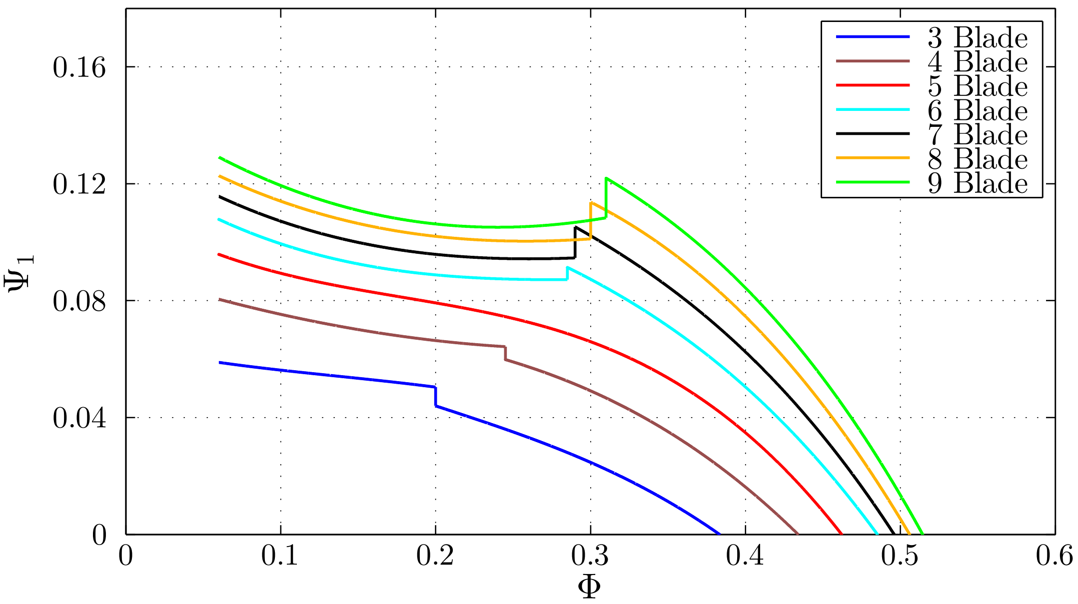

Figure 3.1 Three to nine blade fan characteristic curves

through the span of mass flow rates considered for these fans. All fan configurations, except for the five blade fan, experience a discontinuity in the performance curve. This discontinuity manifests itself as a head rise coefficient jump for three and four blade fans, a smooth curve for the five blade fan, and a head rise coefficient drop for the six through nine blade fans with decreasing flow coefficient. This behavior of the performance curve suggests that the flow is separating through aerodynamic stall. The different behavior at these discontinuities was selected as an area of interest for further study in the present investigation

Torque measurements were also obtained for these operating conditions of the seven fan configurations. These data are presented in Figure 3.2. The non-dimensional torque, T^*, is defined by Equation (3.2). These curves have been plotted over the range of low flow coefficient, 0.5, to the flow coefficient of zero pressure rise for each individual fan. These curves show a similar trend between number of blades and the amount of torque

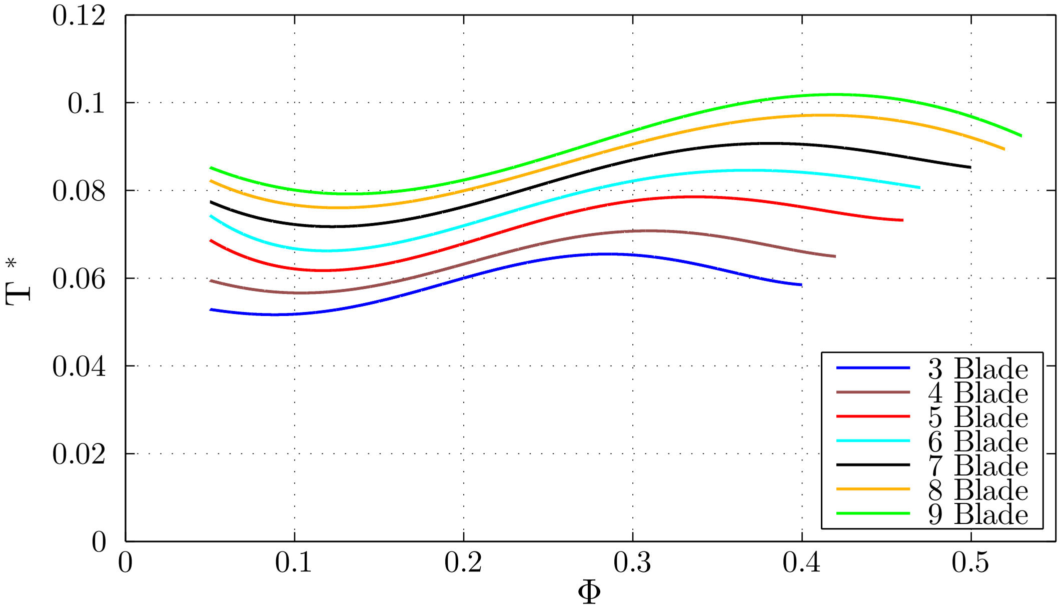

Figure 3.2 Three to nine blade fan torque curves

required to drive the fan at the same flow coefficient. The maximum torque for these fans is located on the right side of the discontinuity of the characteristic curves from Figure 3.1. It is important to note that the minimum operating torque is found on the low flow coefficient side of the characteristic curve and suggests that separated flow on the suction side of the blades is decreasing the necessary torque to drive the fan. The torque will eventually increase as flow coefficient moves to zero from the fan pressurizing the receiver.

$$\mathrm{T}^* = \frac{Torque}{r_{tip} \times \rho V_{tip}^2 r_{tip}^2} \tag{3.2}$$

3.1.2 Operating Configurations and Conditions Selection

Operating conditions were selected from the characteristic curve for further study in the present investigation. The three, five, and nine blade fans were selected to examine the differences between the three characteristic curves at the "stall" condition. Additionally, five operating conditions were selected for these fans. These operating conditions

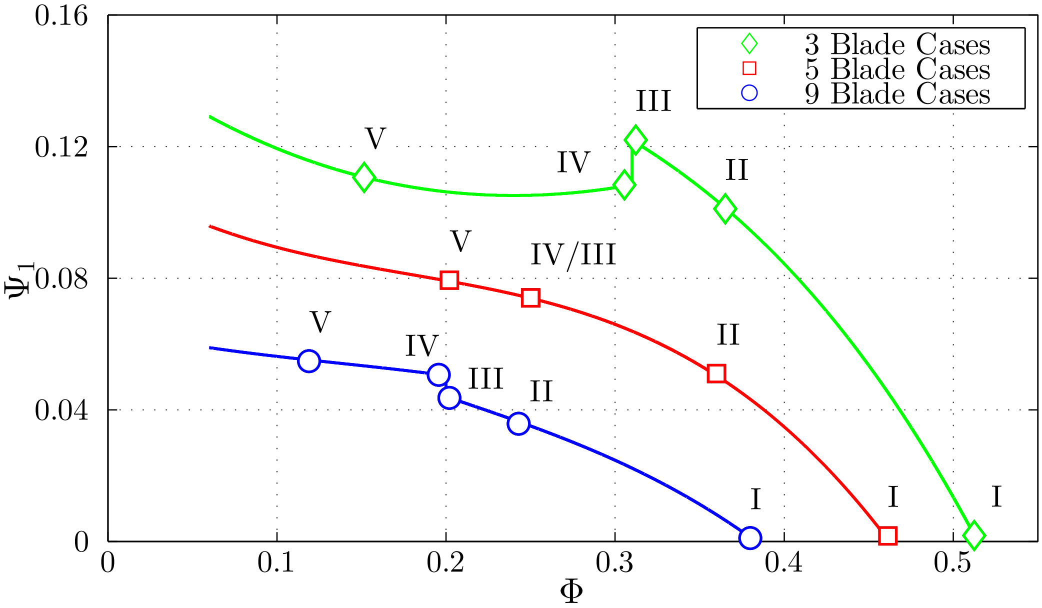

Figure 3.3 Experimental operating conditions indicated on characteristic curves for Control Volume (1)

have been marked on Figure 3.3 with roman numerals to represent Cases: I, II, III, IV, and V. These operating conditions represent five distinct points on the three and nine blade fan configurations and four operating points on the five blade configuration. Case I was selected to compare the zero head rise coefficient condition (Control Volume (1)) for each fan. Case II was selected to represent a point before the onset of the discontinuity for the three and nine blade fans. Case III was selected as the right hand side of the discontinuity on the characteristic curve for the three and nine blade fans. Case IV was selected as the low flow coefficient side of the discontinuity on the characteristic curve for the three and nine blade fans. The five blade fan considers these points as one with paired III and IV operating condition since its characteristic curve is continuous. Case V is a low flow coefficient operating condition for the three, five, and nine blade fans.

The characteristic curve was also evaluated with Control Volume (2) for the fan configurations of interest in the present investigation. These characteristic curves are

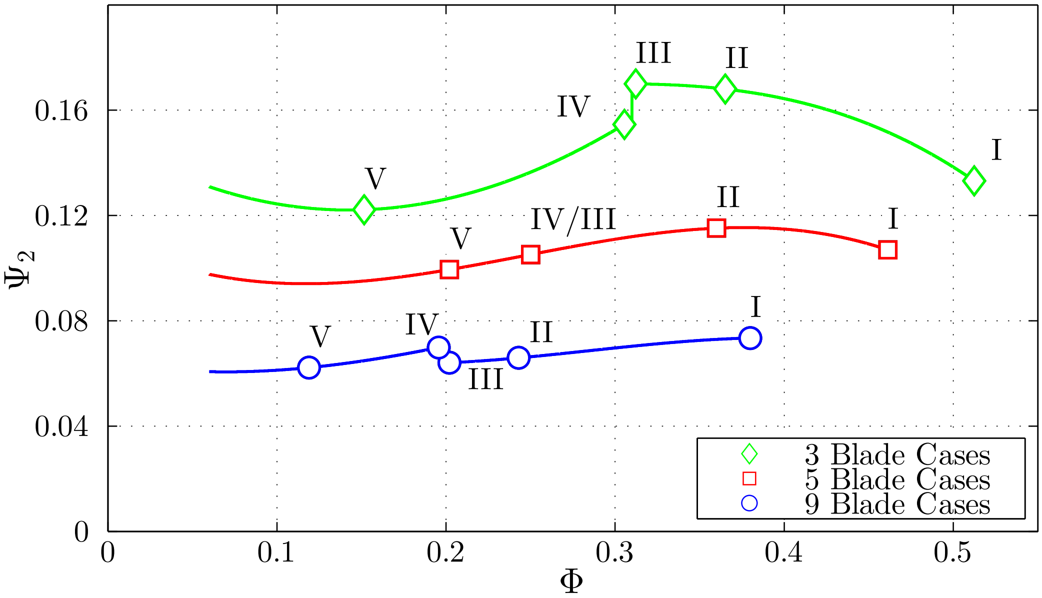

Figure 3.4 Experimental operating conditions indicated on characteristic curves for Control Volume (2)

provided in Figure 3.4. The head rise coefficient for Control Volume (2) is given by Equation (3.3). These data continue to have the discontinuity in the performance curve but they are noticeably flattened. There is less variation between the different conditions in the head rise coefficient as defined for Control Volume (2). The number of blades on the fan has a direct relationship with how much variation in pressure is present as Φ is varied. This is a direct effect of the flow coefficient increasing as the number of blades is increased for similar head rise coefficients in Control Volume (1), where the inlet kinetic energy is negligible into the control volume.

$$\Psi_2 = \frac{P_{rec} - P_{atm} + 1/2\rho\overline{V}^2}{\rho V_{tip}^2} \qquad (3.3)$$

The the torque curves for the selected fan configurations and operating conditions have been indicated on Figure 3.5.

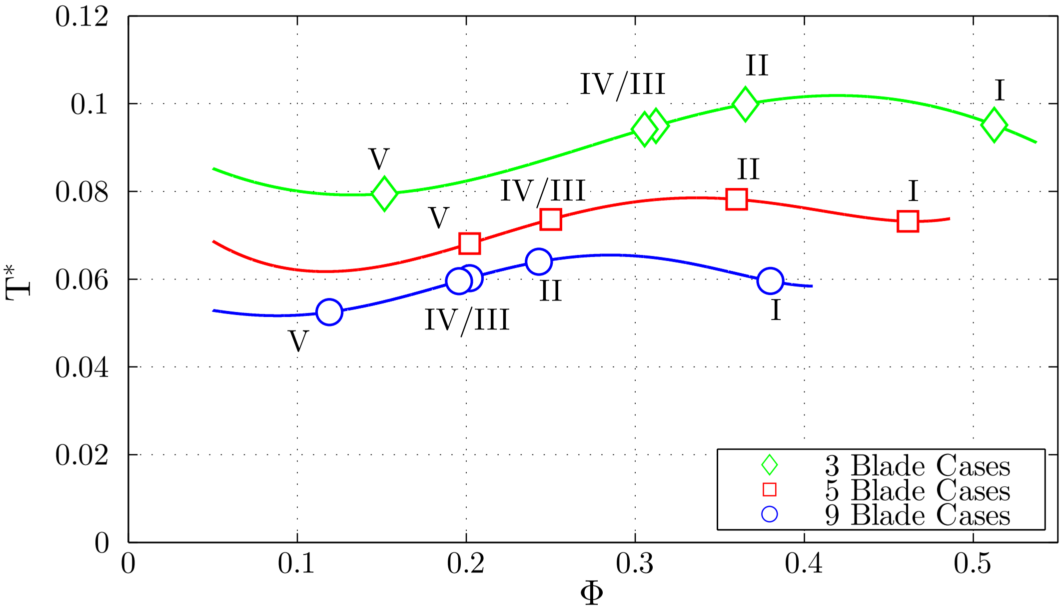

Figure 3.5 Experimental operating conditions indicated on torque curves

Understanding the oncoming flow to the fan blades is paramount in interpreting the results from the present investigation. Figure 3.6, provides the angle of incidence as a function of span location: η for the different fan configurations and operating conditions. As the conditions move up the characteristic curve from I to V there is a distinct increase in angle of incidence. This is caused the change in mass flow rate from condition I to V. Figure 2.9 displays the relationship between the mass flow rate and the angular velocity of the fan that determined the apparent approach velocity and its angle with respect to the tangent of the leading edge of the blade. For all of these experiments the angular velocity was held constant. Therefore, as the mass flow rate is decreased the angle between the apparent incoming velocity, $\vec{W}$, and the leading edge tangent direction will increase. Thus, the angle of incidence will increase in the positive direction. As the incidence angle of the flow is increased it will become difficult for the CD blade to control the flow on the suction side of the blade. The angles of incidence for these operating conditions

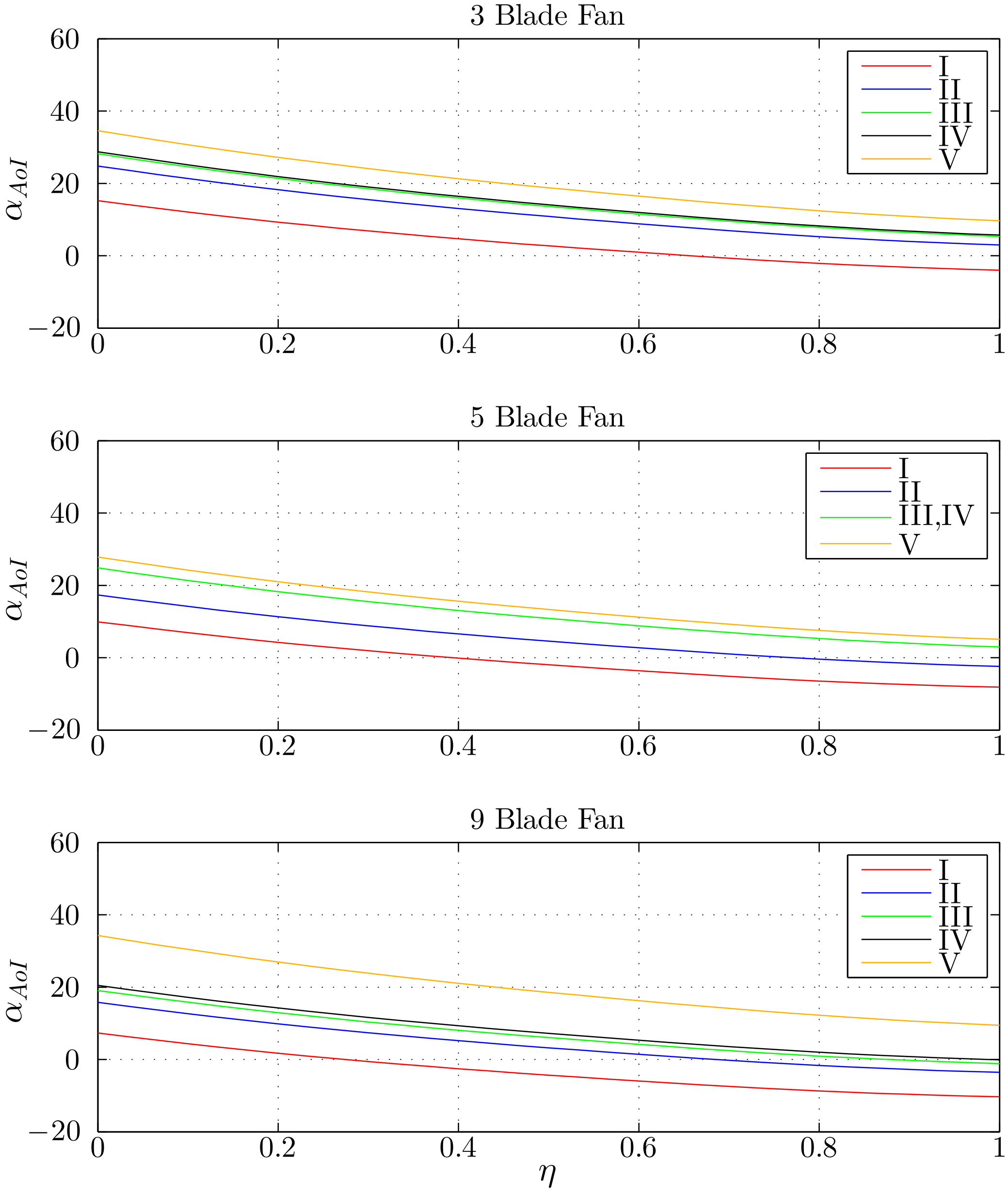

Figure 3.6 Angle of incidence α_{AoI} across the blade for all operating conditions and fan configurations

suggest that there will be flow separation on the suction side of the blade at low flow coefficient. The angle of incidence becomes more favorable at the tip of the blade. This is a product of $\vec{U}(r)$ component of the approach velocity from Figure 2.9. The effects of flow separation from high the angle of incidence occur at a higher flow coefficient as the number of blades installed on the fan is decreased.

3.2 Pressure Coefficients

Time averaged surface pressure measurements were obtained for the selected operating conditions and fan configurations for the present investigation. These measurements provide the pressure difference between the surface pressure and laboratory atmospheric pressure which can be expressed non-dimensionally as the pressure coefficient. Equation (3.4) provides the definition of the pressure coefficient. The pressure coefficients obtained in the present investigation were used to evaluate a non-dimensional lift coefficient for the blade. Equation (3.5) provides the integral that was evaluated across the blade surface to provide a representative value of lift. This lift coefficient is representative of one blade within the system. It is also useful to consider the lift generated by all of the blades installed on the fan to compare each fan configuration. These pressure data were sampled at 5 kHz for a duration of 10 seconds and averaged over five separate samples.

$$\mathrm{C_P} = \frac{(P_{tap} - P_{atm})}{1/2 \rho w_{\infty}^2} \tag{3.4}$$

$$\mathrm{C}_l = \int_0^1 \int_0^1 (\mathrm{C}_{\mathrm{P},pressure} - \mathrm{C}_{\mathrm{P},suction}) \, d(x/c) \, d\eta \tag{3.5}$$

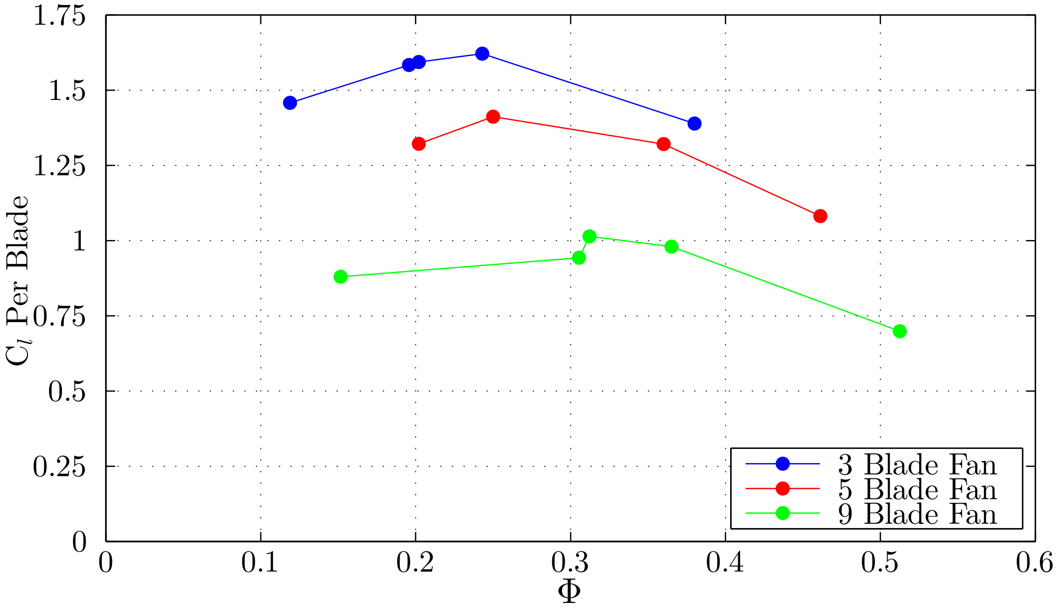

Figure 3.7 Non-dimensional lift coefficient for single blade

3.2.1 Lift Analysis

Figure 3.7 provides the non-dimensional lift coefficient for an individual blade on the three, five, and nine blade fans. An opposite trend between the overall lift coefficient for an individual blade is apparent as the number of blades is increased. The non-dimensional lift per blade is maximized with the three blade fan configuration. Figure 3.8 provides the overall lift for the entire fan assembly which provides greater overall lift with increasing number of blades. This increase in lift correlates with the increase in torque necessary to drive the fan from Figure 3.5. The integral measurements correlate with the measured surface pressure providing validation that these measurement techniques are responding appropriately.

3.2.2 Pressure Coefficient Profiles

Figures 3.9–3.13 provide the complete pressure coefficient profiles for the three, five, and nine blade fan configurations. Each of these figures represents a single operating

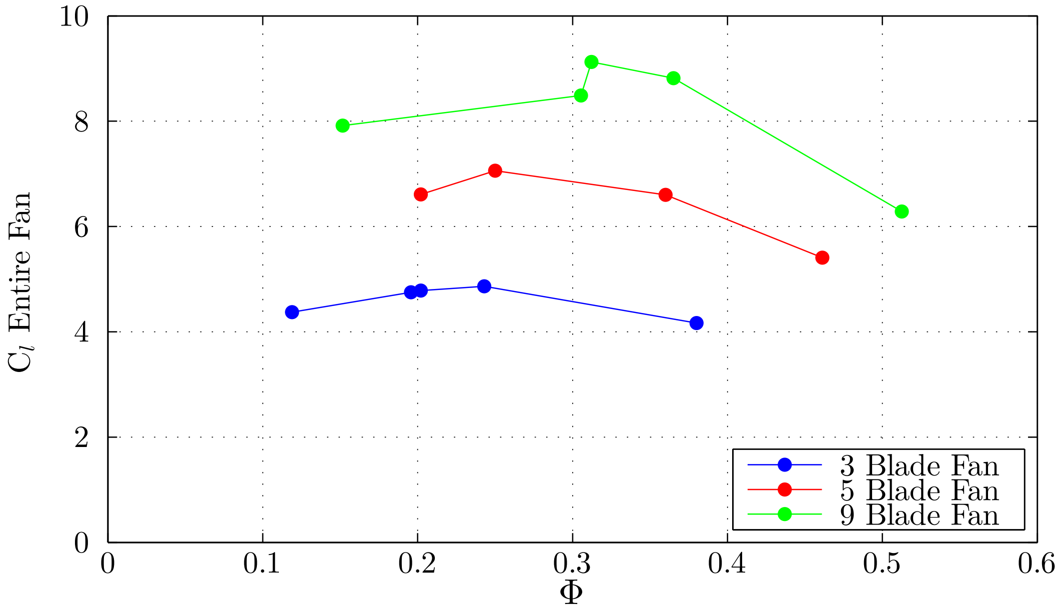

Figure 3.8 Non-dimensional lift coefficient for entire fan

condition (Case I, Case II, etc.) and will be referred to by operating condition in this section of the document. The legend for each of these figures is located in the nine blade fan section of the figure. The ordinates of these axes were reversed to visualize the suction side and pressure side of the blade as they are perceived when viewing the profile of the blade. These distributions were used in Equation (3.5) to evaluate C_l. These figures are provided by Case and fan configuration in Appendix A.

Overall, the magnitude of the pressure coefficients near the leading edge of the suction surface of the blade shows an opposite trend to the number of the installed fan blades. The pressure coefficients are much smaller in magnitude on the nine blade fan compared to the three and five blade fans for all Cases I–V. This is interpreted as a of a blade to blade interaction suppressing the suction side pressure on the nine blade fan. The proximity of the adjacent pressure side of the next blade would have the ability to be the causal factor for these differences. The magnitude of the pressure coefficients is comparable for the three and five blade fans for Cases II–V. Case I shows distinctly different pressure coefficient distributions for the three different fan configurations. The angles of incidence for Case I across the blade for all three fans are more favorable. The boundary layer develops differently from leading to trailing edge at different η locations across the blade surface. The negligible variations between Case IV and V suggest that the flow is separated on the suction surface of the blade at Case IV. Moving to a lower flow coefficient does not significantly impact these distributions. The three and five blade fans do not experience much change between Case II–V. This may indicate that the flow has separated for these fan configurations at Case II. This suggests that the discontinuity in the characteristic curve for the six to nine blade configurations may be influenced by the onset of stall. It is important to note that the fan was designed to operate at a flow coefficient that would create a pressure drop across the fan when considering Control Volume (1). The present investigation was purposefully limited to $\Psi_1 \geq 0$.

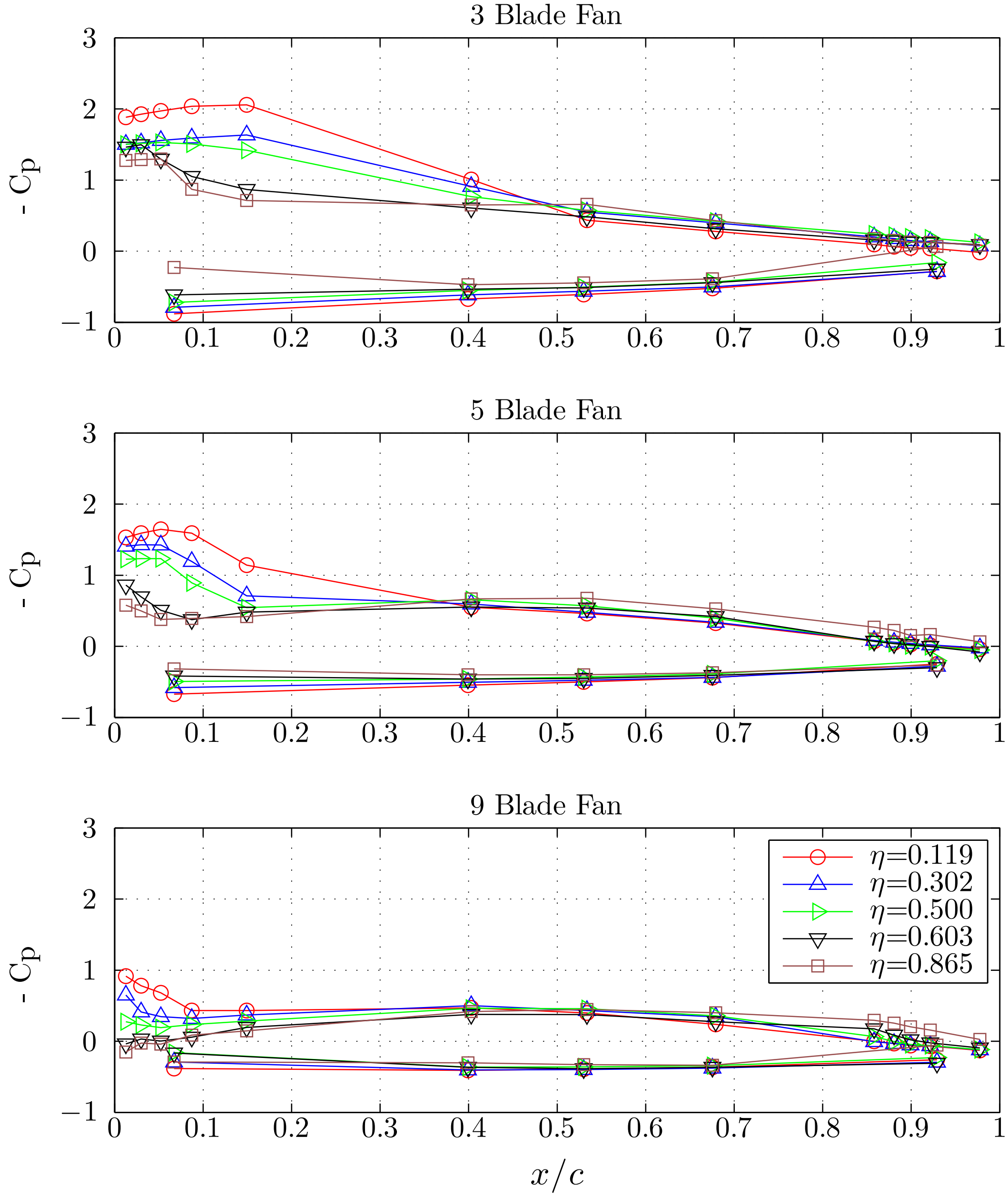

Figure 3.9 Pressure coefficients at Case I

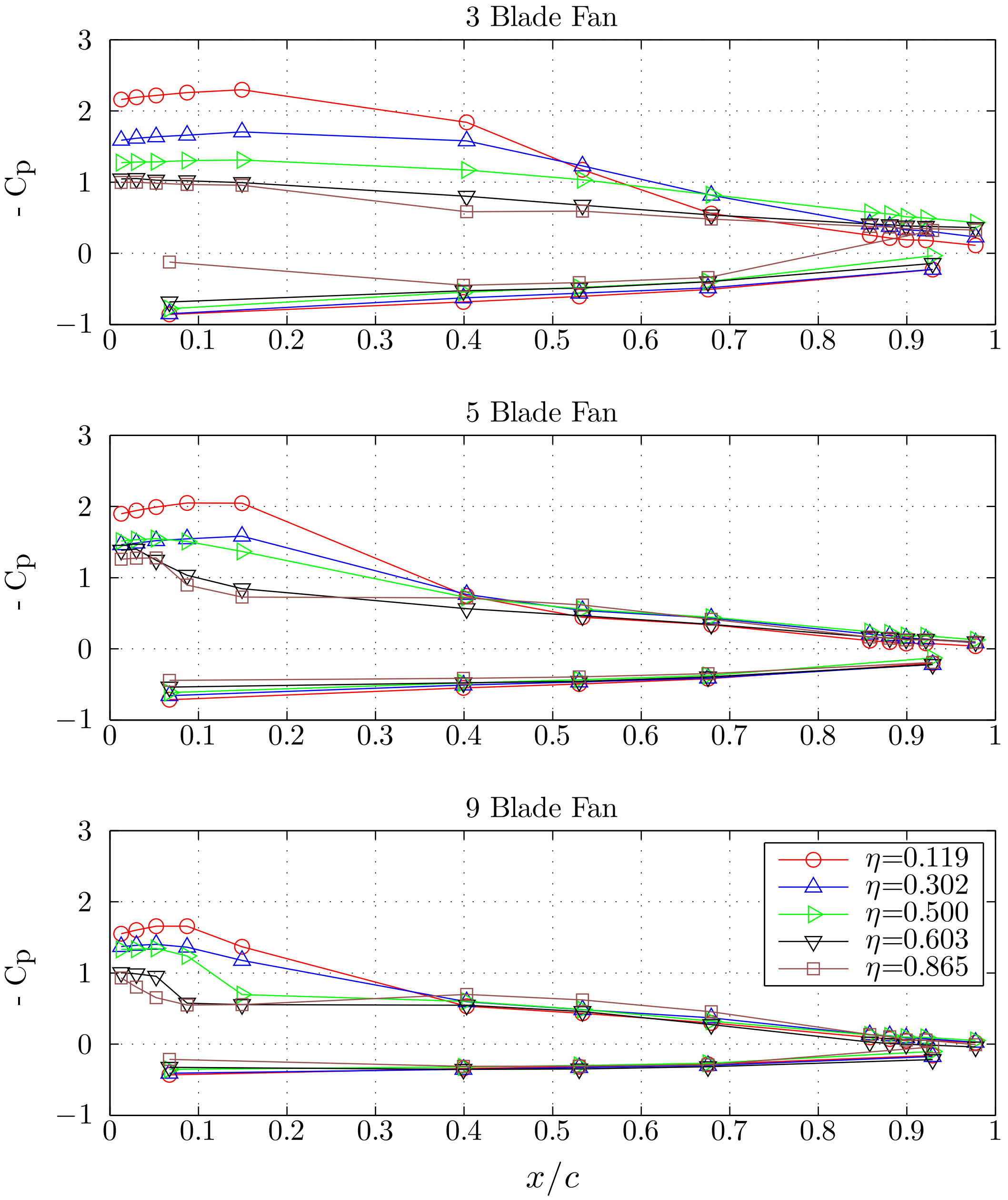

Figure 3.10 Pressure coefficients at Case II

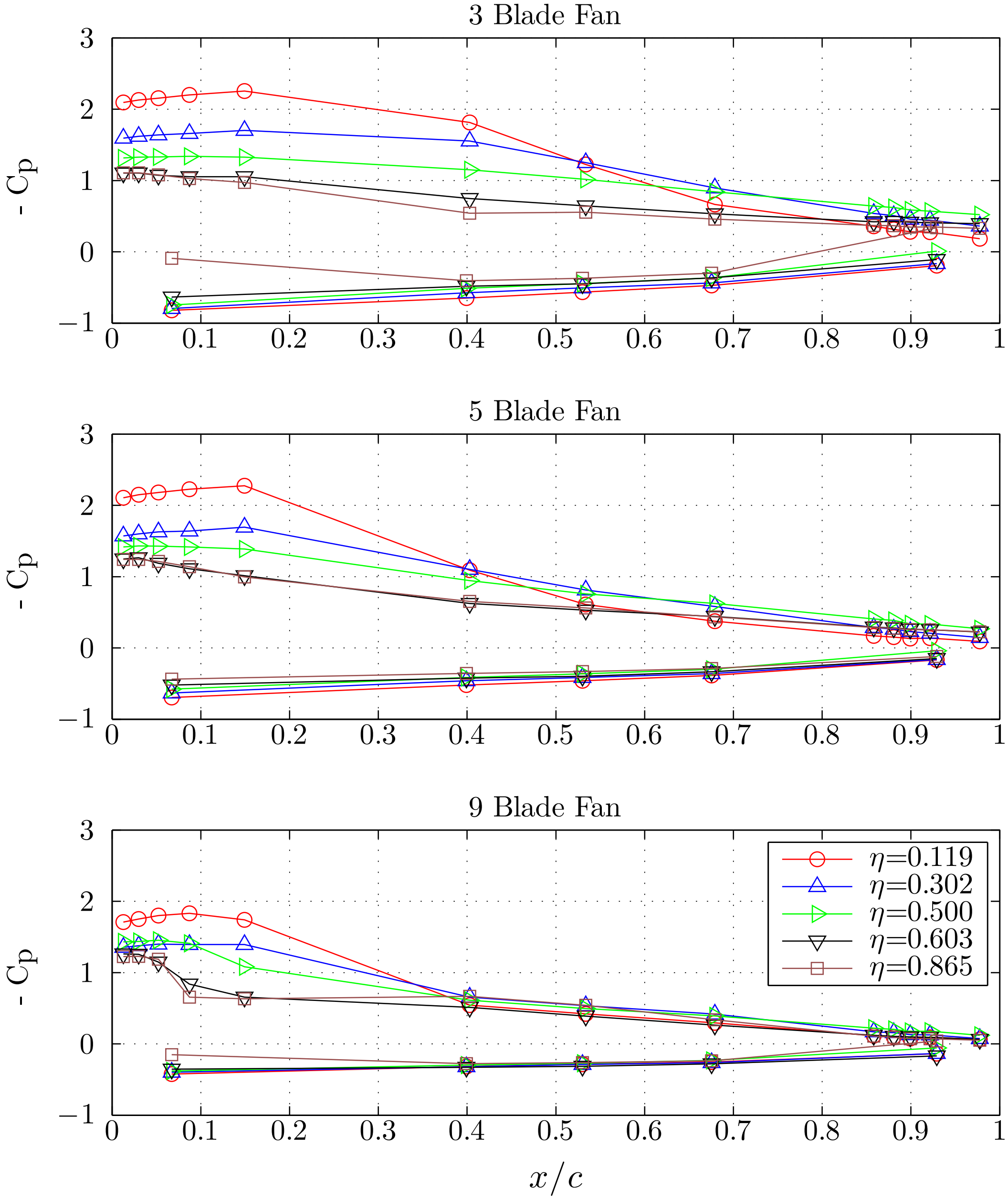

Figure 3.11 Pressure coefficients at Case III

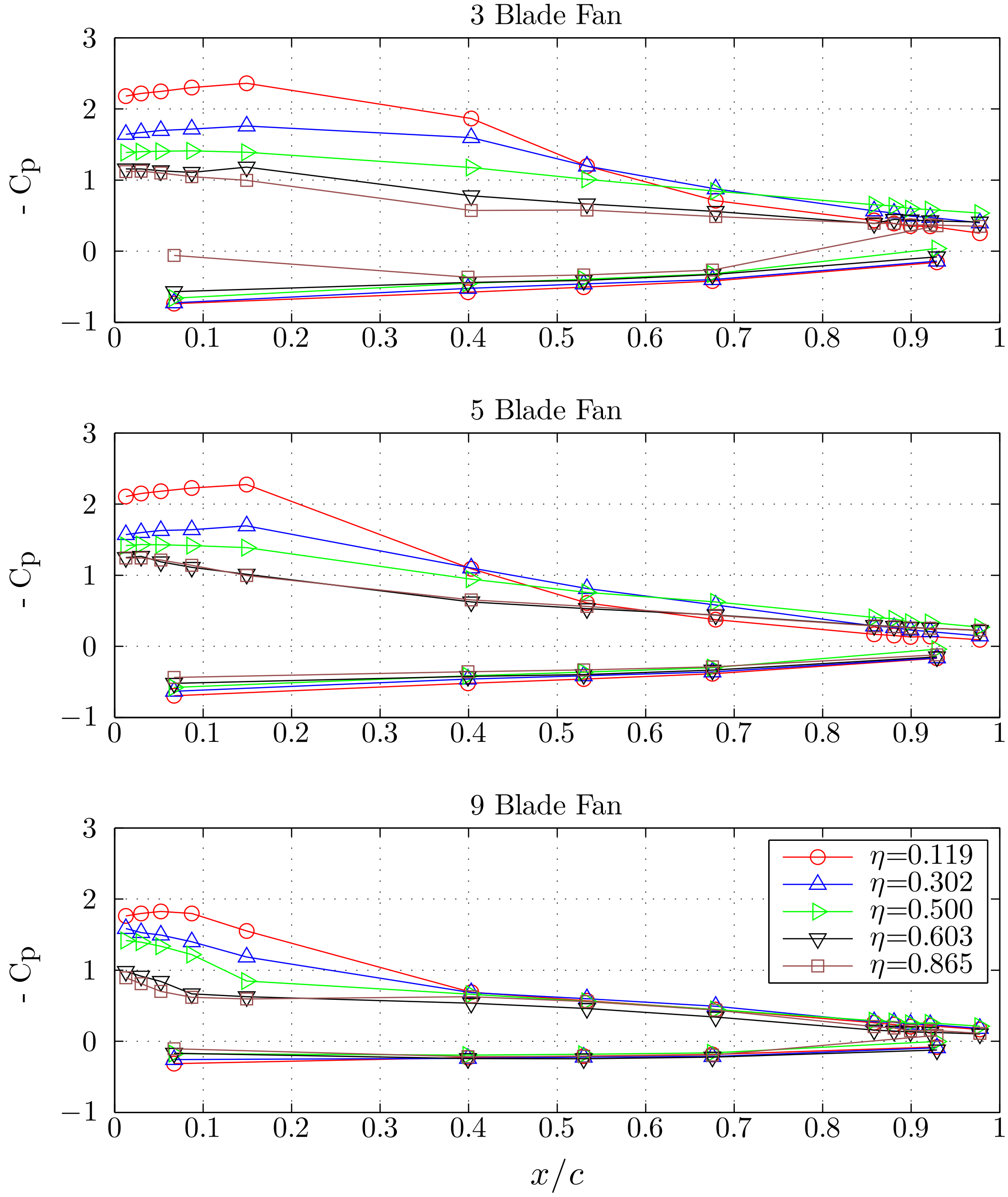

Figure 3.12 Pressure coefficients at Case IV

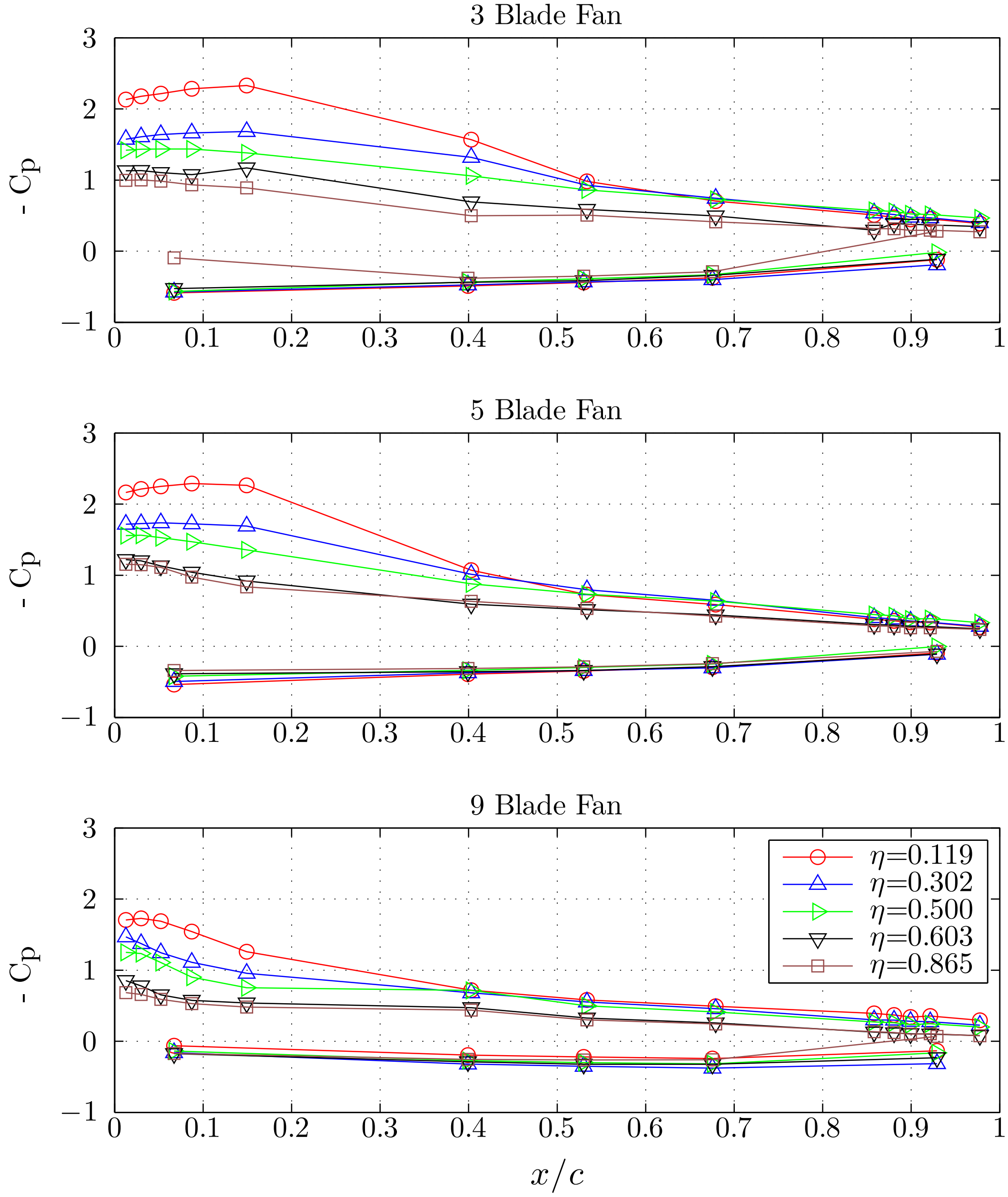

Figure 3.13 Pressure coefficients at Case V

The pressure coefficients from the spanwise trailing edge taps (Table 2.3) were also obtained during these experiments, Figure 3.14. These data show a general trend of increasingly negative pressure as the flow coefficient is decreased.

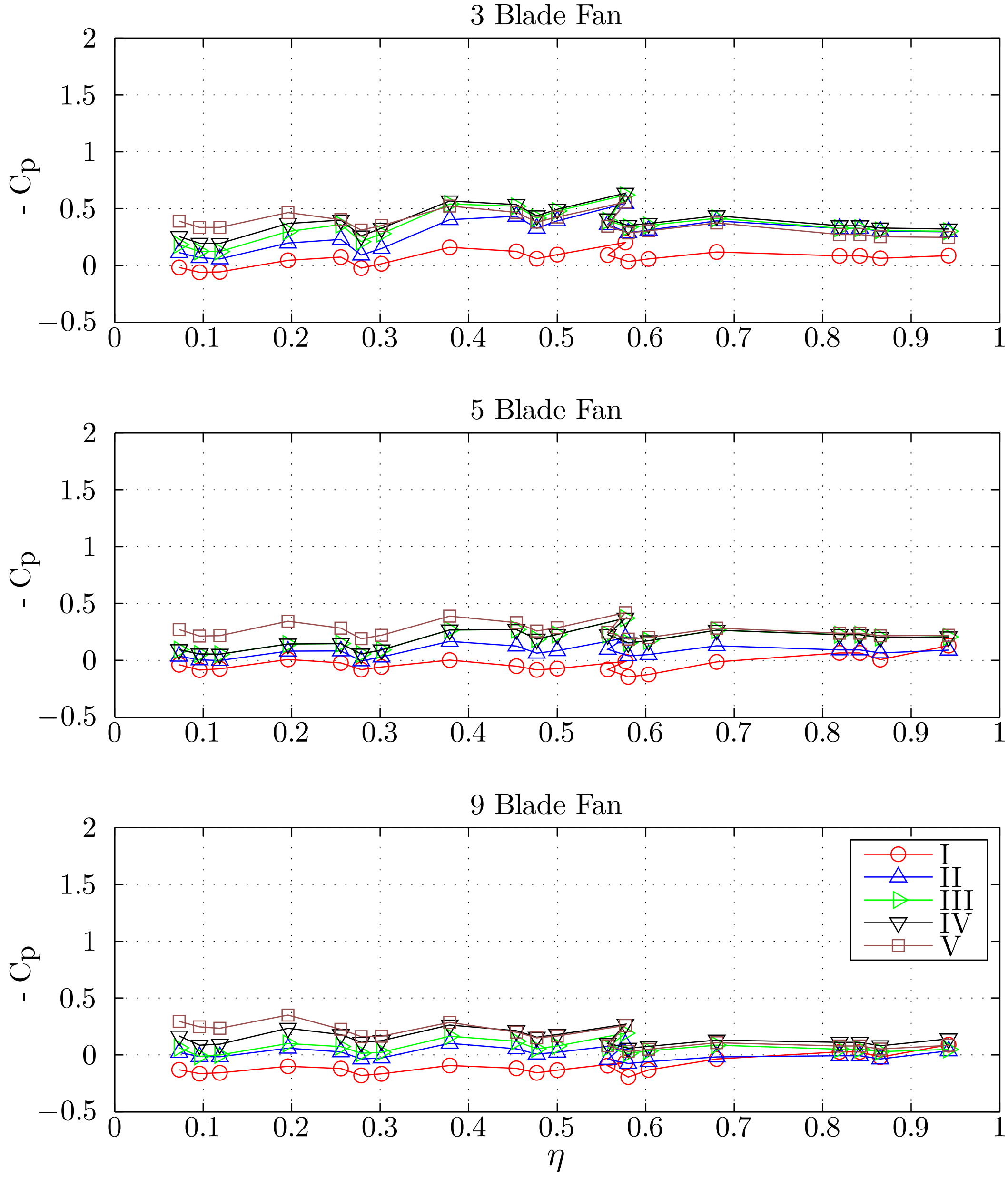

Figure 3.14 Pressure coefficient along the trailing edge of the blade for all cases and fan configurations

3.3 Wake Velocity

Hot-wire velocity measurements were obtained in the near-wake of the fan for the present investigation. These measurements were obtained 6 mm below the fan exit plane at the $\eta = 0.5$ span wise location. The stationary probe was able to resolve velocity components: V_θ, V_z in time with an approximate frequency response of 5 kHz. Velocity statistics, mean and the turbulent fluctuations, were derived from these data using a phase averaging scheme. Figure 3.15 shows a schematic hot-wire measurements in the near-wake of the fan. The right hand coordinate system: r, θ, z, and positive z aligned with $\vec{V}$, results in $\mathbf{\Omega} < 0$ rotational velocity for the blade. $\vec{V}_{meas.}$ is the measured velocity at the probe that is composed of the axial and azimuthal components. The selected coordinate system produces velocity components at the probe of opposite sign $+V_z$ and $-V_\theta$. λ in this figure is detailed later in the document in reference to Figures 3.16 and 3.17.

Table 3.1 Ensemble array used for phase averaging scheme

	Spatial "Bins" in θ				
Revolution	1	2	3	...	6000
1	s_1^1	s_1^2	s_1^3	$s_1^{\cdots}$	s_1^{6000}
2	s_2^1	s_2^2	s_2^3	$s_2^{\cdots}$	s_2^{6000}
3	s_3^1	s_3^2	s_3^3	$s_3^{\cdots}$	s_3^{6000}
...	$s_{\cdots}^1$	$s_{\cdots}^2$	$s_{\cdots}^3$	$s_{\cdots}^{\cdots}$	$s_{\cdots}^{6000}$
∼2600	$s_{\sim 2600}^1$	$s_{\sim 2600}^2$	$s_{\sim 2600}^3$	$s_{\sim 2600}^{\cdots}$	$s_{\sim 2600}^{6000}$

These data were obtained sampling eight 16-bit channels sequentially at 50 kHz for six

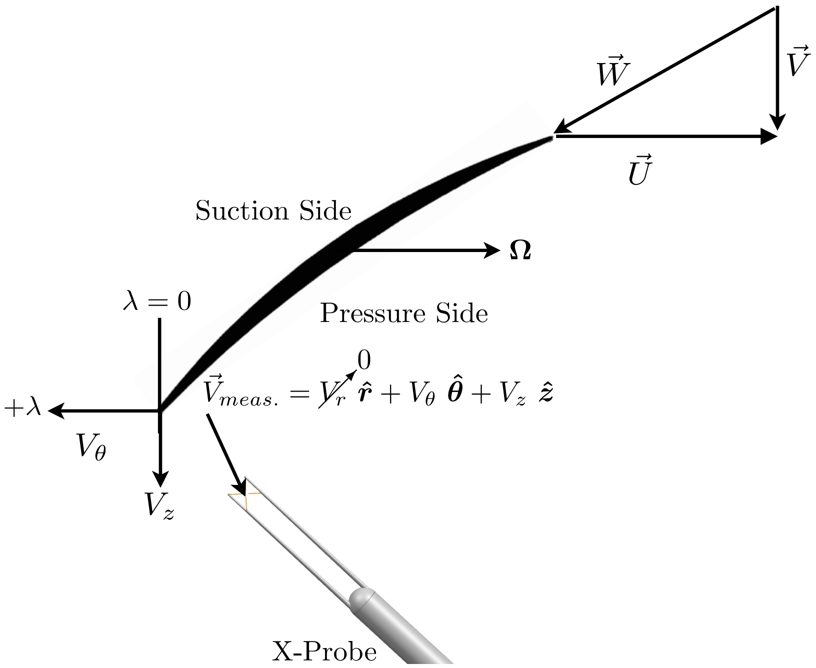

Figure 3.15 Hot-wire measurement schematic at an instant of time

minutes. The constant fan angular velocity of 7.5 Hz allowed for ~2600 revolutions to be obtained for each fan configuration and operating condition. The optical encoder on the shaft, indicating position, allowed for the time signal to decomposed the velocity signal into individual segments that corresponded with a single revolution. These selected data were then filtered into "Bins" that were selected to represent 0.06° in the θ direction. Figure 3.15 provides a visual representations these "Bins". Each "Bin" was filled with selected values from the 2600 total revolutions to build an ensemble array to obtain velocity statistics at 6000 individual points in space. Table 3.1 provides an example of the ensemble array that was created from the time history. Each "Bin" was filled with samples from the time series s_i^j. Subscript i references the revolution the sample was measured in and superscript j references the "bin" in which this value is stored. Note that the "Bin" size was selected to include one sample at minimum from the original signal to ensure that every "Bin" was contributed to per revolution. The average value from multiple points was used in each “Bin” with more than one individual sample. The time series the probe observed begins at s_1^1 traversing left to right and moving down the table until the last sample $s_{\sim 2600}^{6000}$. The vector from the columns in this array represent the “time” history generated for each individual “Bin”. Evaluating velocity statistics for each “Bin” is similar to velocity statistics from measurements in a non-rotating system such as a hot-wire in a turbulent jet.

A representative sample of these data is provided in Figure 3.16. These mean axial velocity data show the blade traces for each fan configuration. Previously, it was noted that the trailing edges of the fan blades are not at a uniform height above the probe. The lowest blade on the fan in the z direction was recorded for each experimental run and has been marked in Figure 3.16. The marked angular segment $\lambda_i \ : \ i = 3, 5, 9$, is the segment that each individual fan blade occupies on the respective fan assembly. These individual segments will be used for comparison between the different velocity measurement values and operating conditions. All of the plotted data from the hot-wire velocity wake measurements from Section 3.3 have been presented in a format similar to Figure 3.16 within Appendix B.

Figure 3.17 provides a view of Figure 3.16 with all three blades centered on the wake minima. This presentation allows for better comparison between the fan configurations at different operating conditions. Additionally, centering the wake minima at $\lambda = 0$ allows for a simple definition of the pressure and suction side of the wake. The probe measures velocities in time and is first exposed to the pressure side of the fan blade as the fan rotates towards it, as indicated in Figure 3.15. The abscissa for Figures 3.16 and 3.17 are plotted with increasing time. Hence, the pressure side of the wake is indicated in $-\lambda$ and the suction side is indicated in $+\lambda$. Figure 3.15 provides a representation of

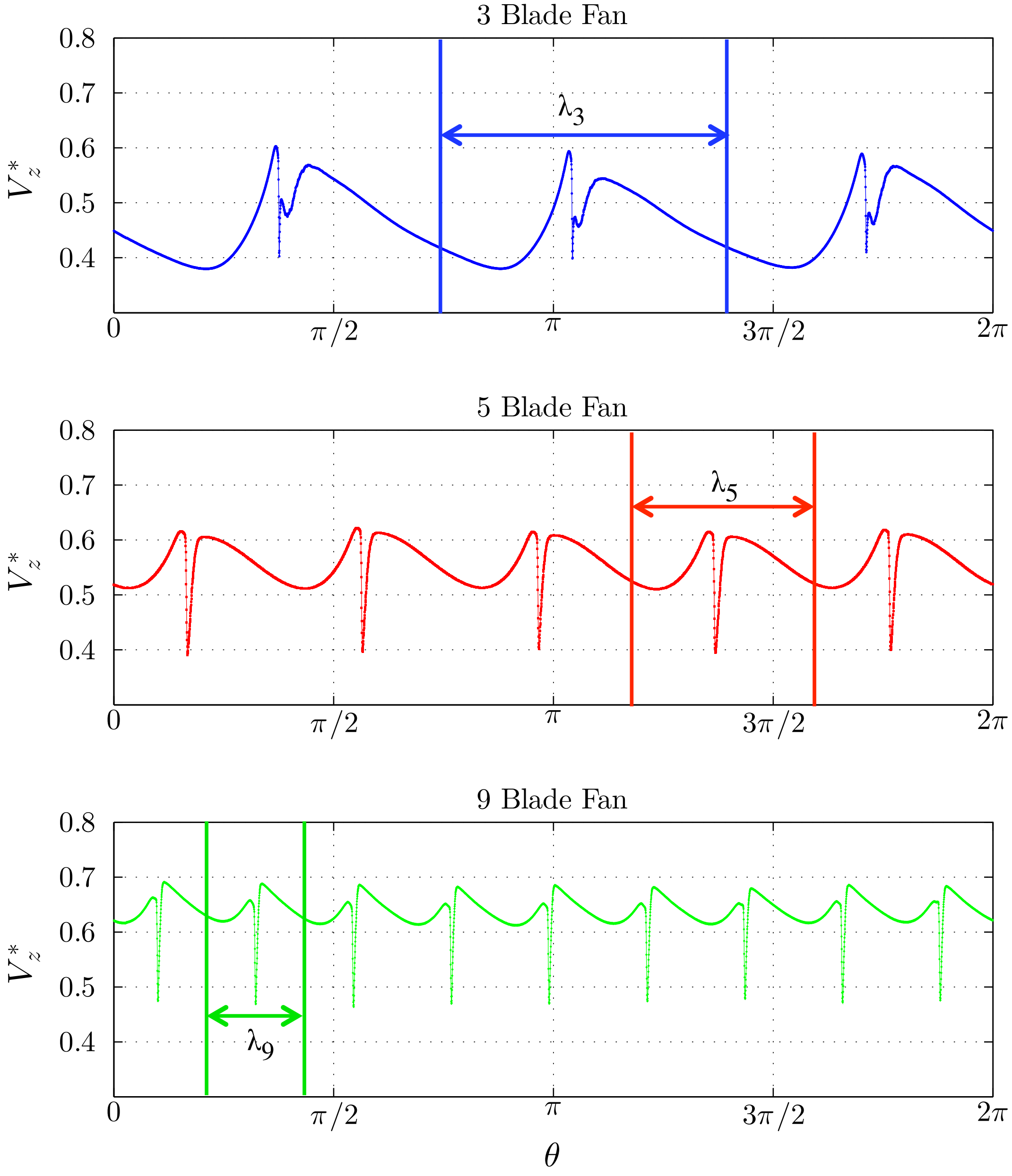

Figure 3.16 Complete fan wake velocity profile sample

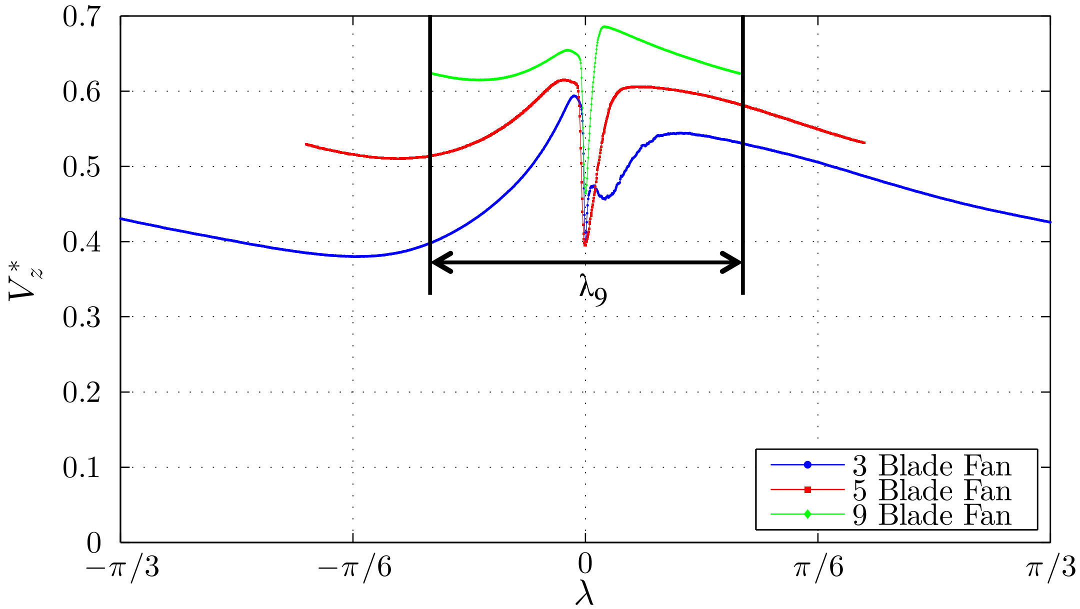

Figure 3.17 Single blade fan wake velocity profile sample

λ with respect to the blade. These designations will be important as they will be used to interpret these results. However, it is important to indicate that the probe observed the effects of the entire blade passing above from suction side to pressure side in time. Therefore, the driving cause for the probe's observations cannot be isolated to the suction or pressure side individually, but rather considered for the entire blade. The indicated λ_9 on Figure 3.17 is the range of lambda in which all hot-wire velocity measurements will be displayed within the body of this document. A complete collection of the figures presented in Section 3.3 are available in a format similar to Figure 3.17 within Appendix B.

3.3.1 Mean Wake Velocities

Mean velocities were evaluated using the phase averaging scheme detailed in the previous section. These phase averages provided 6000 data points in θ with distinct velocities in the θ and z directions. Figures 3.18-3.22 provide the mean axial velocity for the three, five, and nine blade fans for Cases I–V. Equation (3.6) provides the definition of the non-dimensional axial velocity V_z^*. These data are presented in this section and will be discussed in conjunction with evaluation of the kinetic energy flux at the common exit of both control volumes.

$$V_z^* = \frac{\overline{V_z}}{V_{tip}} \tag{3.6}$$

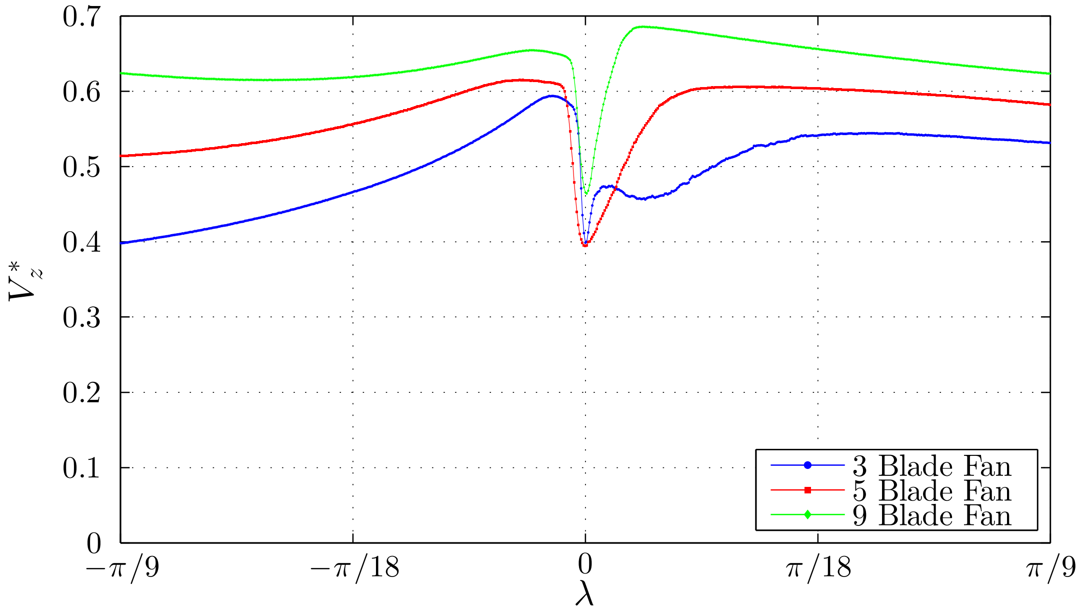

Figure 3.18 Case I Phase averaged axial velocity over λ_9

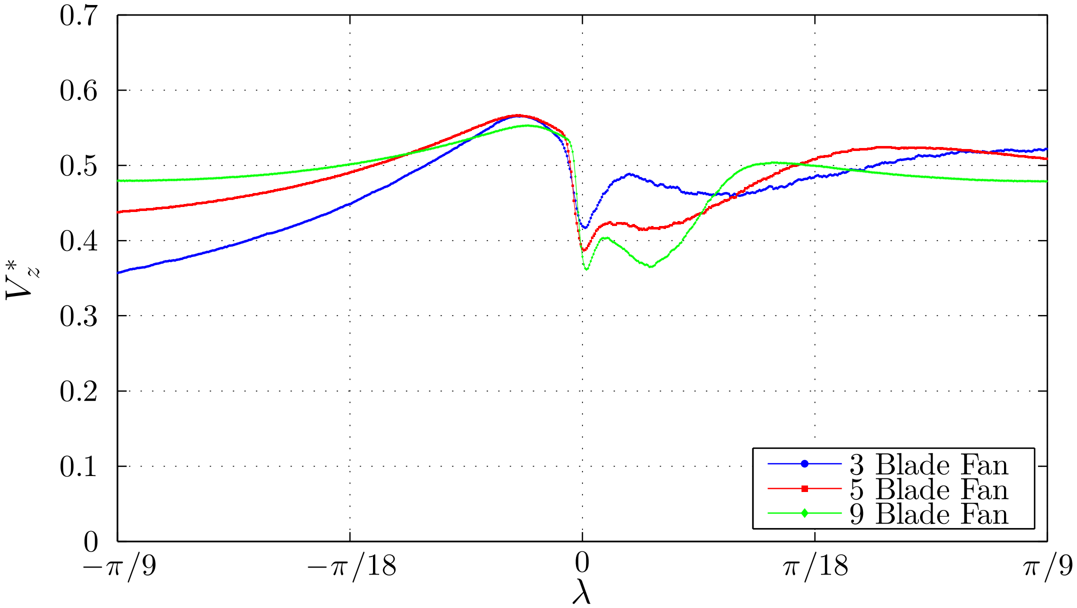

Figure 3.19 Case II Phase averaged axial velocity over λ_9

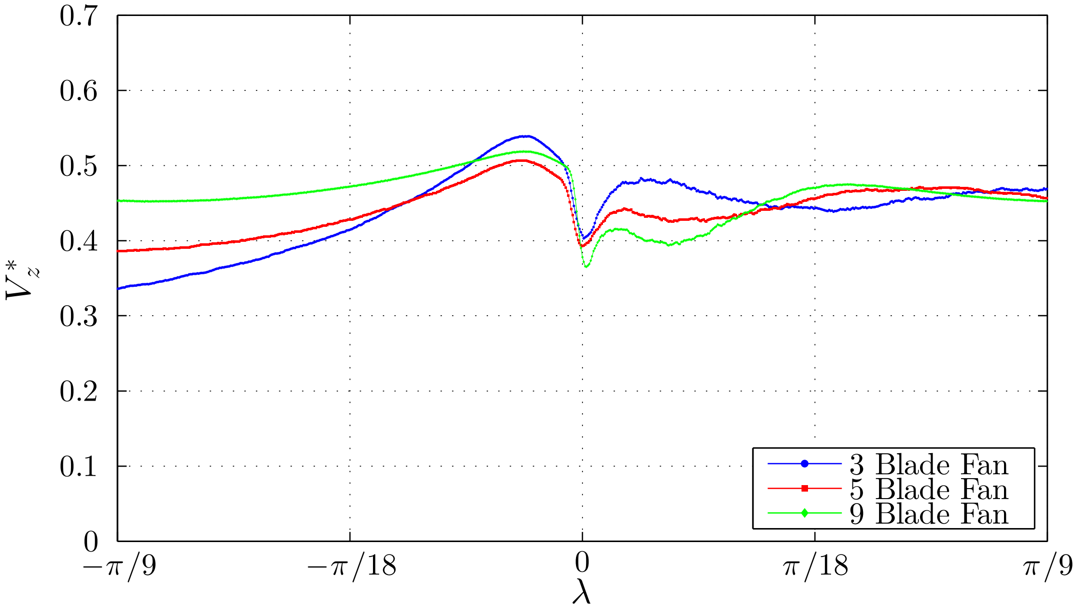

Figure 3.20 Case III Phase averaged axial velocity over λ_9

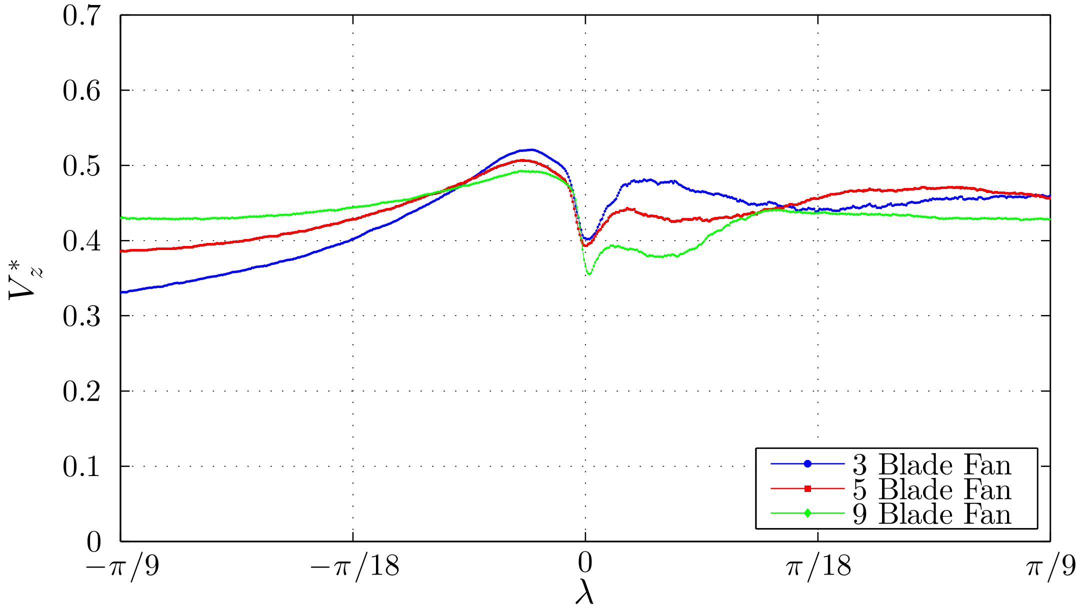

Figure 3.21 Case IV Phase averaged axial velocity over λ_9

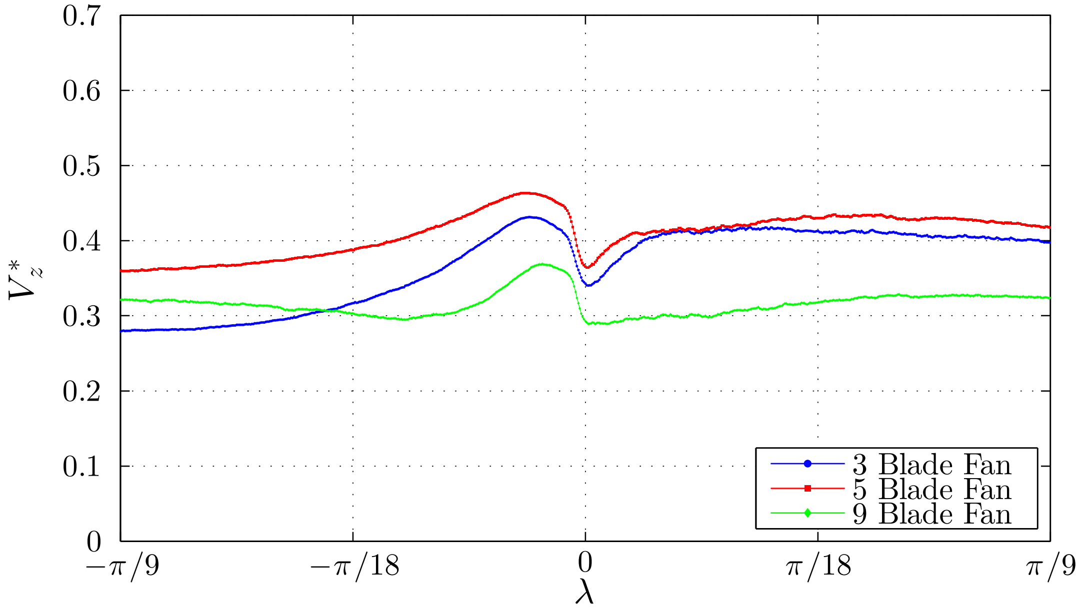

Figure 3.22 Case V Phase averaged axial velocity over λ_9

Figures 3.23-3.27 provide the mean azimuthal velocity for the three five and nine blade fans for Cases I–V. Equation (3.7) provides the definition of the non-dimensional azimuthal velocity V_θ^*. These data are presented in this section and will be discussed in conjunction with evaluation of the kinetic energy leaving the fan plane in both Control Volumes.

$$V_\theta^* = \frac{\overline{V_z}}{V_{tip}} \tag{3.7}$$

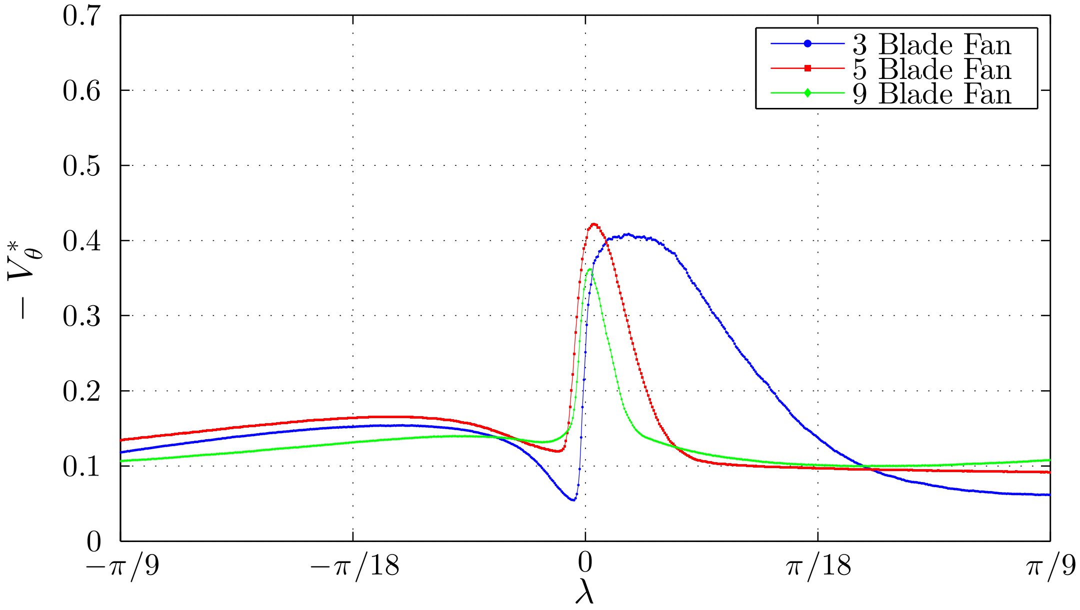

Figure 3.23 Case I Phase averaged azimuthal velocity over λ_9

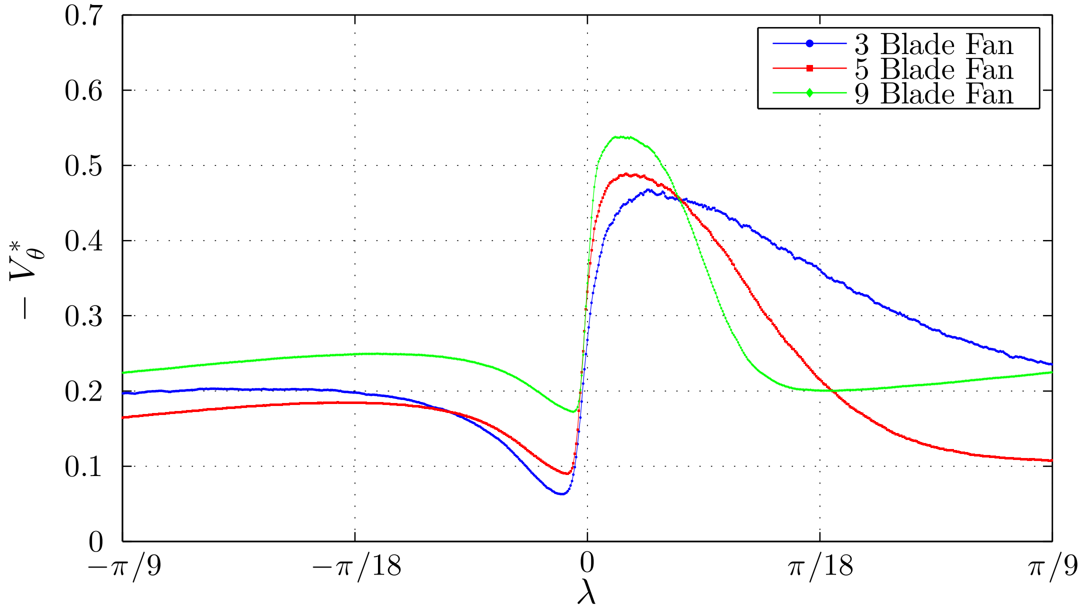

Figure 3.24 Case II Phase averaged azimuthal velocity over λ_9

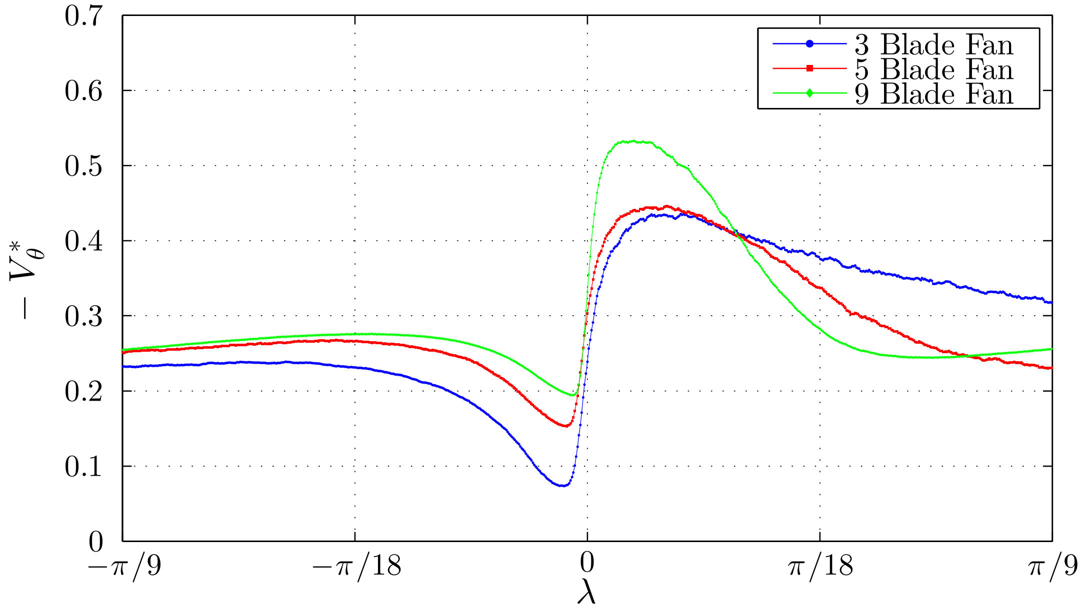

Figure 3.25 Case III Phase averaged azimuthal velocity over λ_9

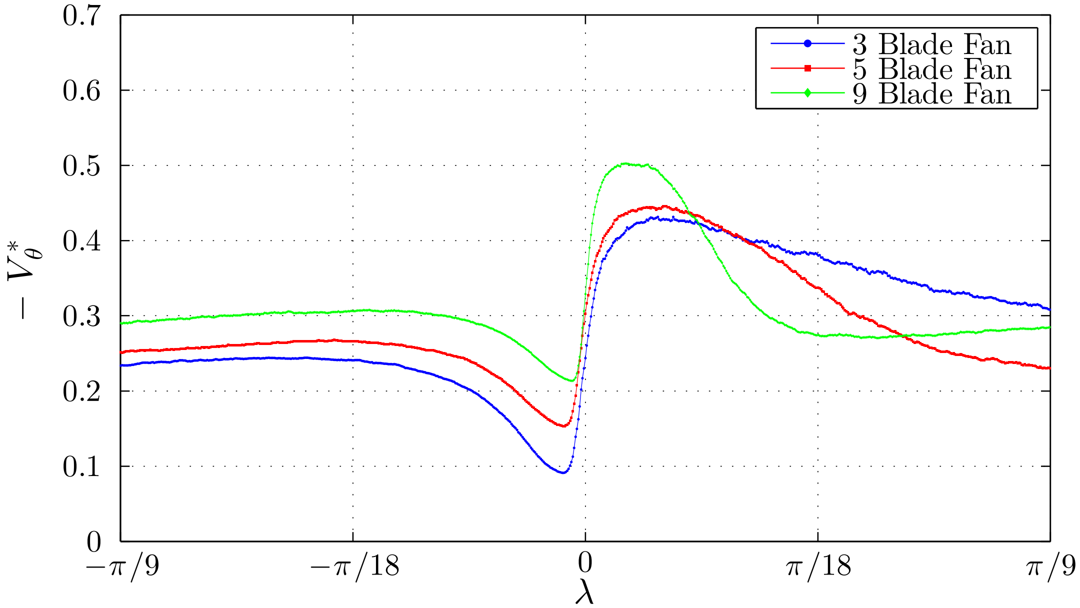

Figure 3.26 Case IV Phase averaged azimuthal velocity over λ_9

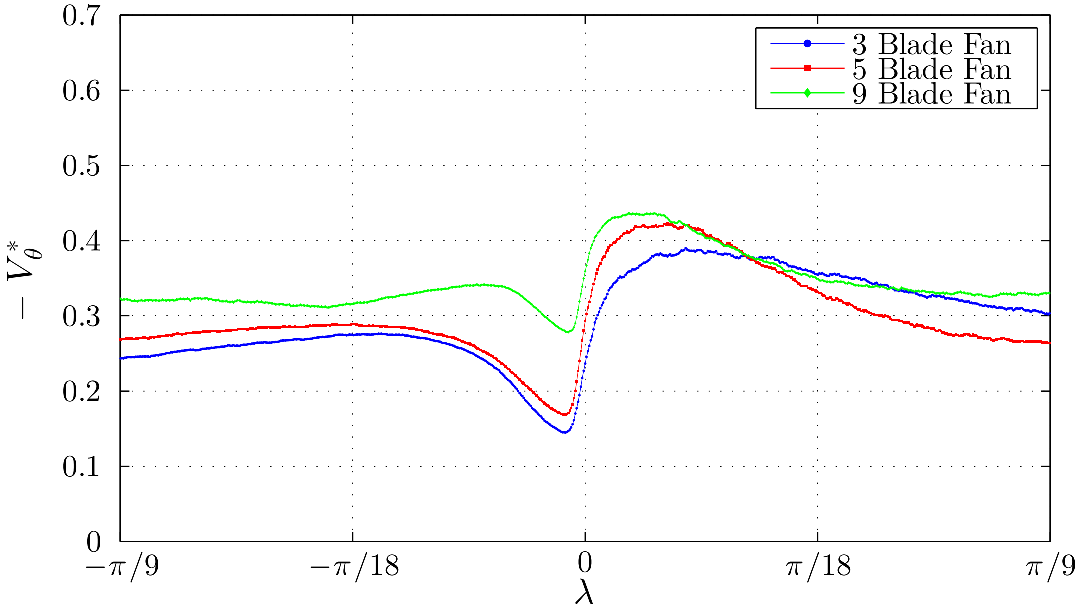

Figure 3.27 Case V Phase averaged azimuthal velocity over λ_9

A representative swirl number has been formulated to express the relative magnitudes of the azimuthal velocities for the different configurations. The swirl number Σ is given by Equation (3.8). Results, provided in Figure 3.28, indicate that there is a direct relationship between the number of blades installed on the fan and the magnitude of the azimuthal velocity at the fan exit plane.

$$\Sigma = \ (Number\ of\ Blades) * \int_{-\lambda_i/2}^{\lambda_i/2} V_\theta^*(s)\ ds \tag{3.8}$$

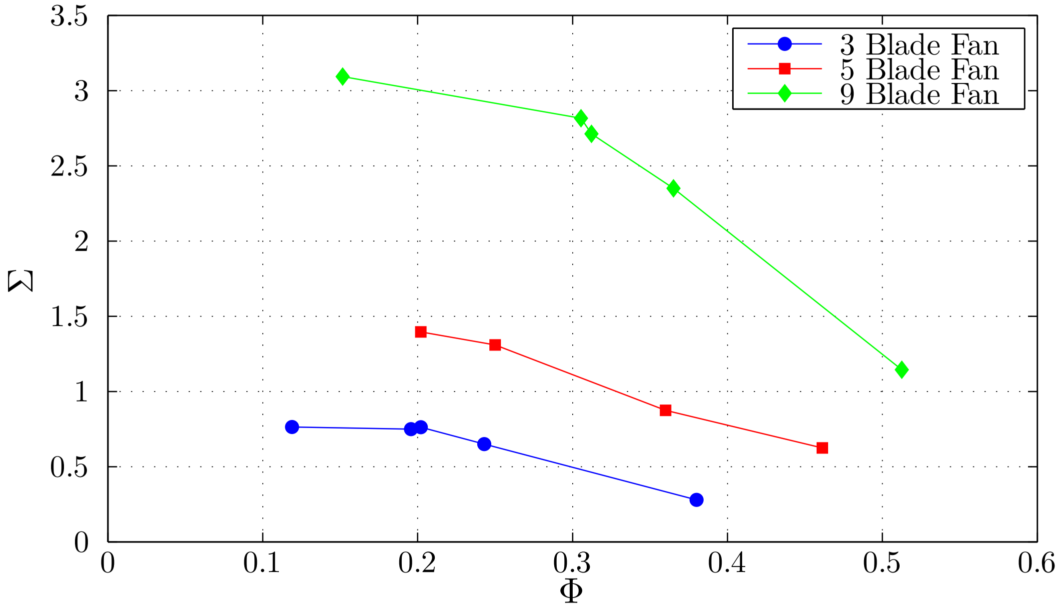

Figure 3.28 Representative comparison in azimuthal velocity between fan configurations

3.3.2 Reynolds Averaged Velocity Statistics

The observed velocity in the near-wake of the fan has been decomposed into the average velocity components and the fluctuating velocity components. The fluctuations of the flow are found from the phase averaging ensemble described in Table 3.1. The velocity component fluctuations contribute to the Reynolds stress tensor evaluated in the Reynolds averaged momentum equations. The two velocity component measurements obtained in the present investigation provide three terms from the Reynolds stress tensor. These stresses exhibit an effect similar to viscous stress on the mean velocity field and are diffusive. Equation (3.9) provides the three terms available from the measurements obtained. These terms are the axial turbulence intensity, azimuthal turbulence intensity, and Reynolds shear stress in the θ–z–plane respectively. A more detailed analysis of the Reynolds averaging process can be found in [Pope (2000)] or [Hinze (1975)] and is also outlined in Appendix D.

$$\overline{V_\theta'^2} \ ; \ \overline{V_z'^2} \ ; \ \overline{V_\theta' V_z'} \tag{3.9}$$

3.3.2.1 Axial Turbulence Intensity

Figures 3.29-3.33 provide the turbulence intensity in the axial direction at the exit of the fan plane. The formulation for the value in these figures is provided in Equation (3.10). Case I (Figure 3.29) shows that the three blade fan takes much longer to return to a low axial turbulence condition after the blade passes by the probe. The angle of incidence for this operating condition and fan configuration may generate this phenomena. Additionally, increasing the number of blades decreased the time taken for the axial turbulence intensity to recover to a magnitude before the blade passes.

$$\widetilde{V}_z = \mathrm{RMS}(V_z') = \sqrt{\overline{V_z'^2}} \tag{3.10}$$

Case II (Figure 3.30) shows that the entire region between the blades of the three blade fan is experiencing greater axial turbulence than in Case I. Note that the nine blade fan now exhibits the shape of the five blade fan at Case I. This suggests that axial turbulence for increased number of blades is similar to that of a fan with less blades operated at a higher flow coefficient. Case III (Figure 3.31) is similar to Case II with the distinction that the five blade fan now has axial turbulence in for the entire region between blades. Case IV (Figure 3.32) now has matching behavior for the three fan configurations as the blade approaches the probe. The magnitude of the axial turbulence intensity has an inverse relationship with the number of blades installed on the fan near the wake region. Case V (Figure 3.33) shows increased fluctuations for the nine blade fan on the pressure side of the wake and that the entire span of λ exhibits axial turbulence for all three fans.

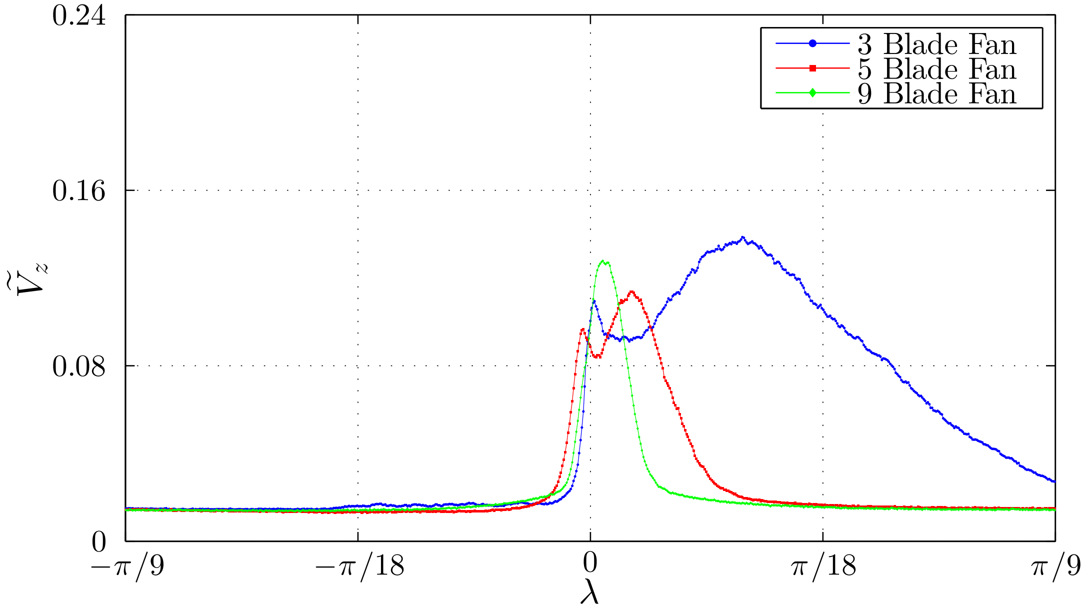

Figure 3.29 Case I Axial turbulence intensity over λ_9

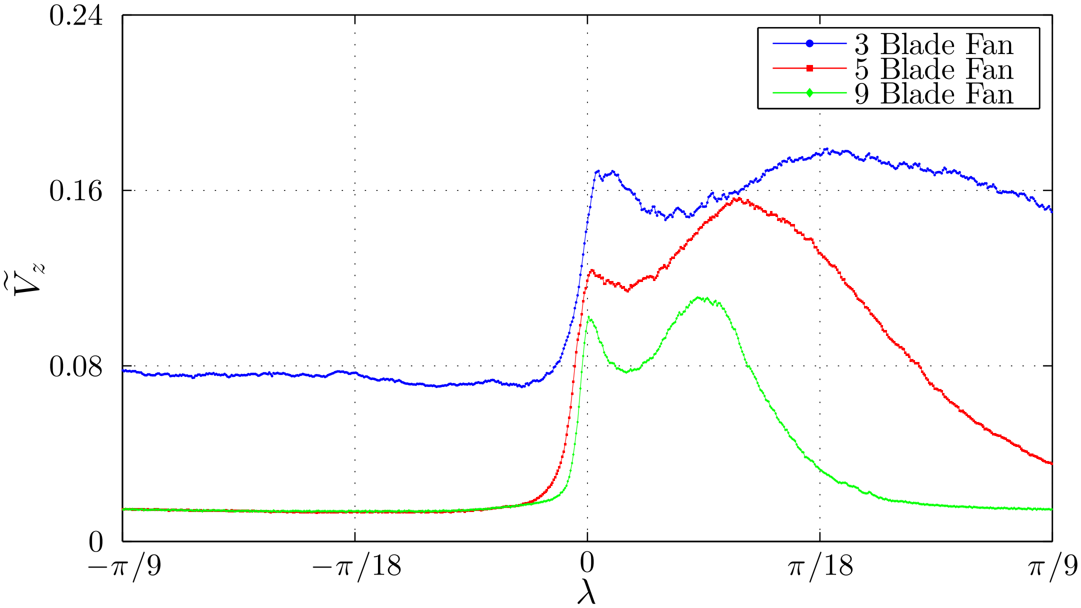

Figure 3.30 Case II Axial turbulence intensity over λ_9

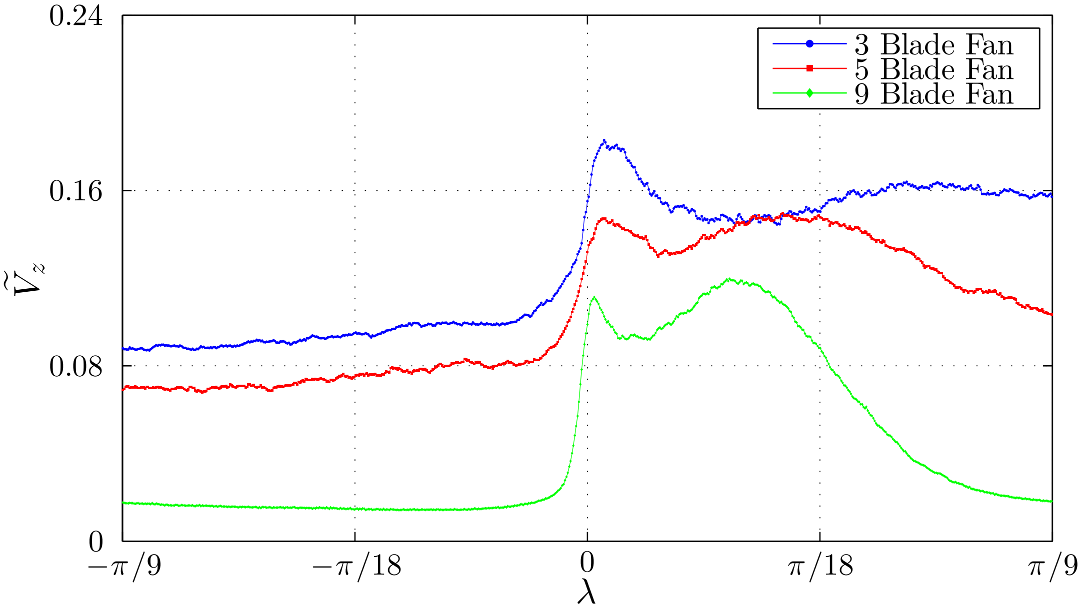

Figure 3.31 Case III Axial turbulence intensity over λ_9

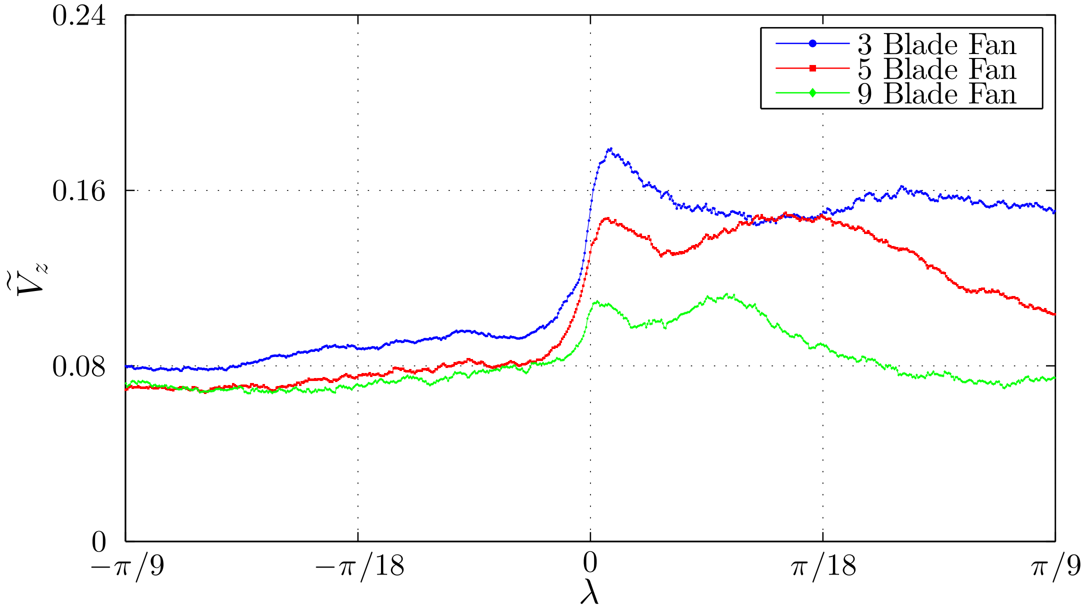

Figure 3.32 Case IV Axial turbulence intensity over λ_9

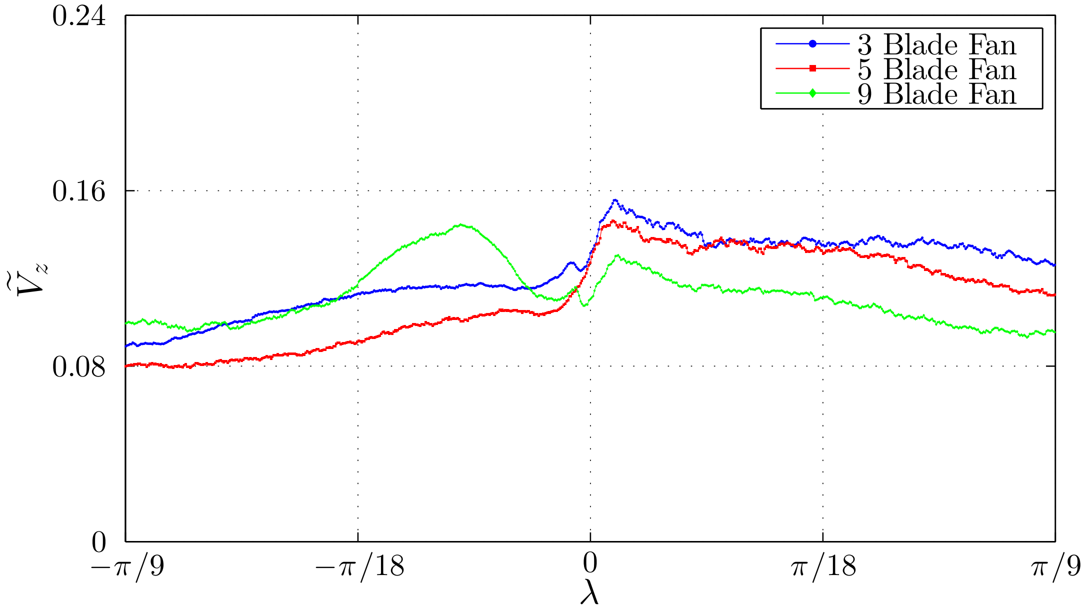

Figure 3.33 Case V Axial turbulence intensity over λ_9

3.3.2.2 Azimuthal Turbulence Intensity

Figures 3.34-3.38 provide the turbulence intensity in the aziumthal direction at the exit of the fan plane. The formulation for the value in these figures is provided in Equation (3.11). These results are similar to the axial turbulent fluctuations. Additionally, the nine blade fan shares similar behavior to the three and five blade fans beginning at Case IV. At Case III the nine blade fan also has the same behavior of the five blade fan at Case II. This suggests that azimuthal turbulence, for increased number of blades, is similar to that of a fan with less blades operated at a higher flow coefficient. The observed axial and azimuthal turbulence intensities provide similar results.

$$\widetilde{V}_\theta = \mathrm{RMS}(V'_\theta) = \sqrt{\overline{V'^2_\theta}} \tag{3.11}$$

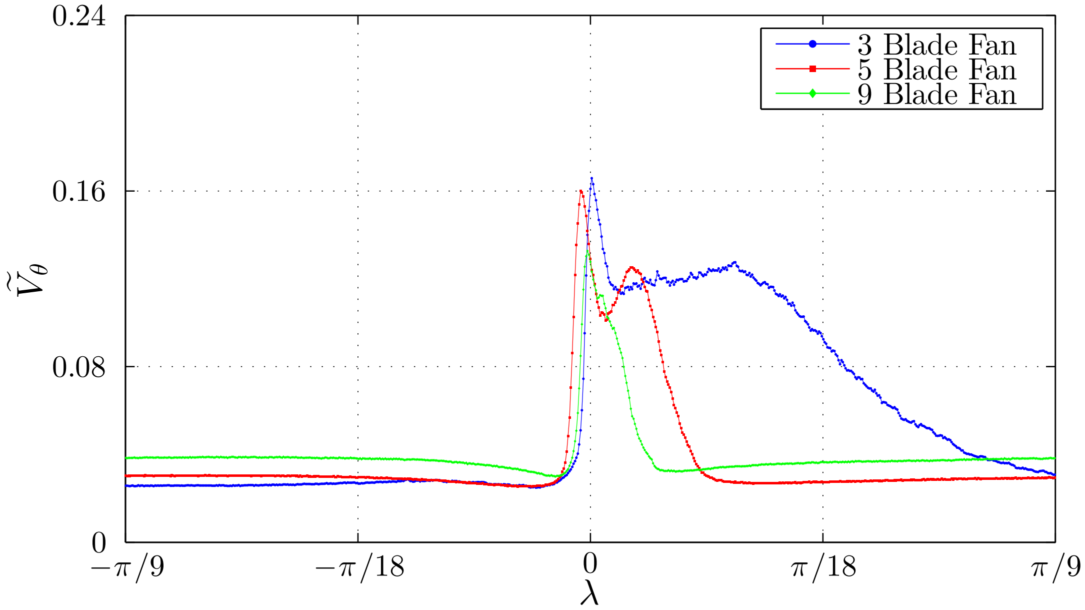

Figure 3.34 Case I Azimuthal turbulence intensity over λ_9

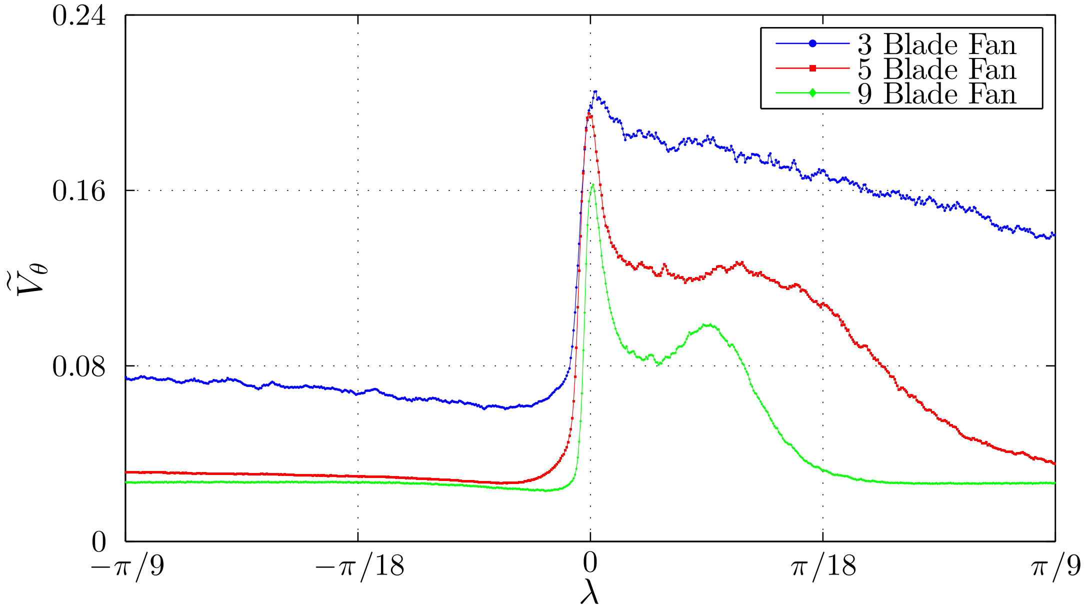

Figure 3.35 Case II Azimuthal turbulence intensity over λ_9

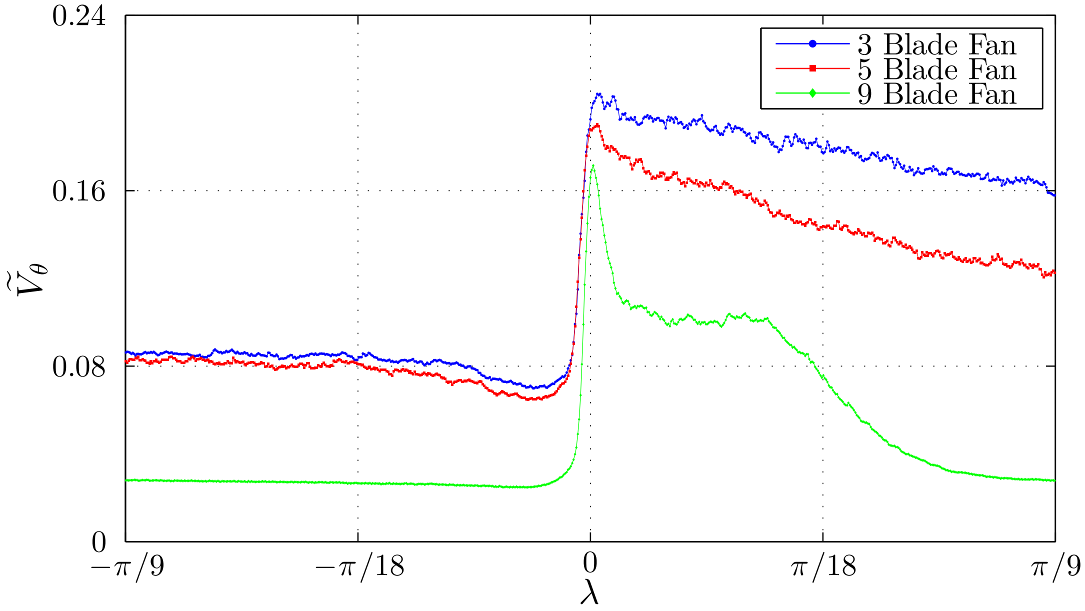

Figure 3.36 Case III Azimuthal turbulence intensity over λ_9

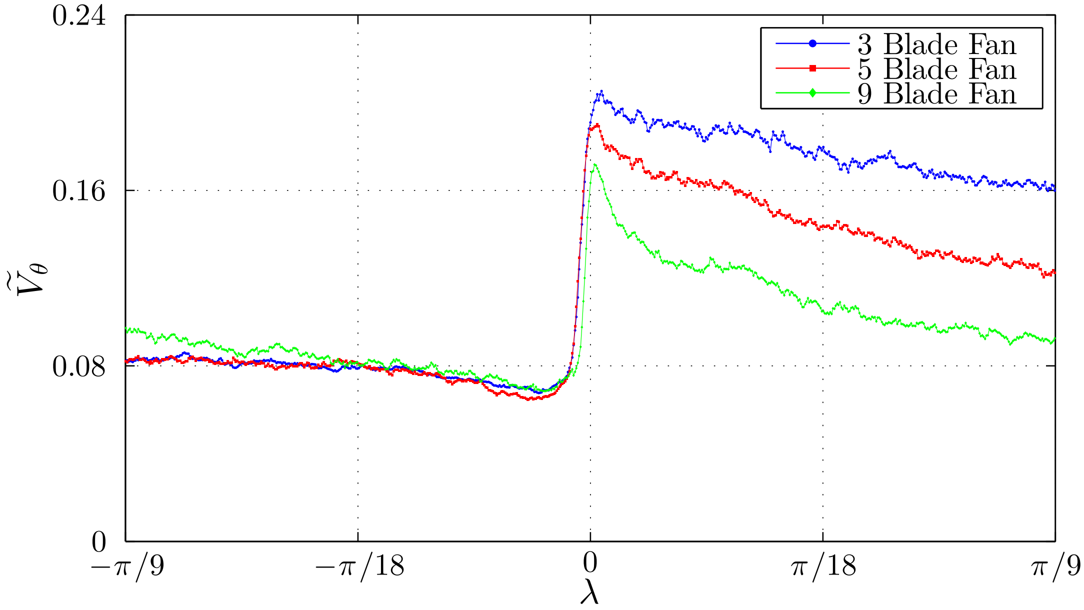

Figure 3.37 Case IV Azimuthal turbulence intensity over λ_9

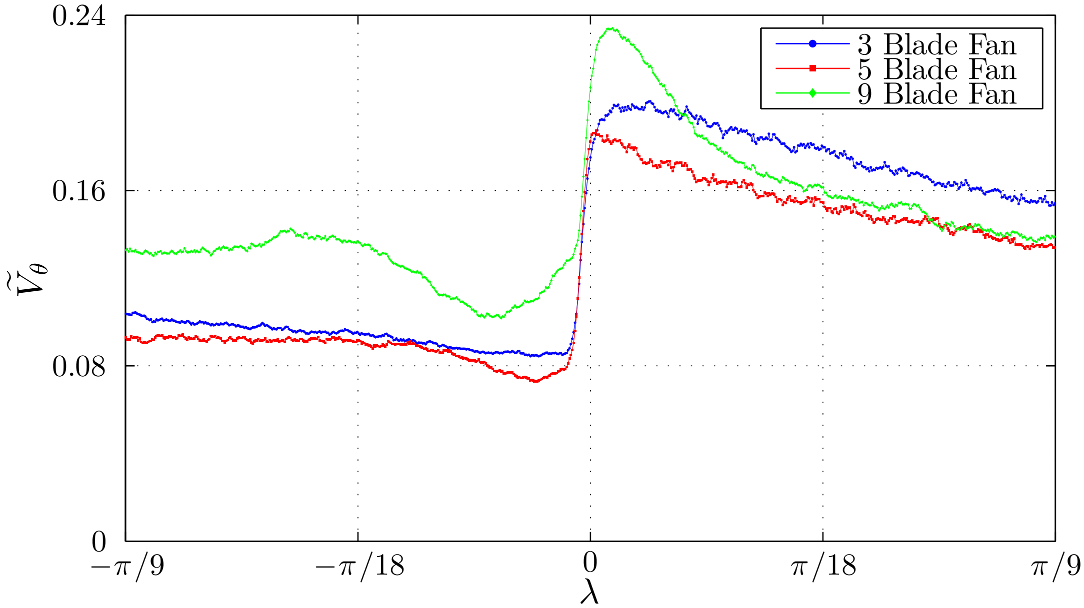

Figure 3.38 Case V Azimuthal turbulence intensity over λ_9

3.3.2.3 Reynolds Shear Stress [z-θ plane]

Figures 3.39-3.43 provide the Reynolds shear stress of the velocity fluctuations. Case I (Figure 3.39) shows that the fluctuations for higher blade fans are greater in magnitude near the wake. However, the effect of the blade passing above the probe is short in λ. The three blade fan wake continues to be disturbed for a longer period of time after the fan blade passes above in Case I. Case II (Figure 3.40) shows that the disturbances of the blade passing propagated much further in λ for the five and blade fans. Additionally the disturbance is carrying over to the pressure side of the next blade. This response is then displayed by the five blade fan at Case III, Figure 3.41, and the nine blade fan at Case IV, Figure 3.42. These observations suggest that a fan with less blades installed will experience similar Reynolds shear stress in the wake at lower flow coefficient. Generally, increasing the number of blades for a given operating condition suppresses turbulent fluctuations in the fan wake. Each of the Reynolds stress tensor terms analyzed provided this observation.

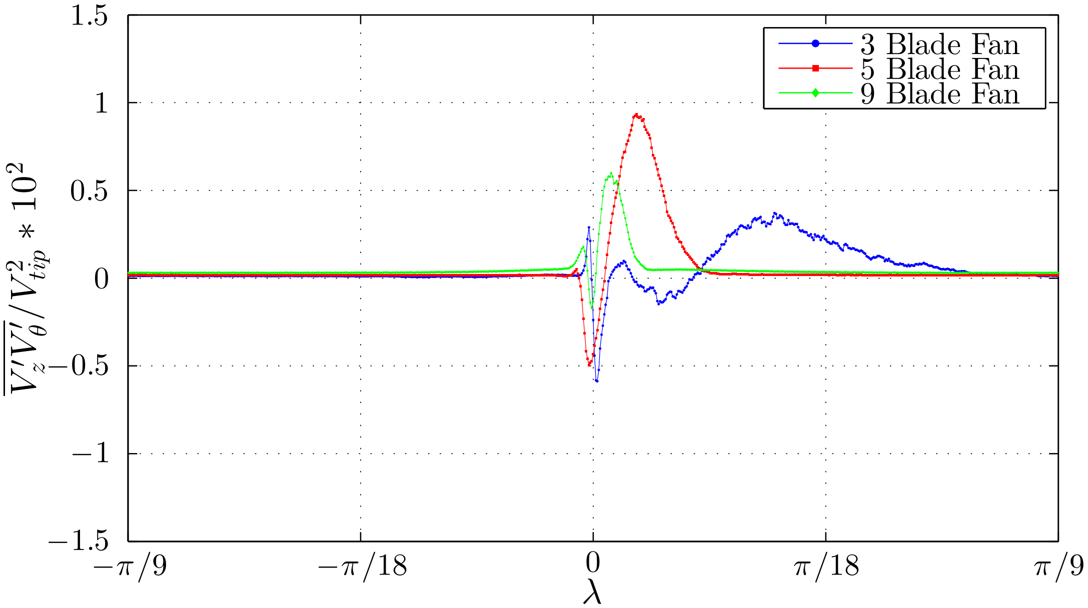

Figure 3.39 Case I Reynolds stress in z-θ − plane over λ_9

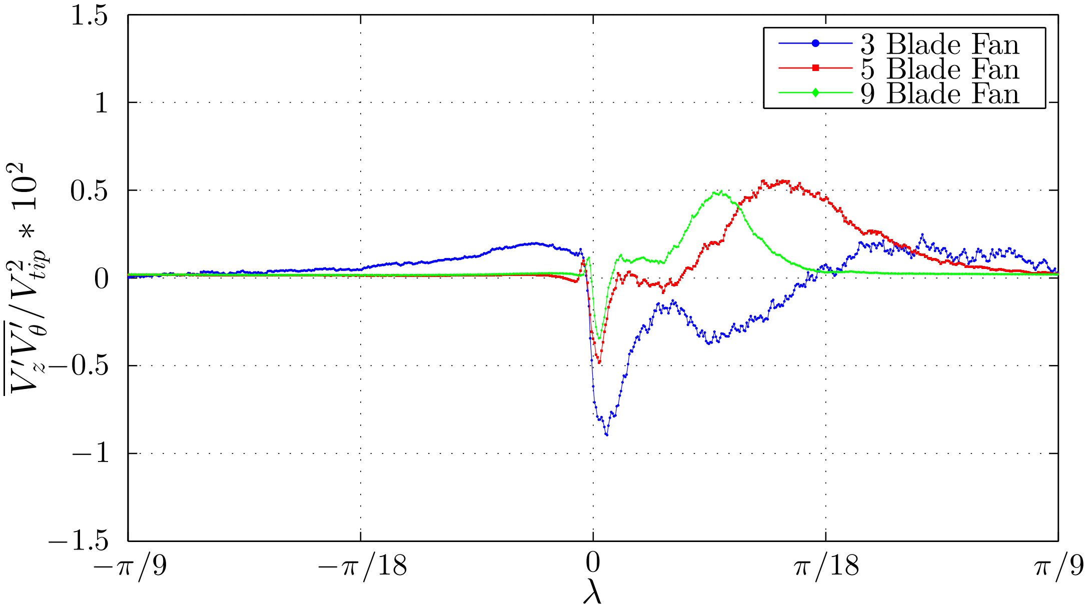

Figure 3.40 Case II Reynolds stress in z-θ − plane over λ_9

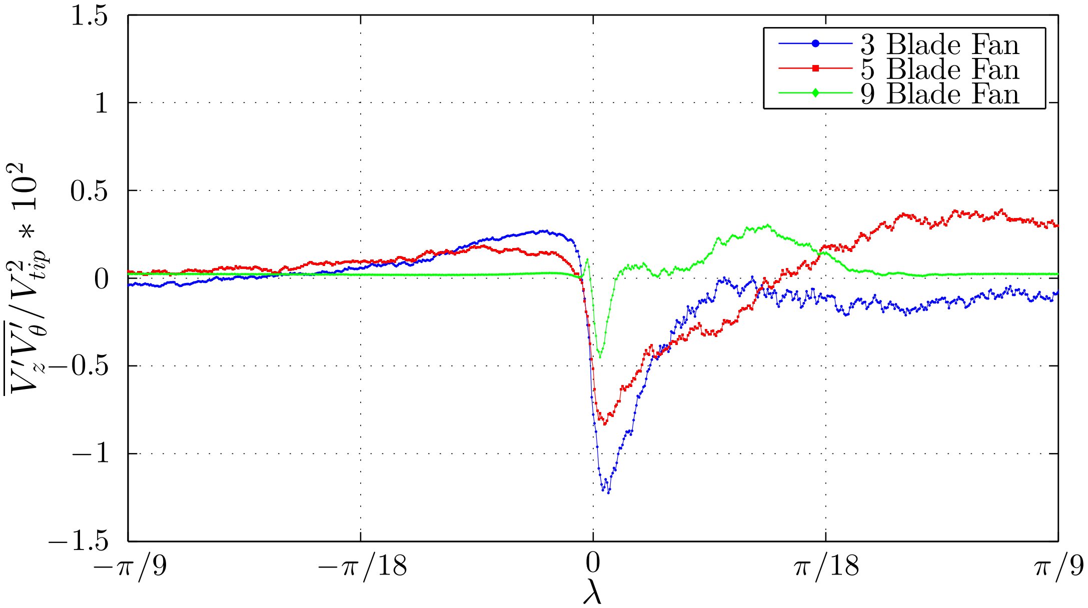

Figure 3.41 Case III Reynolds stress in z-θ – plane over λ_9

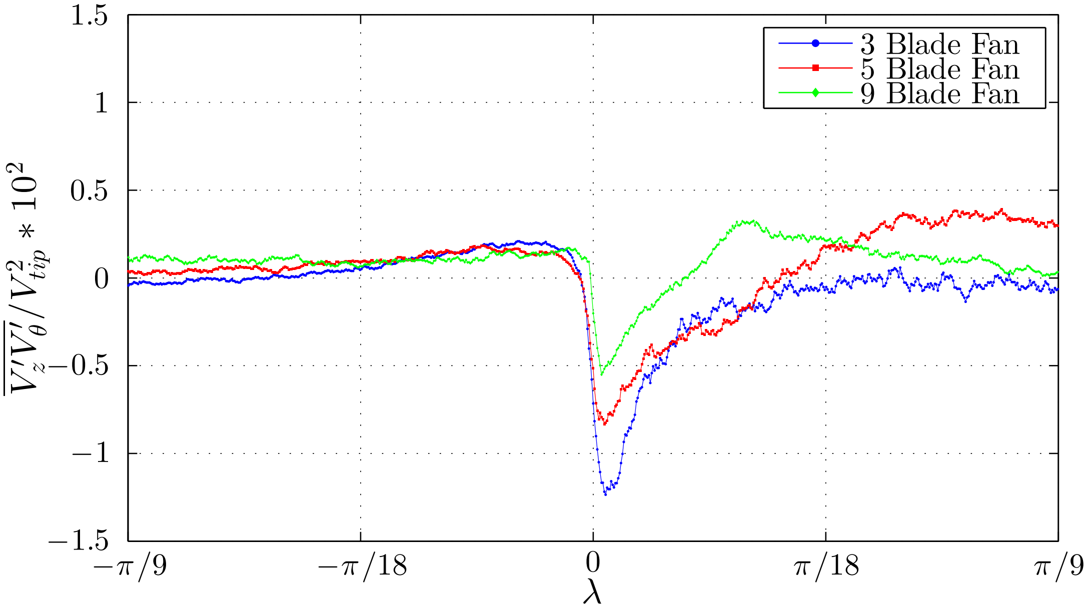

Figure 3.42 Case IV Reynolds stress in z-θ – plane over λ_9

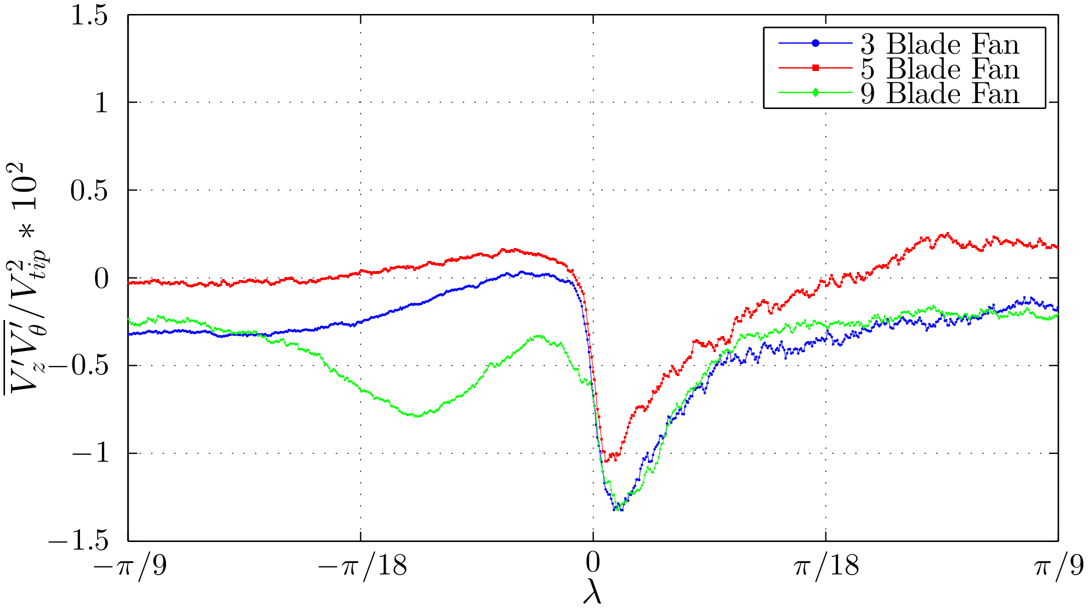

Figure 3.43 Case V Reynolds stress in z-θ – plane over λ_9

3.4 First Law of Thermodynamics Analysis

Section 1.2.1 outlined the work rate equation for the two control volumes that have been identified for the present investigation. Equation (3.12) states the First Law of Thermodynamics in non-dimensional form. The present measurements: input shaft torque , pressure rise across the control volume, the mass flow rate through the fan, and the exit kinetic energy in the wake of the fan at the blade mid-span allow a partial evaluation of the terms in Equation (3.12). A qualitative comparison between the three different fan configurations can be made using the structure of Equation (3.12).

$$P_{shaft}{}^{*} = \left\{ \underbrace{\int_{c.s.} \frac{1}{2}\rho\overline{(\boldsymbol{V}\cdot\boldsymbol{V})\;\boldsymbol{V}\cdot\hat{\boldsymbol{n}}}\;dA}_{\kappa} + \underbrace{\int_{c.s.} \frac{P}{\rho}\;\rho\cdot\boldsymbol{V}\cdot\hat{\boldsymbol{n}}\;dA}_{\chi} + \underbrace{losses}_{\xi} \right\} \frac{1}{r_{tip}\times\rho V_{tip}^{2} r_{tip}^{2}} \tag{3.12}$$

3.4.1 Input Shaft Power – $\mathbf{P}_{shaft}{}^{*}$

The left hand side of Equation (3.12) was evaluated by Equation (3.13). Figure 3.44 provides the input shaft power as function of flow coefficient and marks the operating conditions of interest for the three, five, and nine blade fans. These data are the same as the non-dimensional torque presented in Figure 3.5, scaled with the angular velocity of the fan. These figures indicate that more power is required to operate the fan with a higher number of blades. That observation is consistent with the higher lift force generated by the fan blades from the non-dimensional lift coefficient analysis performed in Section 3.2.1.

$$\mathrm{P}_{shaft}{}^{*} = \mathrm{T}^{*}|\boldsymbol{\Omega}| \tag{3.13}$$

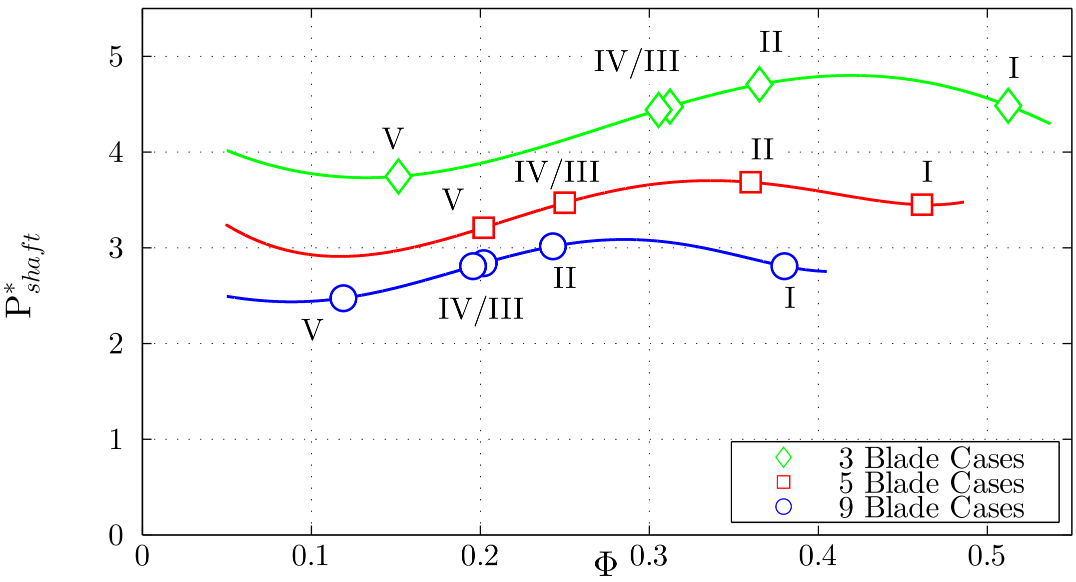

Figure 3.44 Non-dimensional input shaft power

3.4.2 Net Kinetic Energy Flux – κ

The first term on the right hand side of Equation (3.12), κ, can be evaluated for Control Volume (1) and (2) with the velocity data provided in the wake. This integral can only be evaluated as a representative value because the measurements were only taken at one radial location. Therefore, the integral will be approximately evaluated with exit wake kinetic energy that is constant in the radial direction. This assumption allows this value to provide a comparison between the three different fan configurations. However, it does not give an absolute assessment of the net kinetic energy flux through the control volume. Before evaluating this integral the non-dimensional kinematic integrand will be presented in Figures 3.45–3.49. These data show the kinetic energy flux values of the fluid for the pressure and suction sides of the blade. For Case I (Figure 3.45) the trend shows that increasing the number of blades increases the overall kinetic energy exiting the control volume. Additionally, the magnitude kinetic energy produced by the blade passing above the probe near the suction side overtakes the pressure side in magnitude as the number of blades is increased. Cases II–V (Figures 3.46–3.49) provide distinctly different and consistent observations of the exit kinetic energy regardless from Case I. There is a trend in these figures where the three blade fan produces the highest kinetic energy flux out of the control volume as the blade passes above the probe and the nine the least. The pressure side near the wake collapses onto a curve for all four of these operating conditions. Case II–V show that the exit kinetic energy produced by the blade passing above the probe shows an opposite trend to the number of blades installed on the fan. This is self consistent with the swirl number results that indicate that the lower mass flow rate operating conditions have a direct relationship with azimuthal mean velocity and number of fan blades installed. A complete collection of the figures presented in Section 3.4.2 are available in a format similar to Figures 3.16 and 3.17 within Appendix C.

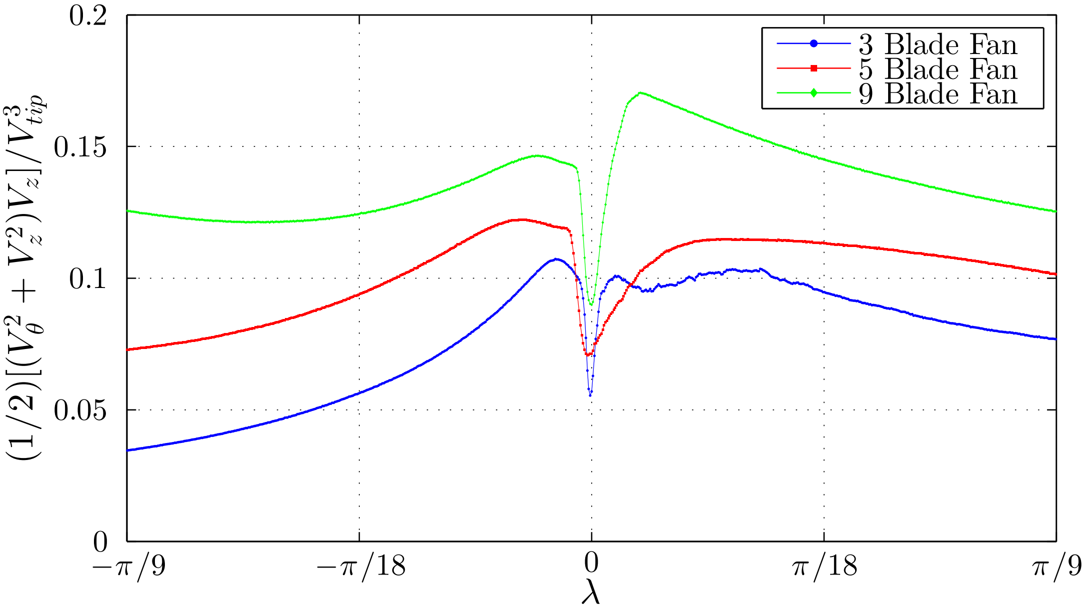

Figure 3.45 Case I kinematic integrand exit kinetic energy flux over λ_9

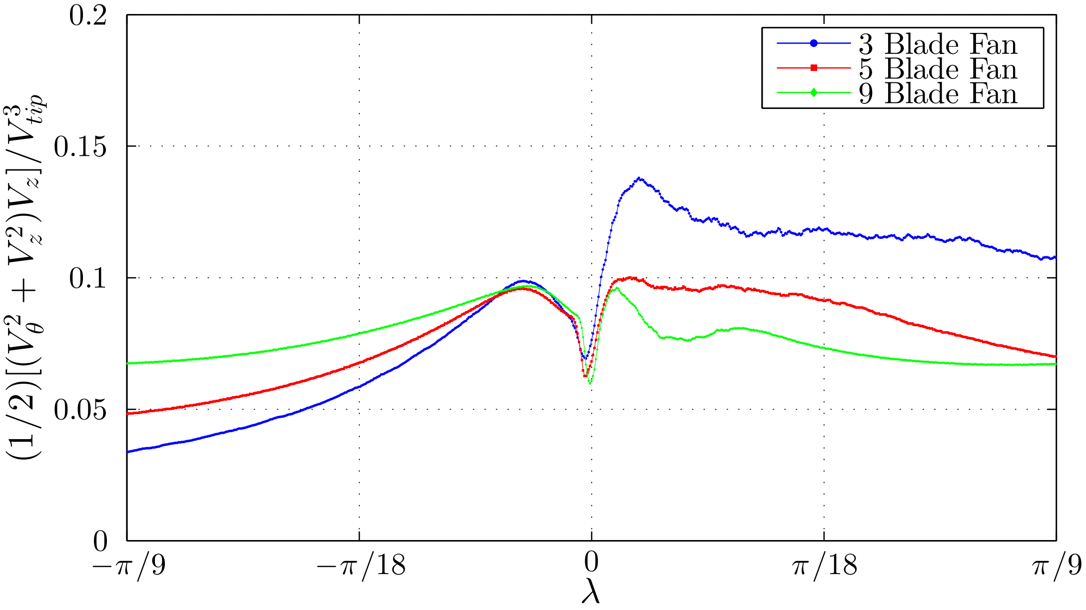

Figure 3.46 Case II kinematic integrand exit kinetic energy flux over λ_9

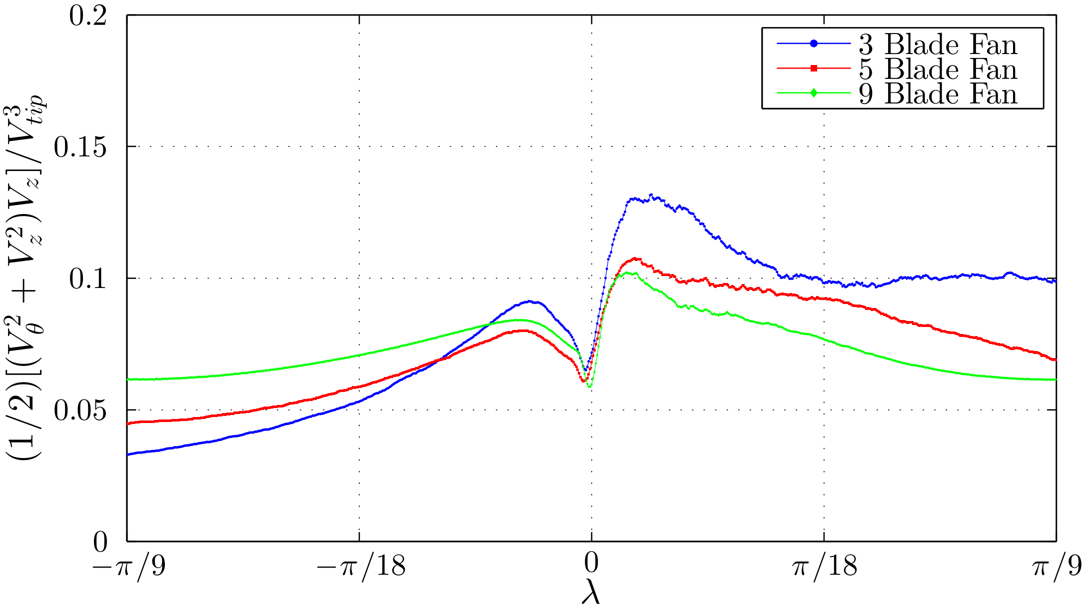

Figure 3.47 Case III kinematic integrand exit kinetic energy flux over λ_9

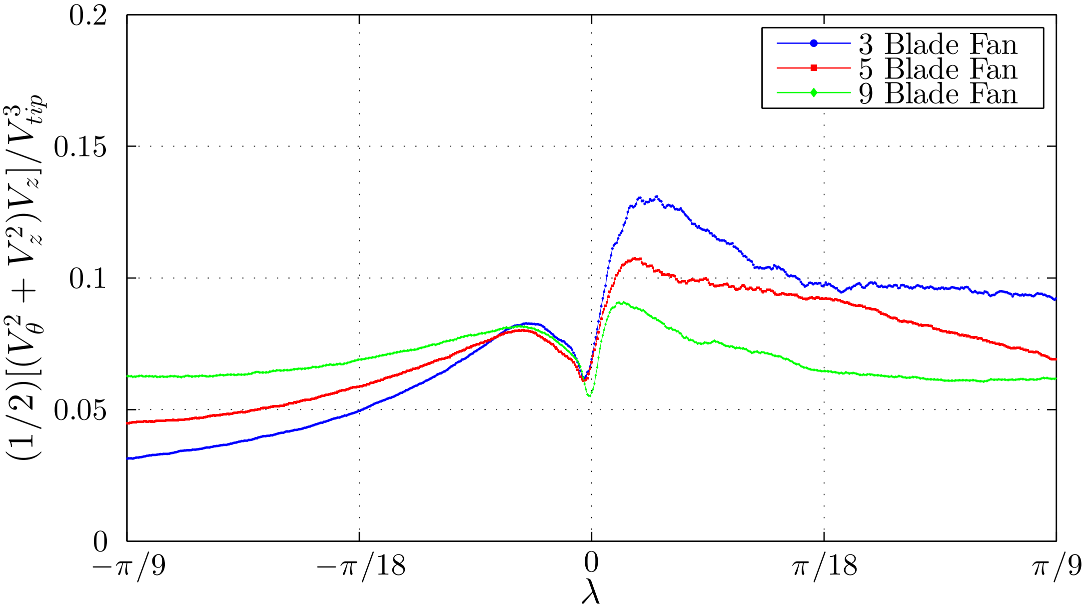

Figure 3.48 Case IV kinematic integrand exit kinetic energy flux over λ_9

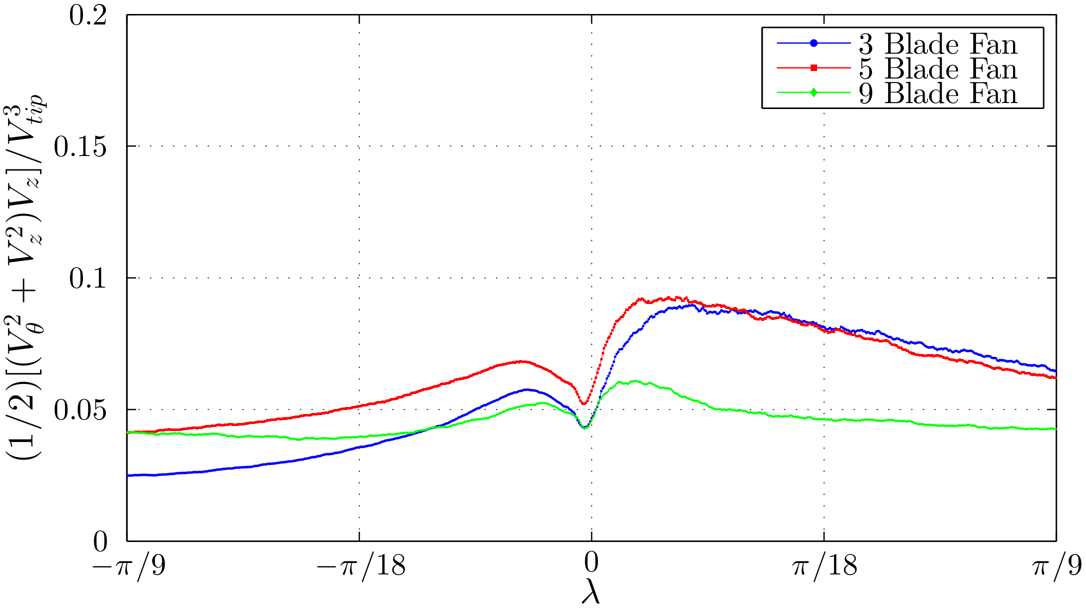

Figure 3.49 Case V kinematic integrand exit kinetic energy flux over λ_9

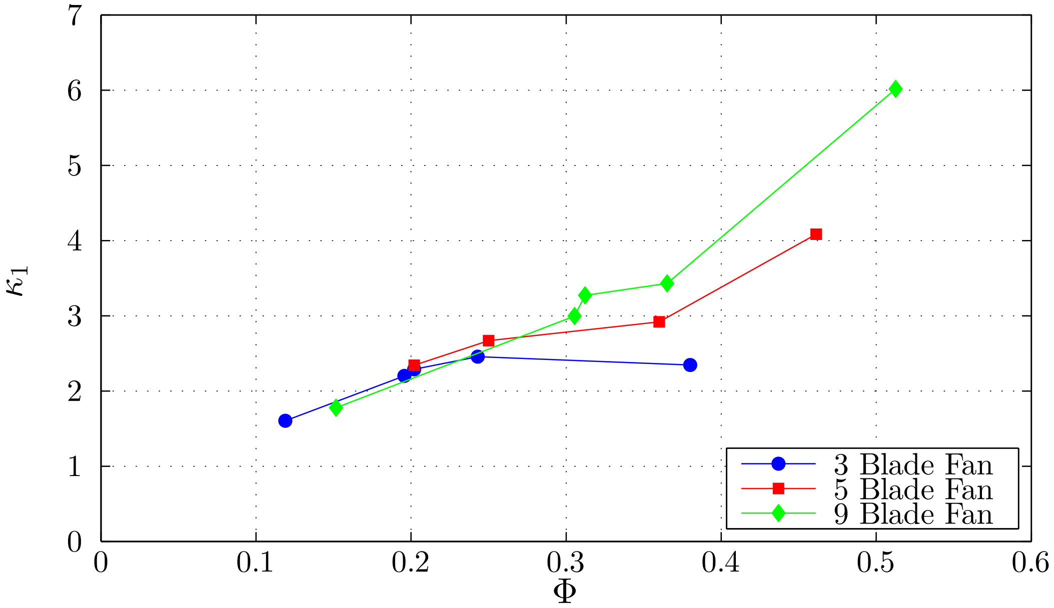

Figure 3.50 Net kinetic energy flux Control Volume (1)

The integrands in Figures 3.45–3.49 were evaluated for Control Volume (1) and (2). The inlet air to Control Volume (1) had negligible kinetic energy; therefore, the integrands from Figures 3.45–3.49 can be evaluated directly from the obtained dimensional values. Equation (3.14) provides the integral evaluated to find κ_1. Figure 3.50 provides the results from evaluating this integral. For this control volume the kinetic energy is high for all three fan configurations at high flow coefficient. Case I displays a similar trend between κ_1 and the number of blades installed on the fan. This trend disappears as the flow coefficient is reduced from Case I. These results are consistent with the plotted integrands. At lower flow coefficients the net kinetic energy flux through Control Volume (1) is significantly lower than the net kinetic energy flux at Case I. These results are supported by the increased influence of lower flow coefficient on the azimuthal velocity at the fan exit plane.

$$\kappa_1 = \frac{1}{r_{tip} \times \rho V_{tip}^2 r_{tip}^2} \int_{r_{hub}}^{r_{tip}} \int_0^{2\pi} \frac{1}{2} \rho \overline{({V_\theta}^2 + {V_z}^2) V_z} \; r d\theta \; dr \tag{3.14}$$

The kinetic energy at the inlet of Control Volume (2) is given by the average velocity profile at the inlet of the fan by the mass flow rate through the fan. This velocity, $\overline{V}$, is assumed to be uniform over the inlet. Equation (3.15) provides the integral to find the net kinetic energy flux through Control Volume (2). This integral cannot be properly evaluated given the limitation of one radial position for the wake velocity measurements.

$$\kappa_2 = \frac{1}{r_{tip} \times \rho V_{tip}^2 r_{tip}^2} \int_{r_{hub}}^{r_{tip}} \int_0^{2\pi} \frac{1}{2} \rho [\overline{({V_\theta}^2 + {V_z}^2) V_z} - \overline{V}^3] \; r d\theta \; dr \tag{3.15}$$

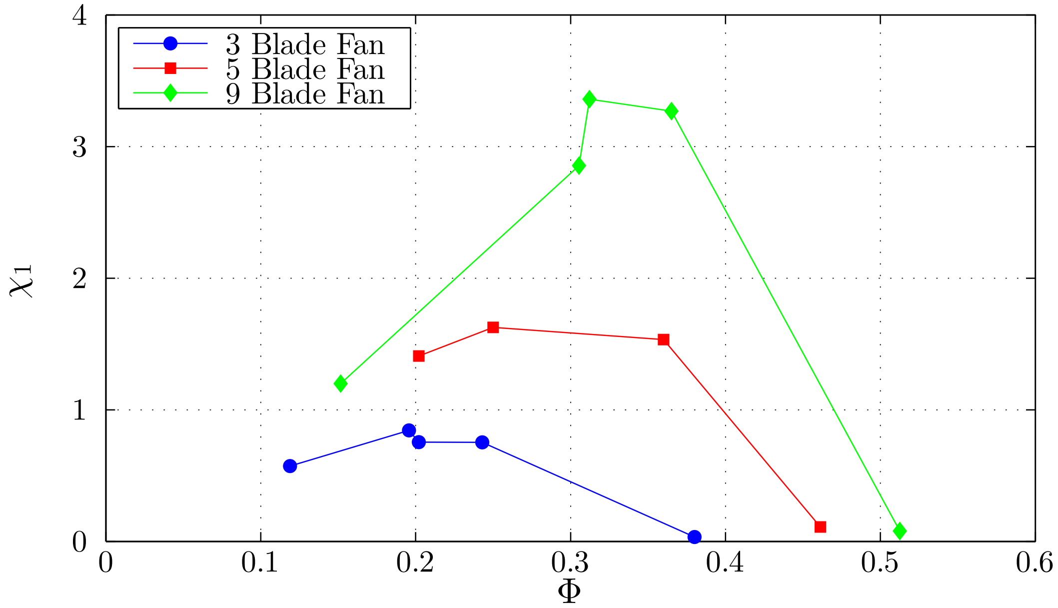

Figure 3.51 Flow-work rate Control Volume (1)

3.4.3 Flow-Work Rate – χ

The second term on the right hand side of Equation (3.12) was evaluated from the integral measurements obtained from experiment. The present analysis assumes that the pressure at the control volume exit plane is uniform and equal to the receiver pressure. In reality, the curved streamlines at the exit fan plane indicate an increase in pressure with increasing radius. Equation (3.16) provides the evaluation of the integral from Equation (3.12) for Control Volume (1). Figure 3.51 provides the flow-work rate as a function of flow coefficient for Control Volume (1). Each of these curves reach a maximum around the discontinuity region of the characteristic curve.

$$\chi_1 = \left(\frac{[P_{rec} - P_{atm}]}{\rho}\right)\dot{m} \tag{3.16}$$

Equation (3.17) provides the evaluation of the integral from Equation (3.12) for Control Volume (2). Figure 3.52 provides the flow-work rate as a function of flow coefficient for Control Volume (2). This formulation for χ_2 shows higher flow-work rate for the higher flow coefficient operating conditions. This is due to the dynamic pressure of the inlet velocity being added to the previous pressure used for the definition of χ_1. The comparison for Control Volume (1) and (2) arises from observing where energy is transferred between terms on the right hand side of Equation (3.12). In Control Volume (1), a majority of the power transferred from the fan to the fluid is through kinetic energy. This is due to the negligible kinetic energy that the fluid has entering the control volume. Control Volume (2) shifts this energy into the flow-work rate term which is given by the pressure difference across the fan. This pressure difference is increased because the pressure at the inlet surface of the control volume is lower from the dynamic pressure of the moving air entering the control volume.

$$\chi_2 = \left(\frac{[P_{rec} - P_{atm}] + 1/2 \rho \overline{V}^2}{\rho} \right) \dot{m} \tag{3.17}$$

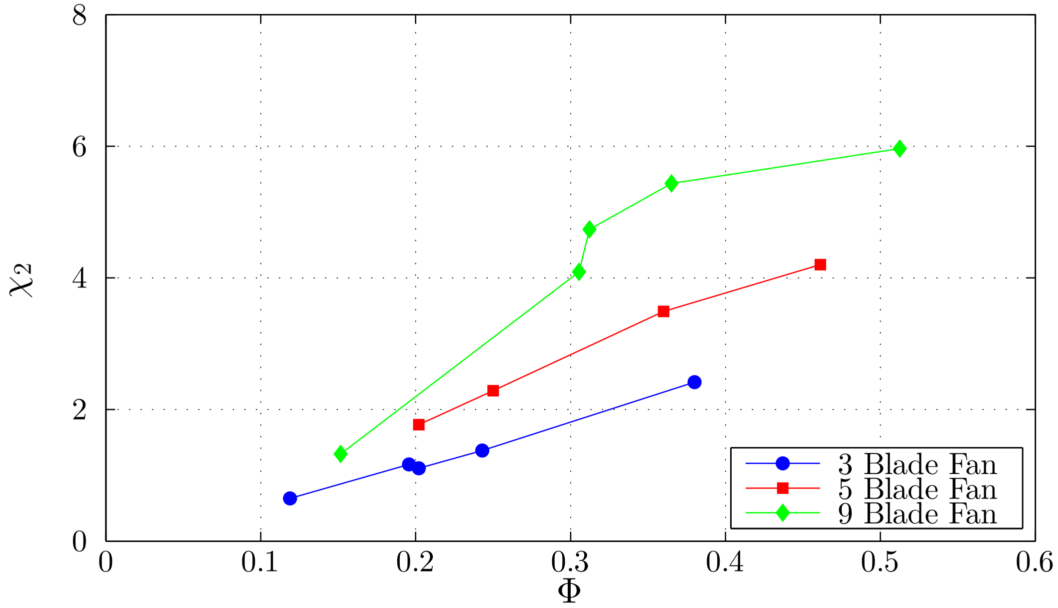

Figure 3.52 Flow-work rate Control Volume (2)

3.4.4 Turbulent Kinetic Energy Losses – ξ

The last term to consider in Equation (3.12) is the loss term ξ. The mechanical losses in this system are considered to be a summation with multiple causes. This term cannot be evaluated as the others have previously in this document. An indirect way to observe how this term is changing between operating conditions is to look at the turbulence kinetic energy. Figures 3.53-3.57 provide the turbulence kinetic energy of the fluid at the exit plane in the wake of the fan. These measurements are not directly loss terms; however, this energy is not recoverable in the system and will take away from the available input shaft power. As the flow coefficient is decreased the turbulence kinetic energy magnitude is increased for all the fan configurations. Again, the response of the probe to the passing blade overhead is similar for a fan with less blades and higher flow coefficient. This suggests that similar flow conditions occur for the different fans in a inverse relationship with flow coefficient and number of blades. For example, the nine blade fan will experience similar flow conditions at a lower flow coefficient as the five blade fan does. This may be influenced by the increased mass flow rate through the fan when blades are added. A complete collection of the figures presented in Section 3.4.4 are available in a format similar to Figures 3.16 and 3.17 within Appendix C.

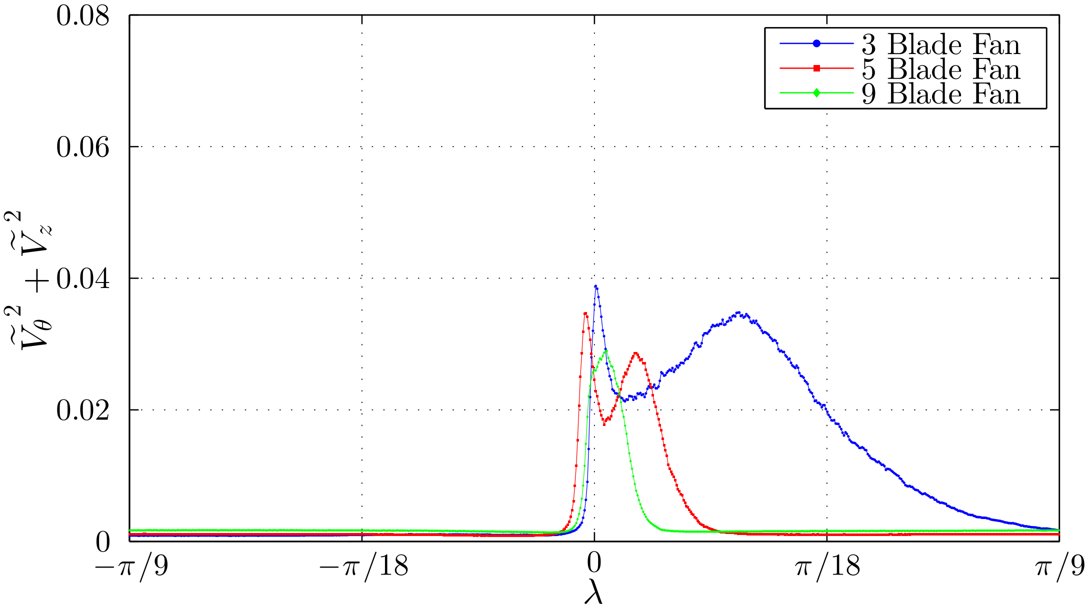

Figure 3.53 Case I turbulence kinetic energy at fan exit over λ_9

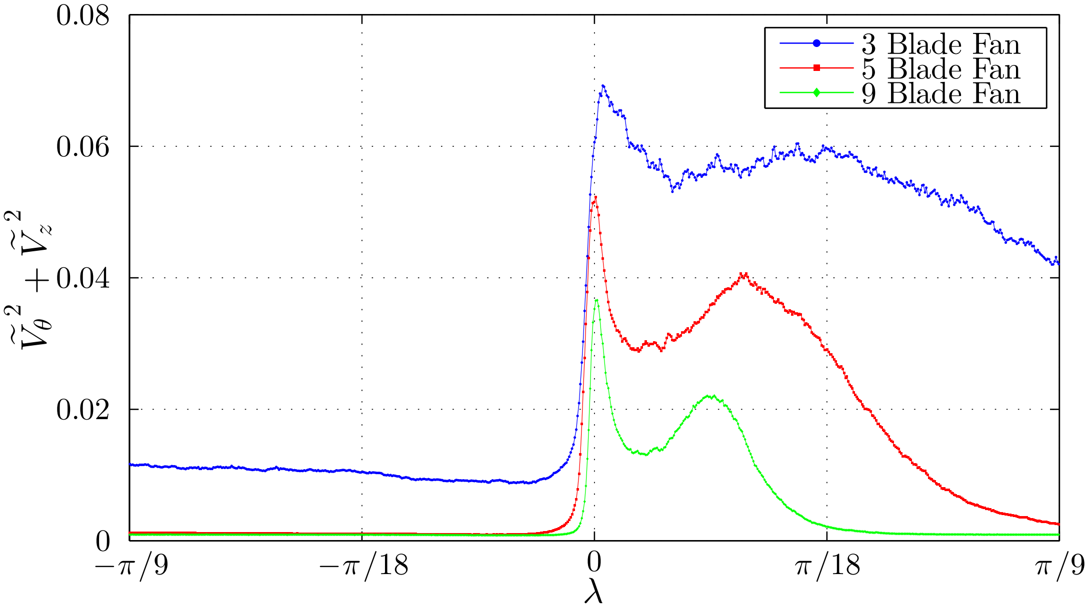

Figure 3.54 Case II turbulence kinetic energy at fan exit over λ_9

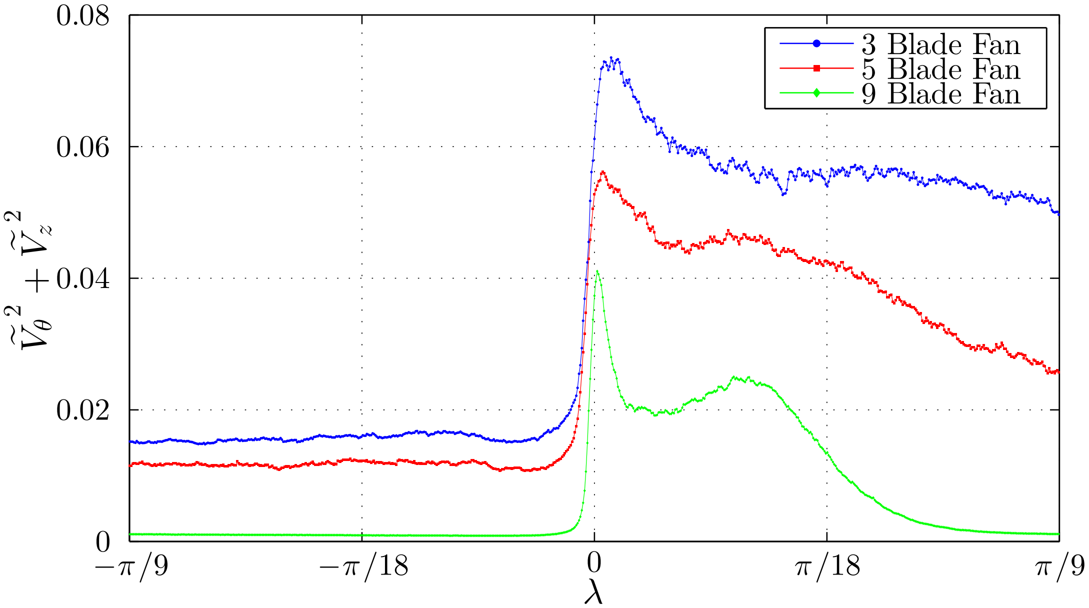

Figure 3.55 Case III turbulence kinetic energy at fan exit over λ_9

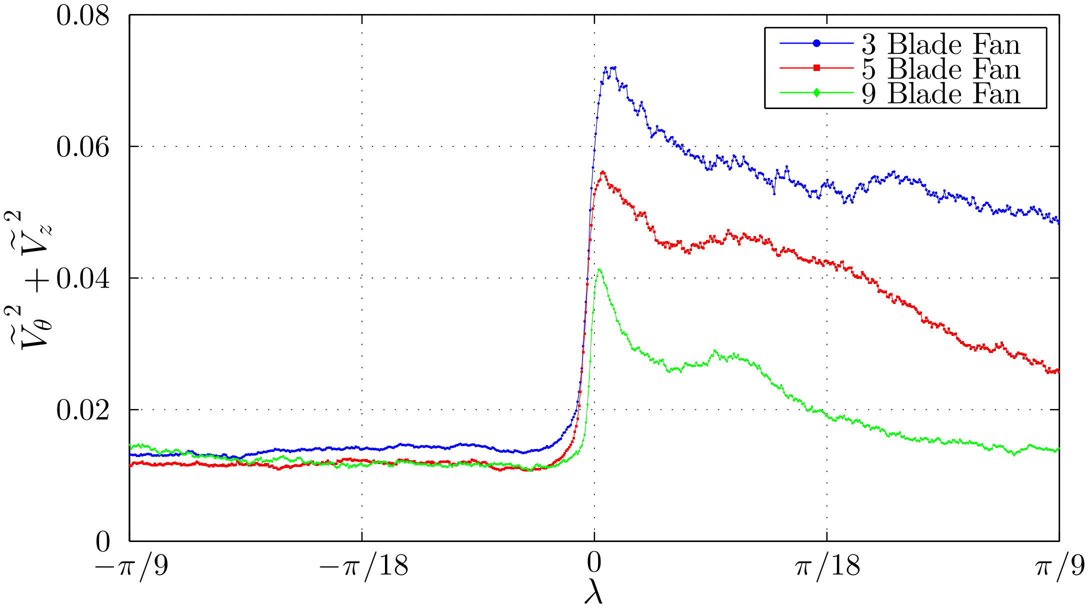

Figure 3.56 Case IV turbulence kinetic energy at fan exit over λ_9

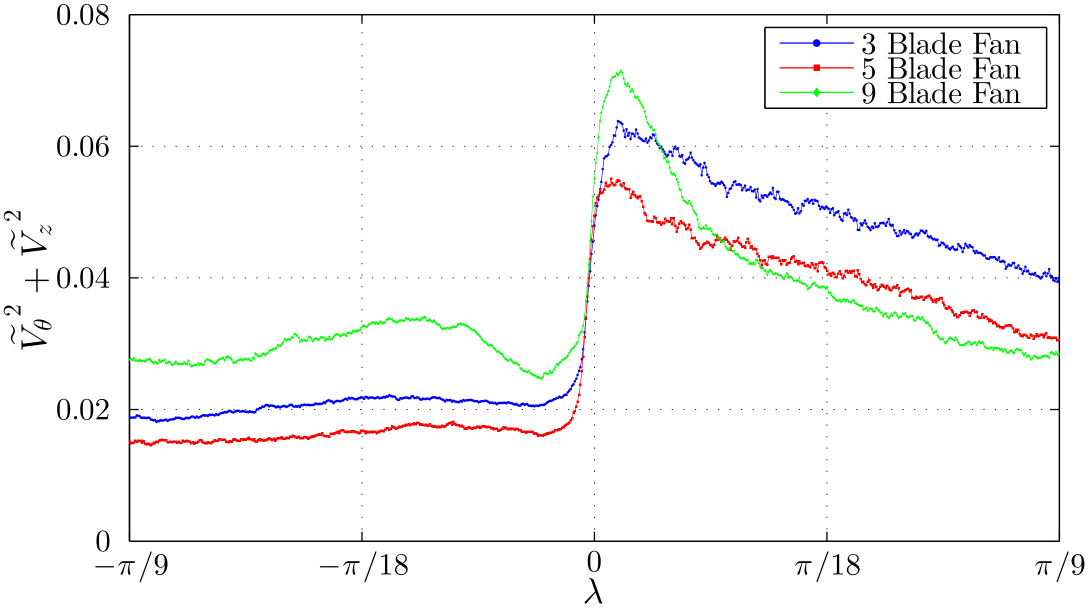

Figure 3.57 Case V turbulence kinetic energy at fan exit over λ_9

Chapter 4

SUMMARY AND CONCLUSIONS

The present investigation examined differences in flow behavior over fan blade varying the number of blades installed on the fan. This fan had nine identical blade sections that were installed in configurations with 3–9 blades. These fans were compared using integral fan measurements including: pressure rise across the fan, mass flow rate through the fan, and the input shaft torque to the fan. The characteristic curves (Figure 3.1) for these fans displayed a trend with a discontinuous portion of the performance curve for the 3–4 and 6–9 blade fans. The discontinuity on the 3 and 4 blade fans experienced a decrease in the head-rise coefficient with increasing flow coefficient. The 6–9 blade fans experienced an increase in the head-rise coefficient with increasing flow coefficient. The 5 blade fan did not have a discontinuity in its characteristic curve. The extreme cases: 3 and 9 blade fans, and the 5 blade fan were selected to be examined with other experimental techniques. These data were also used to select operating conditions to be investigated in detail using surface pressure measurements on the blade as well as near-wake hot-wire velocity measurements. Five operating conditions (Cases I–V) were selected for experimentation; they are defined in Figure 3.3. These data were used to interpret two different control volumes.

Surface pressure measurements were obtained across the span of the blade for the selected fan configurations and operating conditions. These data were used to evaluate a non-dimensional lift coefficient for an individual blade for each configuration as well as an overall value for the entire fan. Figure 3.7 provided that there was an opposite trend with the non-dimensional lift coefficient per blade and the number of blades installed on the fan. Figure 3.8 showed that there was a similar trend with the overall fan non-dimensional lift coefficient and the number of blades installed on the fan. The latter result indicates that the pressure measurements are self consistent with the input shaft torque measurements; see Figure 3.5. The surface pressure measurements have been provided for each operating condition in Figures 3.9–3.13. Additionally, surface pressures obtained from twenty taps along the trailing edge of the blade were obtained and presented in Figure 3.14.

Wake velocity measurements were obtained with a two velocity component X-probe in the present investigation. These measurements were evaluated as a phase ensemble to find the statistics of the measured velocity. This method provided these data at 6000 discrete points in the azimuthal direction in the near-wake of the fan for one revolution of the fan. These data provide another way to compare the three fan configurations and five operating conditions in the present investigation. The statistics from the velocity measurements suggest that the blade to blade interactions suppress turbulent fluctuations at a given operating condition in the fan wake. The obtained mean axial and azimuthal velocities in the fan wake are presented in Figures 3.18–3.27. A representative value for the azimuthal portion of the velocity in the fan wake was presented, as a swirl number, in Figure 3.28. These data indicate that the magnitude of the azimuthal component of velocity increases as the number of blades installed on the fan increases. Also the swirl number decreases as the with flow coefficient is increased. The fluctuating velocity components from these data were evaluated as the terms in the Reynolds stress tensor from the Reynolds averaged momentum equations. (Section D) The obtained axial and azimuthal turbulence intensities are presented in Figures 3.29–3.38. The obtained Reynolds shear stress values are presented in Figures 3.39-3.43. These data suggest that increasing the number of blades suppresses turbulence at a given value of the flow coefficient.

The integral and wake velocity measurements were used to evaluate the First Law of Thermodynamics for the two control volumes considered in the present investigation. The input shaft power is presented in Figure 3.44. A surrogate for the net kinetic energy flux was evaluated for each control volume. These results are presented in Figures 3.50 and **??**. The flow work rate was also evaluated for these control volume analyses. These results are presented in Figures 3.51 and 3.52. The turbulence kinetic energy was also considered as a contributor to energy lost in the control volume. These data, provided in Figures 3.53–3.57, indicate that the turbulence kinetic energy increases as function of flow coefficient. Additionally, there is an inverse relationship between the magnitude of turbulence kinetic energy and number of blades installed on the fan.

The following conclusions are supported by the results of the present investigation:

- Non-dimensional lift coefficient per blade decreases as the number of blades installed on the fan is increased
- Non-dimensional lift coefficient for the entire fan increases as the number of blades installed on the fan is increased and self consistent with the measured input shaft torque to the fan
- Magnitude of azimuthal velocity in the wake of the fan increases as the number of blades installed on the fan is increased
- Turbulent fluctuations are suppressed as the number of blades installed on the fan increases.

APPENDICES

A PRESSURE COEFFICIENT FIGURES

Complete collection of pressure coefficient data for every operating condition (Case I–V) and fan configuration (3–9 Blades). These data are represented in Figures 3.9-3.10 for a given operating condition.

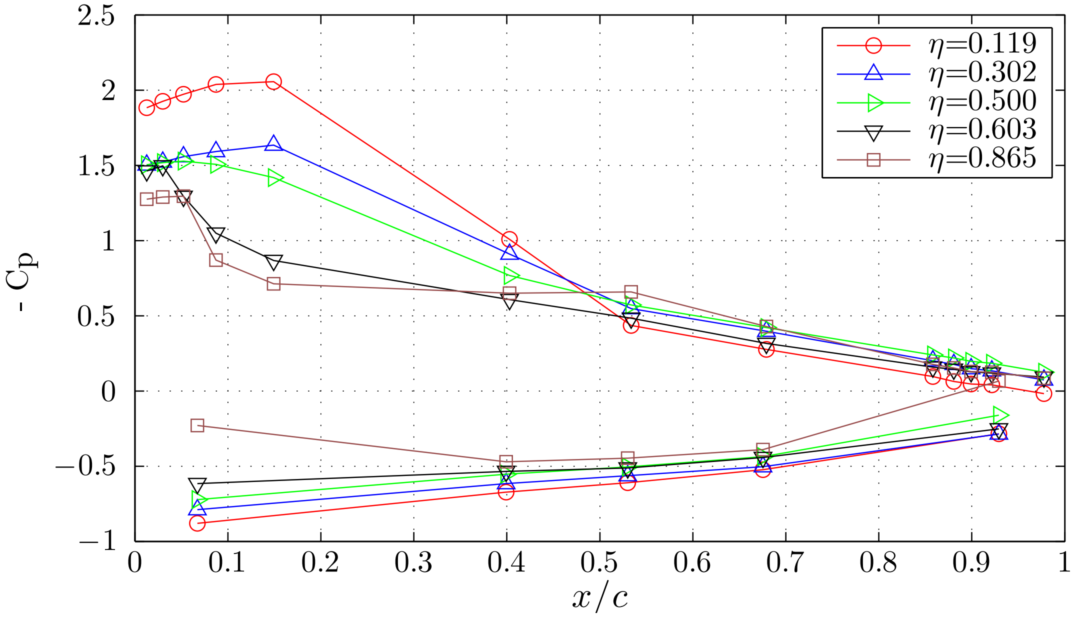

Figure 1 Case I pressure coefficients 3 blade fan

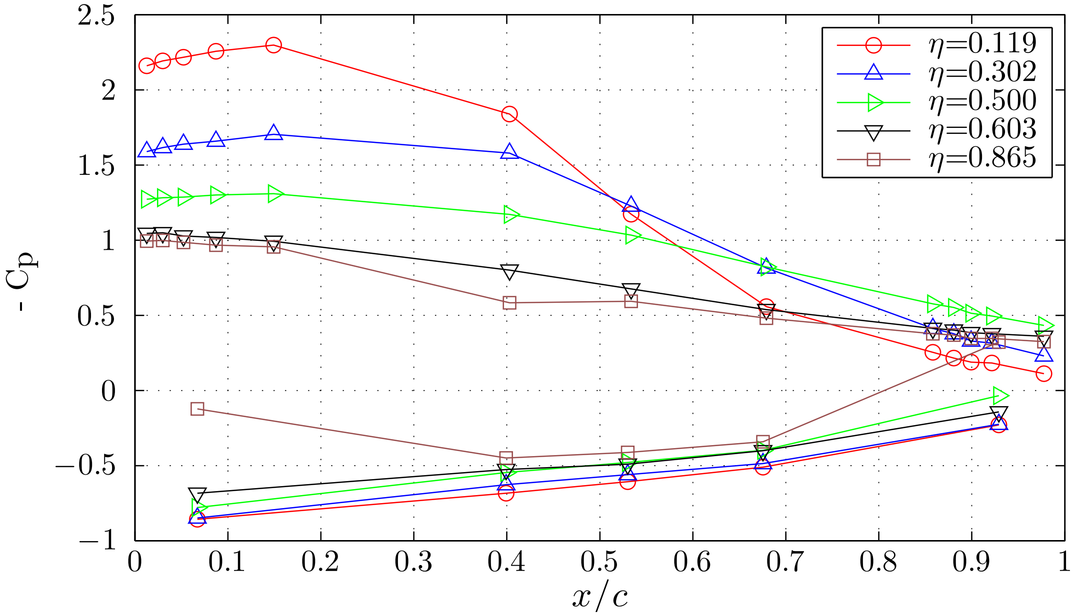

Figure 2 Case II pressure coefficients 3 blade fan

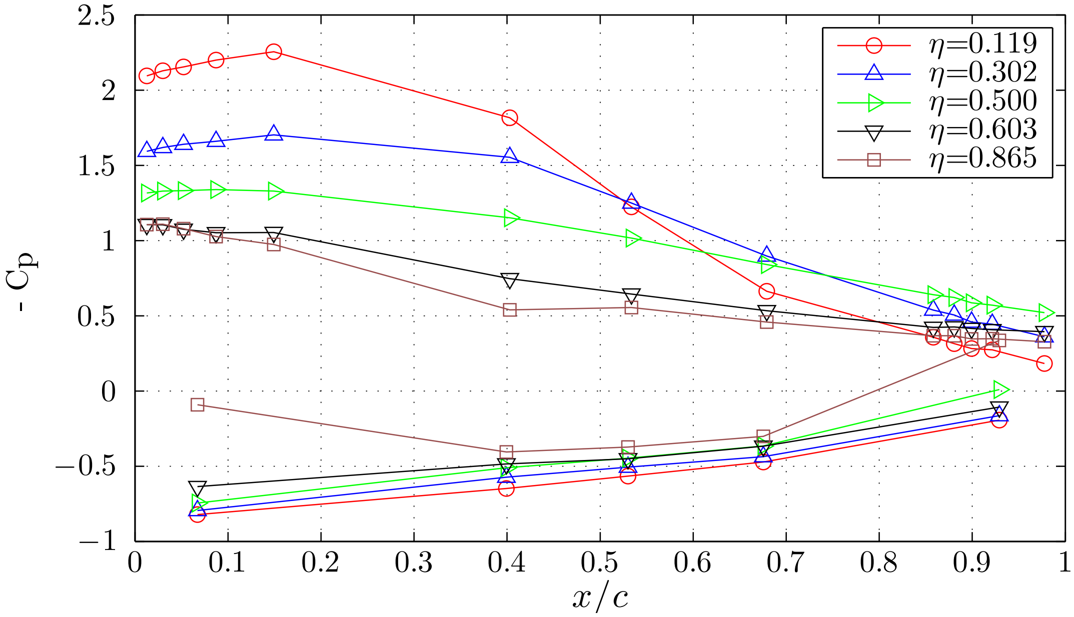

Figure 3 Case III pressure coefficients 3 blade fan

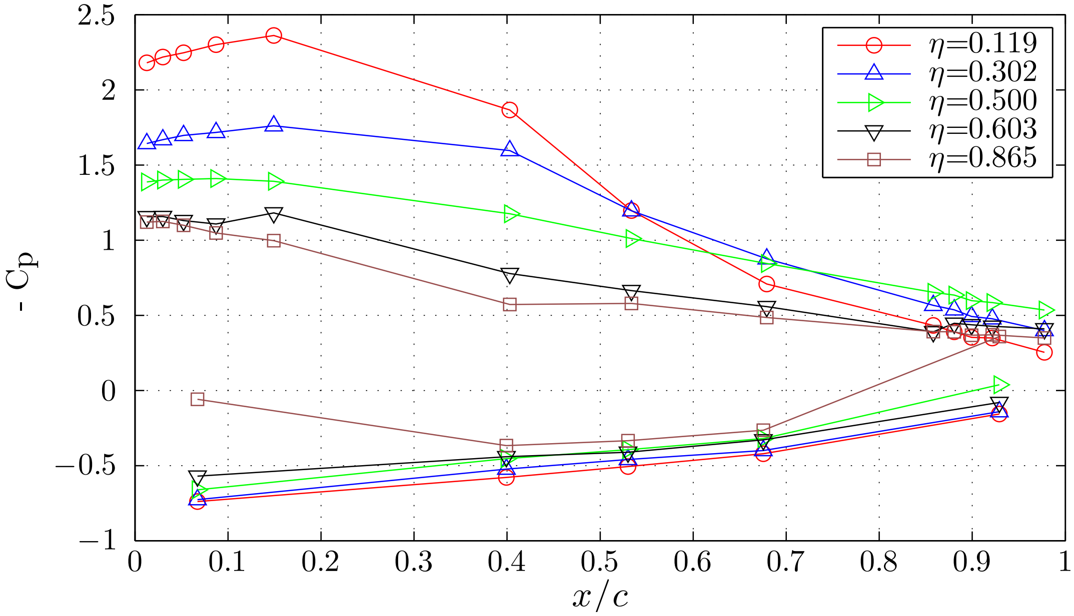

Figure 4 Case IV pressure coefficients 3 blade fan

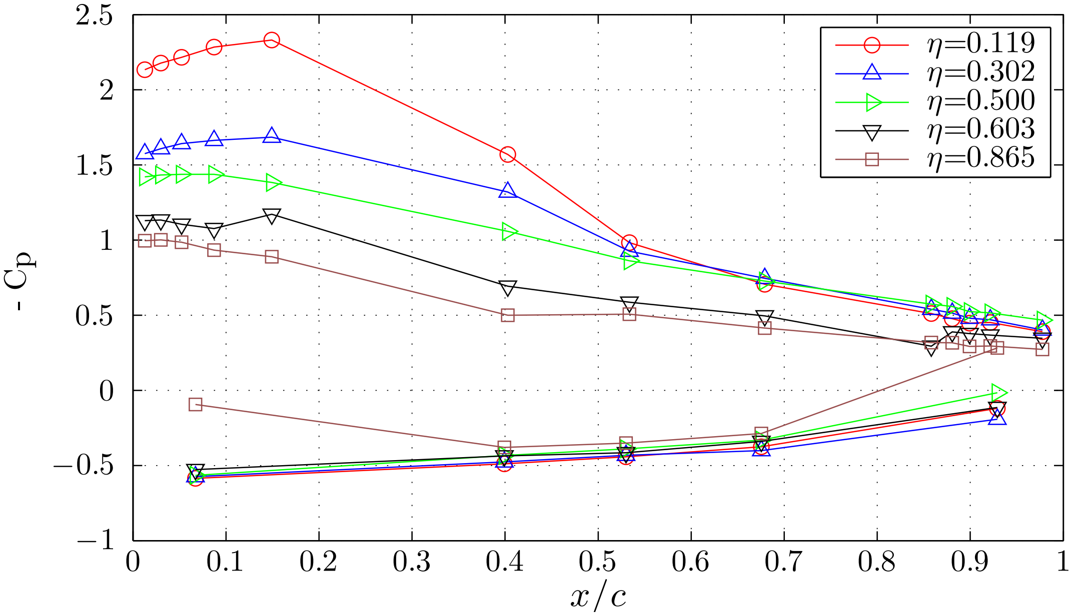

Figure 5 Case V pressure coefficients 3 blade fan

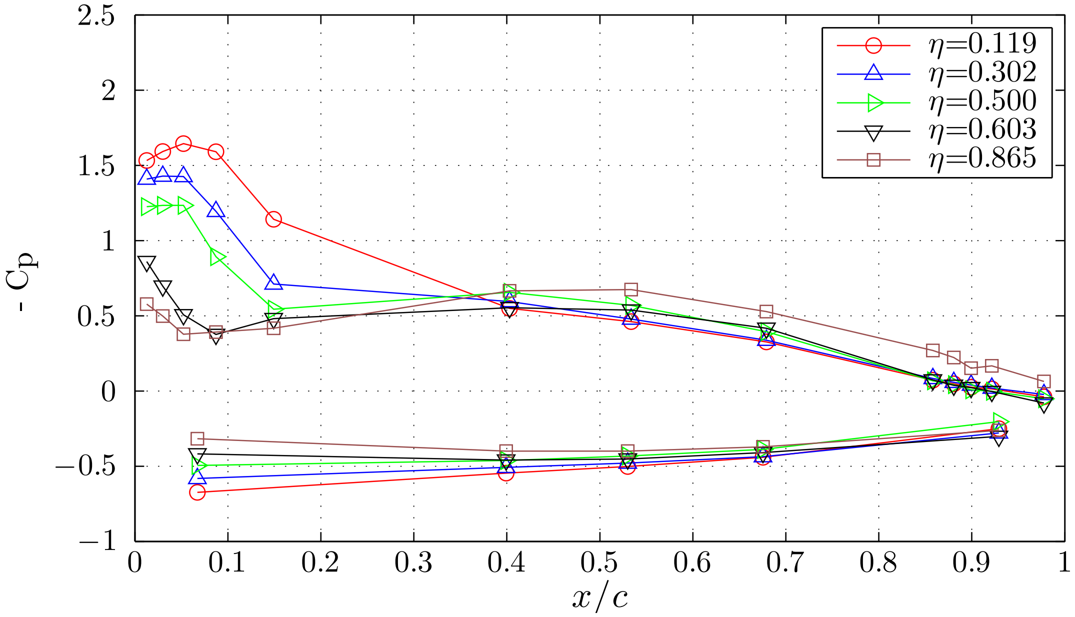

Figure 6 Case I pressure coefficients 5 blade fan

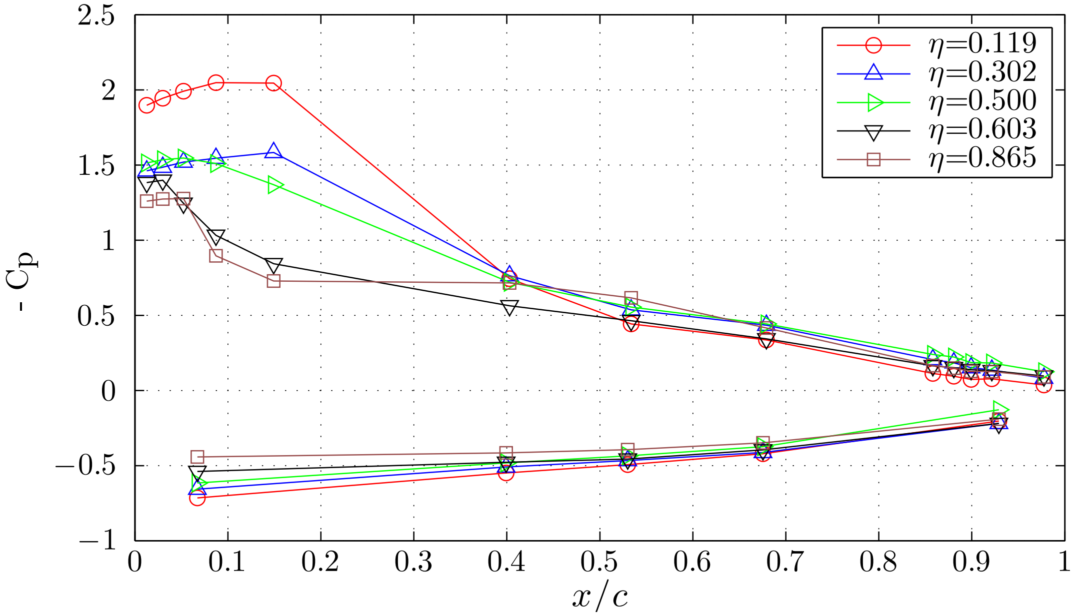

Figure 7 Case II pressure coefficients 5 blade fan

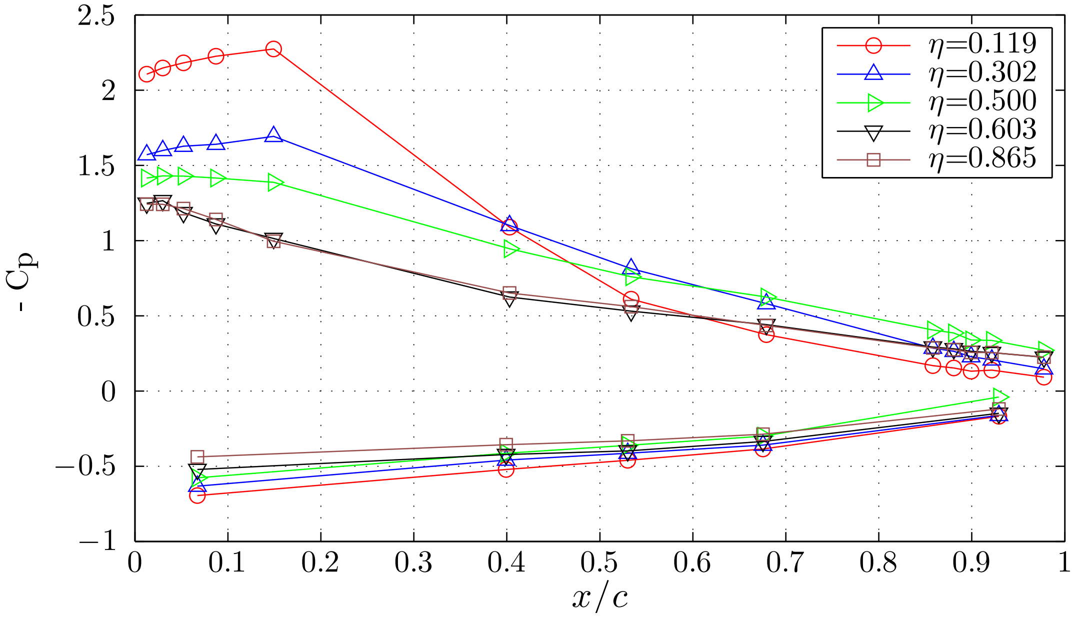

Figure 8 Case III/IV pressure coefficients 5 blade fan

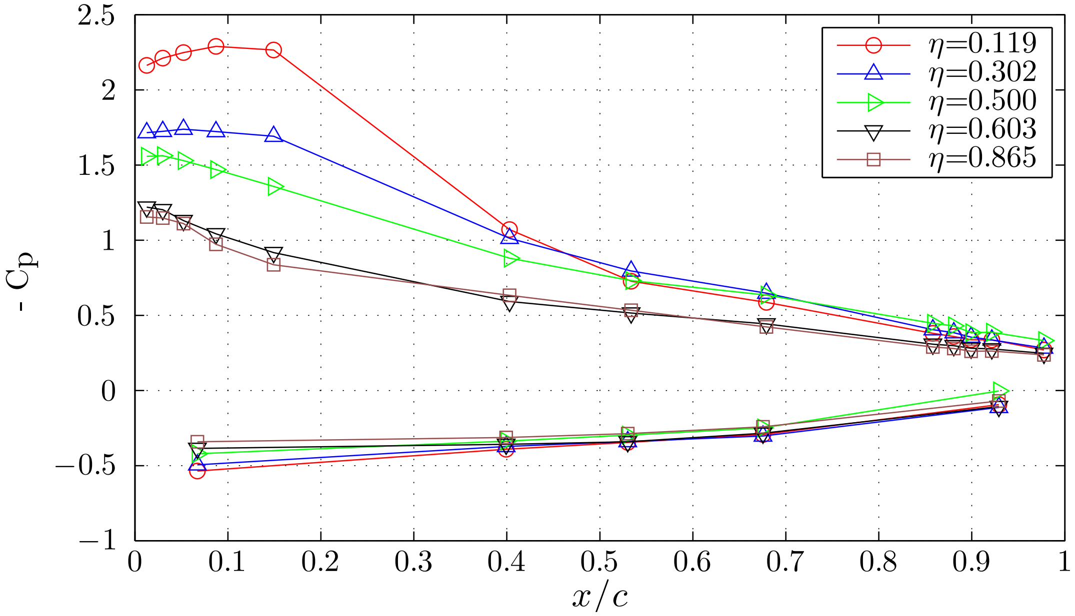

Figure 9 Case V pressure coefficients 5 blade fan

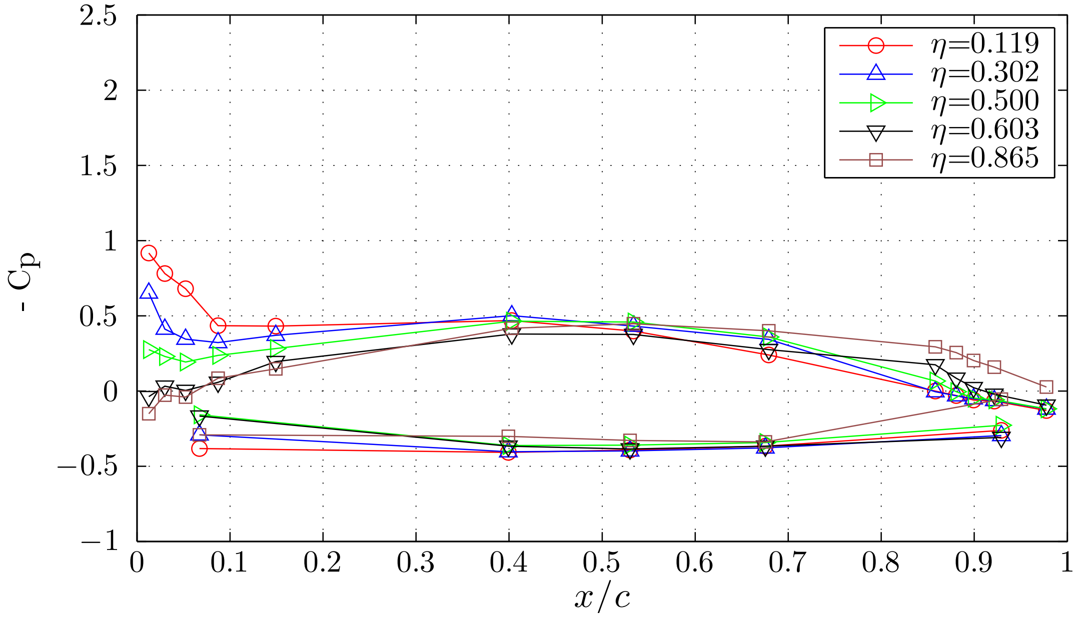

Figure 10 Case I pressure coefficients 9 blade fan

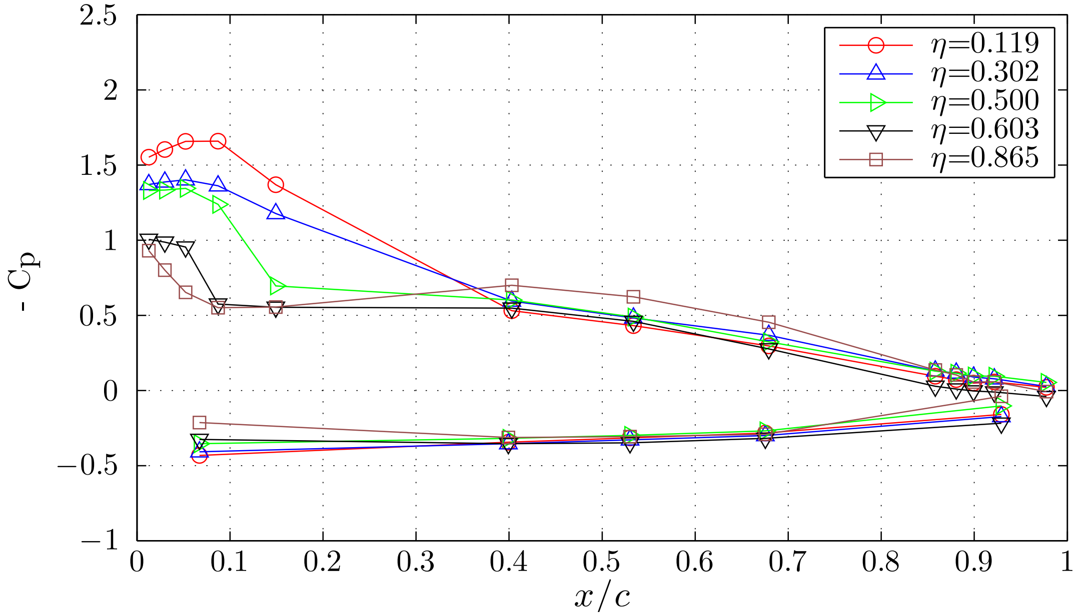

Figure 11 Case II pressure coefficients 9 blade fan

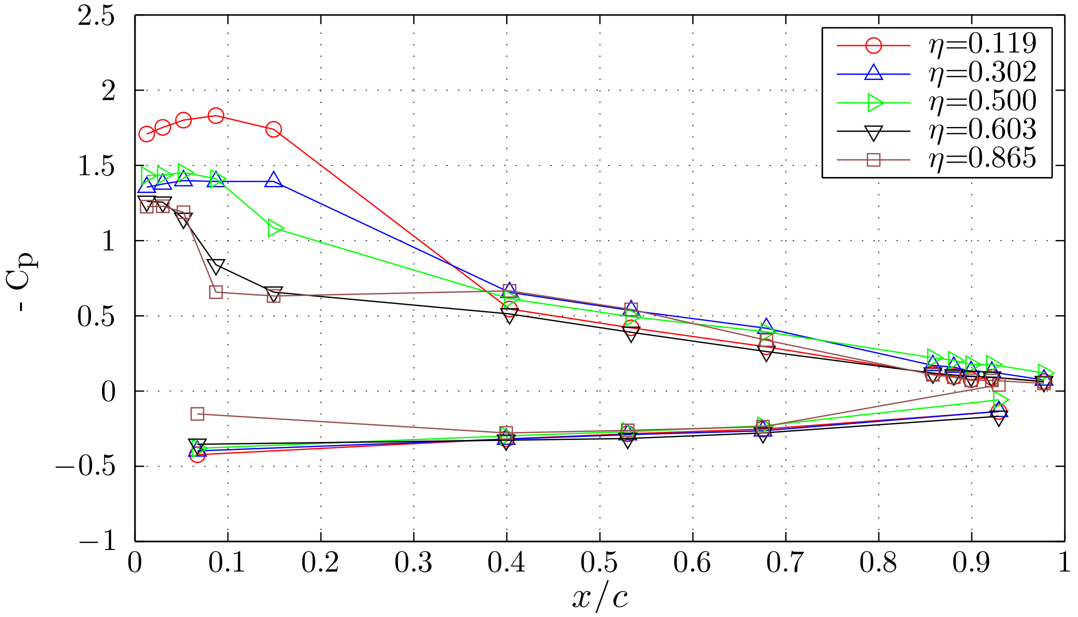

Figure 12 Case III pressure coefficients 9 blade fan

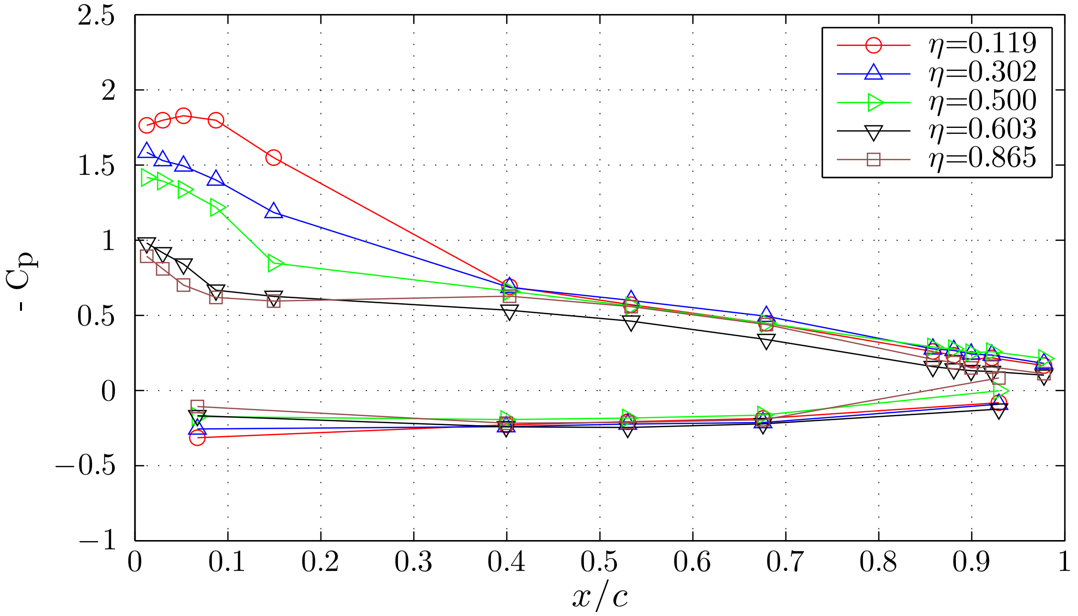

Figure 13 Case IV pressure coefficients 9 blade fan

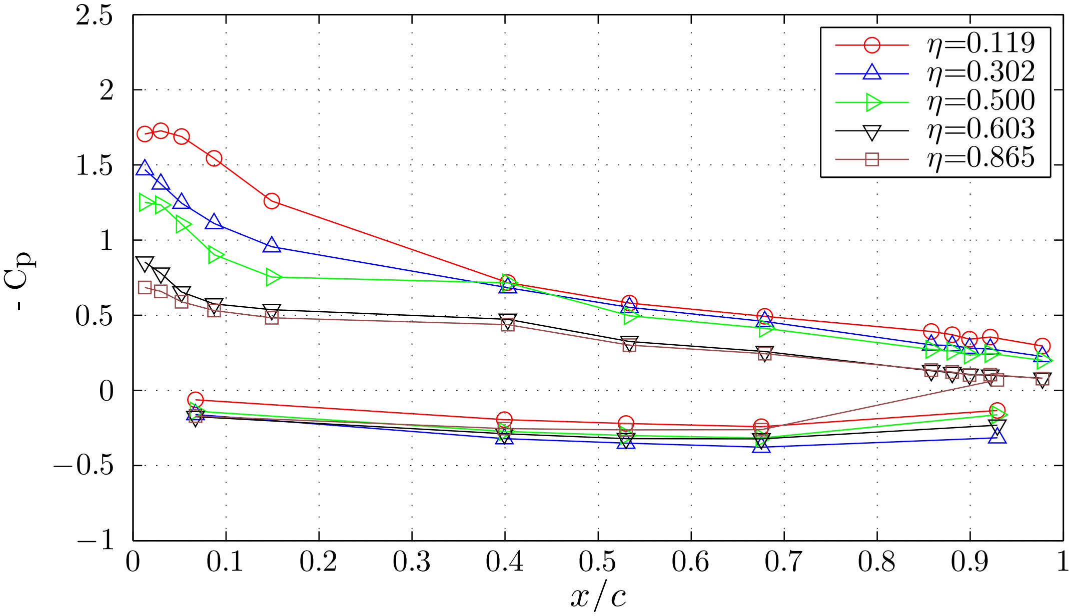

Figure 14 Case V pressure coefficients 9 blade fan

B WAKE VELOCITY STATISTICS FIGURES

This appendix contains the entire collection of figures that were used to generate the wake velocity statistics with the method presented in Section 3.3. These figures are presented in the same sequence as they are in Section 3.3 and include these statistics: V_z, V_θ, $\widetilde{V}_z$, $\widetilde{V}_\theta$, and $\overline{V_z' V_\theta'}$.

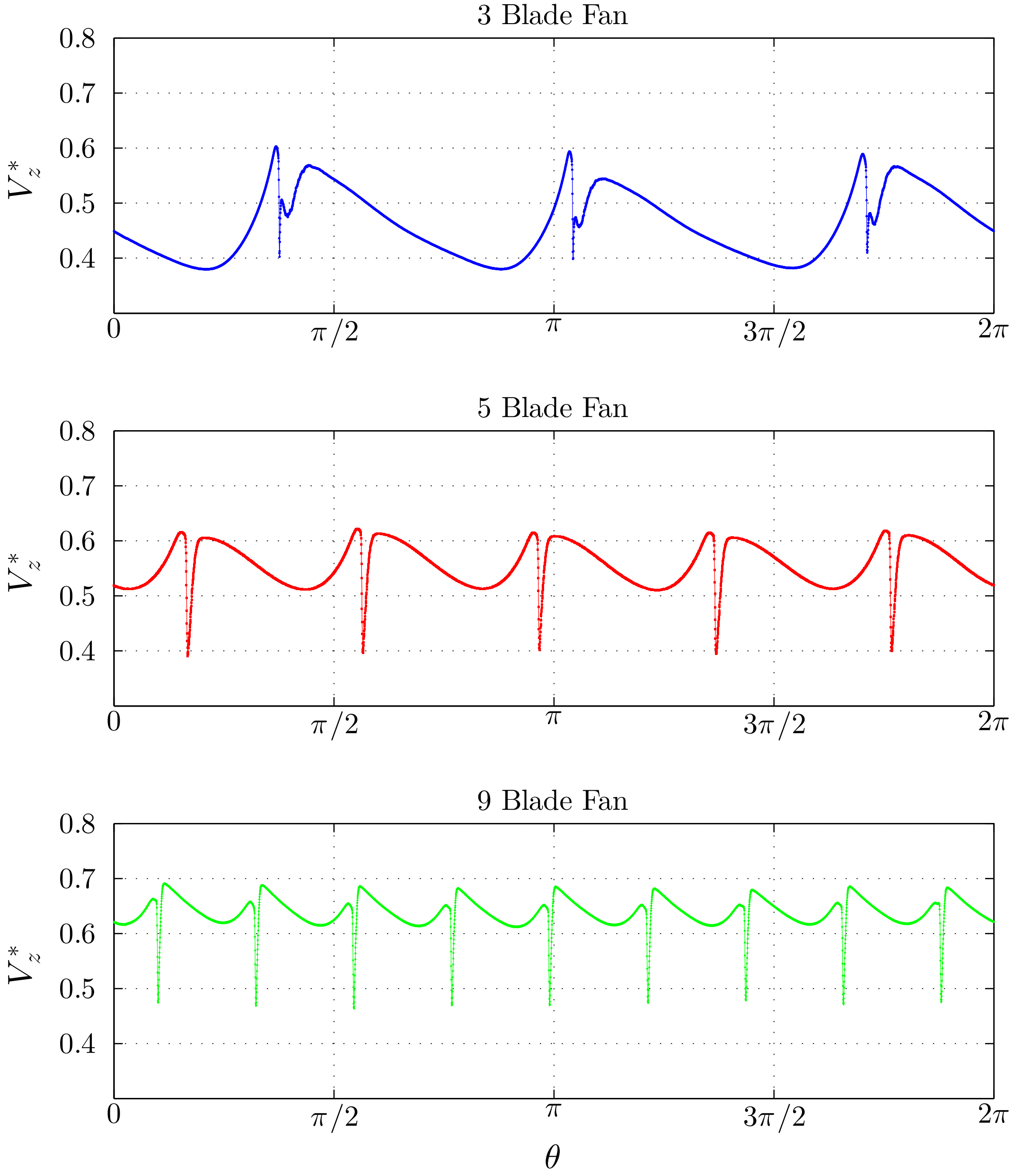

Figure 15 Case I Phase averaged axial velocity over $0 \leq \theta \leq 2\pi$

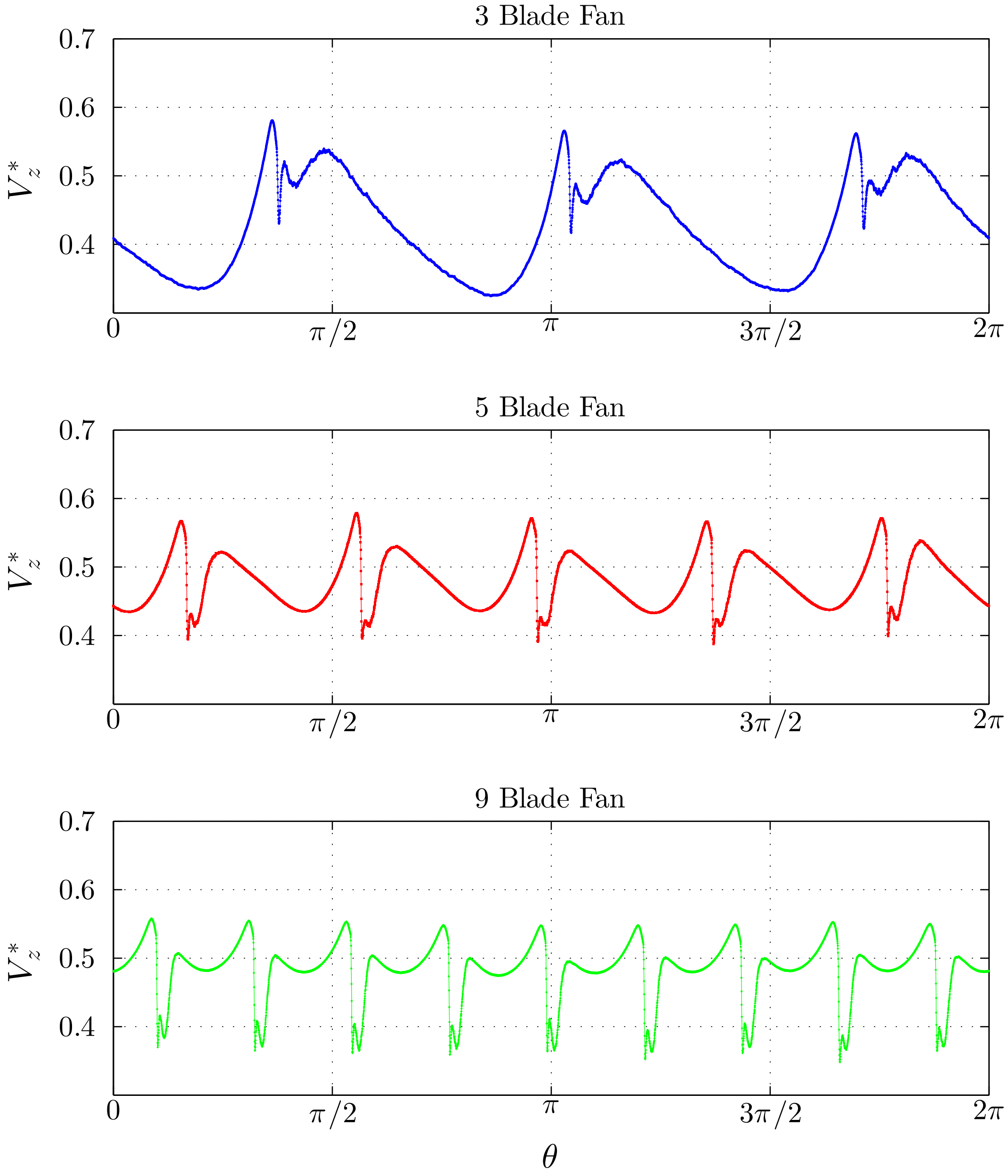

Figure 16 Case II Phase averaged axial velocity over $0 \leq \theta \leq 2\pi$

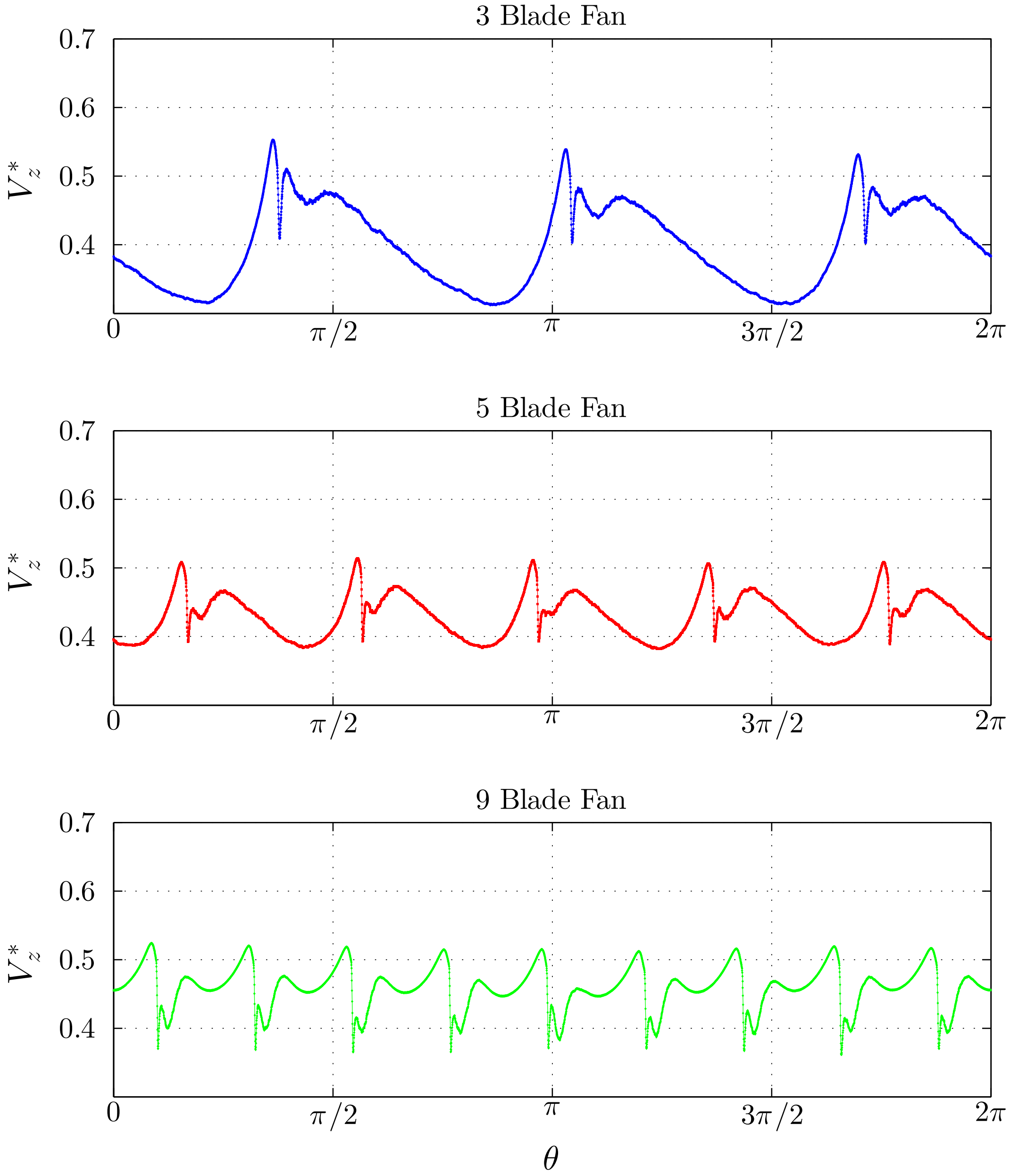

Figure 17 Case III Phase averaged axial velocity over $0 \leq \theta \leq 2\pi$

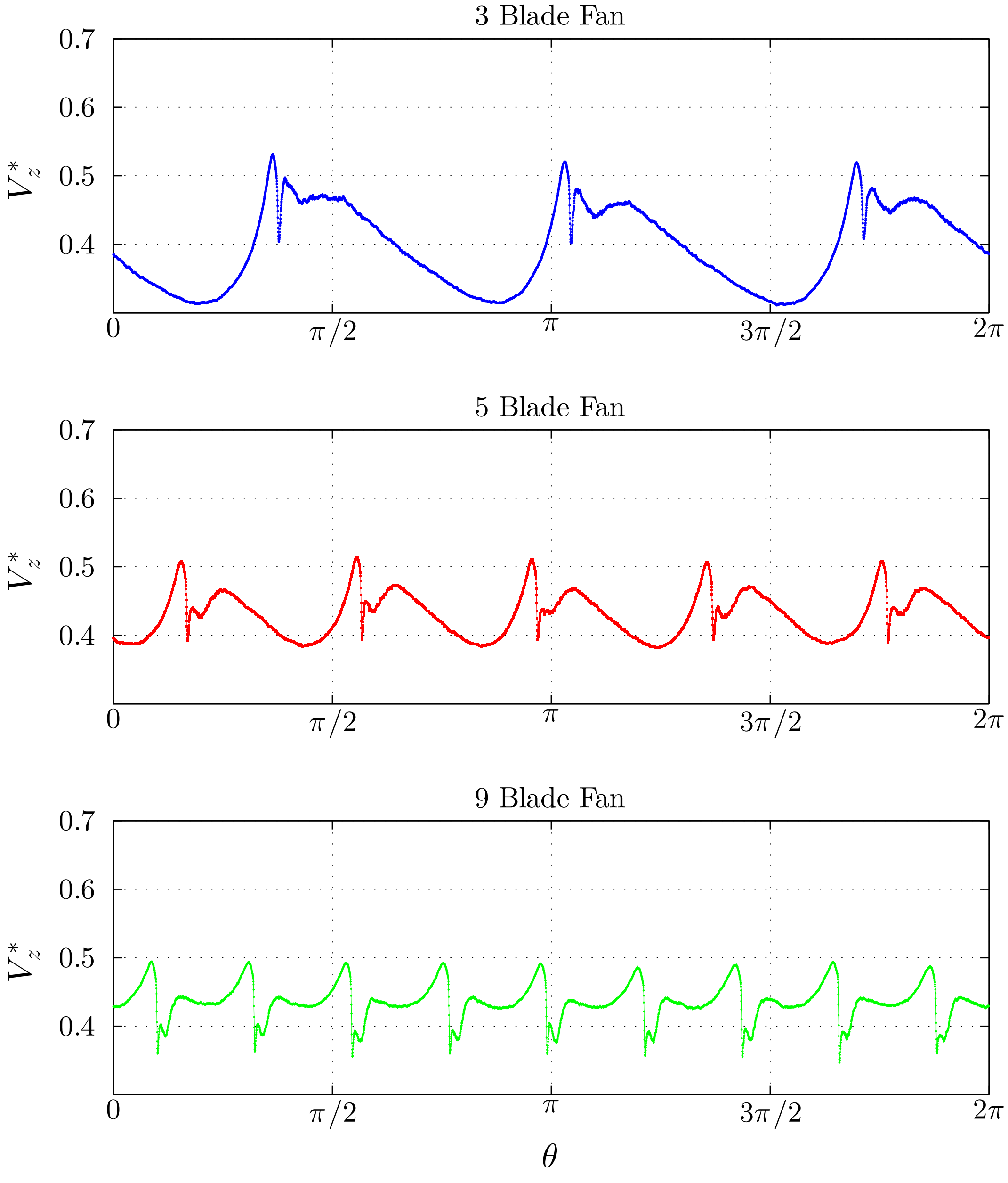

Figure 18 Case IV Phase averaged axial velocity over $0 \leq \theta \leq 2\pi$

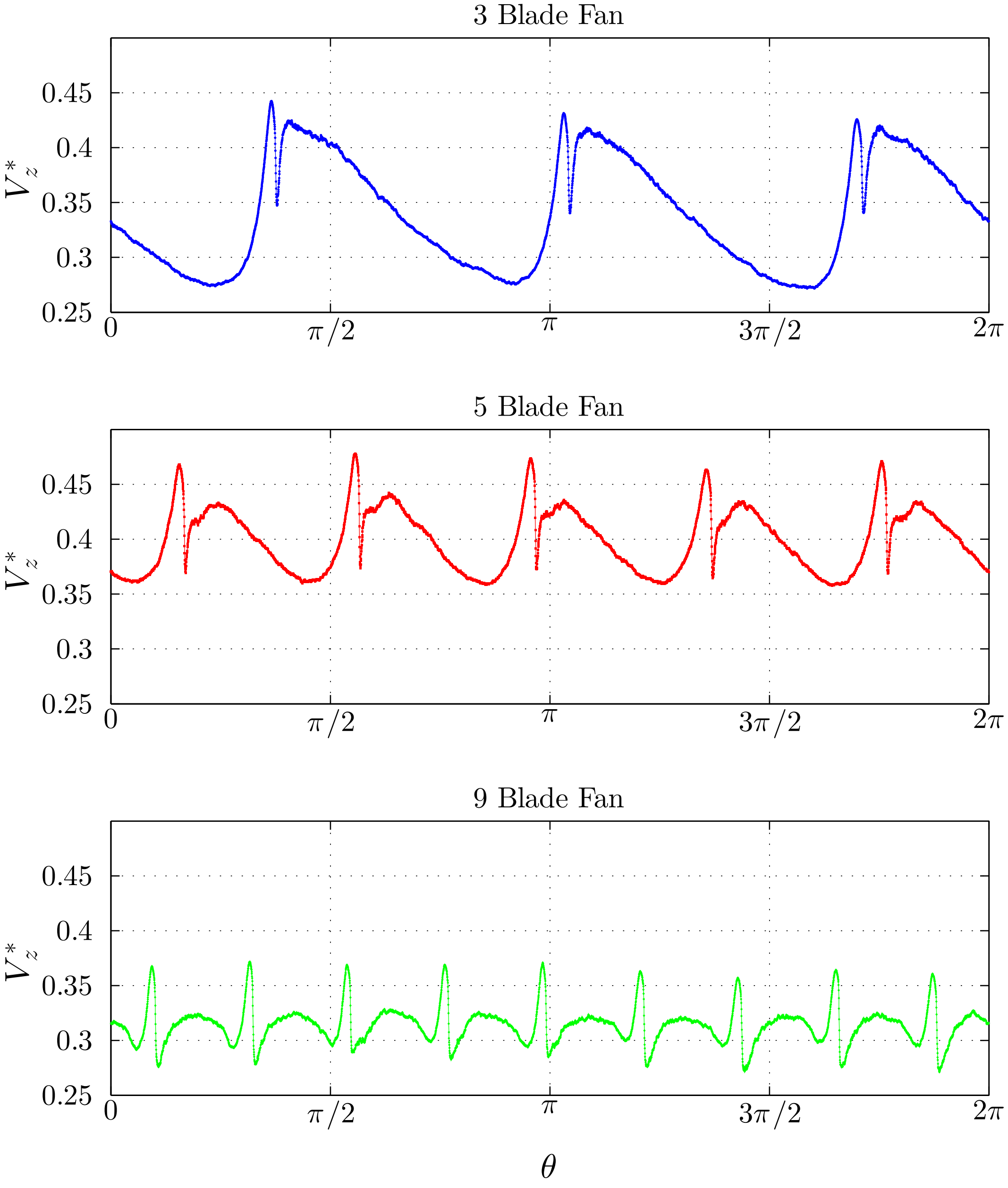

Figure 19 Case V Phase averaged axial velocity over $0 \leq \theta \leq 2\pi$

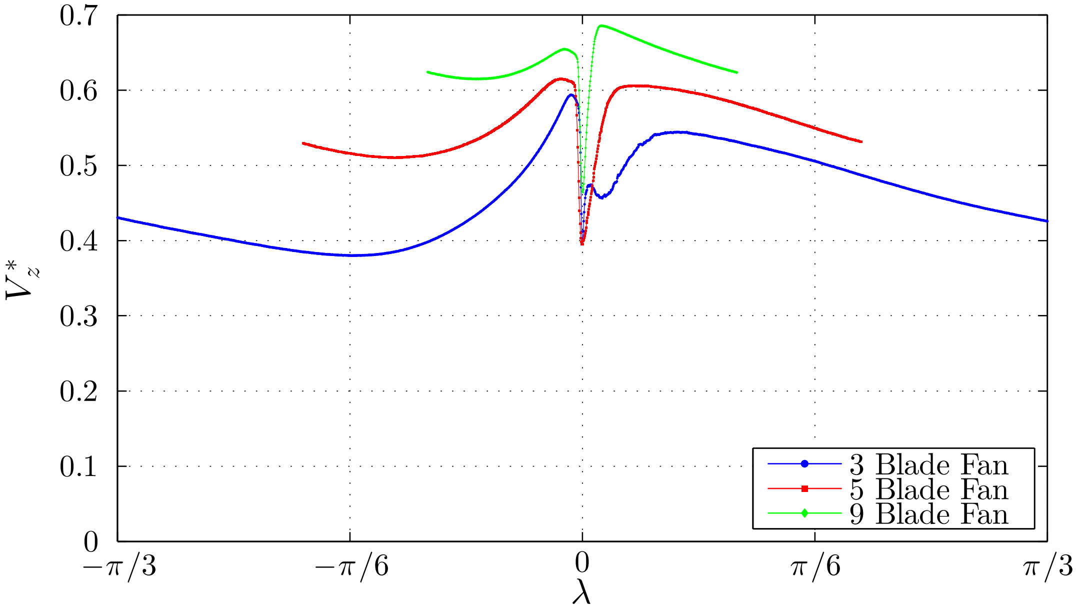

Figure 20 Case I Phase averaged axial velocity over λ_3

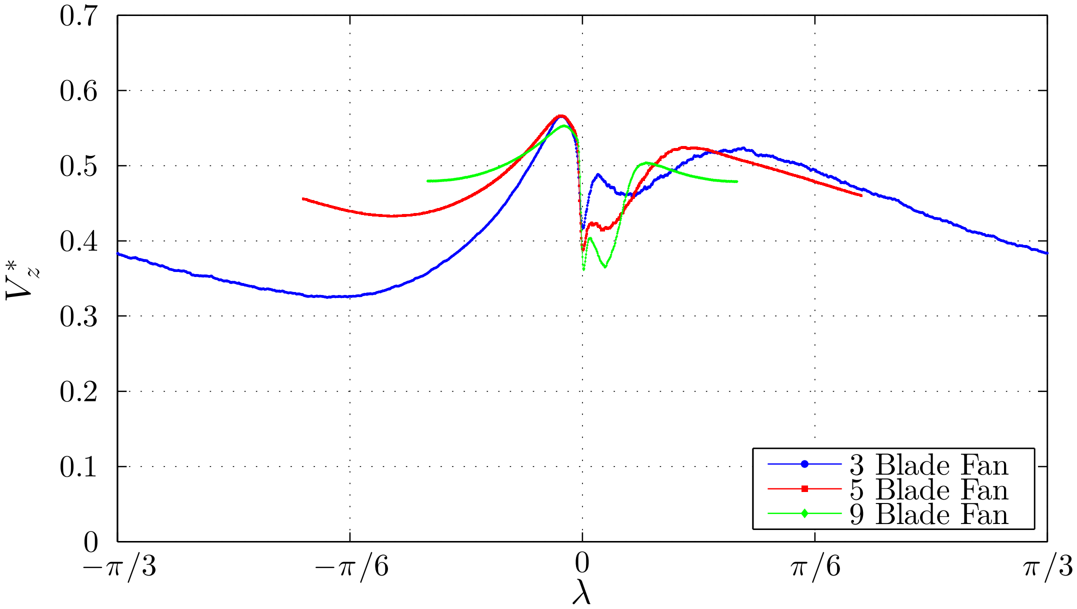

Figure 21 Case II Phase averaged axial velocity over λ_3

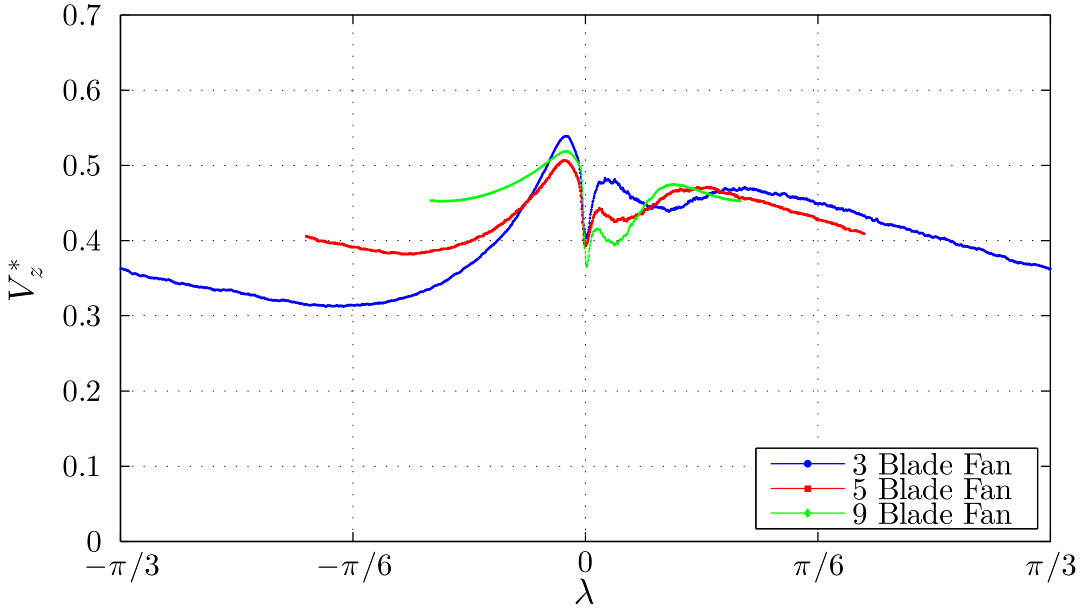

Figure 22 Case III Phase averaged axial velocity over λ_3

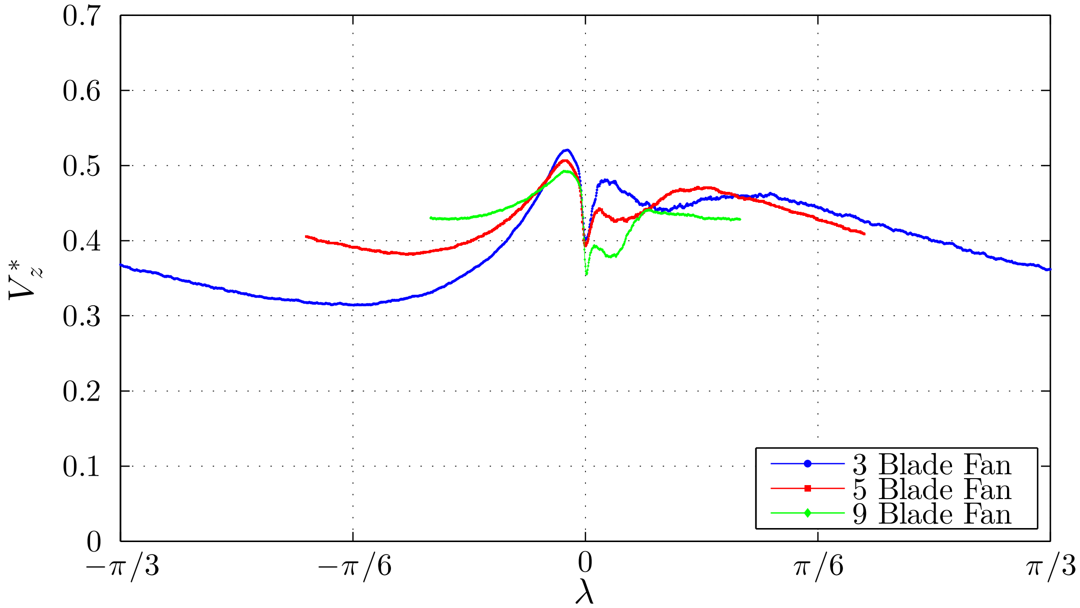

Figure 23 Case IV Phase averaged axial velocity over λ_3

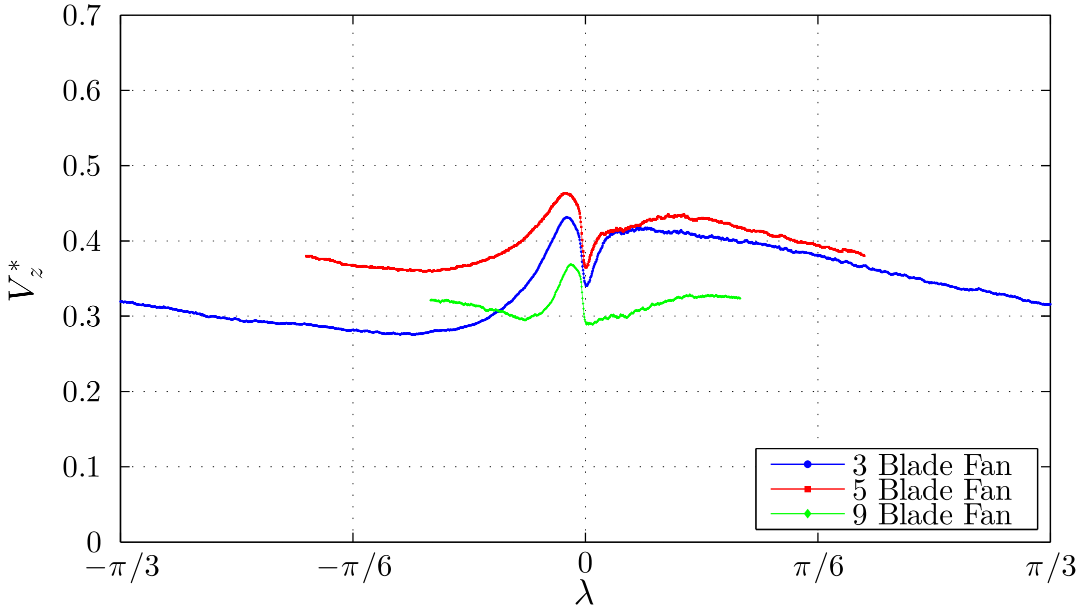

Figure 24 Case V Phase averaged axial velocity over λ_3

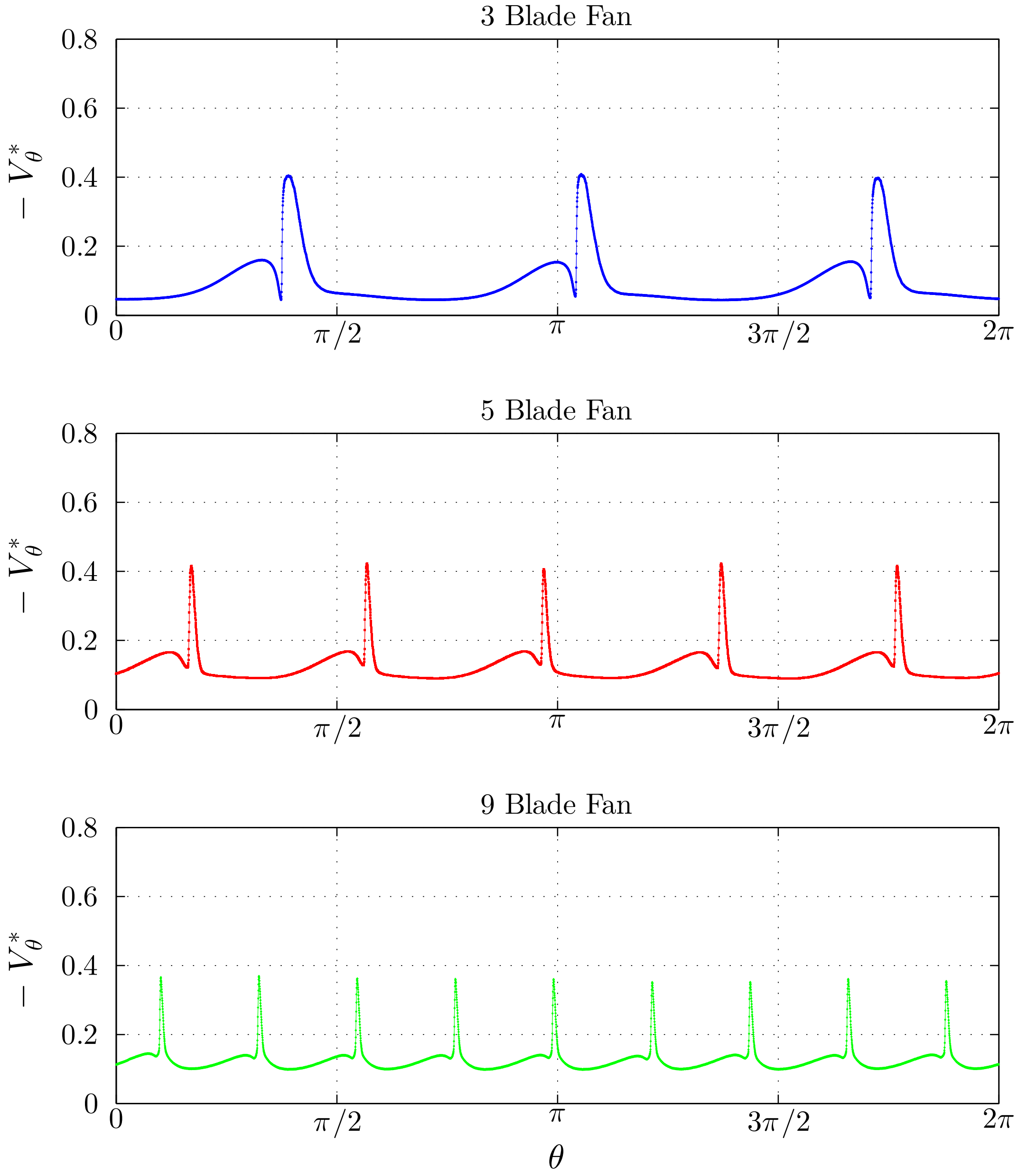

Figure 25 Case I Phase averaged azimuthal velocity over $0 \leq \theta \leq 2\pi$

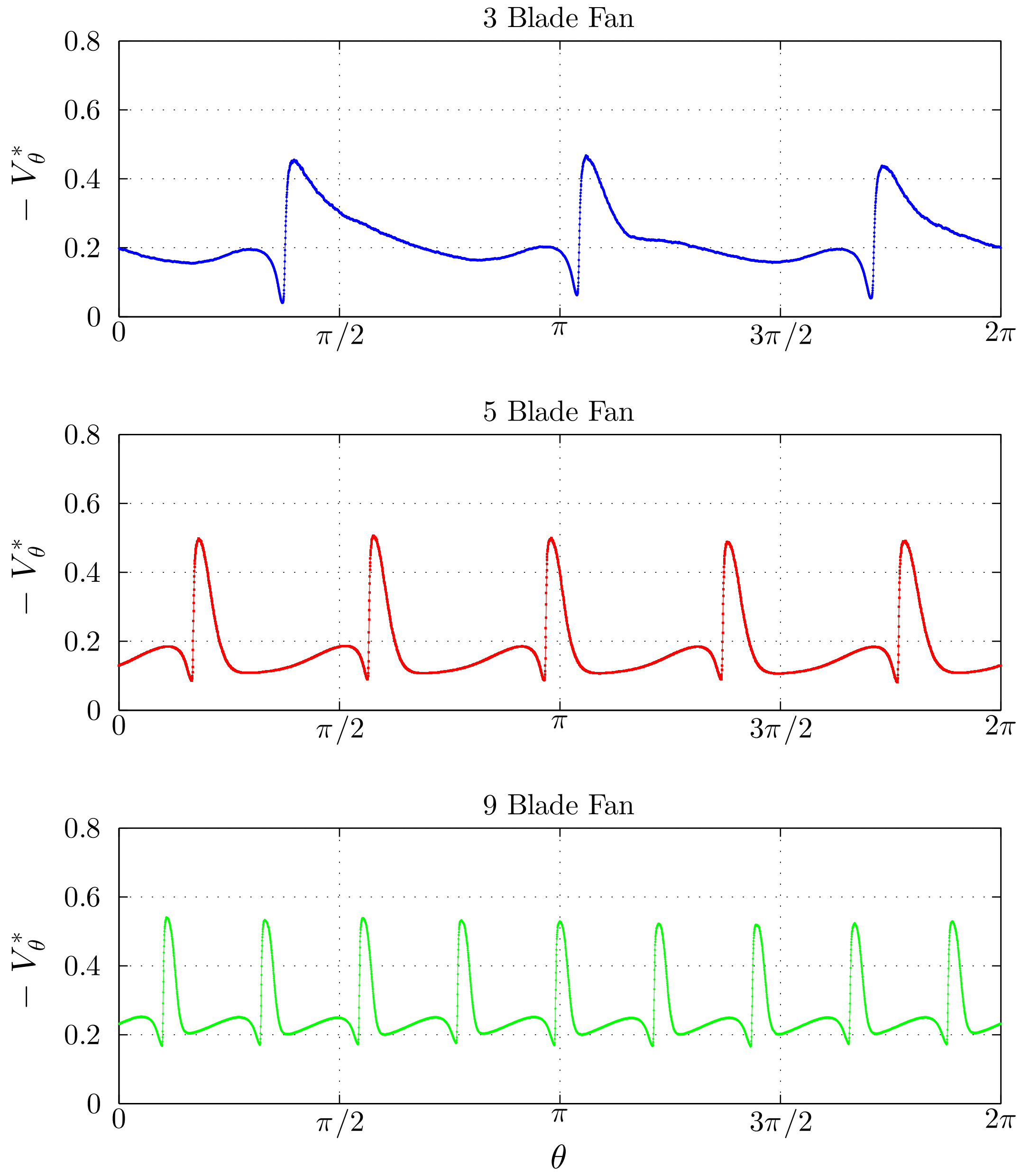
3 Blade Fan

5 Blade Fan

9 Blade Fan

Figure 26 Case II Phase averaged azimuthal velocity over $0 \leq \theta \leq 2\pi$

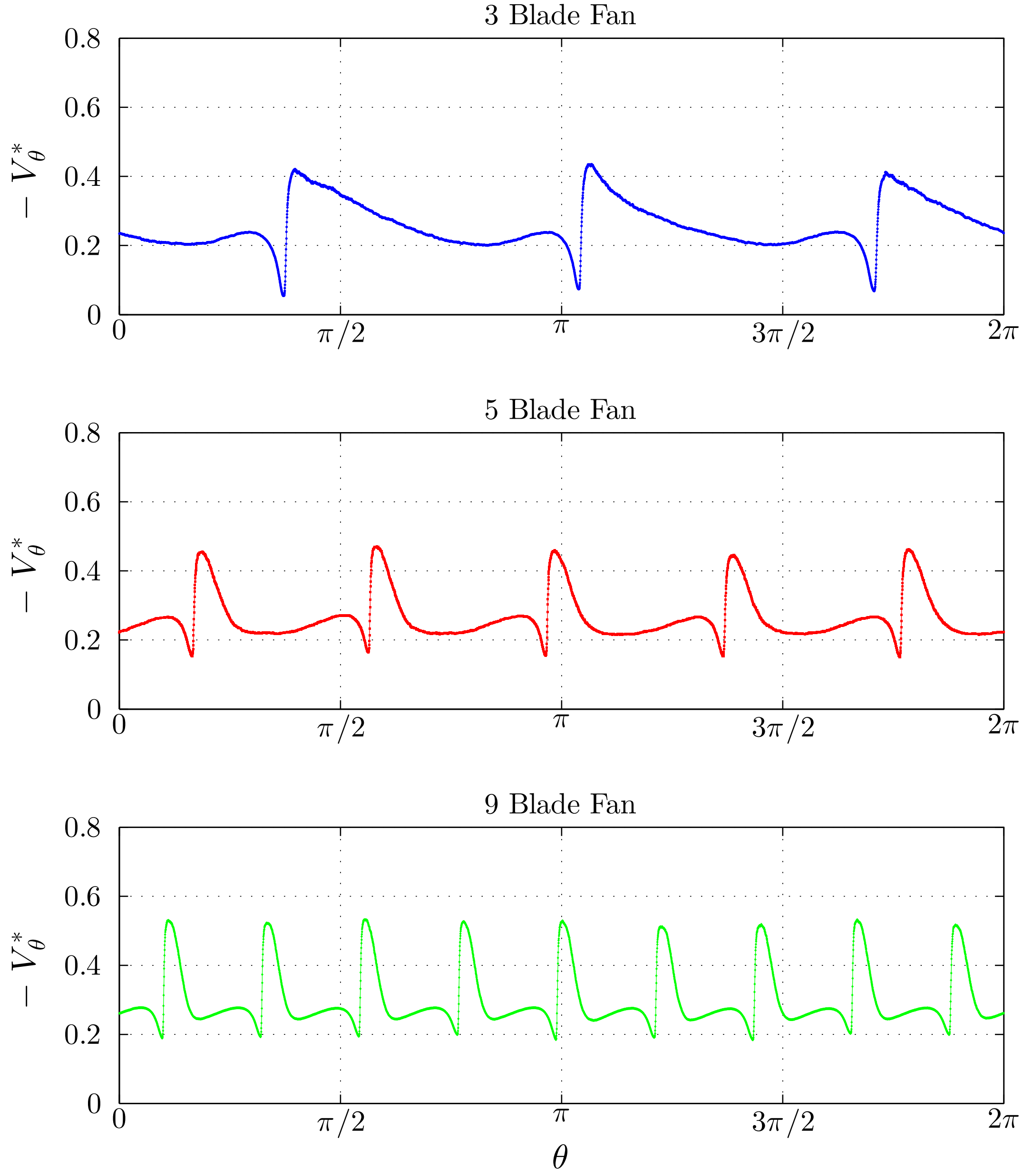
3 Blade Fan

5 Blade Fan

9 Blade Fan

Figure 27 Case III Phase averaged azimuthal velocity over $0 \leq \theta \leq 2\pi$

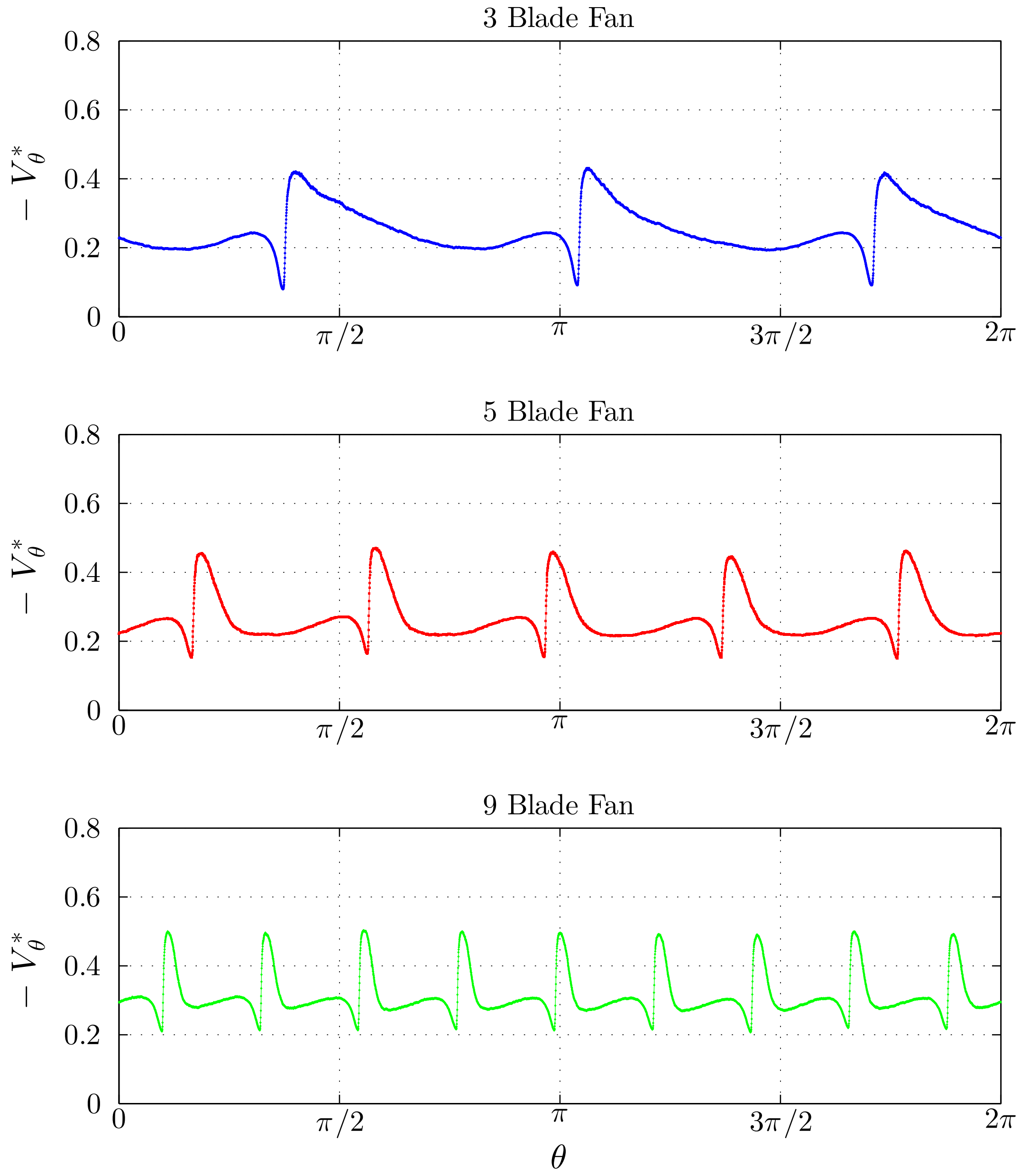

Figure 28 Case IV Phase averaged azimuthal velocity over $0 \leq \theta \leq 2\pi$

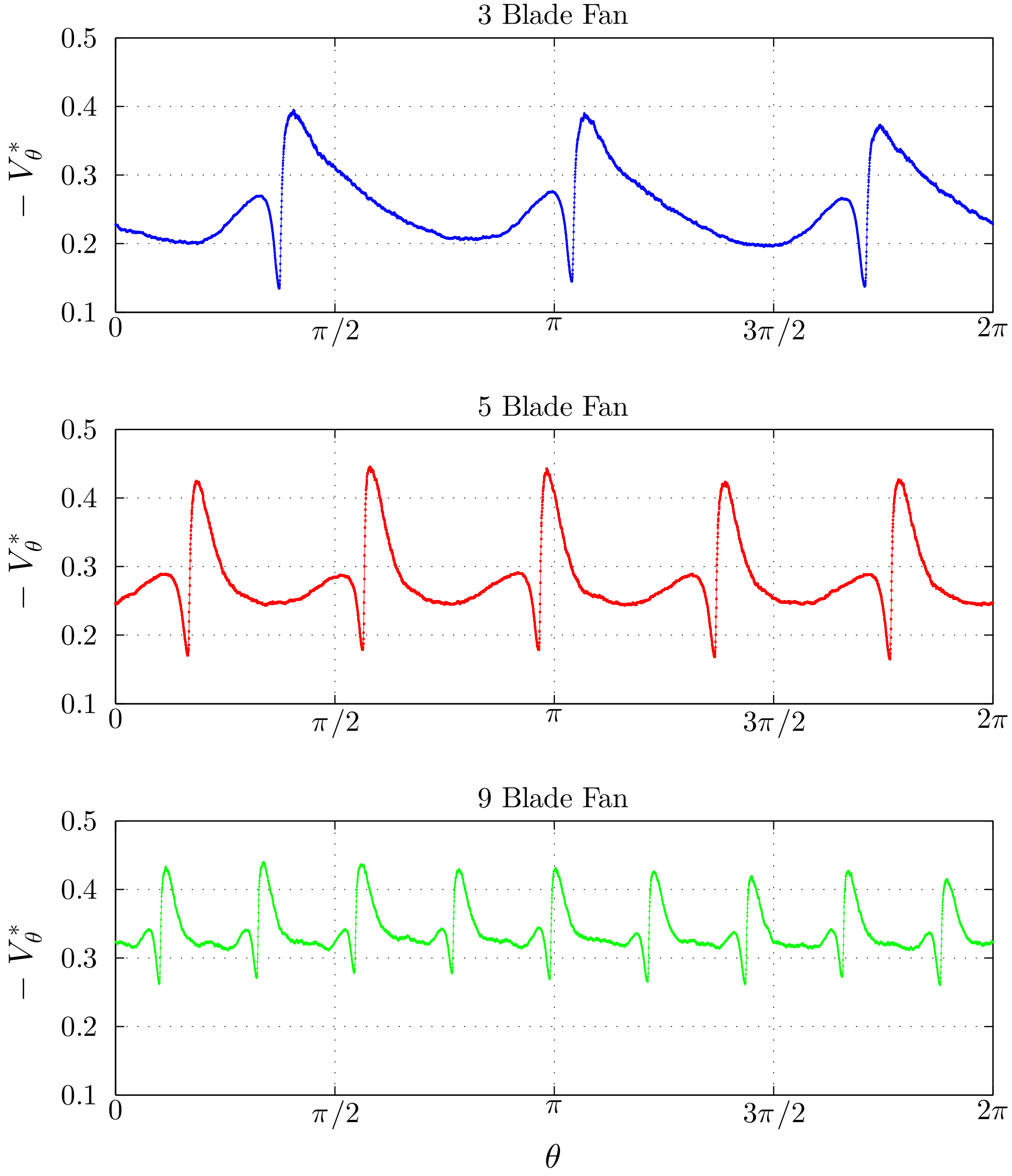

Figure 29 Case V Phase averaged azimuthal velocity over $0 \leq \theta \leq 2\pi$

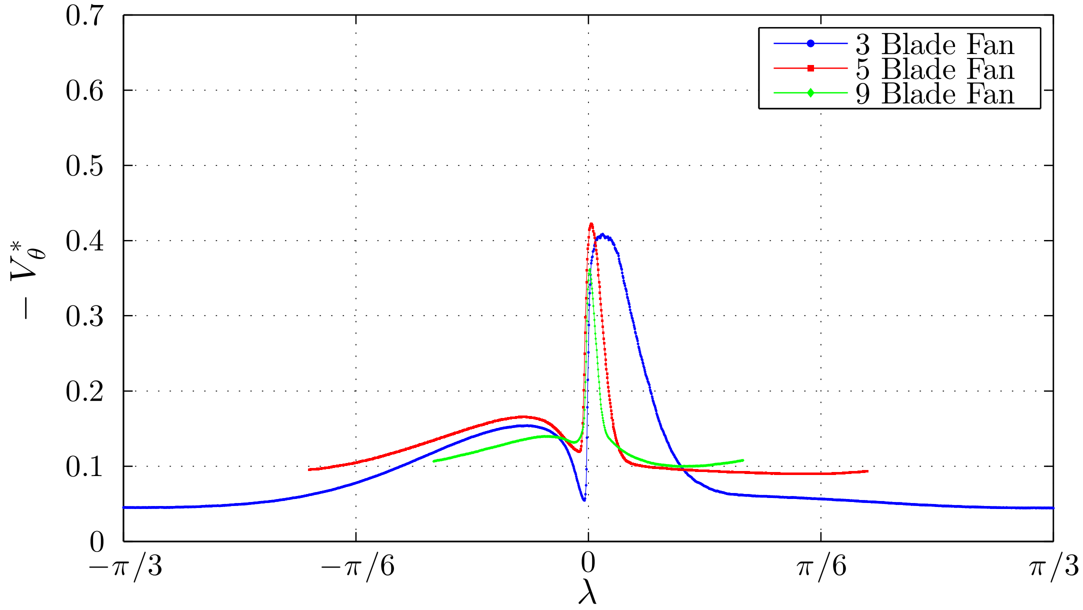

Figure 30 Case I Phase averaged azimuthal velocity over λ_3

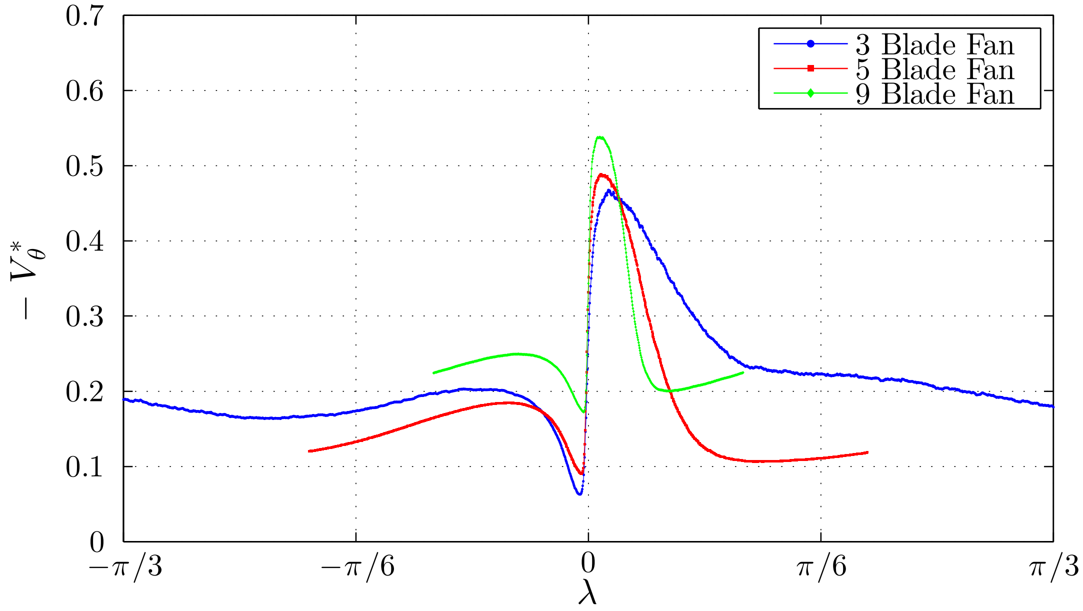

Figure 31 Case II Phase averaged azimuthal velocity over λ_3

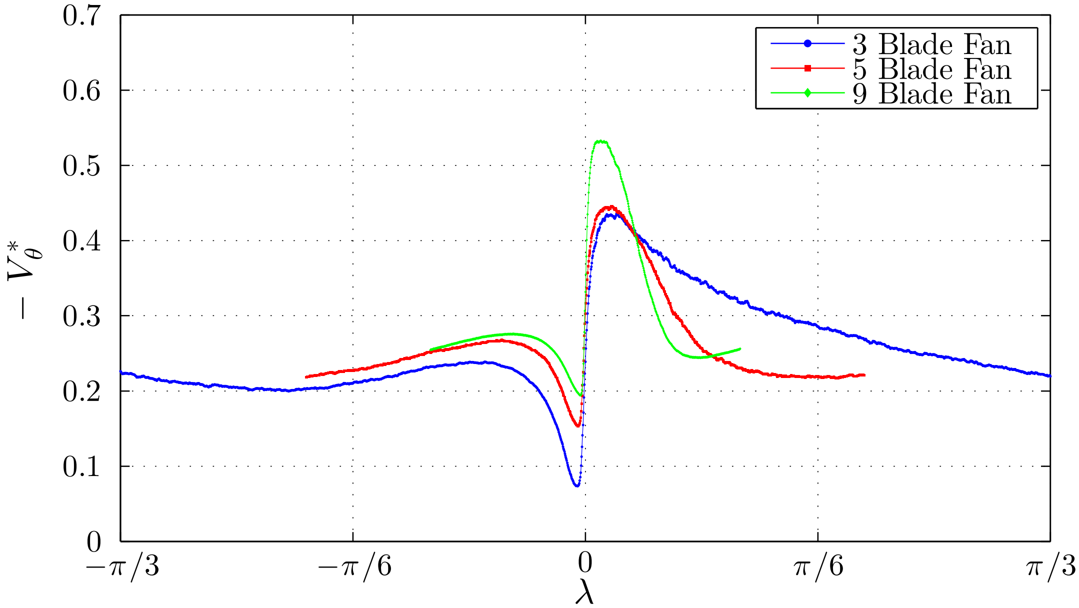

Figure 32 Case III Phase averaged azimuthal velocity over λ_3

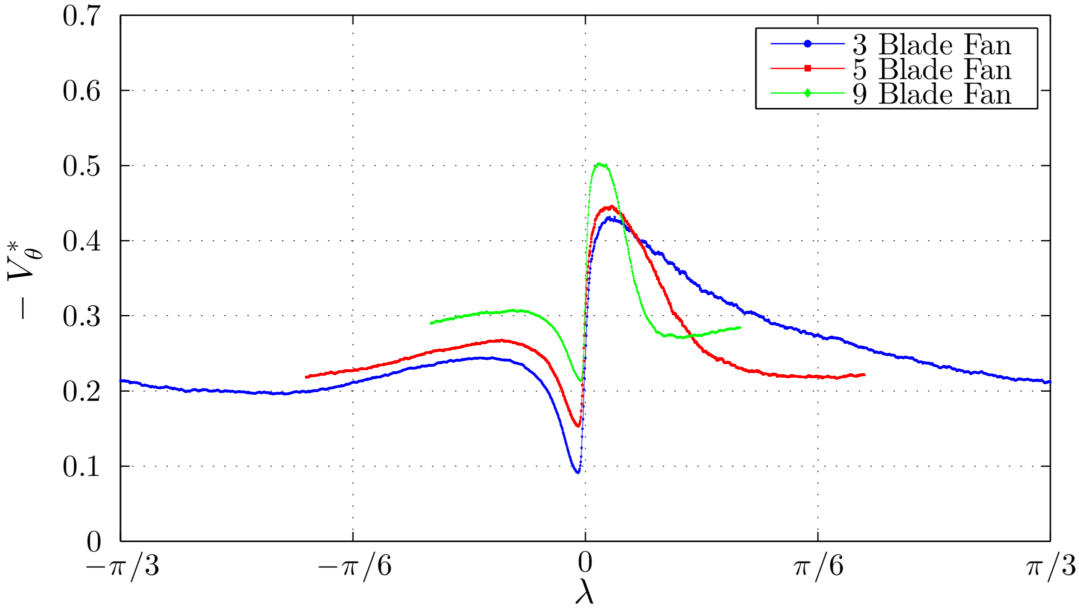

Figure 33 Case IV Phase averaged azimuthal velocity over λ_3

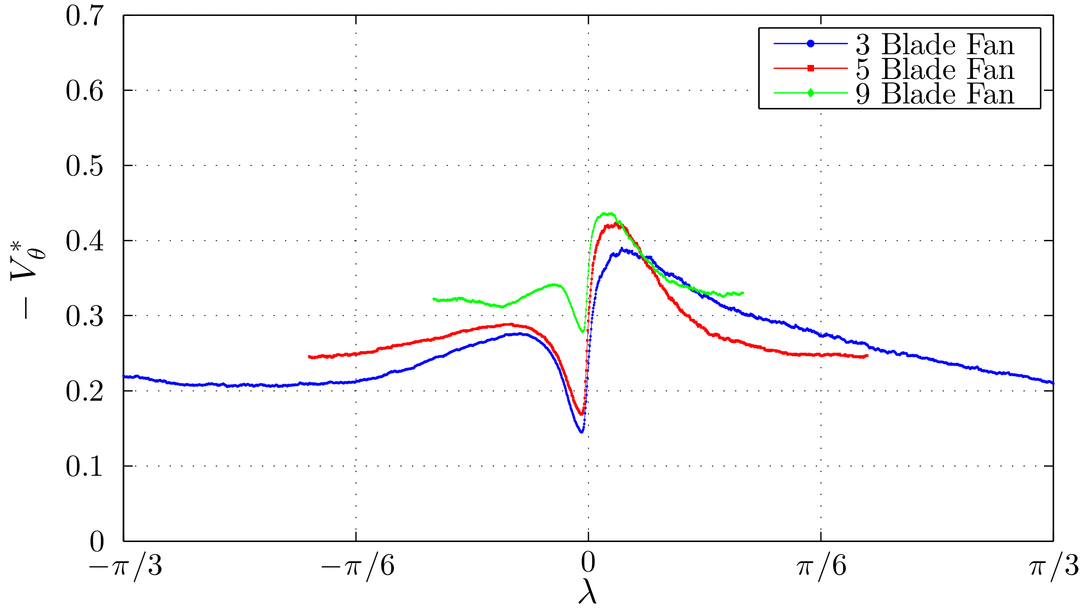

Figure 34 Case V Phase averaged azimuthal velocity over λ_3

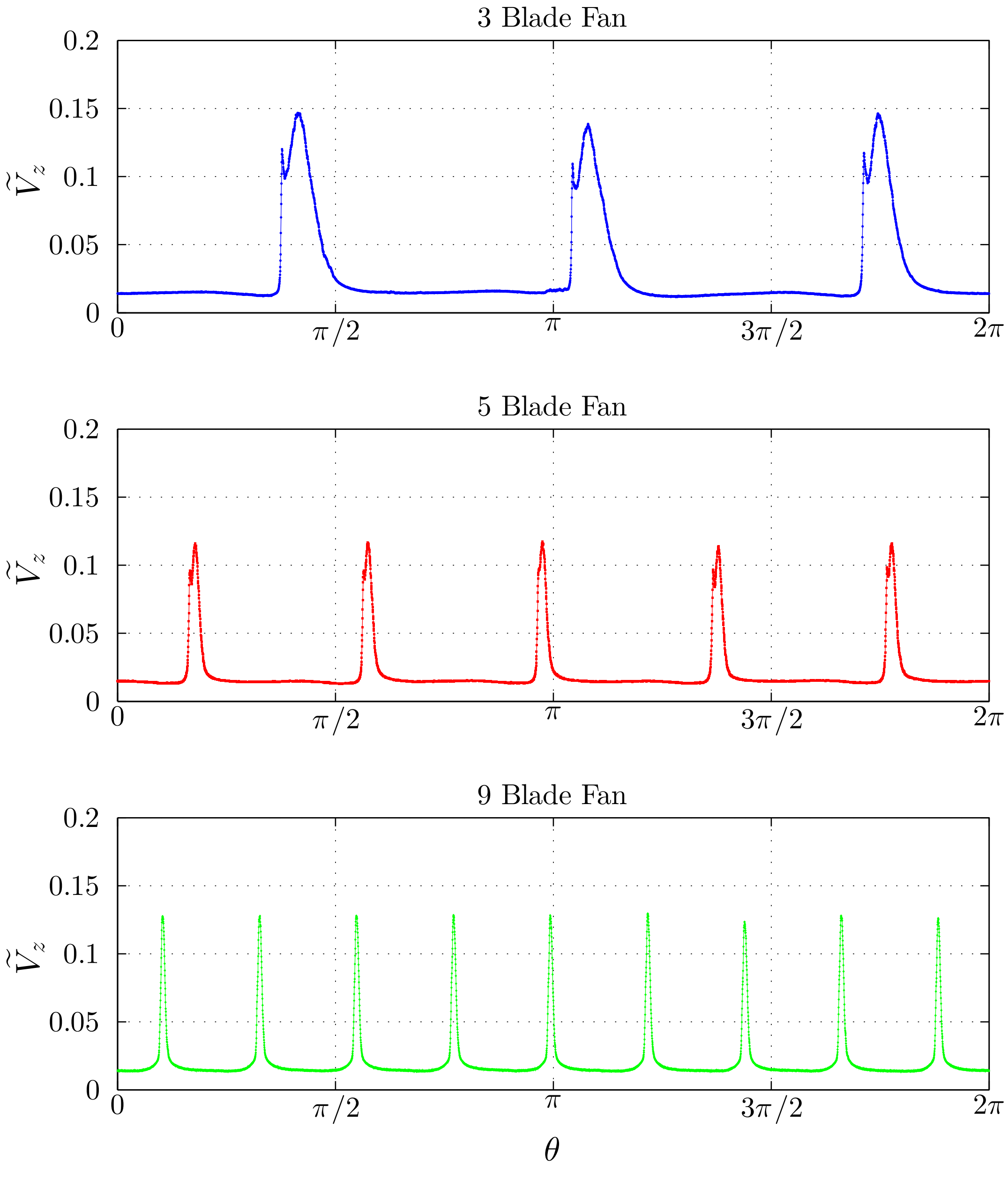

Figure 35 Case I Axial turbulence intensity over $0 \leq \theta \leq 2\pi$

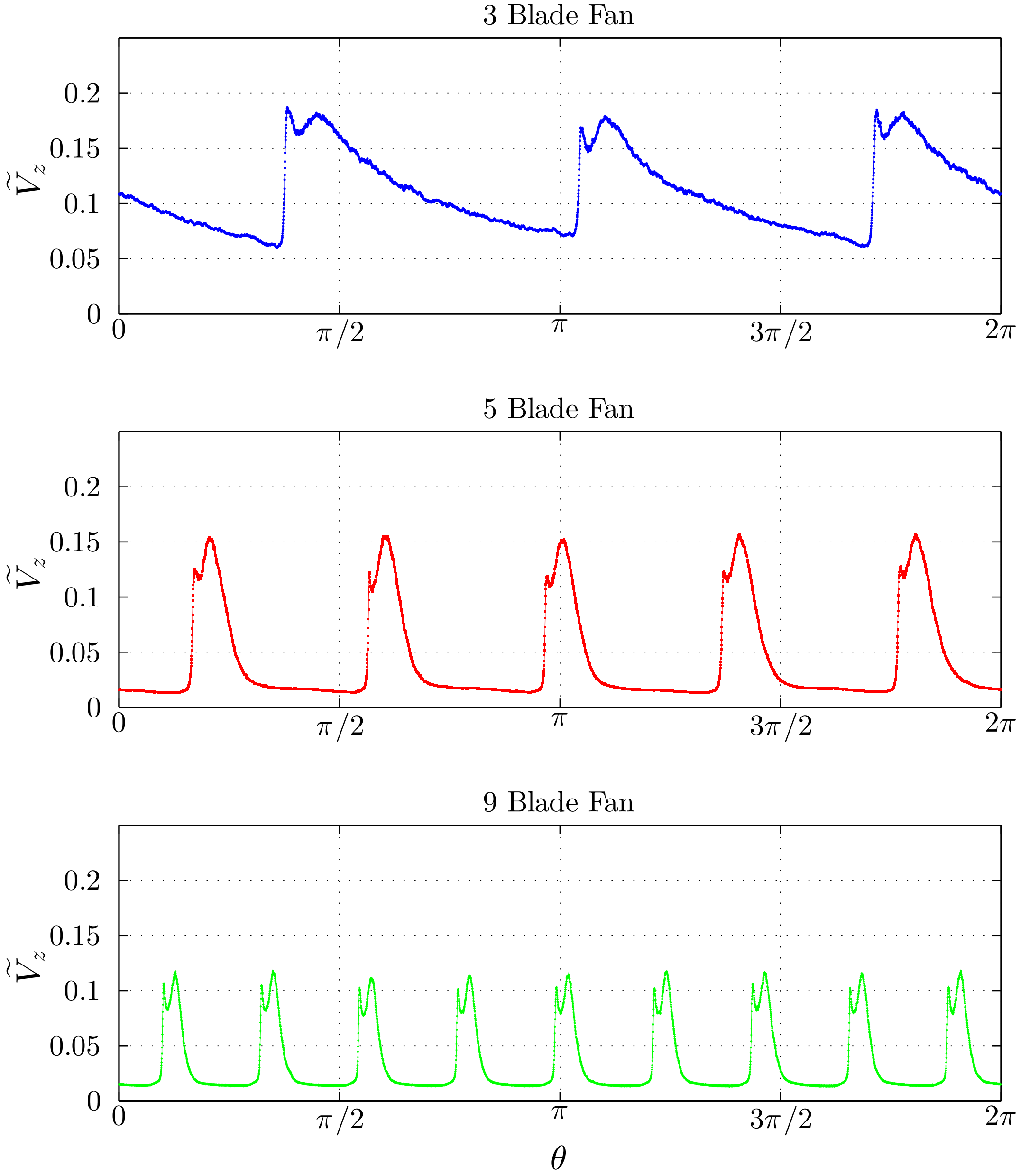

Figure 36 Case II Axial turbulence intensity over $0 \leq \theta \leq 2\pi$

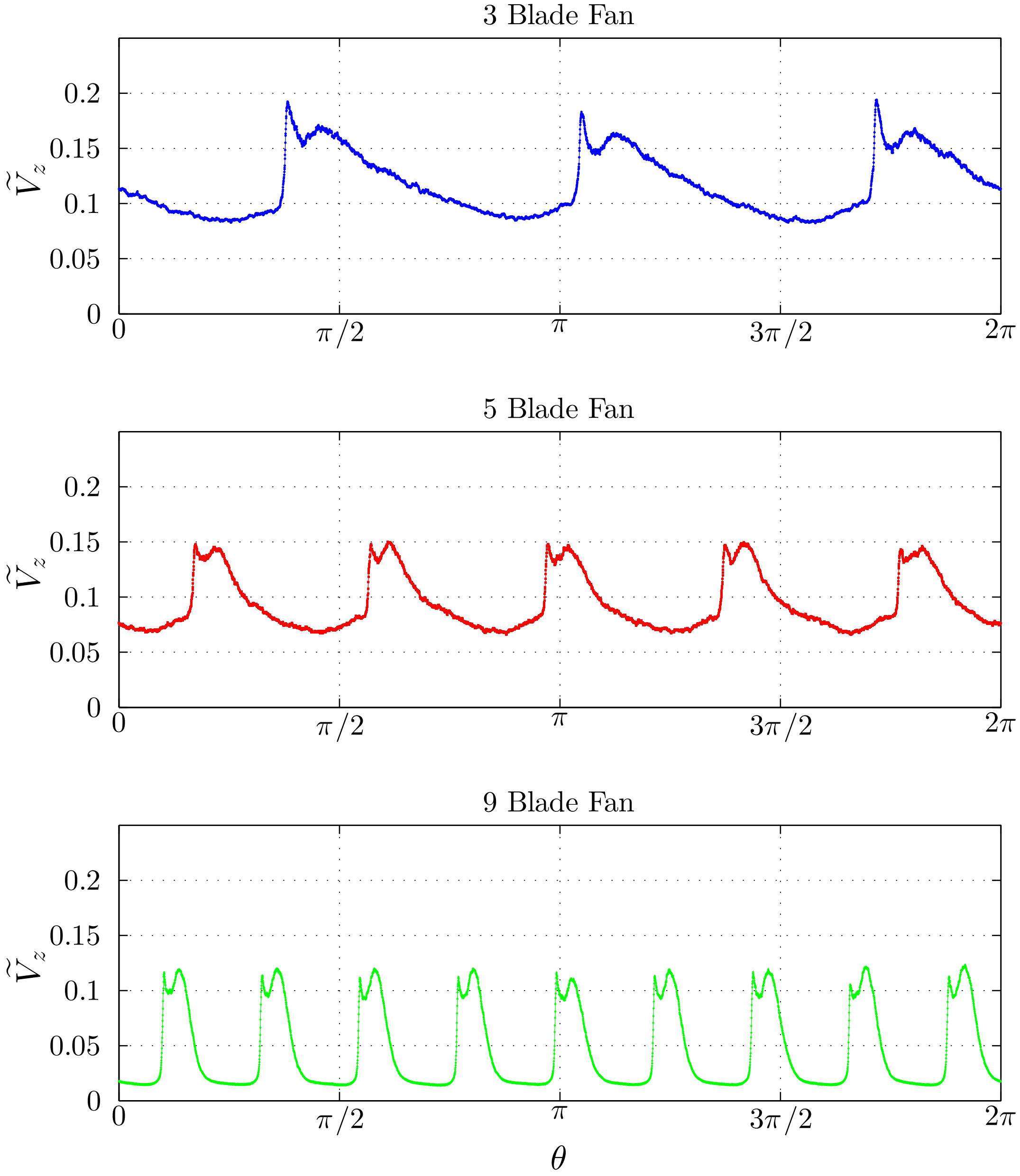

Figure 37 Case III Axial turbulence intensity over $0 \leq \theta \leq 2\pi$

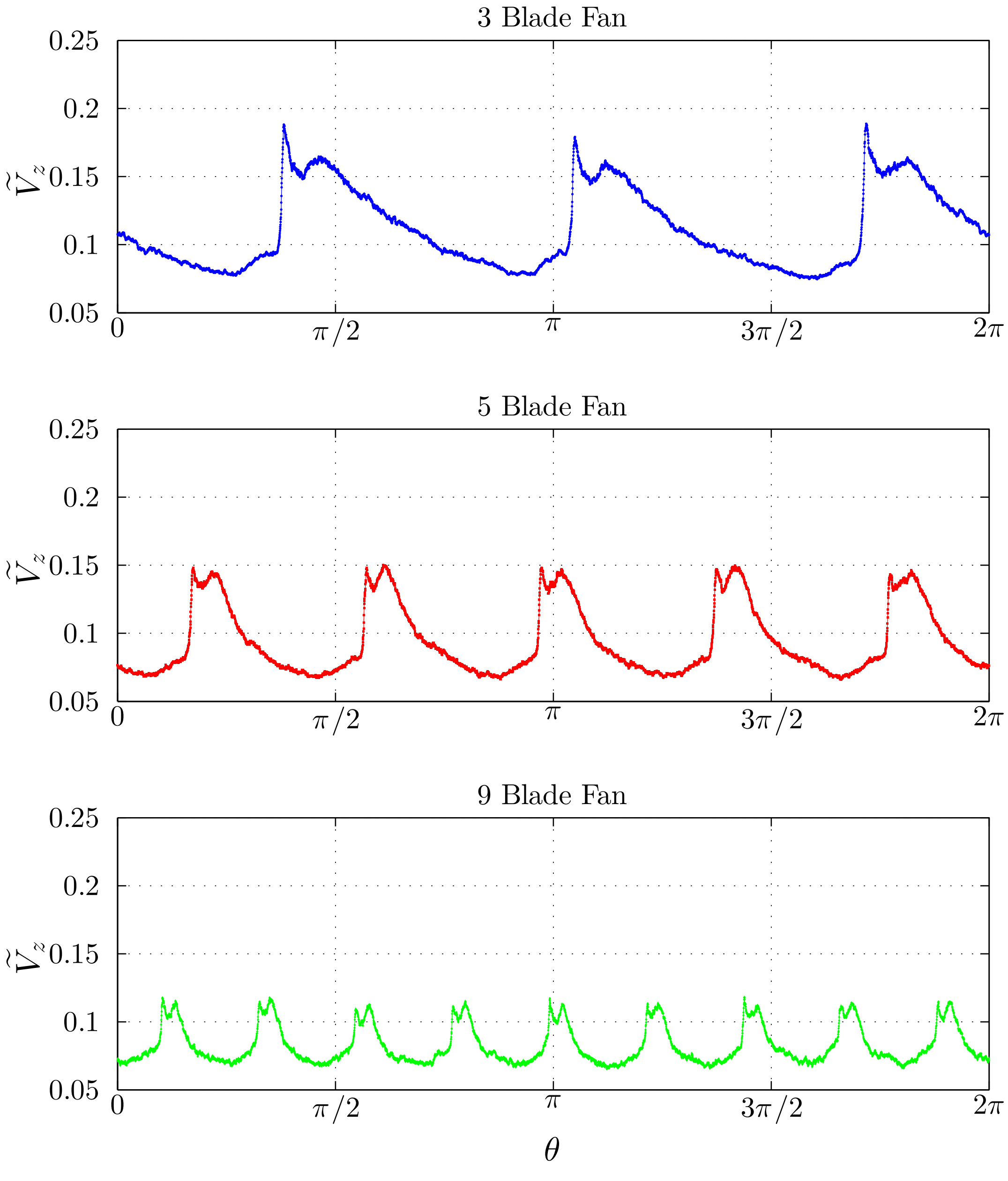

Figure 38 Case IV Axial turbulence intensity over $0 \leq \theta \leq 2\pi$

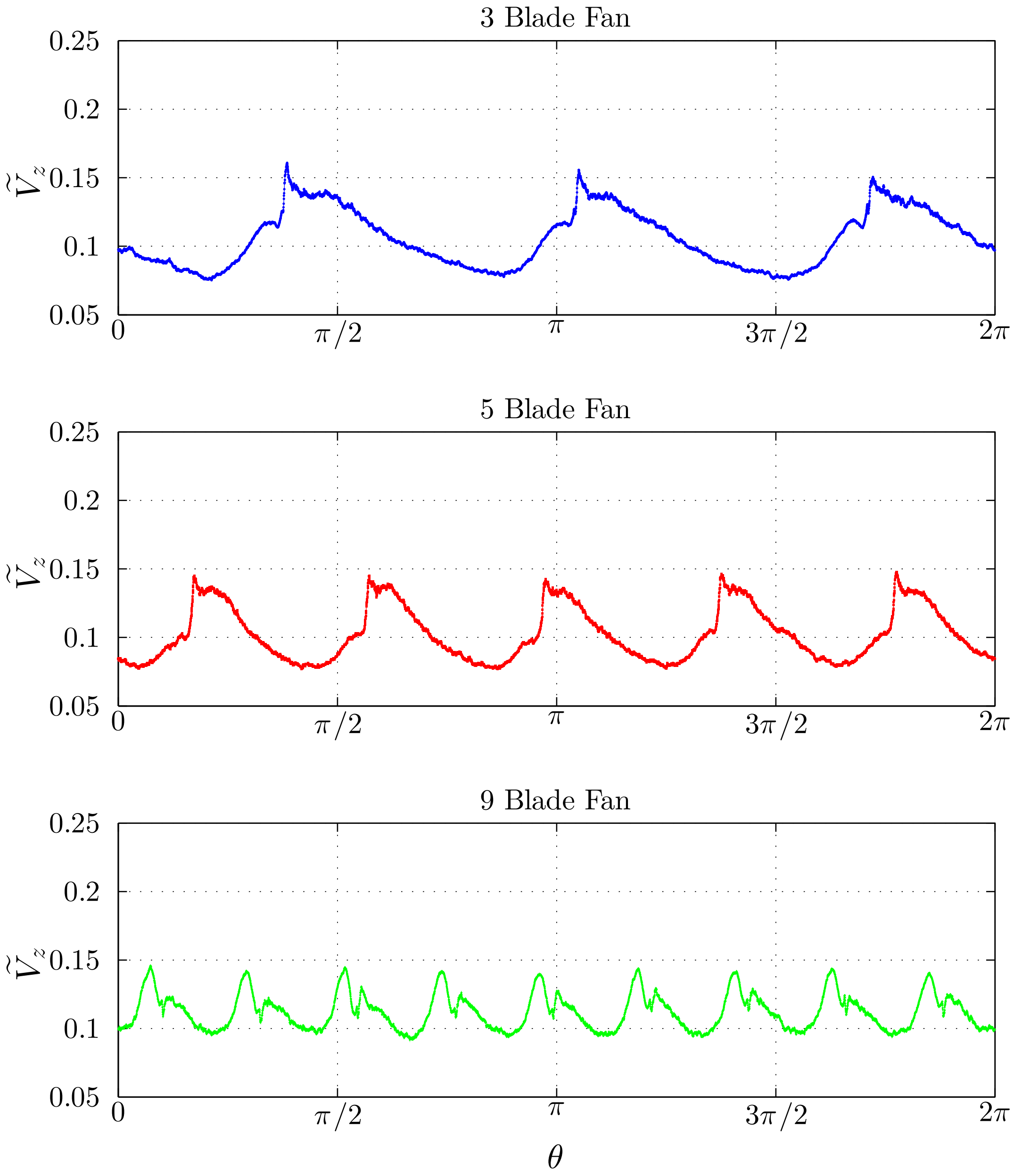

Figure 39 Case V Axial turbulence intensity over $0 \leq \theta \leq 2\pi$

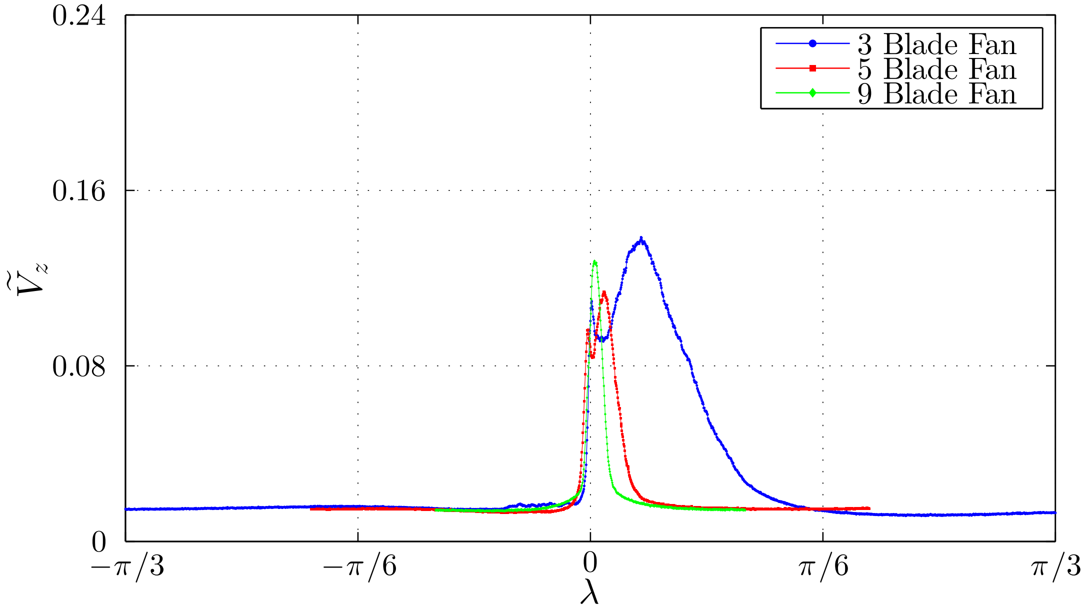

Figure 40 Case I Axial turbulence intensity over λ_3

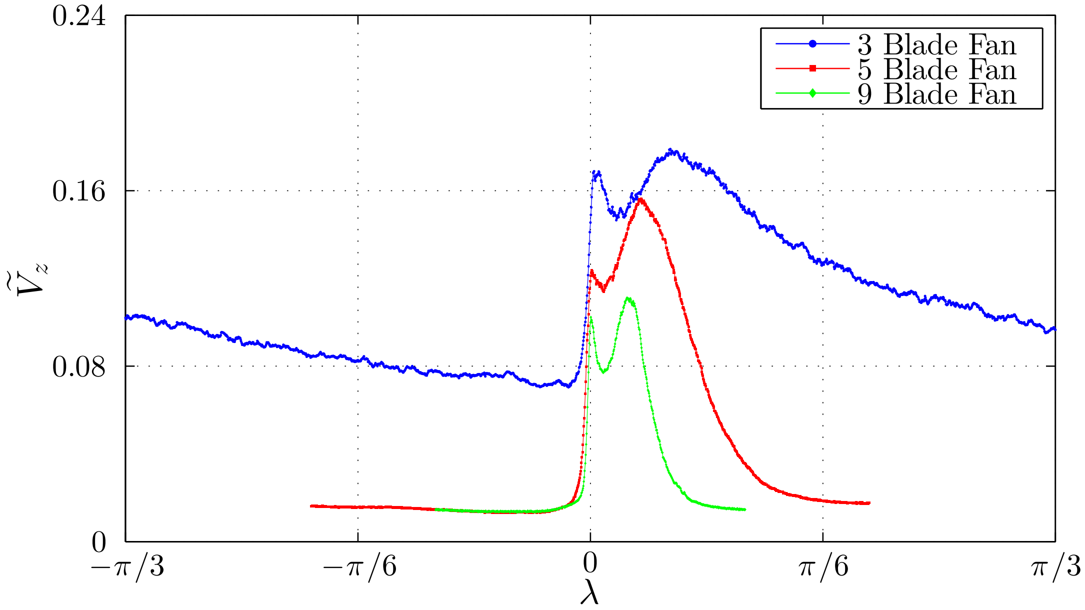

Figure 41 Case II Axial turbulence intensity over λ_3

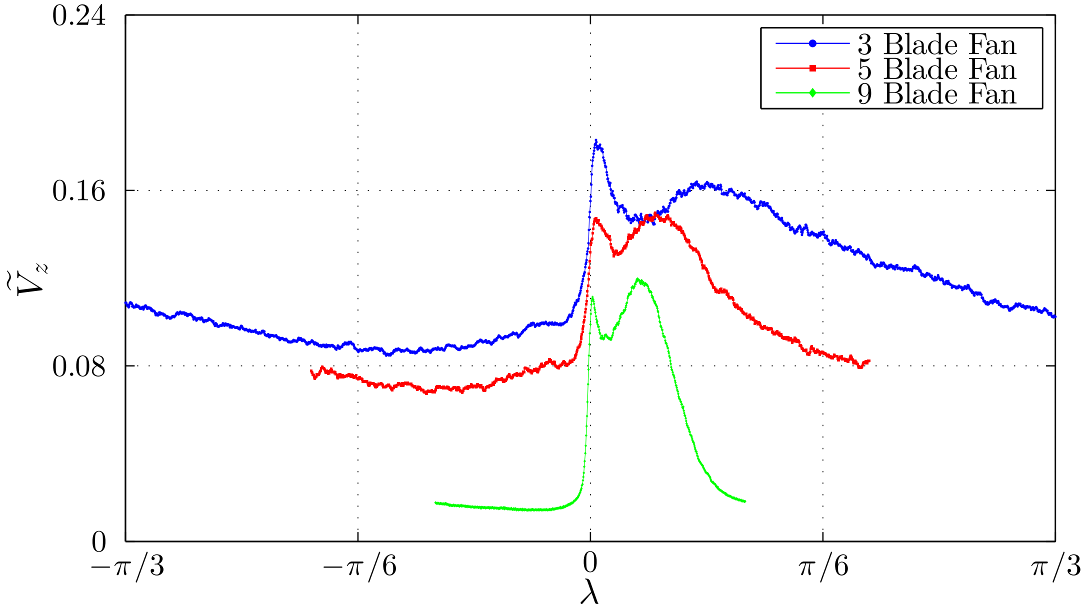

Figure 42 Case III Axial turbulence intensity over λ_3

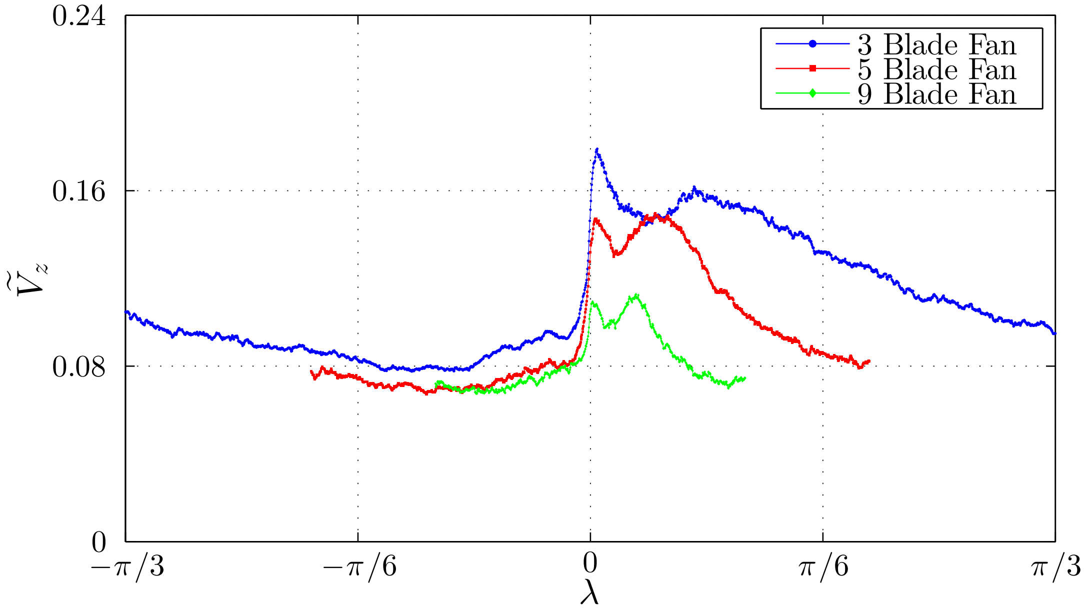

Figure 43 Case IV Axial turbulence intensity over λ_3

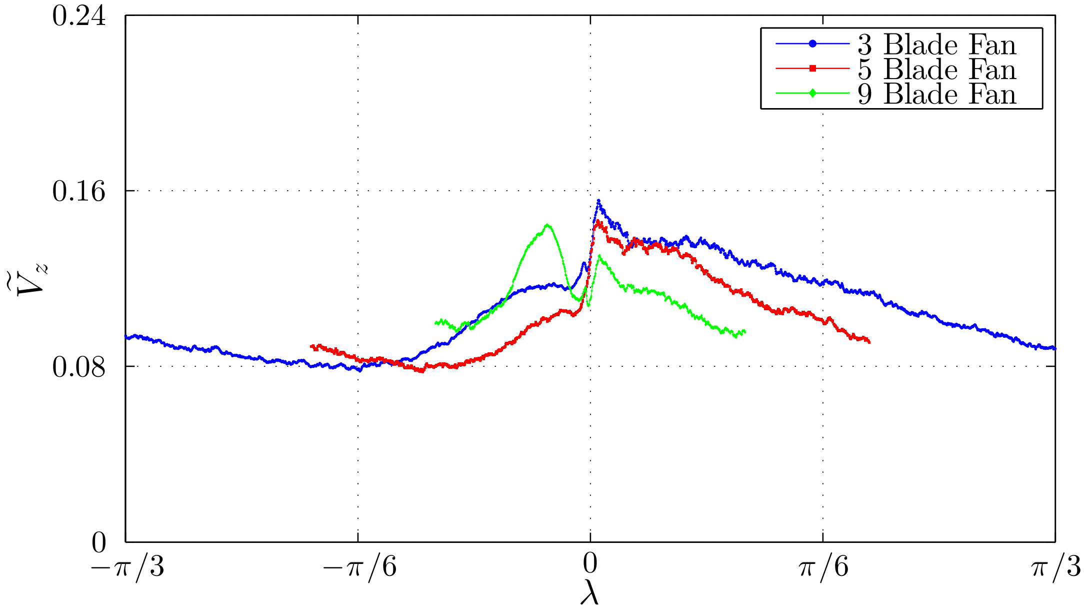

Figure 44 Case V Axial turbulence intensity over λ_3

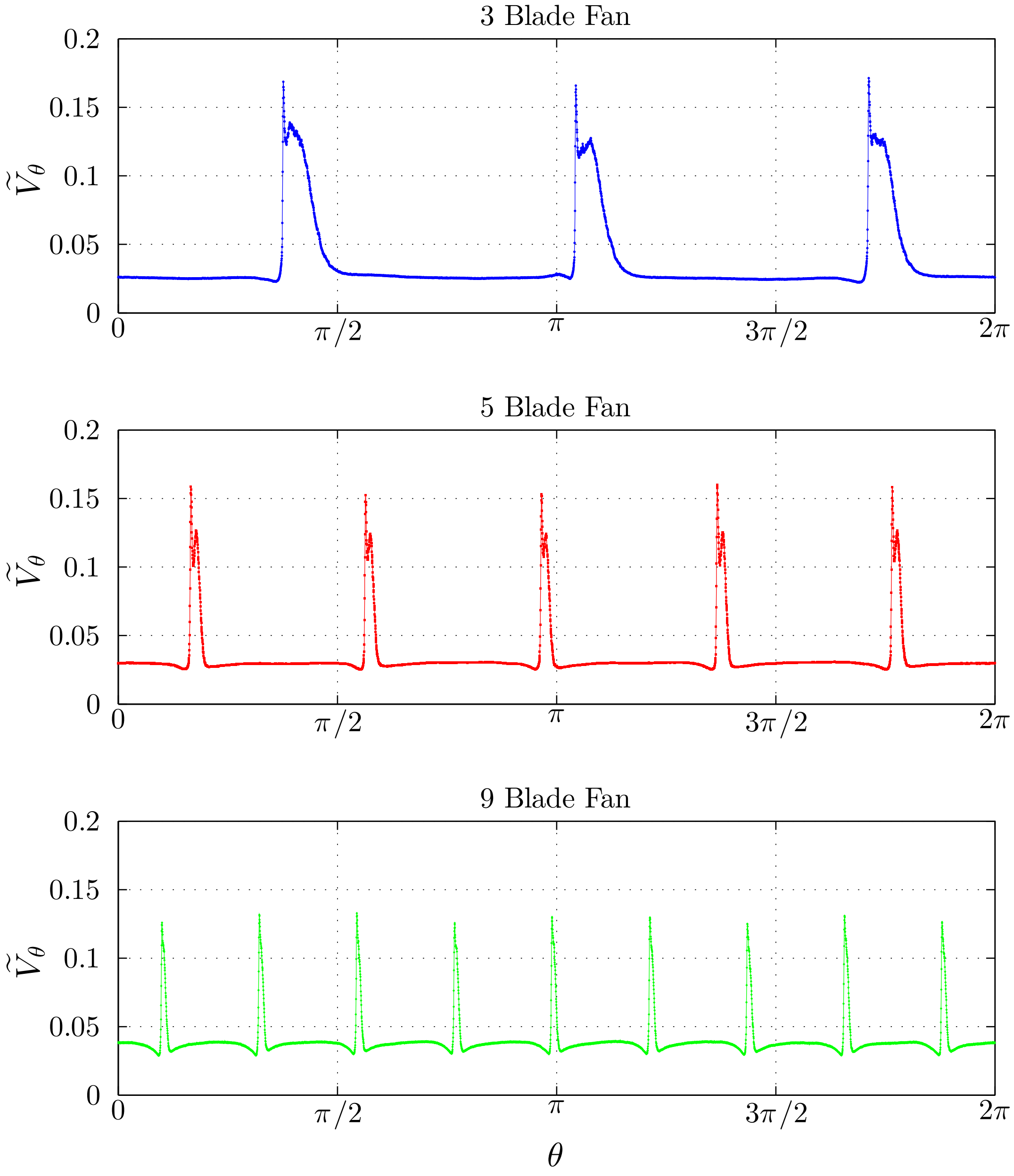

Figure 45 Case I Azimuthal turbulence intensity over $0 \leq \theta \leq 2\pi$

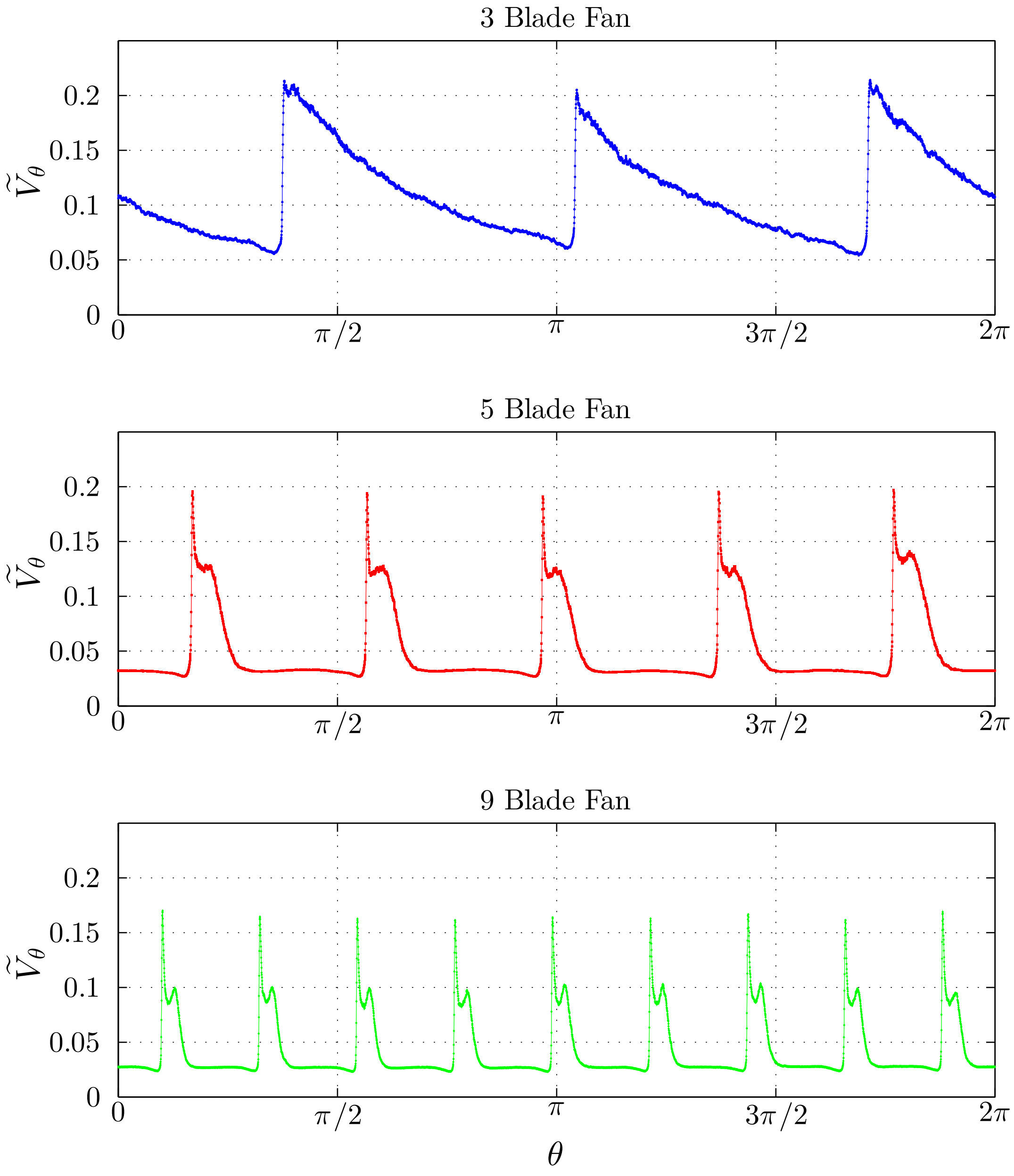
3 Blade Fan

5 Blade Fan

9 Blade Fan

Figure 46 Case II Azimuthal turbulence intensity over $0 \leq \theta \leq 2\pi$

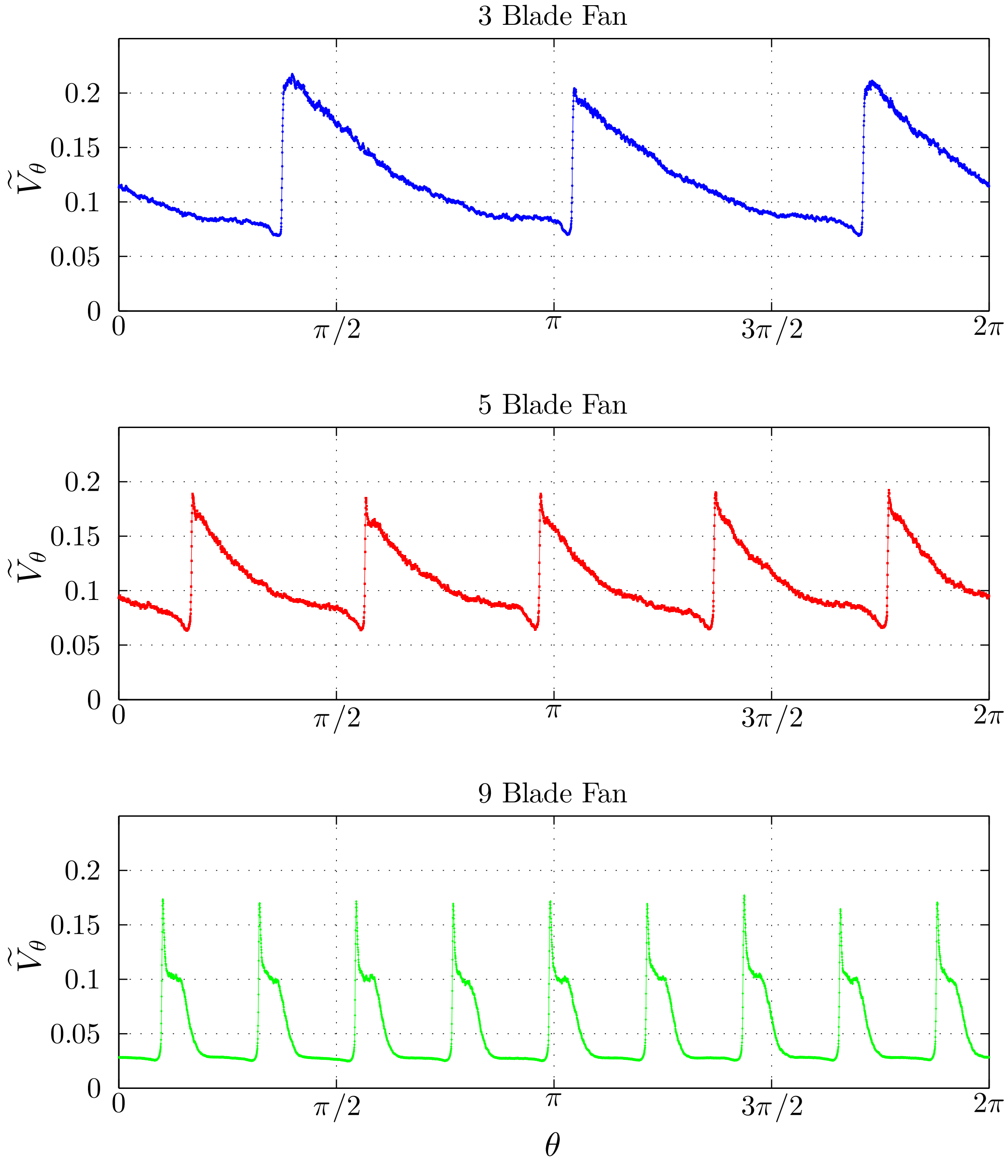

Figure 47 Case III Azimuthal turbulence intensity over $0 \le \theta \le 2\pi$

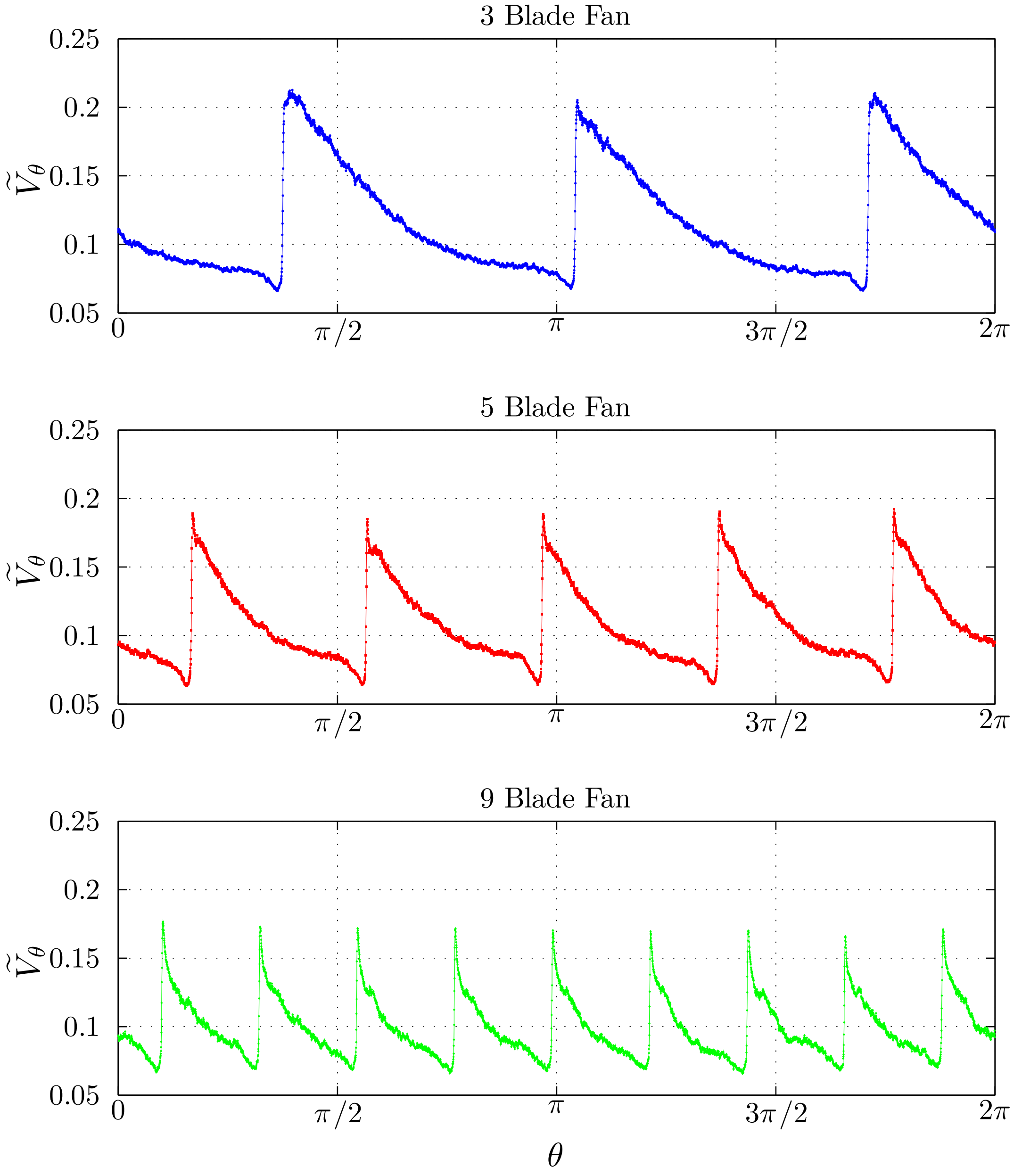
3 Blade Fan

5 Blade Fan

9 Blade Fan

Figure 48 Case IV Azimuthal turbulence intensity over $0 \leq \theta \leq 2\pi$

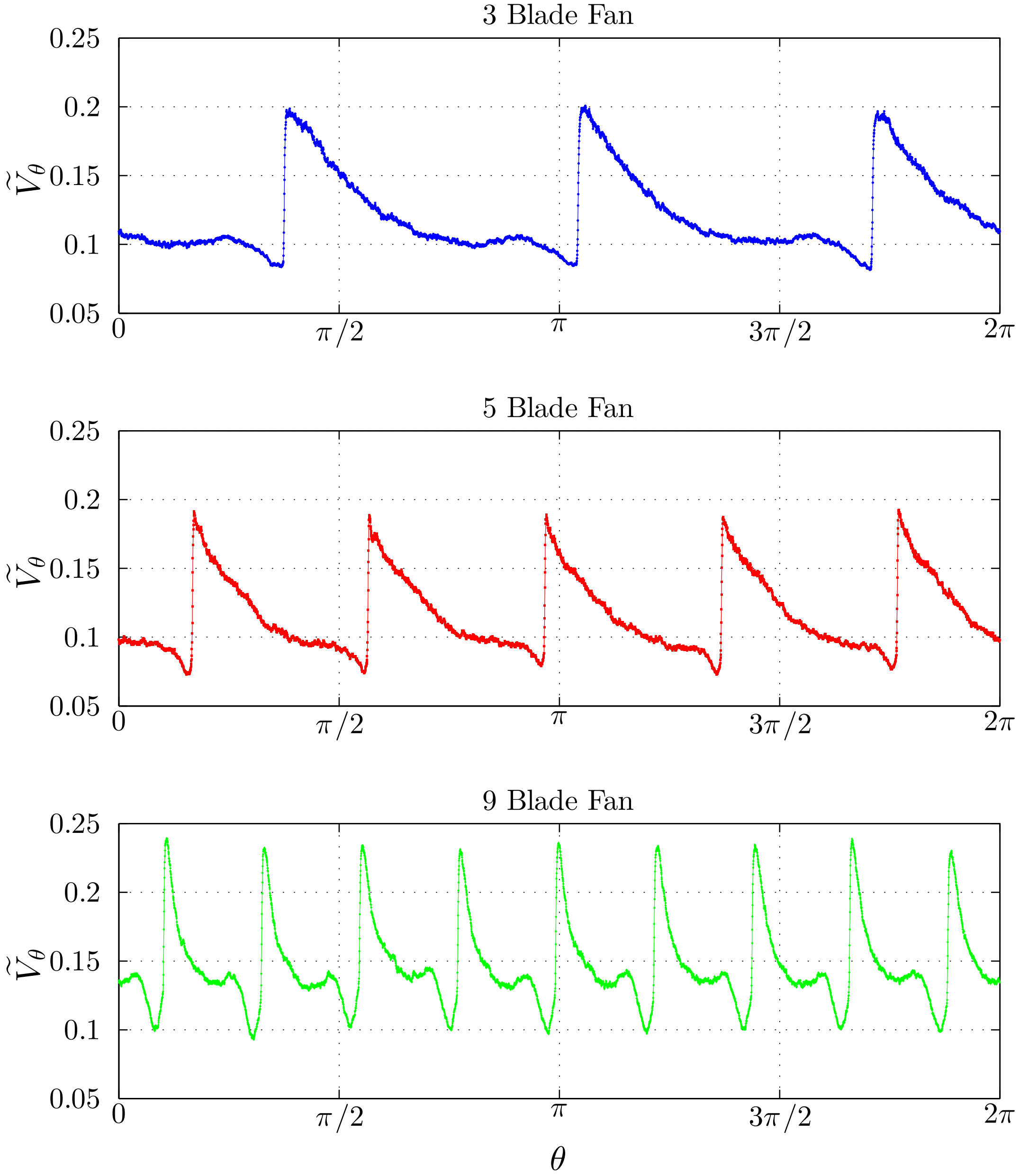

Figure 49 Case V Azimuthal turbulence intensity over $0 \leq \theta \leq 2\pi$

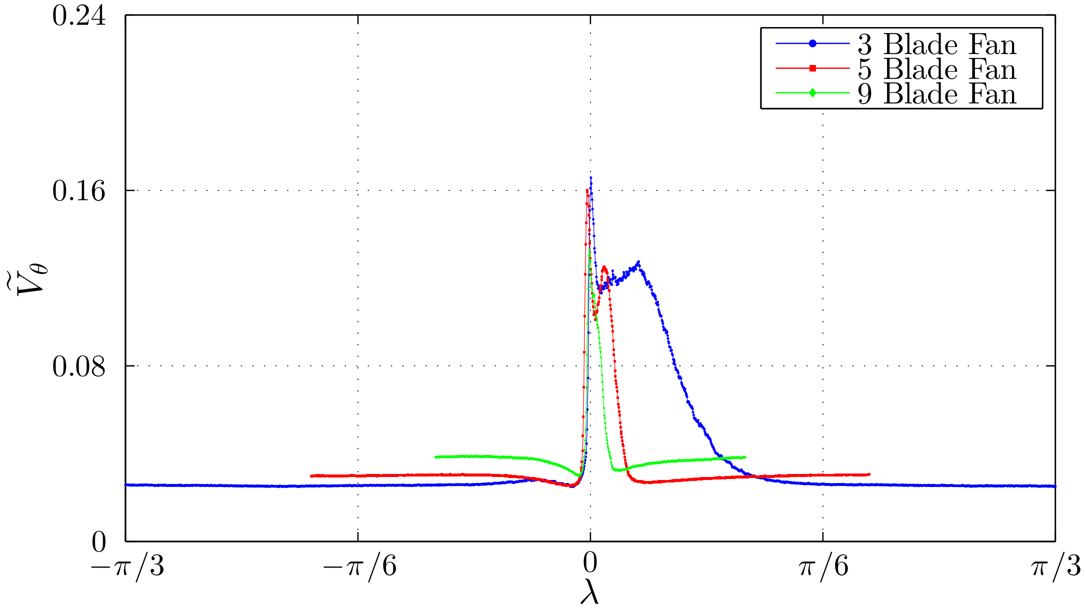

Figure 50 Case I Azimuthal turbulence intensity over λ_3

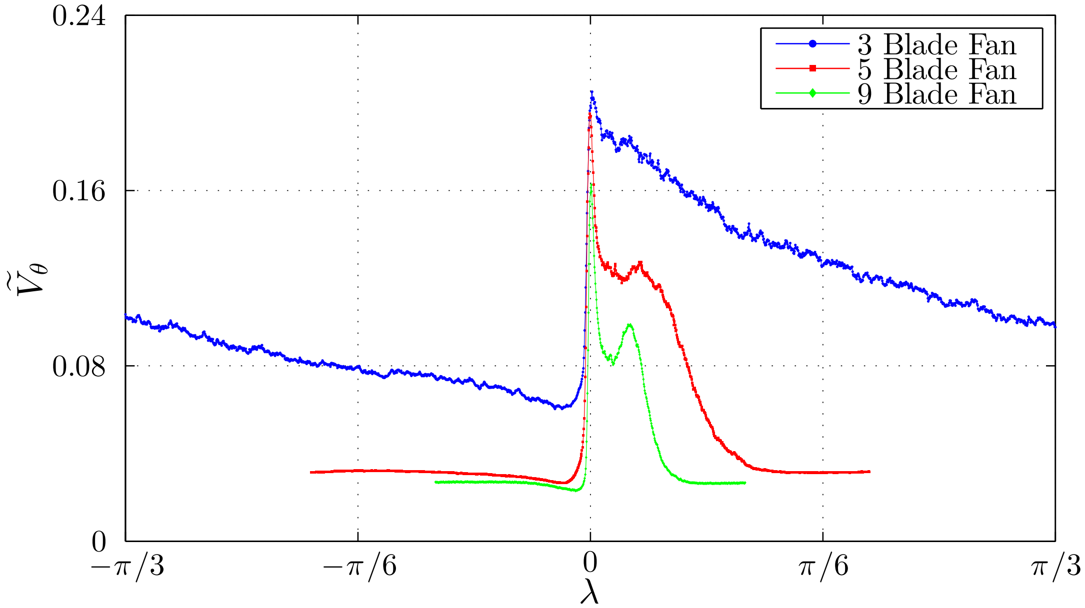

Figure 51 Case II Azimuthal turbulence intensity over λ_3

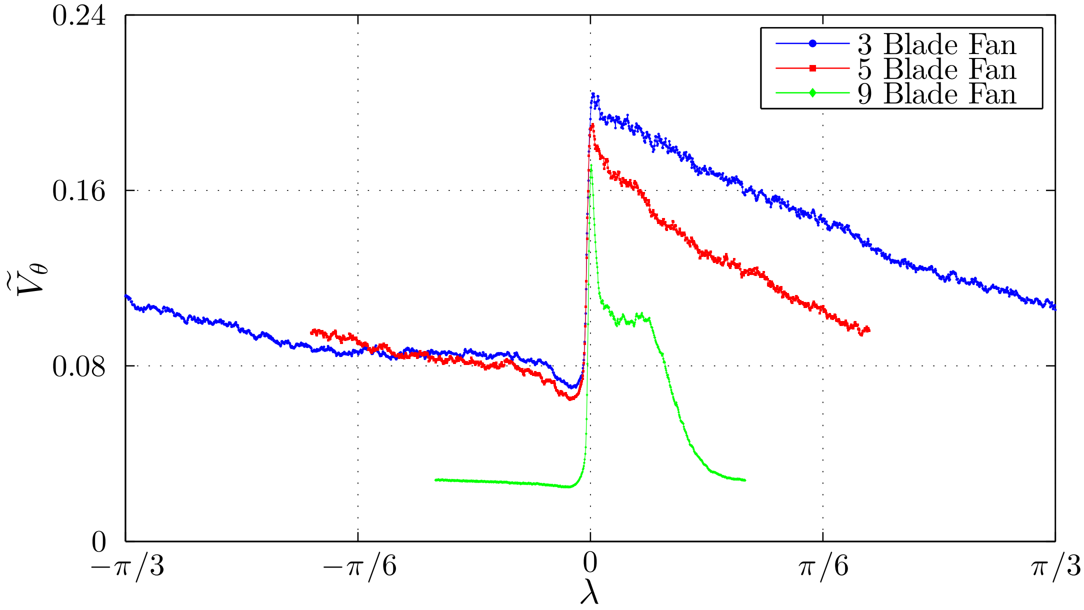

Figure 52 Case III Azimuthal turbulence intensity over λ_3

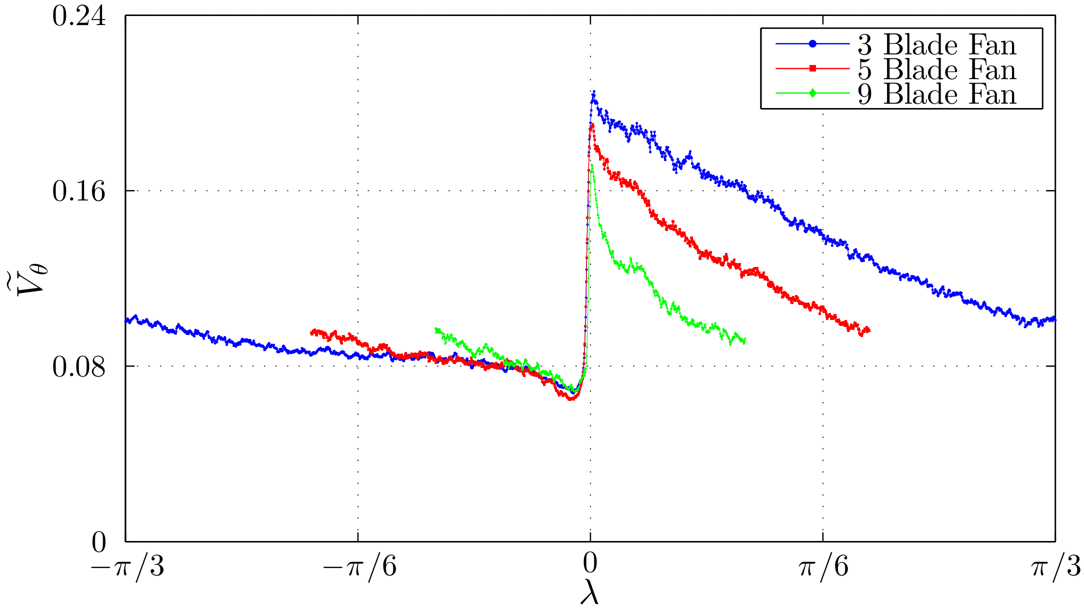

Figure 53 Case IV Azimuthal turbulence intensity over λ_3

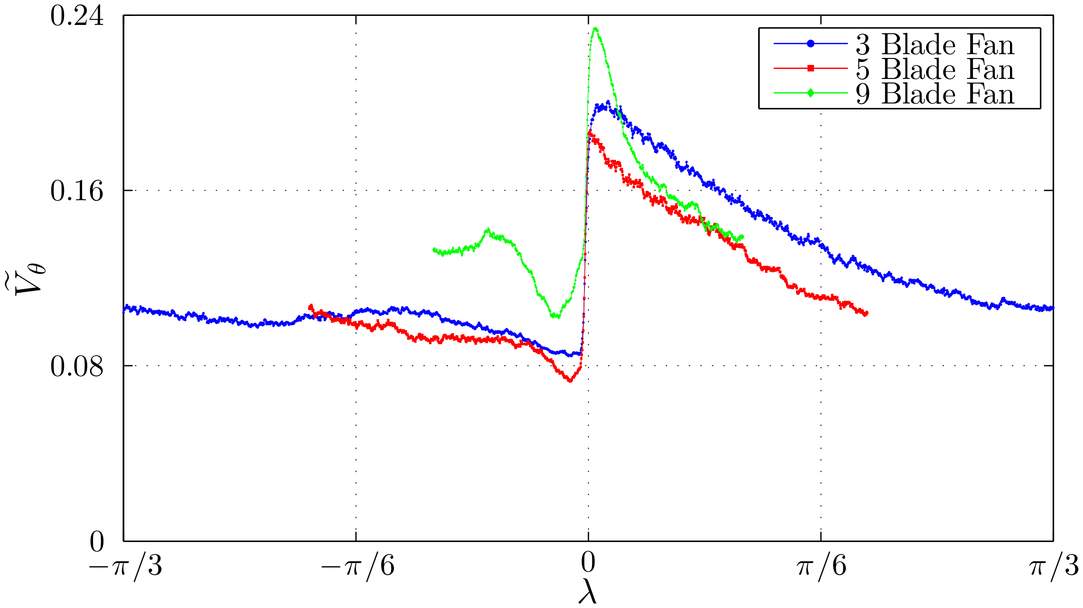

Figure 54 Case V Azimuthal turbulence intensity over λ_3

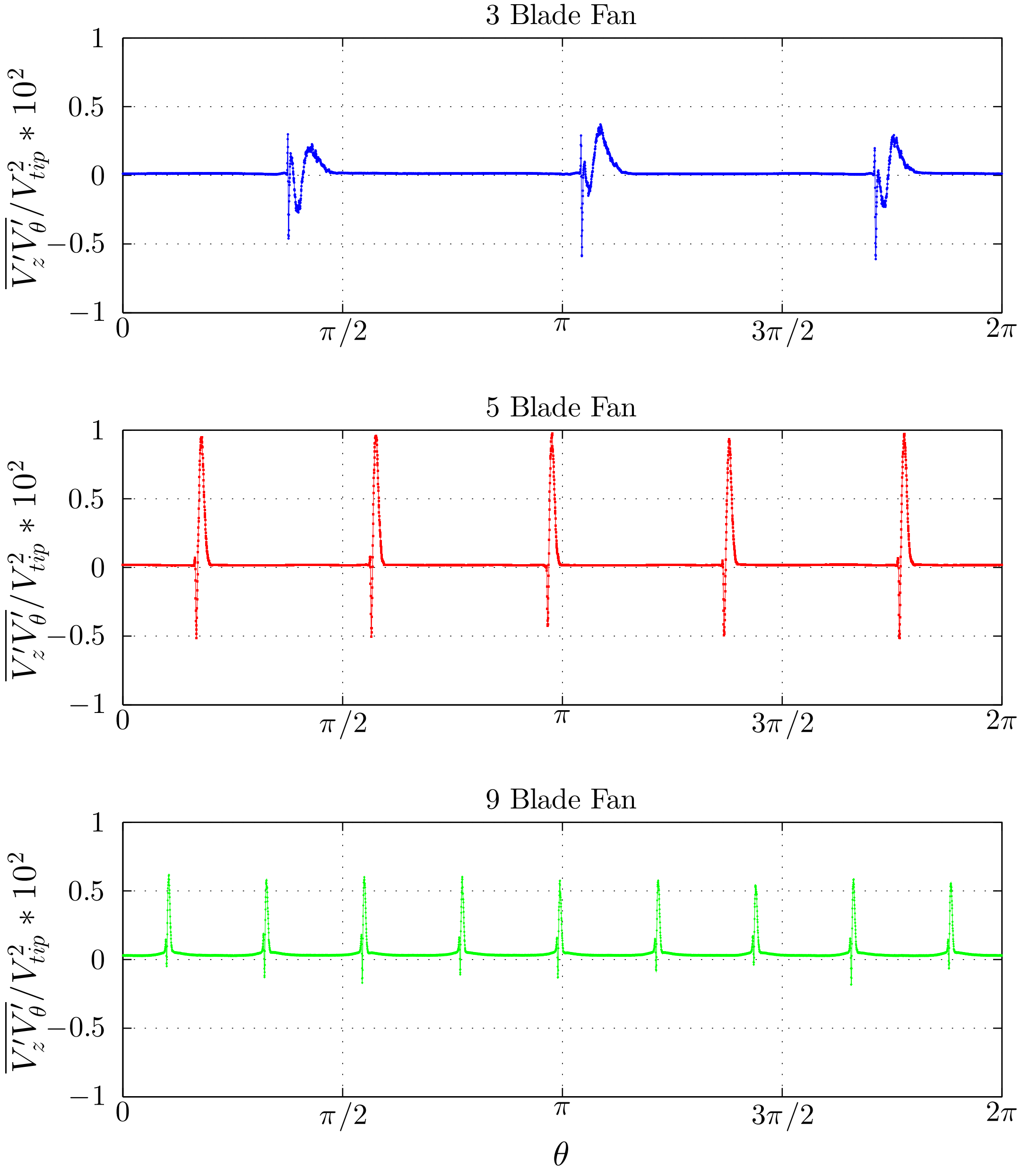

Figure 55 Case I Reynolds stress in z-θ – plane over $0 \leq \theta \leq 2\pi$

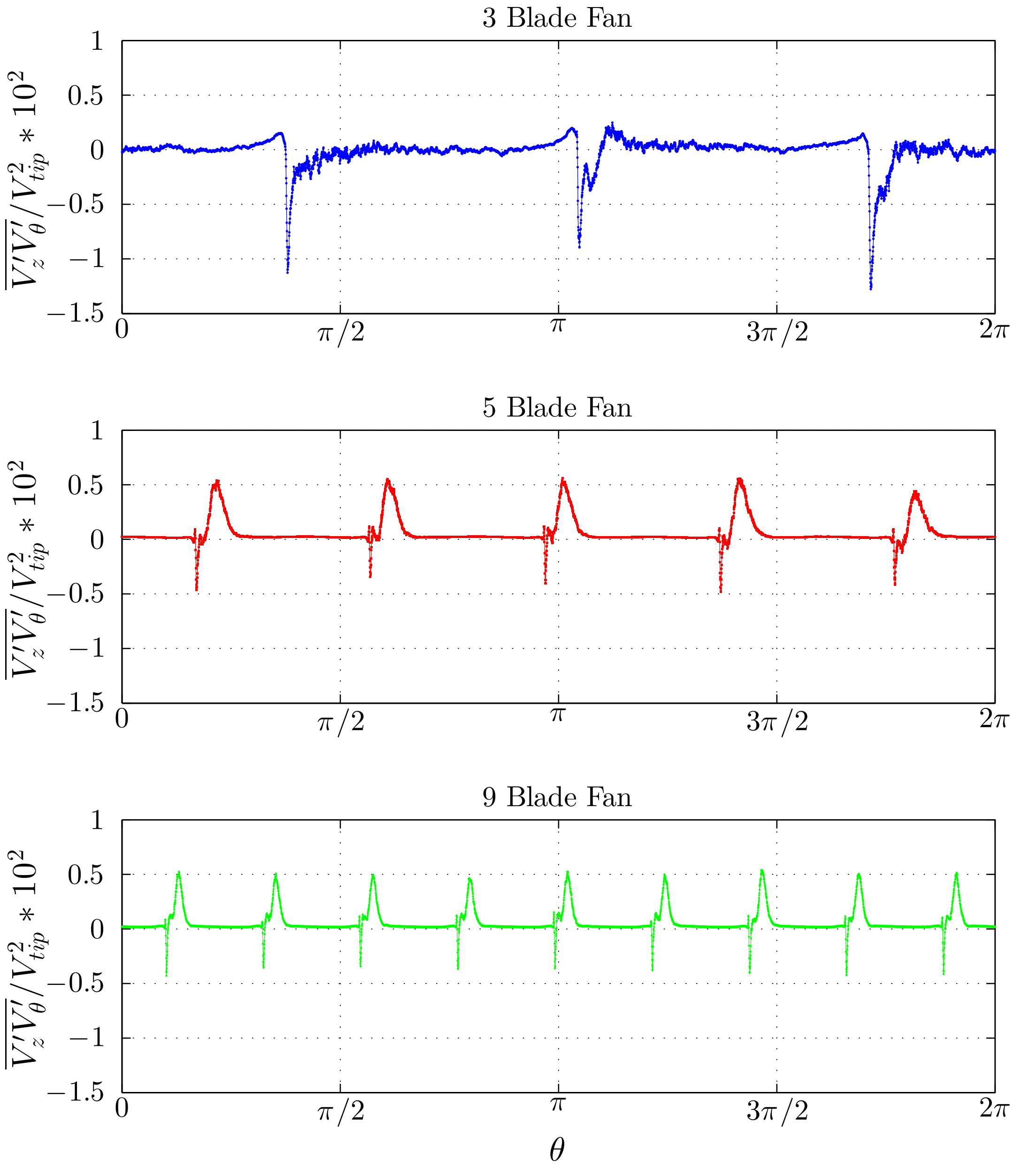

Figure 56 Case II Reynolds stress in z-θ – plane over $0 \leq \theta \leq 2\pi$

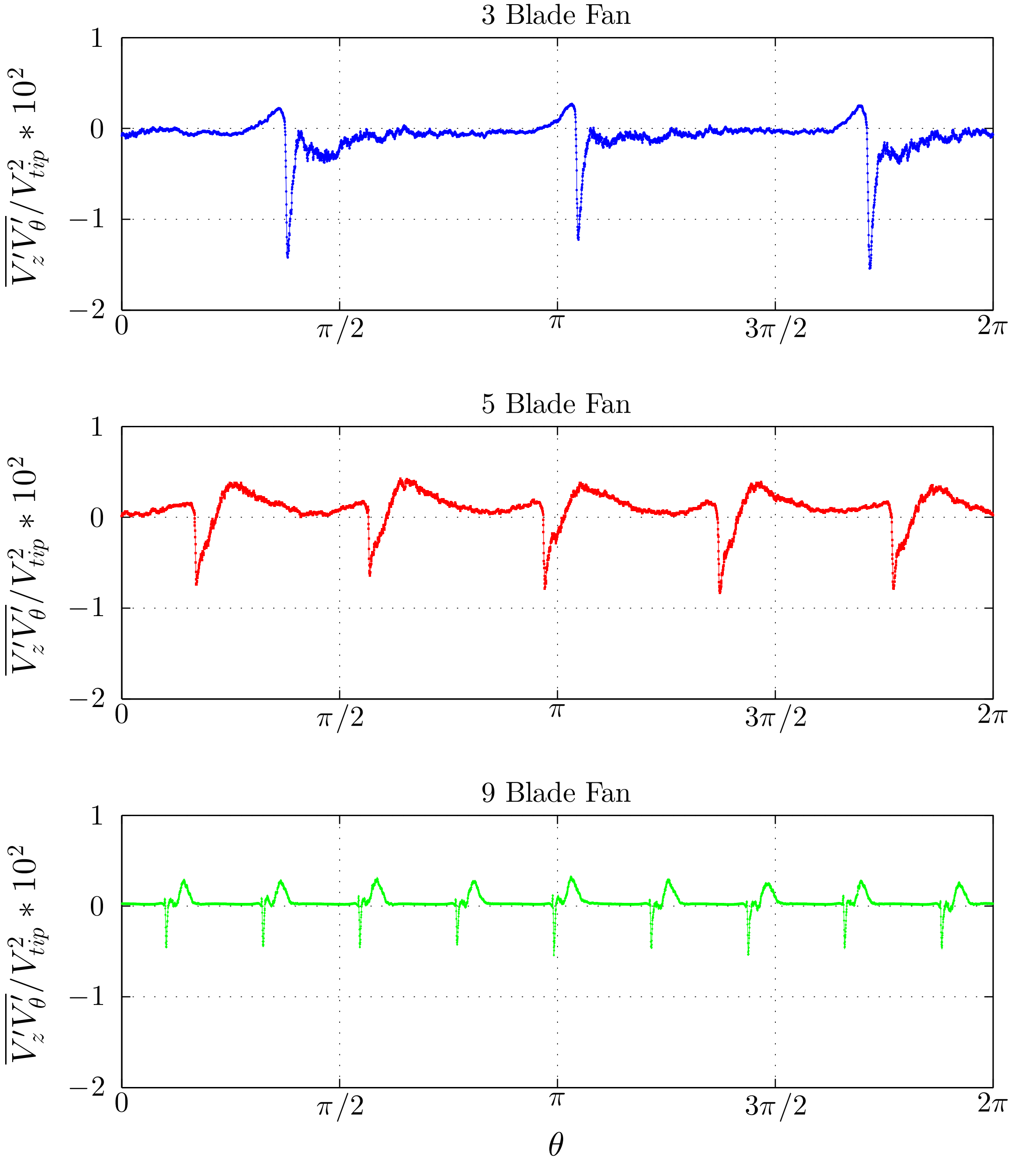

Figure 57 Case III Reynolds stress in z-θ – plane over $0 \leq \theta \leq 2\pi$

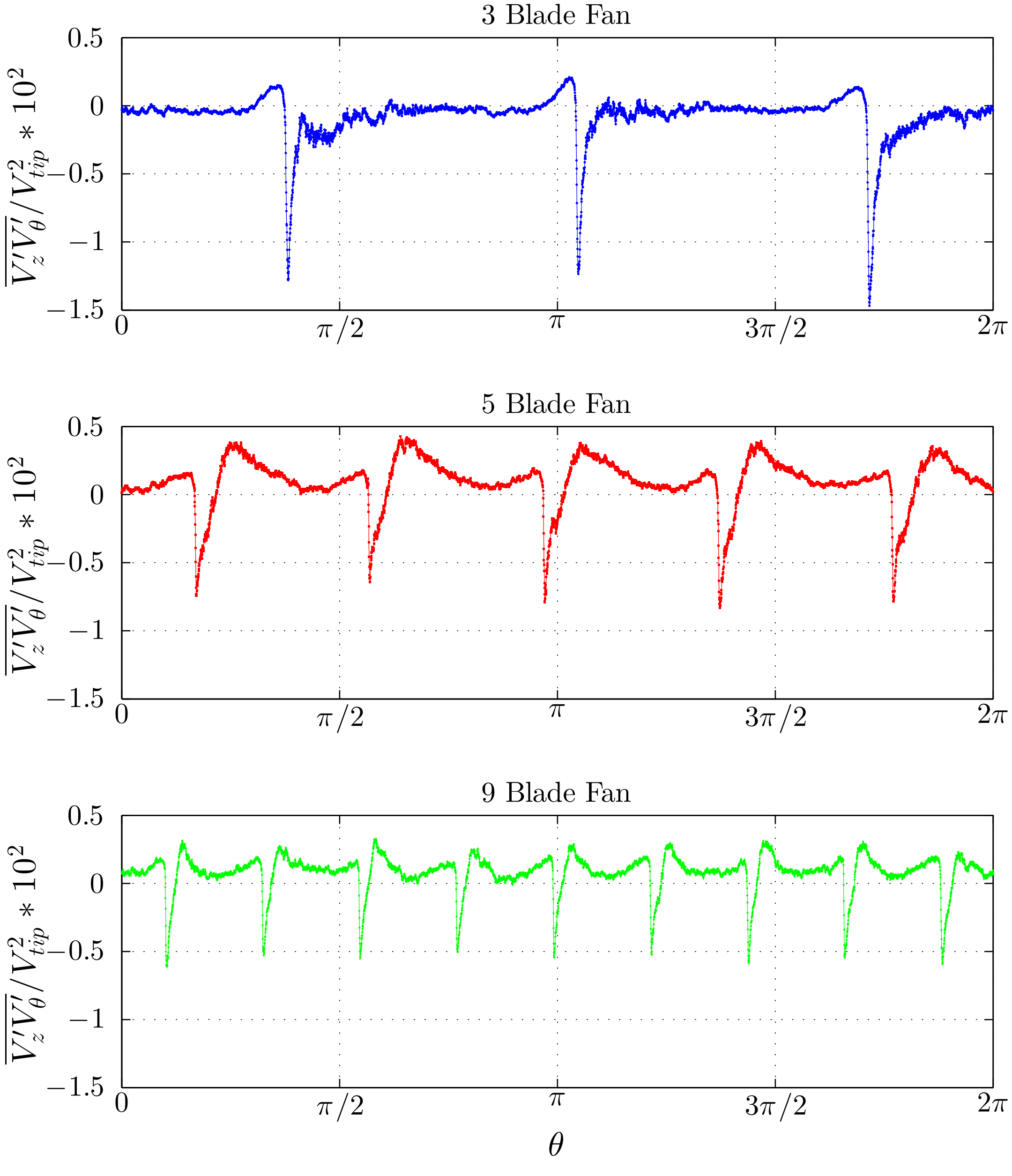
3 Blade Fan

5 Blade Fan

9 Blade Fan

Figure 58 Case IV Reynolds stress in z-θ – plane over $0 \leq \theta \leq 2\pi$

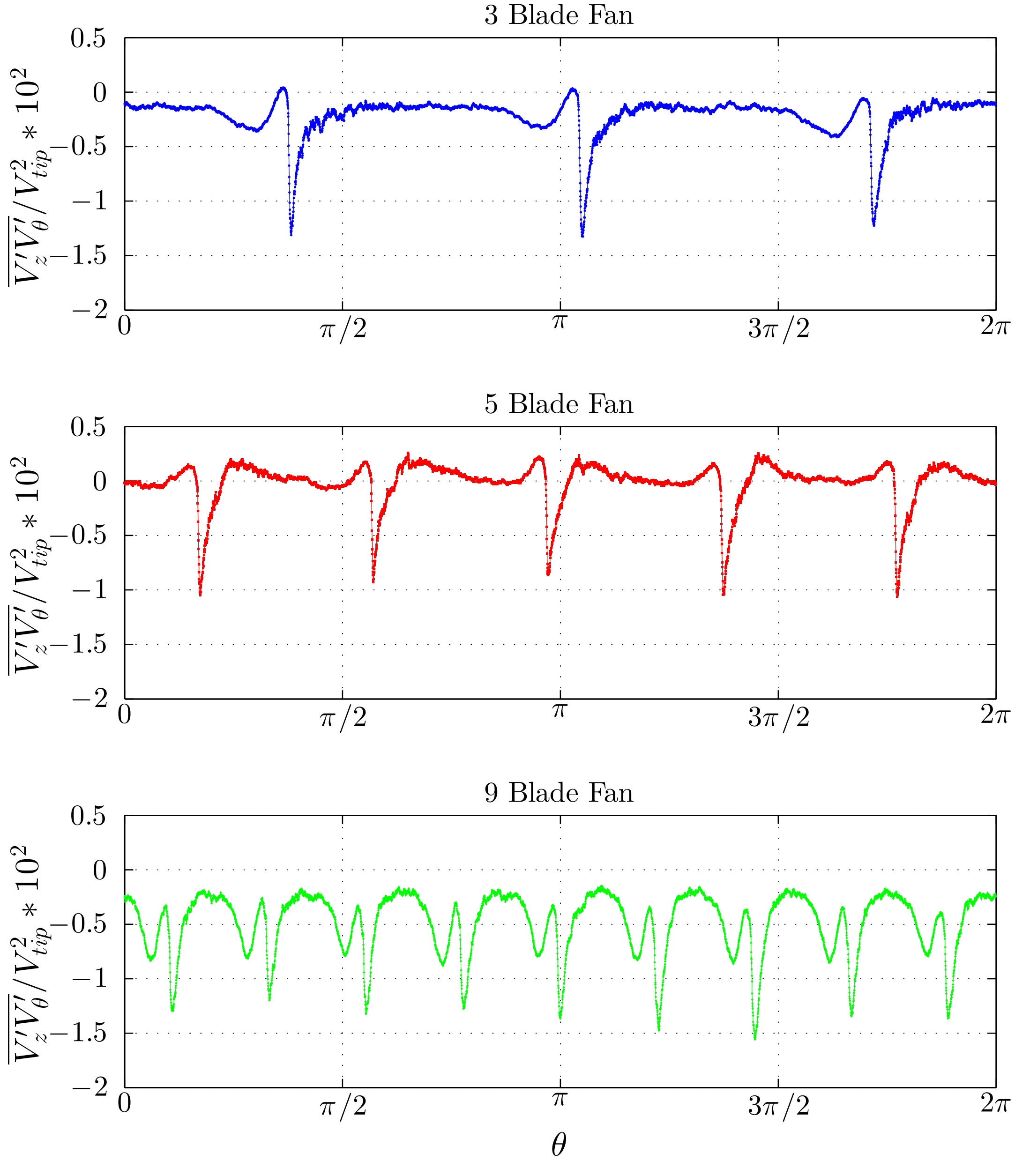

Figure 59 Case V Reynolds stress in z-θ – plane over $0 \leq \theta \leq 2\pi$

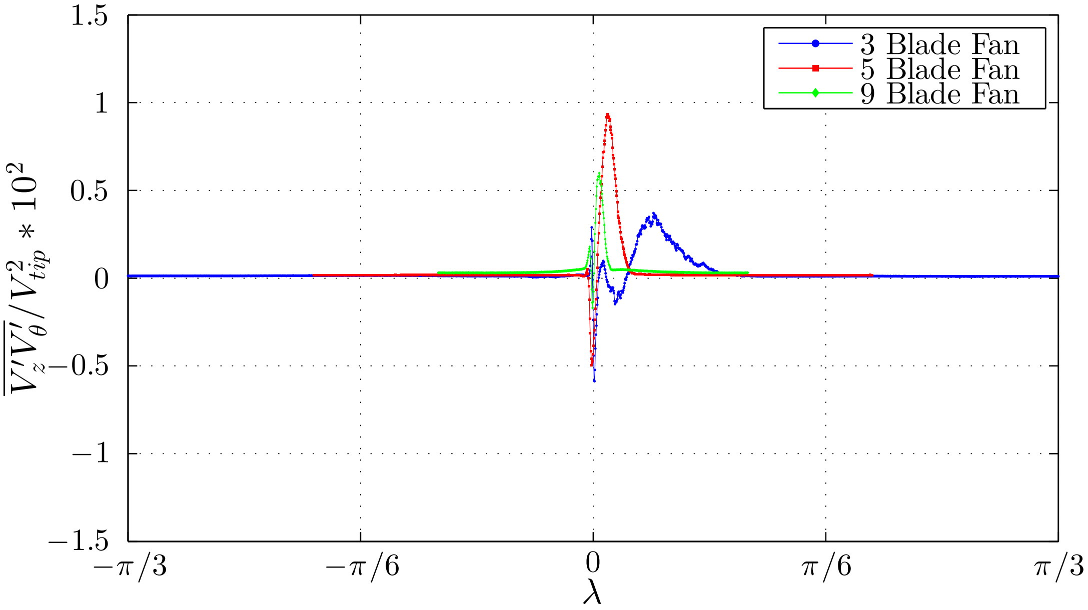

Figure 60 Case I Reynolds stress in z-θ – plane over λ_3

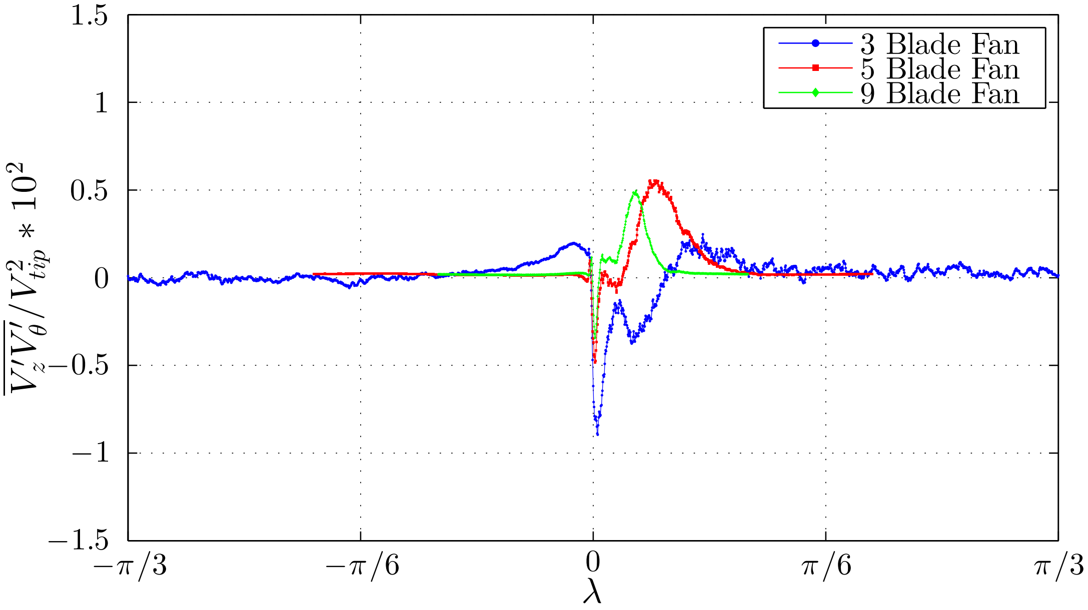

Figure 61 Case II Reynolds stress in z-θ – plane over λ_3

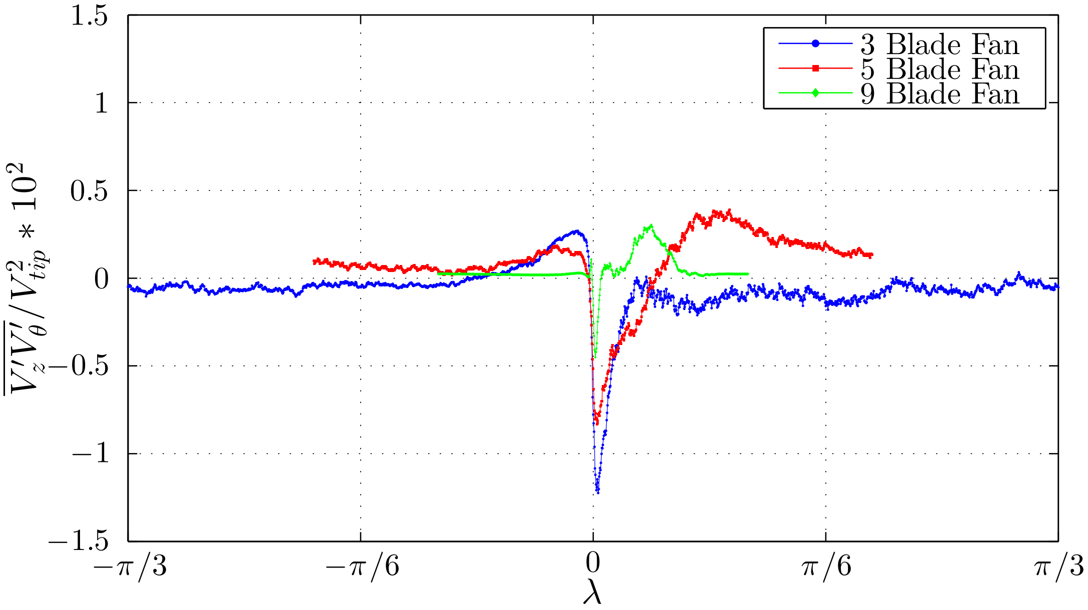

Figure 62 Case III Reynolds stress in z-θ − plane over λ_3

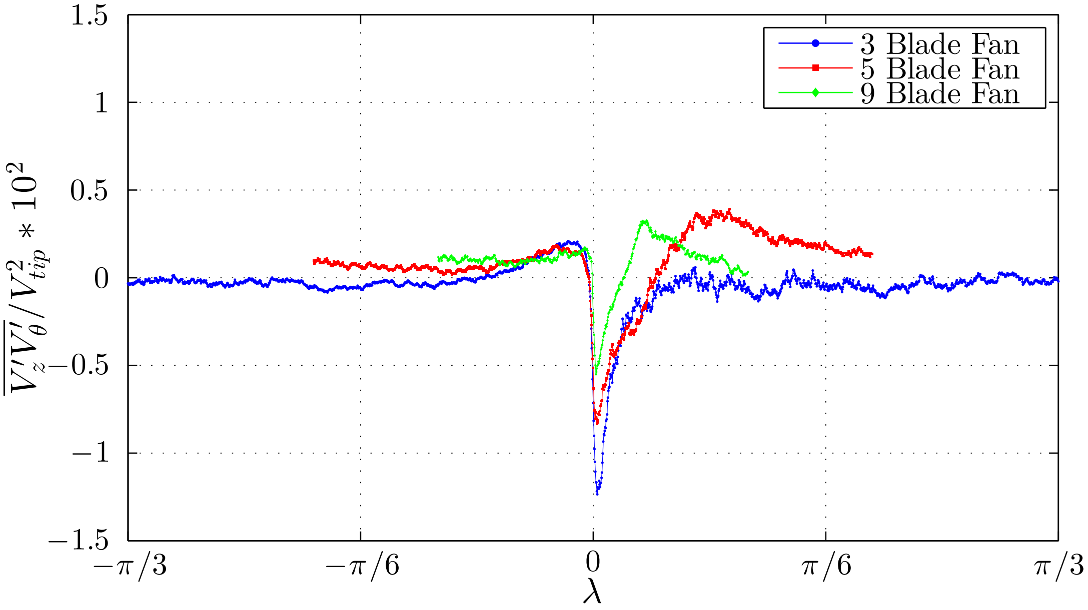

Figure 63 Case IV Reynolds stress in z-θ − plane over λ_3

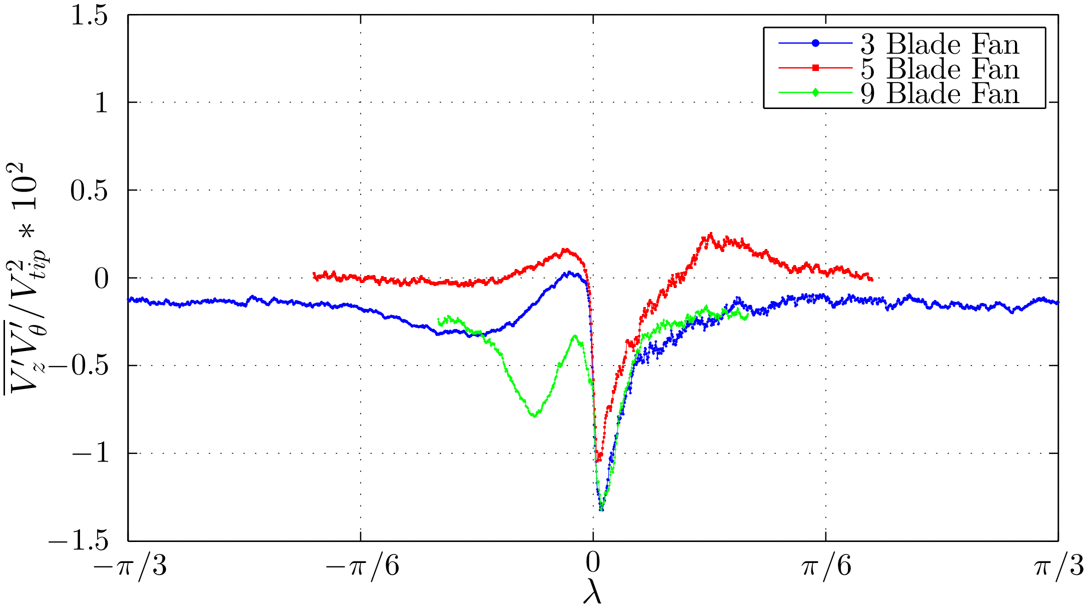

Figure 64 Case V Reynolds stress in z-θ – plane over λ_3

C WORK RATE EVALUATION FIGURES

This appendix contains the entire collection of figures that were used to generate the kinematic kinetic energy integrand and the turbulence kinetic energy from Sections 3.4.2 and 3.4.4, respectively. (Method in Section 3.3) These figures are presented in the same sequence as they are in Sections 3.4.2 and 3.4.4 and include: $(1/2)\overline{[(V_z^2 + V_\theta^2)V_z]}/V_{tip}^3$ and $\widetilde{V}_z^2 + \widetilde{V}_\theta^2$.

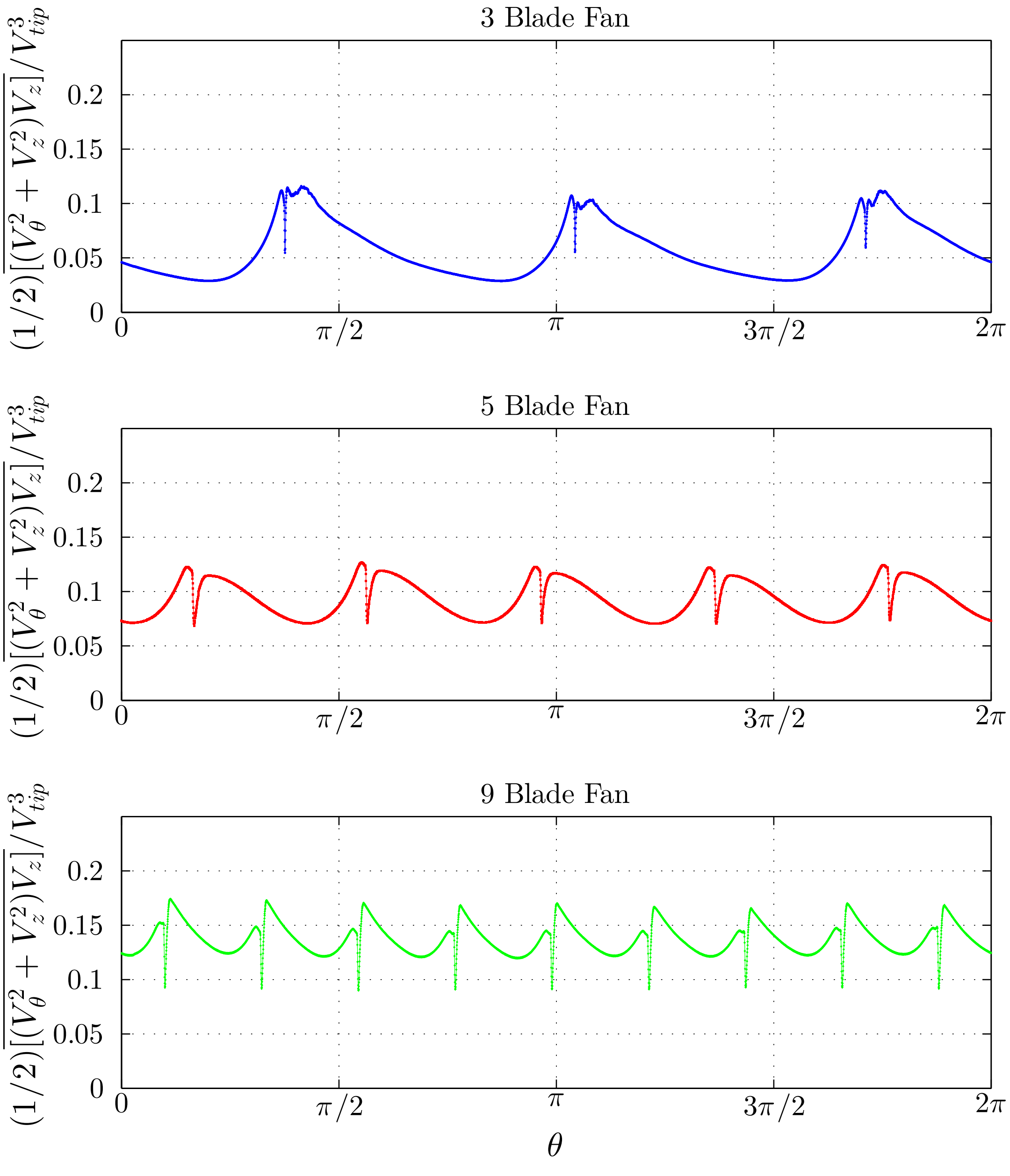

Figure 65 Case I kinematic integrand exit kinetic energy flux over $0 \leq \theta \leq 2\pi$

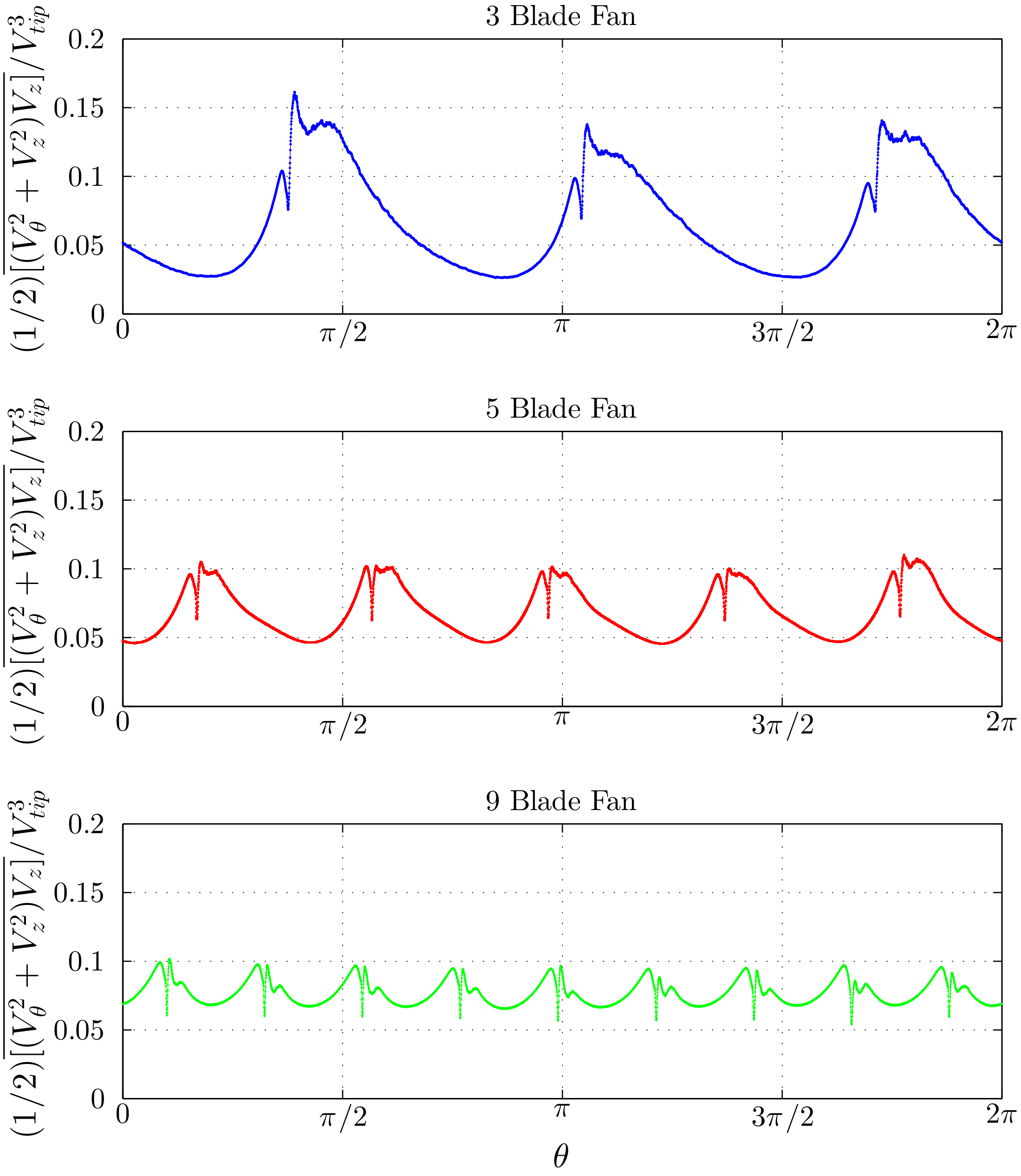

Figure 66 Case II kinematic integrand exit kinetic energy flux over $0 \leq \theta \leq 2\pi$

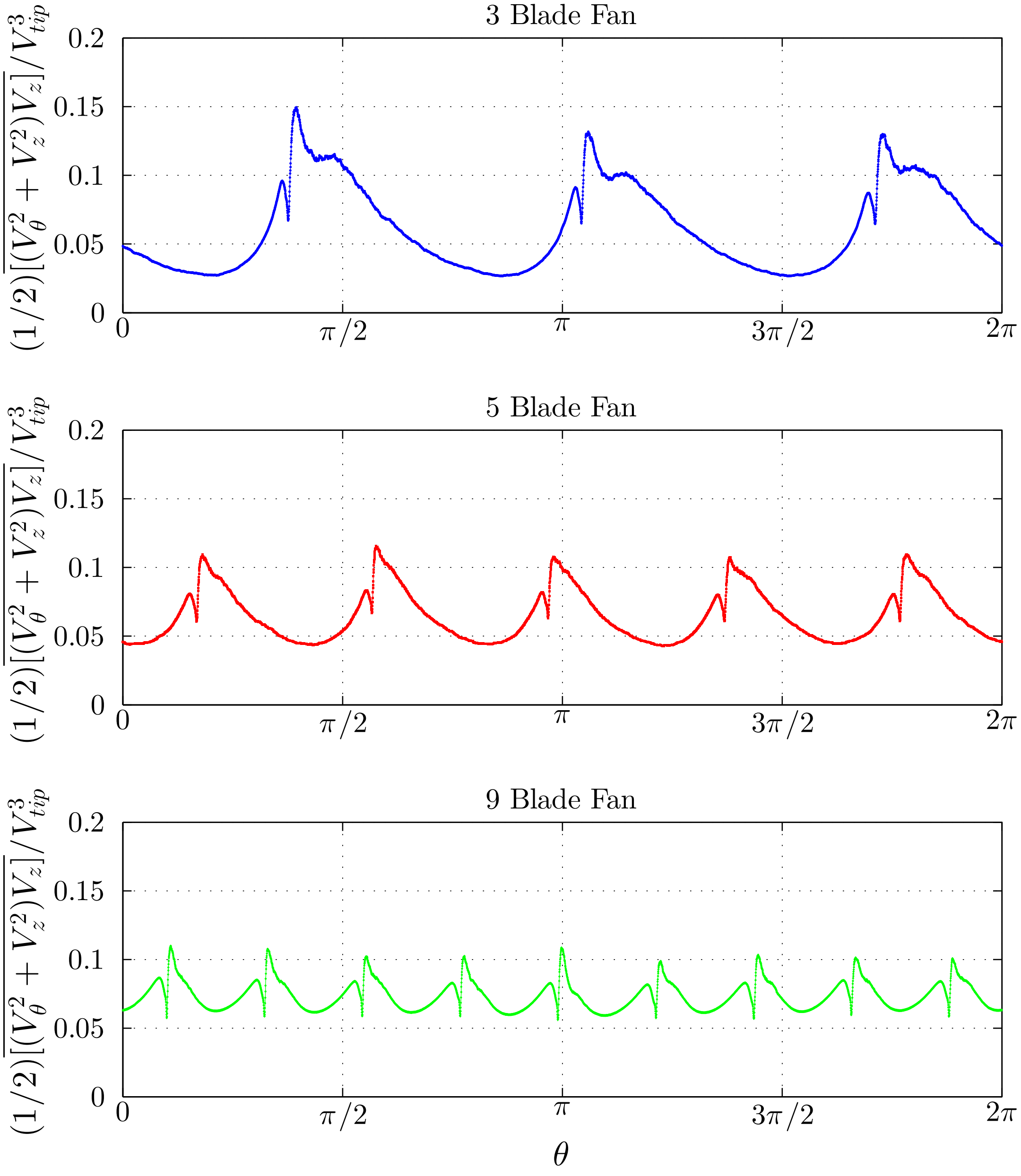
3 Blade Fan

5 Blade Fan

9 Blade Fan

Figure 67 Case III kinematic integrand exit kinetic energy flux over $0 \leq \theta \leq 2\pi$

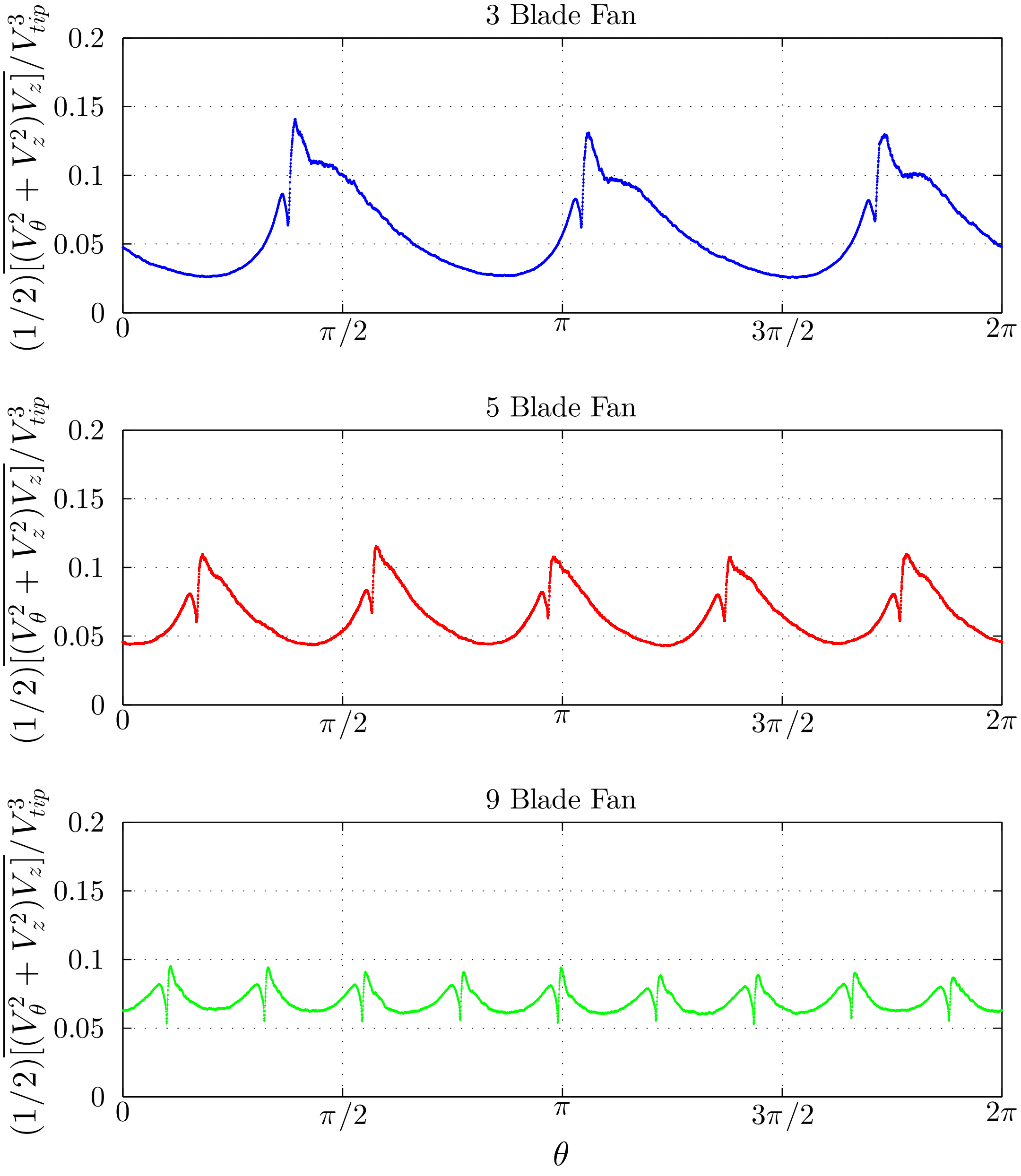

Figure 68 Case IV kinematic integrand exit kinetic energy flux over $0 \leq \theta \leq 2\pi$

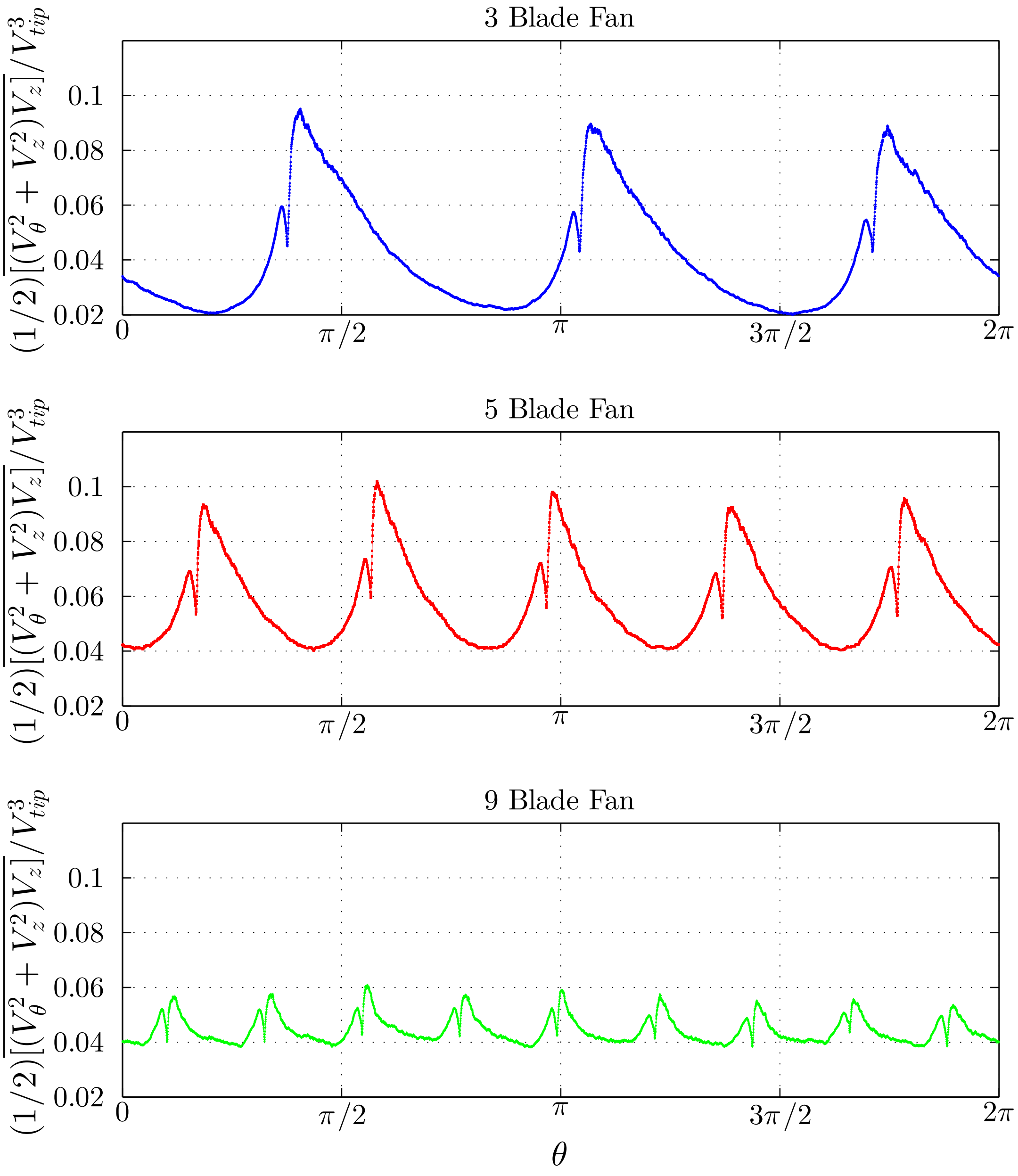

Figure 69 Case V kinematic integrand exit kinetic energy flux over $0 \leq \theta \leq 2\pi$

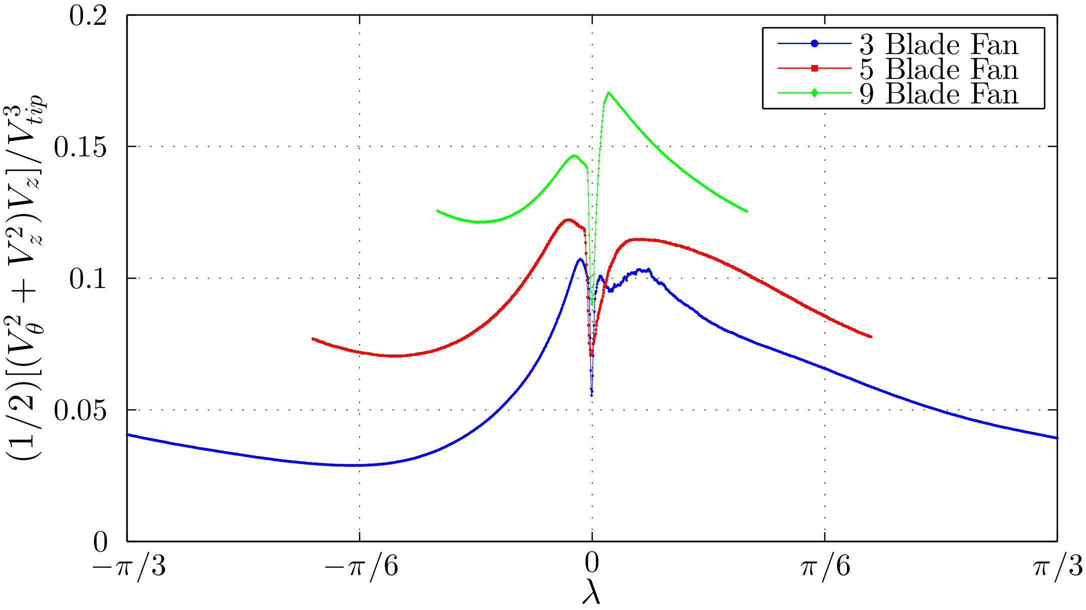

Figure 70 Case I kinematic integrand exit kinetic energy flux over λ_3

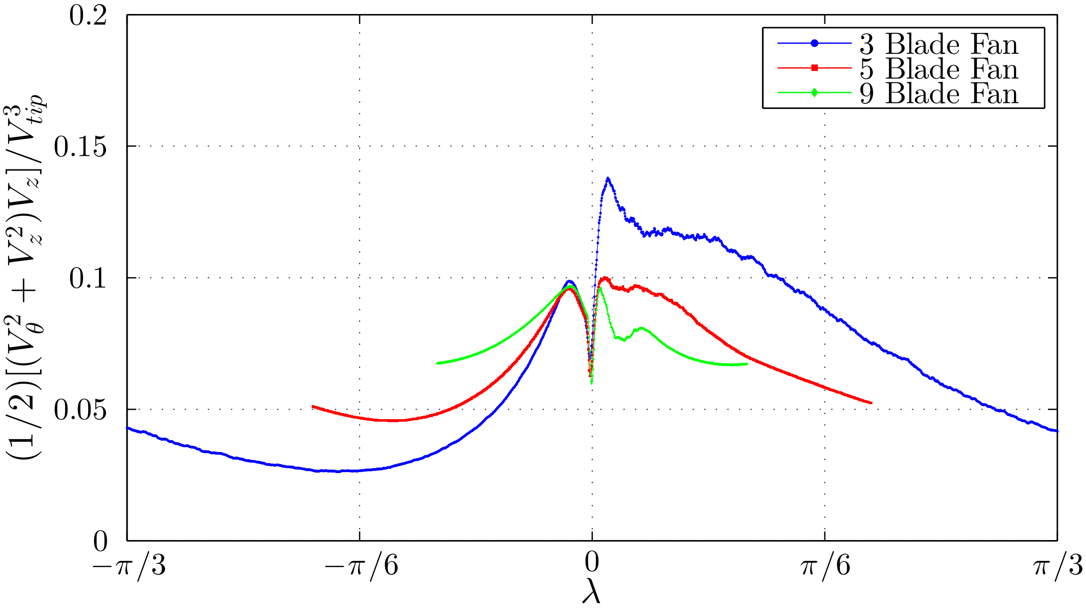

Figure 71 Case II kinematic integrand exit kinetic energy flux over λ_3

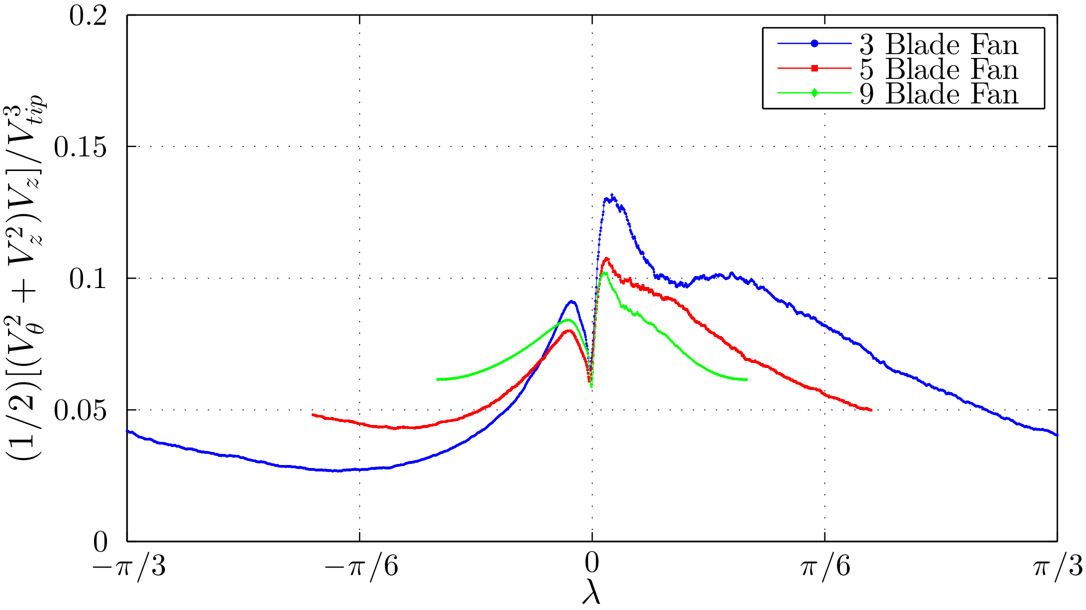

Figure 72 Case III kinematic integrand exit kinetic energy flux over λ_3

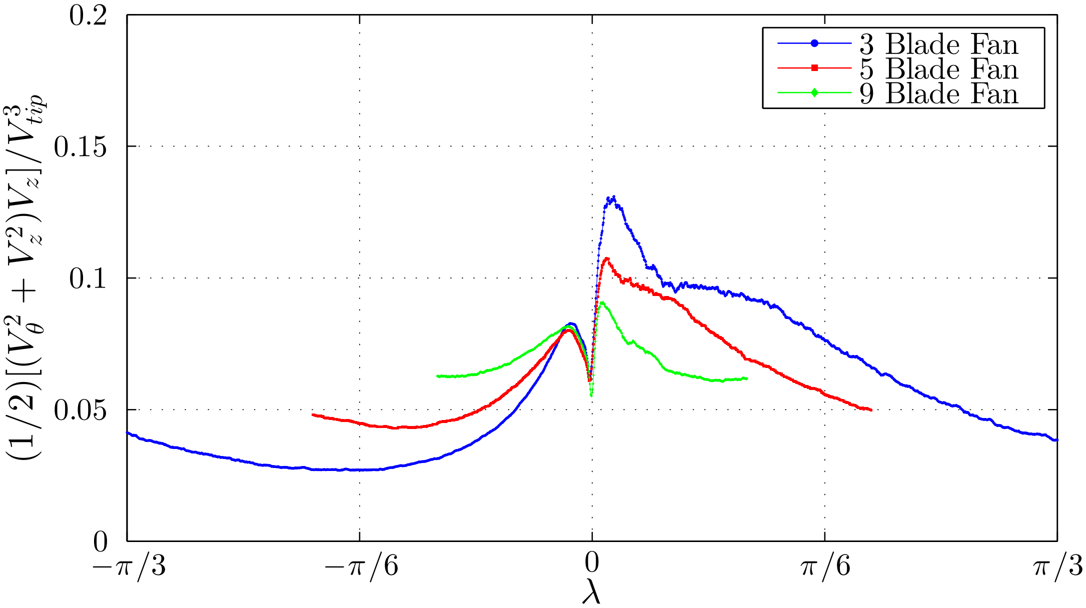

Figure 73 Case IV kinematic integrand exit kinetic energy flux over λ_3

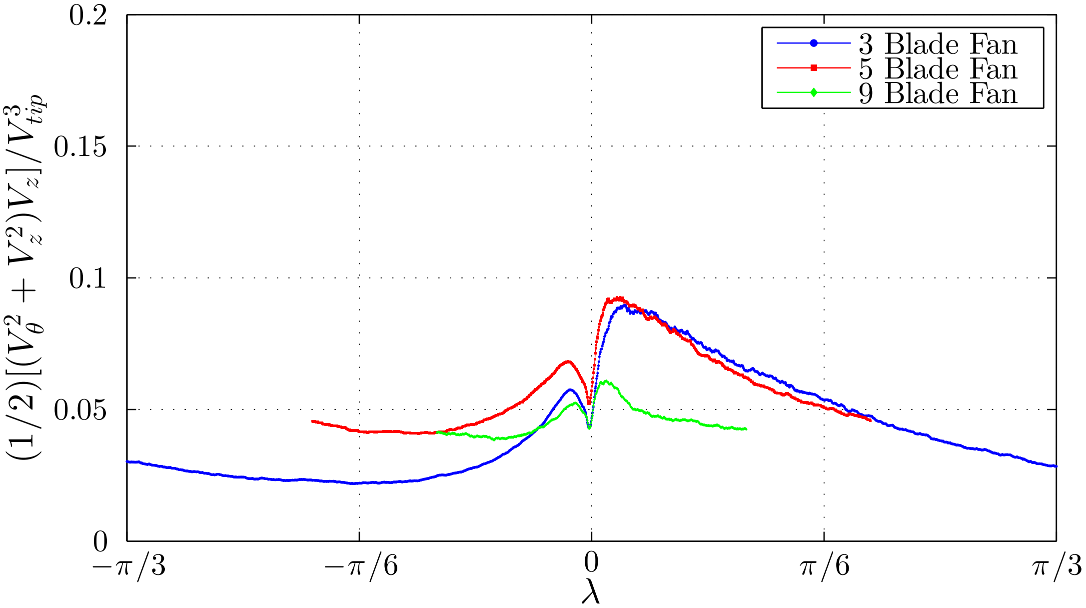

Figure 74 Case V kinematic integrand exit kinetic energy flux over λ_3

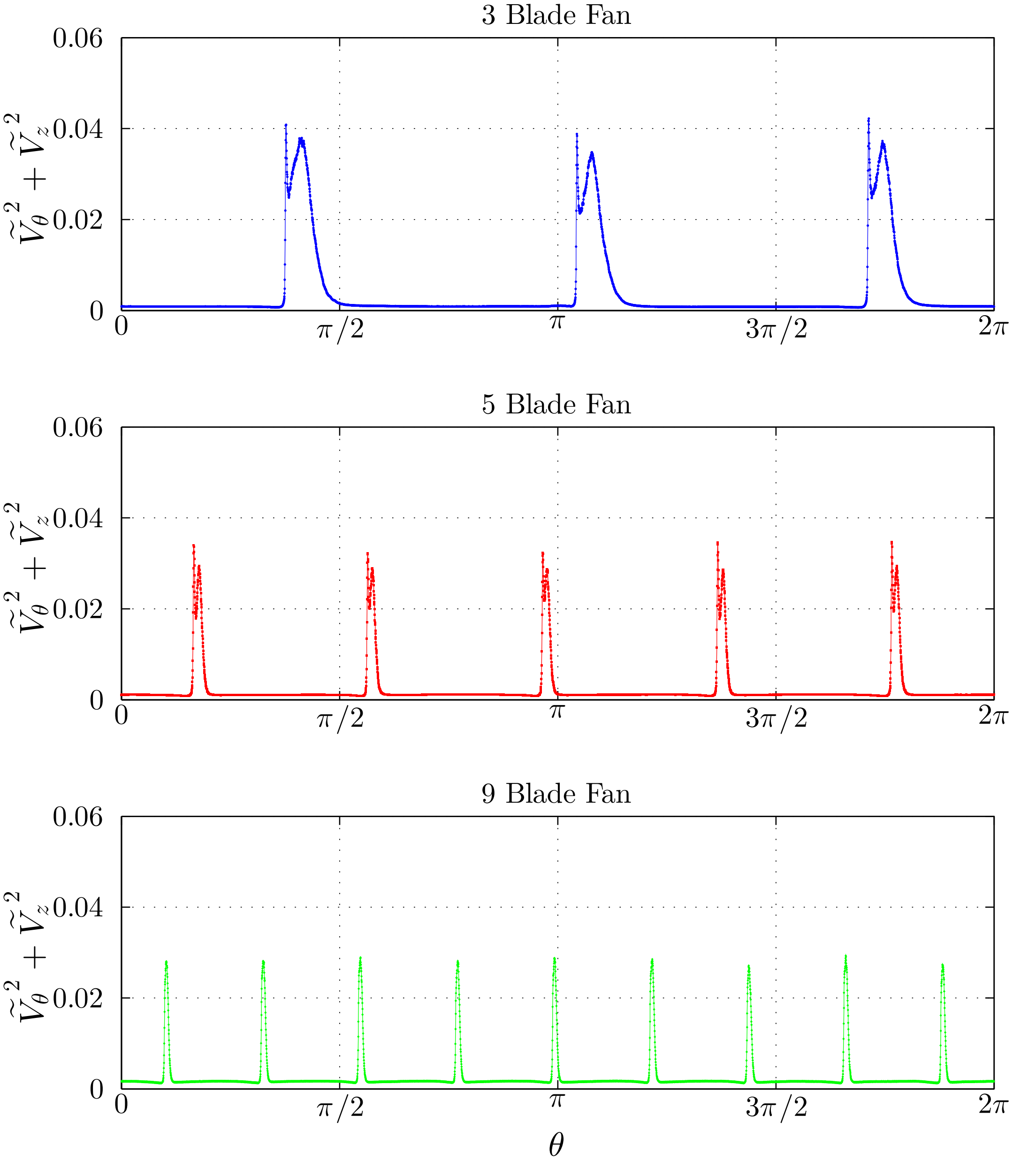

Figure 75 Case I turbulence kinetic energy at fan exit over $0 \leq \theta \leq 2\pi$

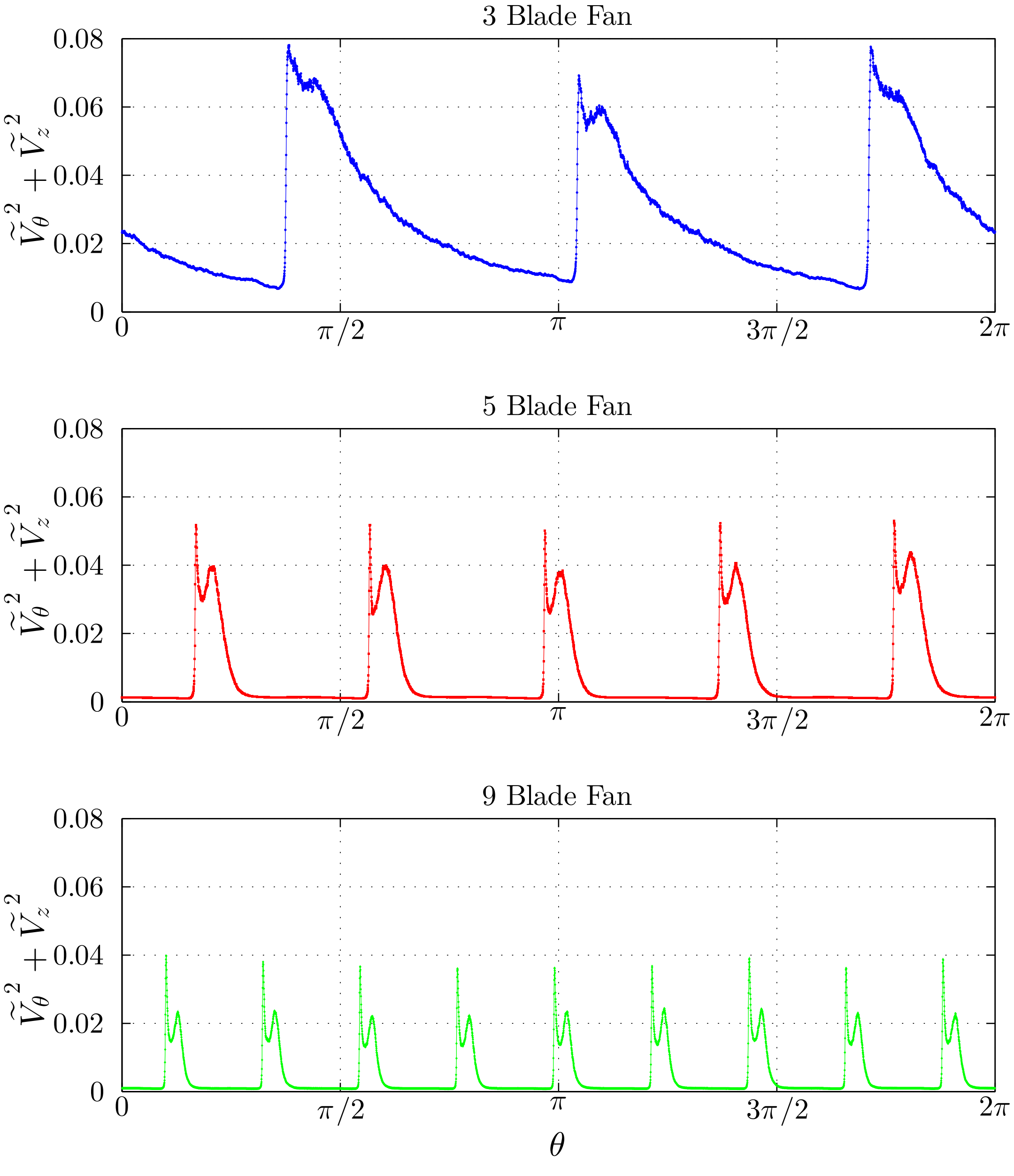

Figure 76 Case II turbulence kinetic energy at fan exit over $0 \leq \theta \leq 2\pi$

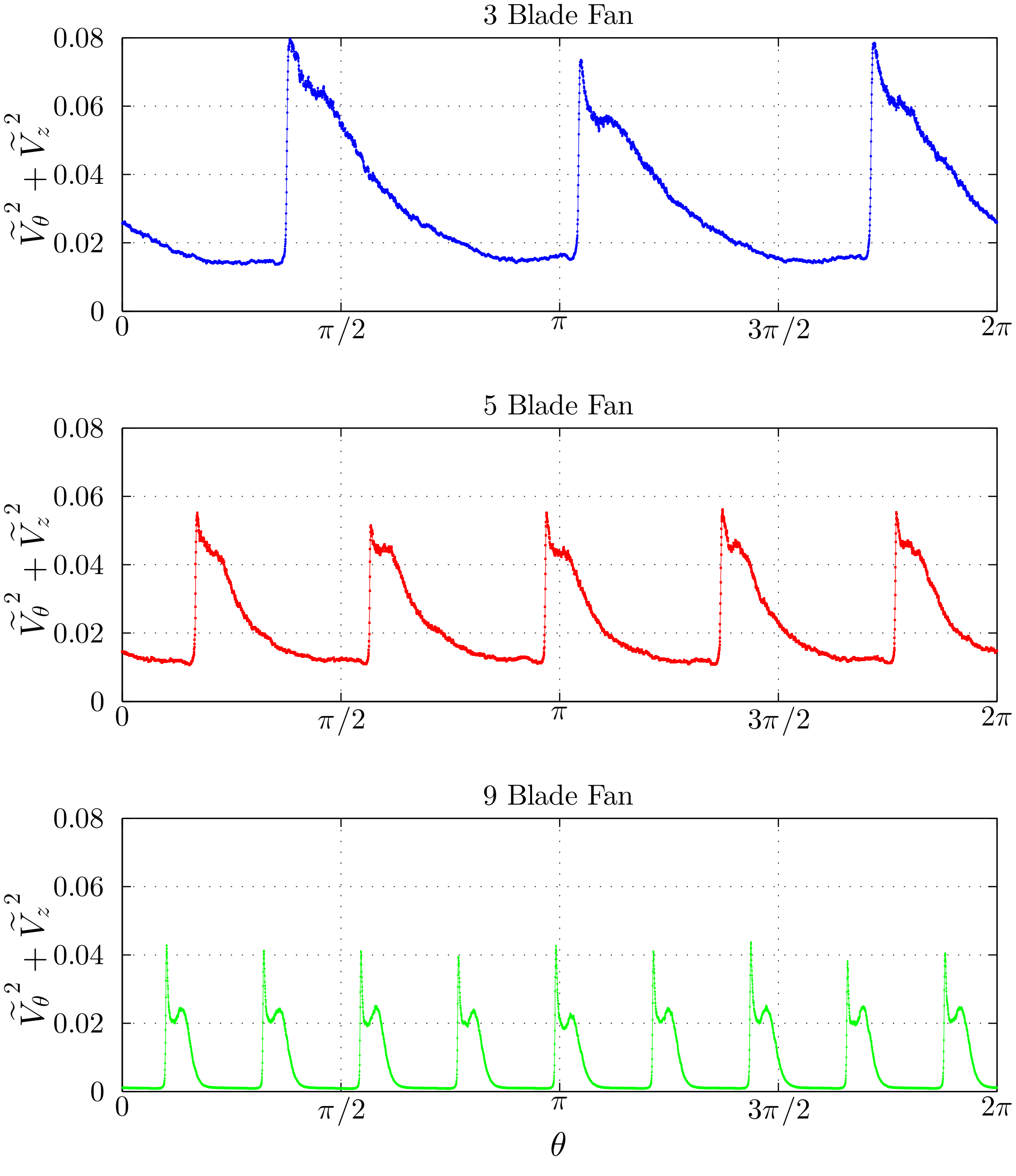

Figure 77 Case III turbulence kinetic energy at fan exit over $0 \leq \theta \leq 2\pi$

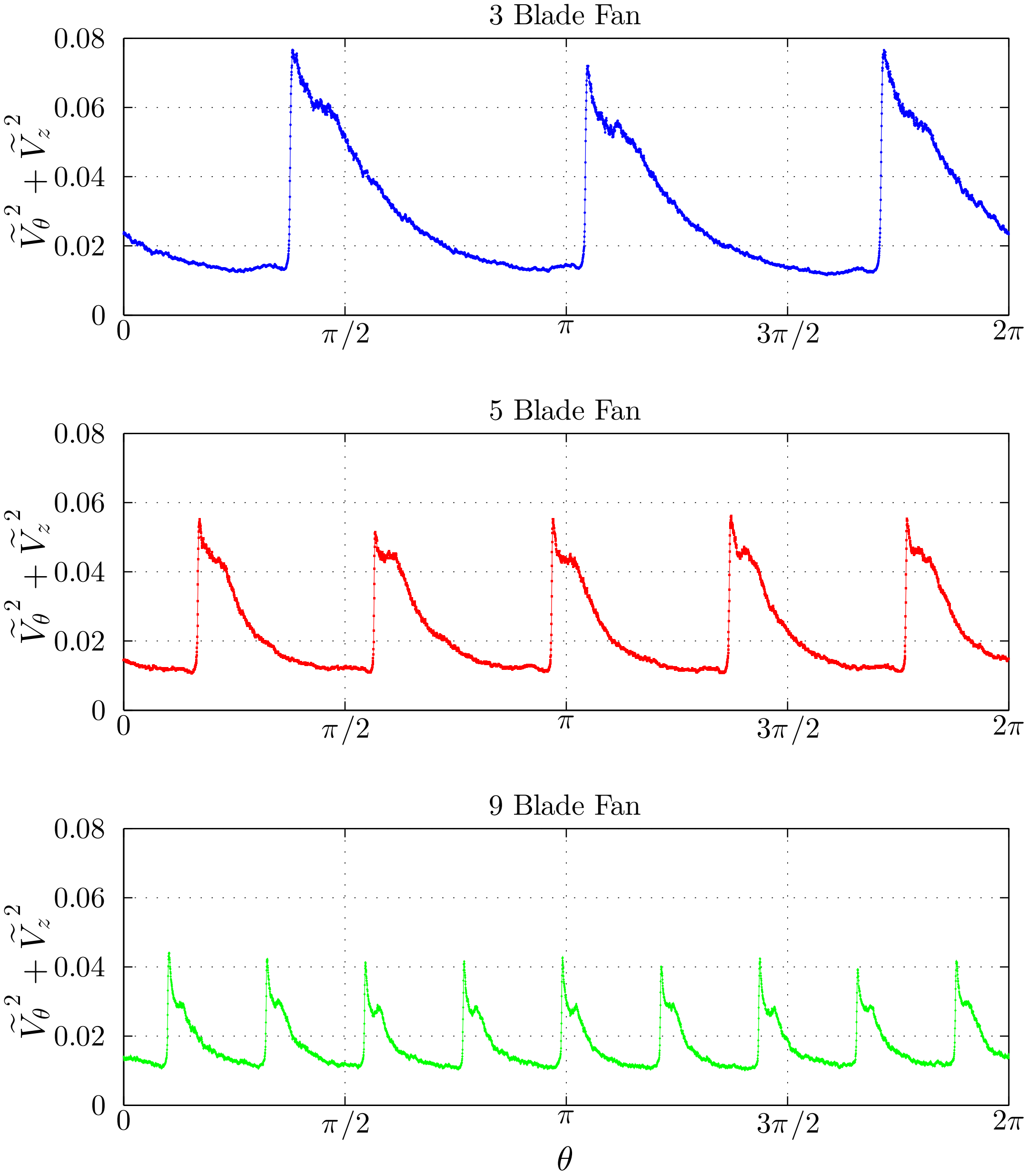

Figure 78 Case IV turbulence kinetic energy at fan exit over $0 \leq \theta \leq 2\pi$

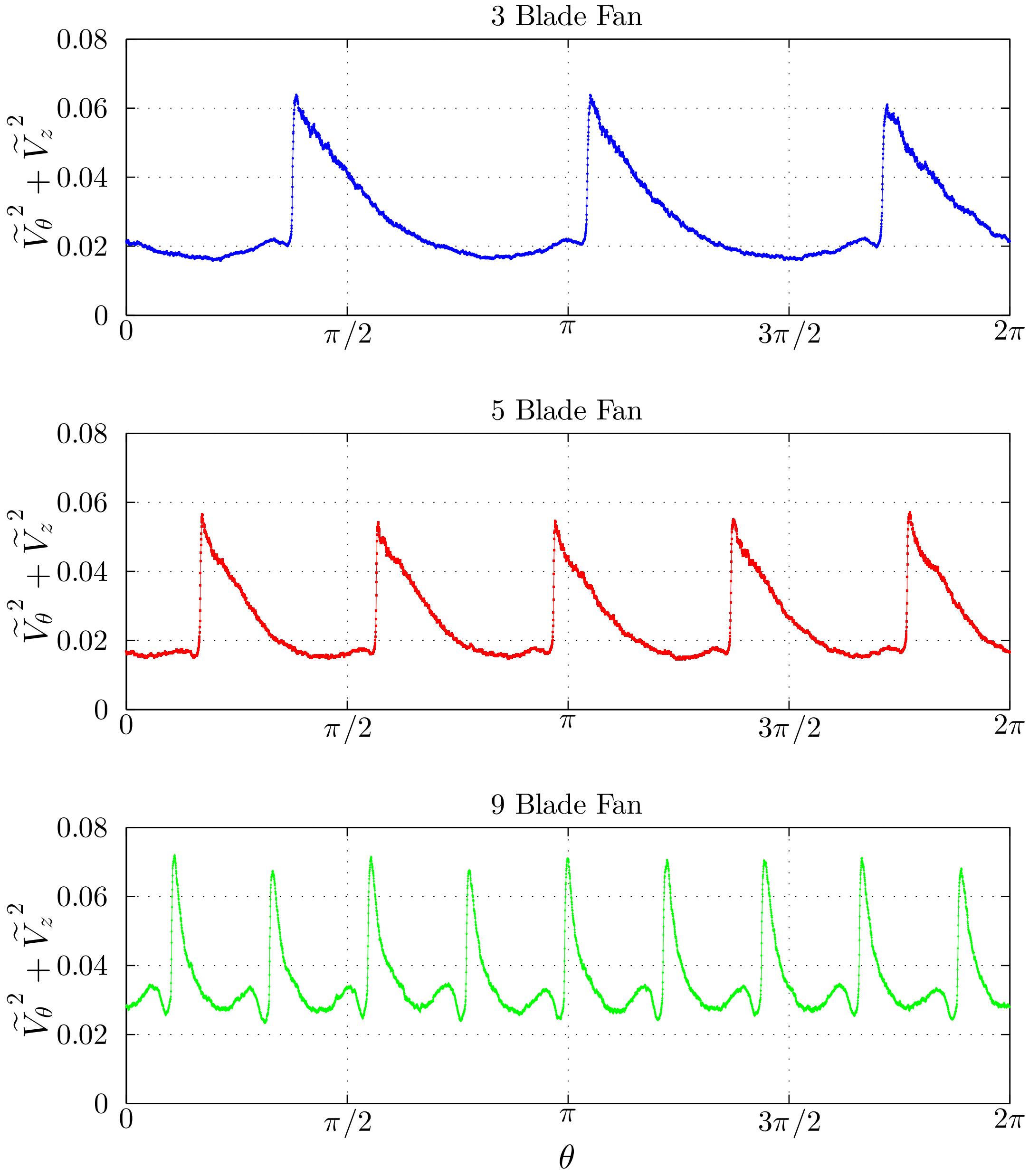

Figure 79 Case V turbulence kinetic energy at fan exit over $0 \leq \theta \leq 2\pi$

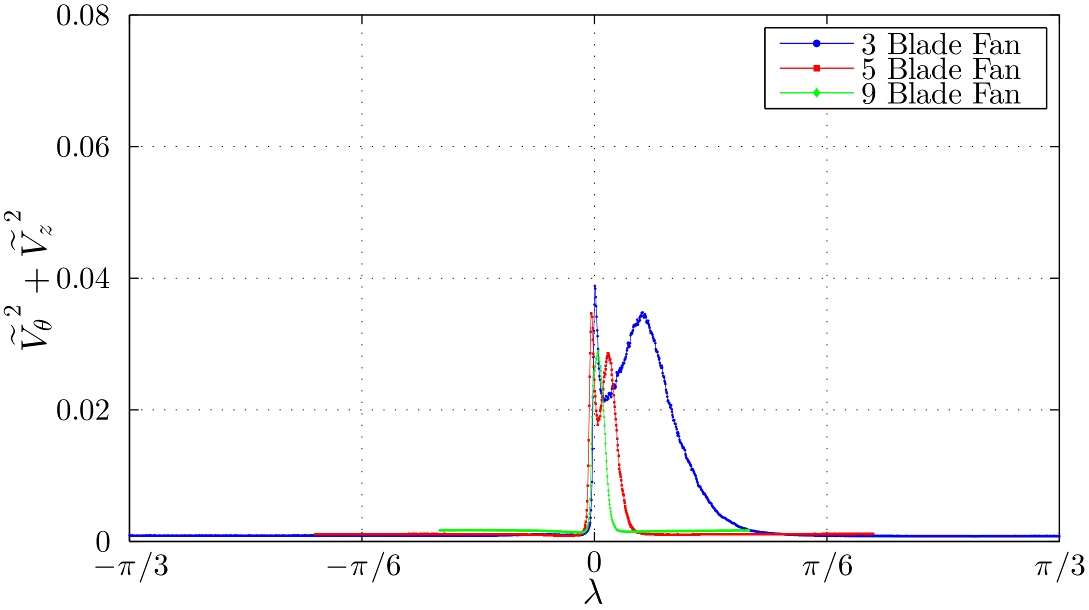

Figure 80 Case I turbulence kinetic energy at fan exit over λ_3

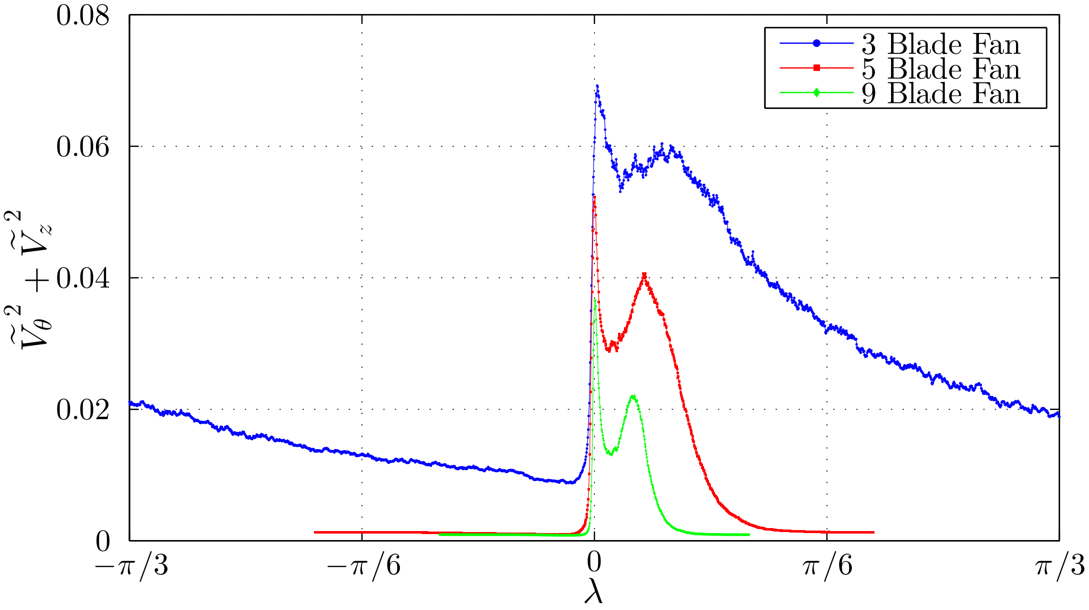

Figure 81 Case II turbulence kinetic energy at fan exit over λ_3

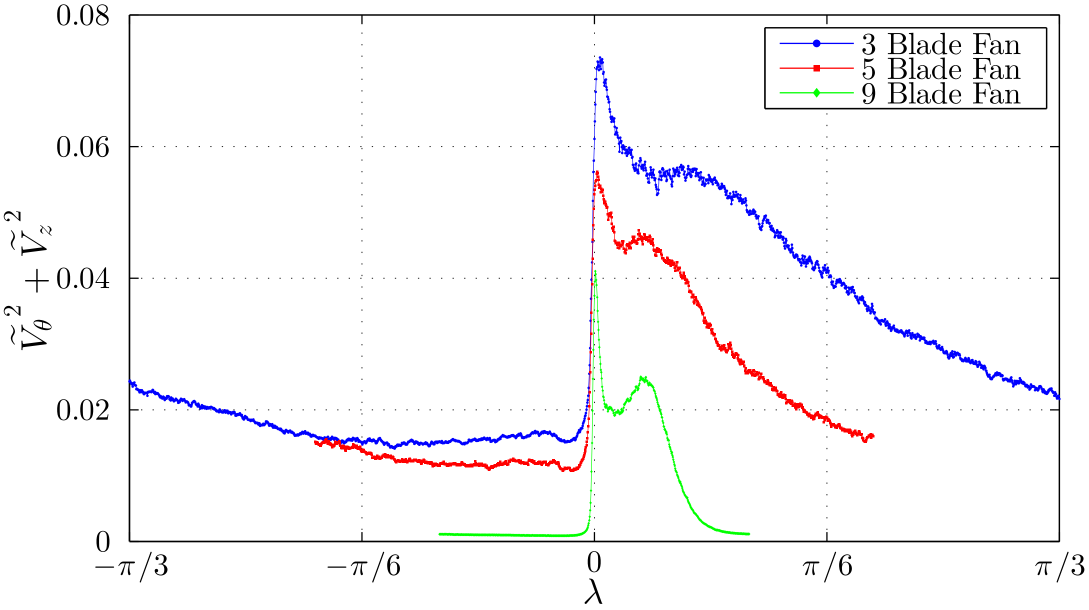

Figure 82 Case III turbulence kinetic energy at fan exit over λ_3

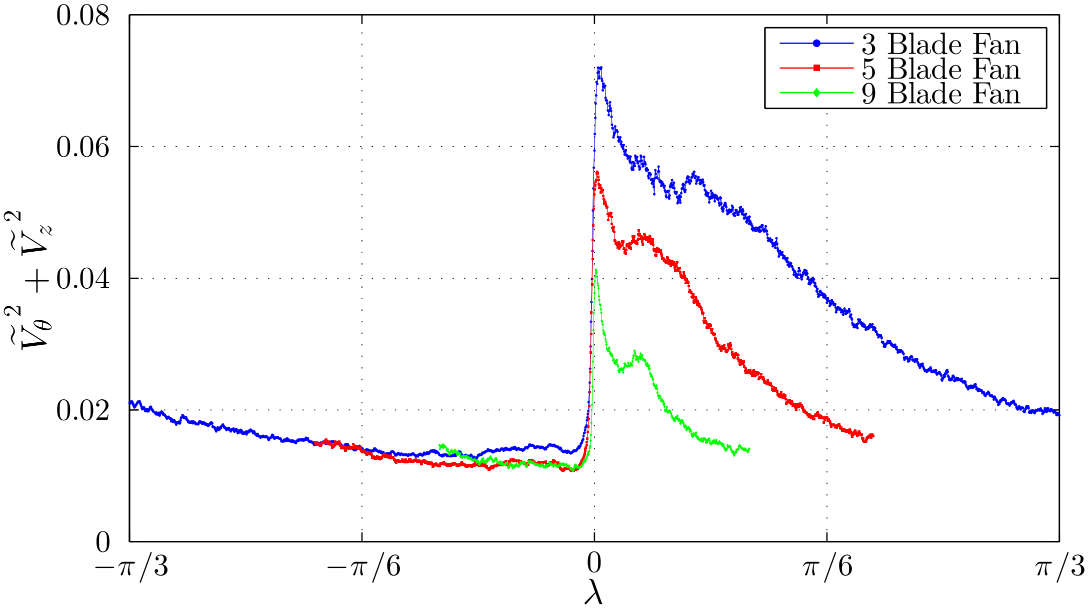

Figure 83 Case IV turbulence kinetic energy at fan exit over λ_3

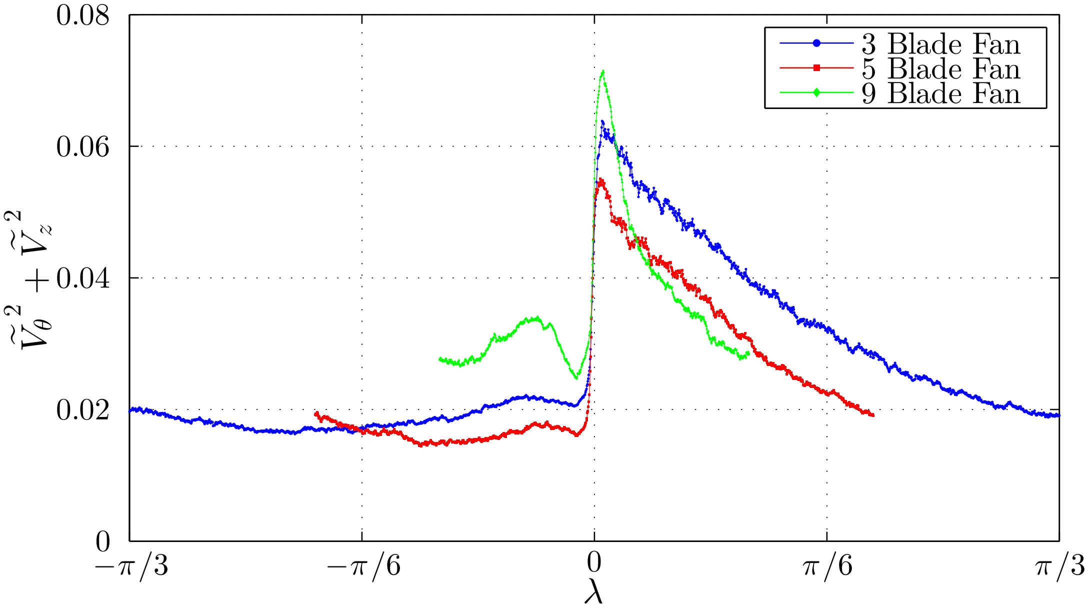

Figure 84 Case V turbulence kinetic energy at fan exit over λ_3

D REYNOLDS AVERAGED FORMULATIONS

The velocity data obtained in the present investigation have been processed to provide representative values for available terms in the Reynolds averaged momentum equations in cylindrical coordinates and the turbulence kinetic energy balance. A short introduction to these formulations is provided in the following section.

Measurements obtained in turbulent flows will have fluctuating and average statistical values that can be derived from the total sample. Equation (1) provides how the velocity vector and pressure field are separated into an averaged component, indicated by over-bars, and a fluctuating component, in lowercase. Traditionally experimental measurements for the average component for these quantities are obtained over time in a fixed position. As discussed in Section 3.3 a phase averaging scheme was utilized for these measurements to provide velocity statistics for all θ locations in the fan wake. This was found by building a time history for each discrete position from each revolution. It is convenient to consider these new equations in tensor notation for an intuitive understanding of the terms.

$$\underbrace{V_i = \overline{V_i} + v_i}_{\text{(A)}}\ ;\ \underbrace{P = \overline{P} + p'}_{\text{(B)}} \tag{1}$$

Substituting (1)(A) and (1)(B) into the momentum equation for constant viscosity and incompressible flow provides Equation (2) [Hinze (1975)]. Equations (3) and (4) are the θ and z momentum equations, respectively, derived from Equation (2). These equations have omitted radial velocity components which are negligible in the near wake of this fan [Neal (2010)]. Terms A, B, C, and D from Equations (3) and (4) have been evaluated with the measured from the wake velocity measurements. and are presented in the following section. A represents the advection of the θ–component momentum per unit mass. B represents the net normal Reynolds stress in θ. C represents the advection of the z–component momentum per unit mass. D represents the net Reynolds shear stress in the z–θ–plane.

$$\rho\left(\frac{\partial \overline{V_i}}{\partial t} + \overline{V_j} \cdot \frac{\partial \overline{V_i}}{\partial x_j}\right) = -\frac{\partial \overline{P}}{\partial x_i} + \frac{\partial}{\partial x_j}\left(\mu \frac{\partial \overline{V_i}}{\partial x_j} - \rho \overline{v_i' v_j'}\right) - \overline{F_i} \tag{2}$$

$$\underbrace{\overline{V}_\theta \frac{\partial \overline{V}_\theta}{r\partial\theta}}_{\text{A}} + \overline{V}_z \frac{\partial \overline{V}_\theta}{\partial z} = -\frac{\partial \overline{\boldsymbol{P}}}{r\partial\theta} + \tau_{viscous} - \rho\Big(\underbrace{\frac{\partial}{r\partial\theta}\overline{V_\theta'^2}}_{\text{B}} + \frac{\partial}{\partial z}\overline{V_z' V_\theta'}\Big) \tag{3}$$

$$\underbrace{\overline{V}_\theta \frac{\partial \overline{V}_z}{r\partial\theta}}_{\text{C}} + \overline{V}_z \frac{\partial \overline{V}_z}{\partial z} = -\frac{\partial \overline{\boldsymbol{P}}}{\partial z} + \tau_{viscous} - \rho\Big(\frac{\partial}{r\partial\theta}\overline{V_\theta'^2} + \underbrace{\frac{\partial}{\partial z}\overline{V_z' V_\theta'}}_{\text{D}}\Big) \tag{4}$$

Equation (5) provides the balance of turbulence kinetic energy [Hinze (1975)] ; where q represents turbulent kinetic energy. This steady flow will set the left hand side of Equation (5) to zero. The turbulence kinetic energy production term: E, has been evaluated with the wake velocity measurements considering $x_i = \hat{\boldsymbol{r}} + \hat{\boldsymbol{\theta}} + \hat{\boldsymbol{z}}$. These results are provided in the following section.

$$\frac{\partial\overline{q^2}}{\partial t} = -\overline{V}_j\frac{\partial\overline{q^2}}{\partial x_j} + -\frac{\partial}{\partial x_i}\overline{v_i(\frac{p'}{\rho} + \frac{q^2}{2})} - \underbrace{\overline{v_i v_j}\frac{\partial\overline{V_j}}{\partial x_i}}_{\text{E}} + \nu\frac{\partial}{\partial x_i}\overline{v_i(\frac{\partial v_i}{\partial x_j} + \frac{\partial v_j}{\partial x_i})} - \nu\overline{(\frac{\partial v_i}{\partial x_j} + \frac{\partial v_j}{\partial x_i})\frac{\partial v_j}{\partial x_i}} \tag{5}$$

This section contains the entire collection of figures that were generated for the Reynolds averaged terms identified in Equations (3), (4), and (5). The derivatives in the azimuthal direction were evaluated with a central differencing scheme provided by Equation (6). $\Delta\theta$ is given by the "bin" size from the phase averaging scheme $(0.06^\circ * {}^{\pi}/_{180})$ *radians*. (Section 3.3) All of these terms were evaluated non-dimensionally. Therefore C, and D from Equations (3) and (4), are kinematic in the data presented. The radius at mid-span used in the derivative in the theta direction was made non-dimensional by the tip radius: $\overline{r} = {}^{r_{mid-span}}/_{r_{tip}}$. The following pages include all of the evaluated values for the parameters in Equation (7) from Equations (3–5).

$$\frac{\partial}{\overline{r}\partial\theta}f(\theta) = \frac{f(\theta + \Delta\theta) - f(\theta - \Delta\theta)}{\overline{r}2\Delta\theta} \tag{6}$$

$$\underbrace{V_\theta^*\frac{\partial V_\theta^*}{\overline{r}\partial\theta}}_{\text{A}}\ ;\ \underbrace{\frac{\partial}{\overline{r}\partial\theta}\widetilde{V}_\theta^2}_{\text{B}}\ ;\ \underbrace{V_\theta^*\frac{\partial V_z^*}{\overline{r}\partial\theta}}_{\text{C}}\ ;\ \underbrace{\frac{\partial}{\overline{r}\partial\theta}\overline{V_\theta' V_z'}/V_{tip}^2}_{\text{D}}\ ;\ \underbrace{(\overline{V_z' V_\theta'}/V_{tip}^2)\frac{\partial V_z^*}{\overline{r}\partial\theta}}_{\text{E}} \tag{7}$$

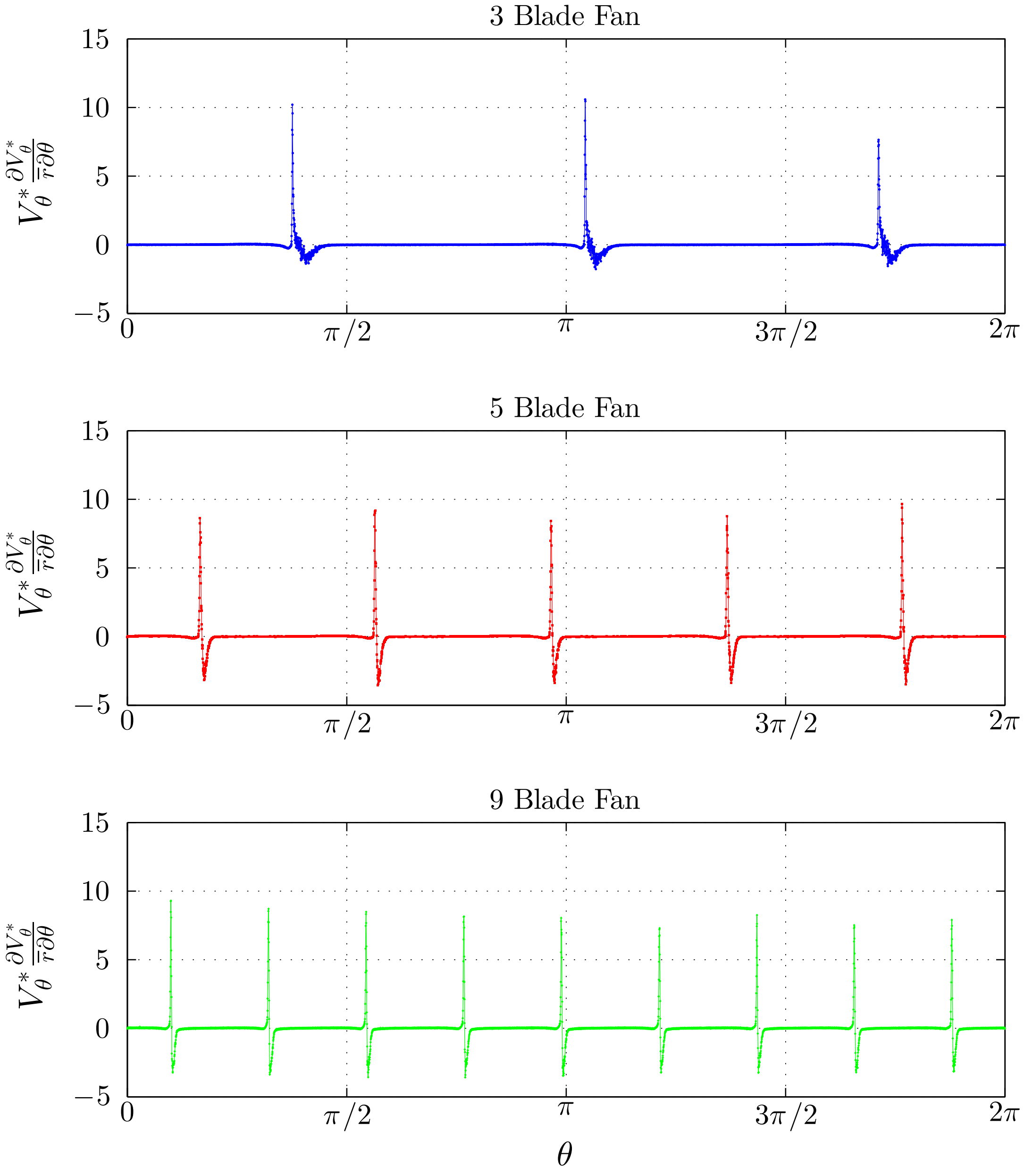

Figure 85 Case I advection of θ–component momentum per unit mass over $0 \leq \theta \leq 2\pi$

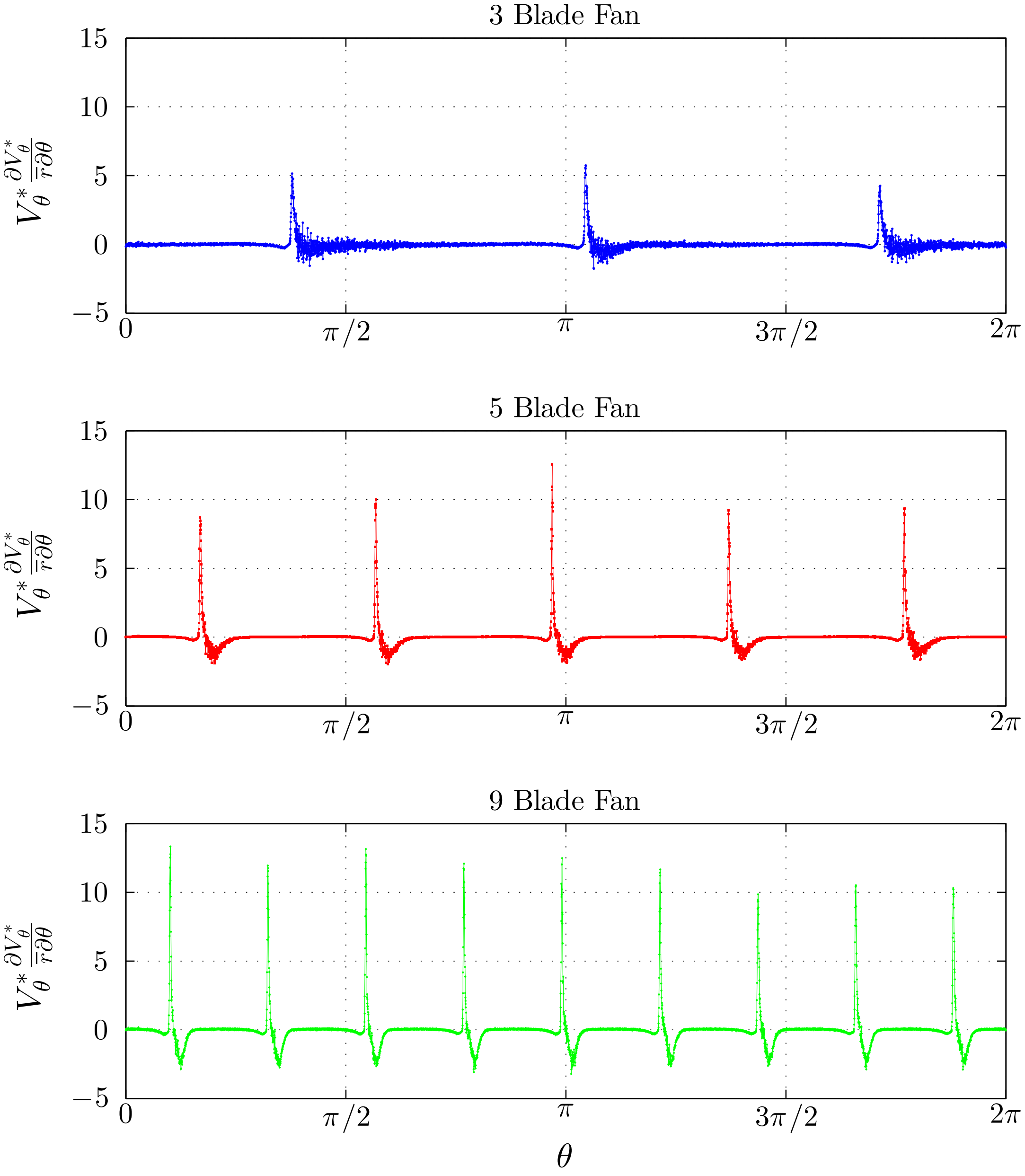

Figure 86 Case II advection of θ–component momentum per unit mass over $0 \leq \theta \leq 2\pi$

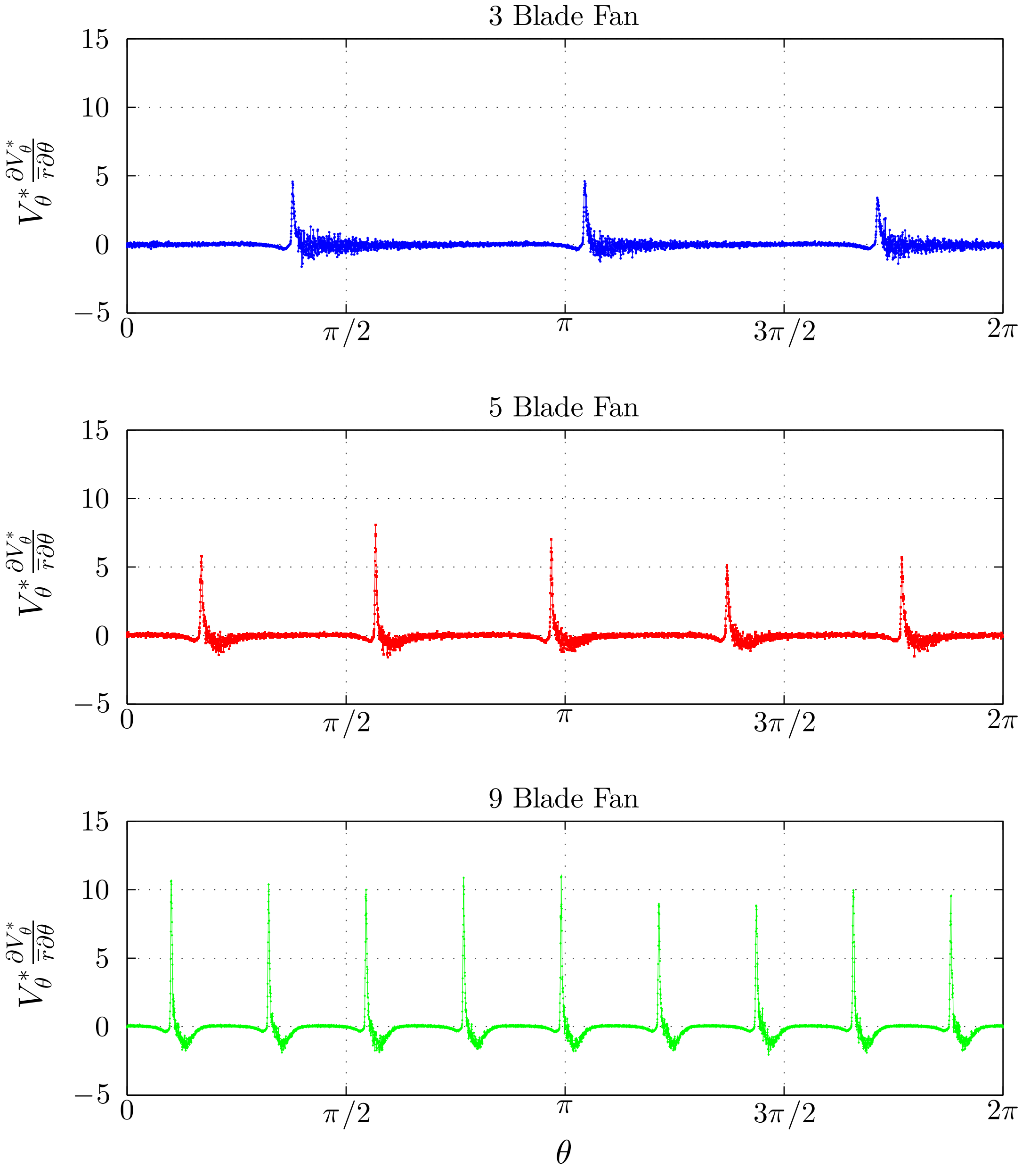

Figure 87 Case III advection of θ–component momentum per unit mass over $0 \leq \theta \leq 2\pi$

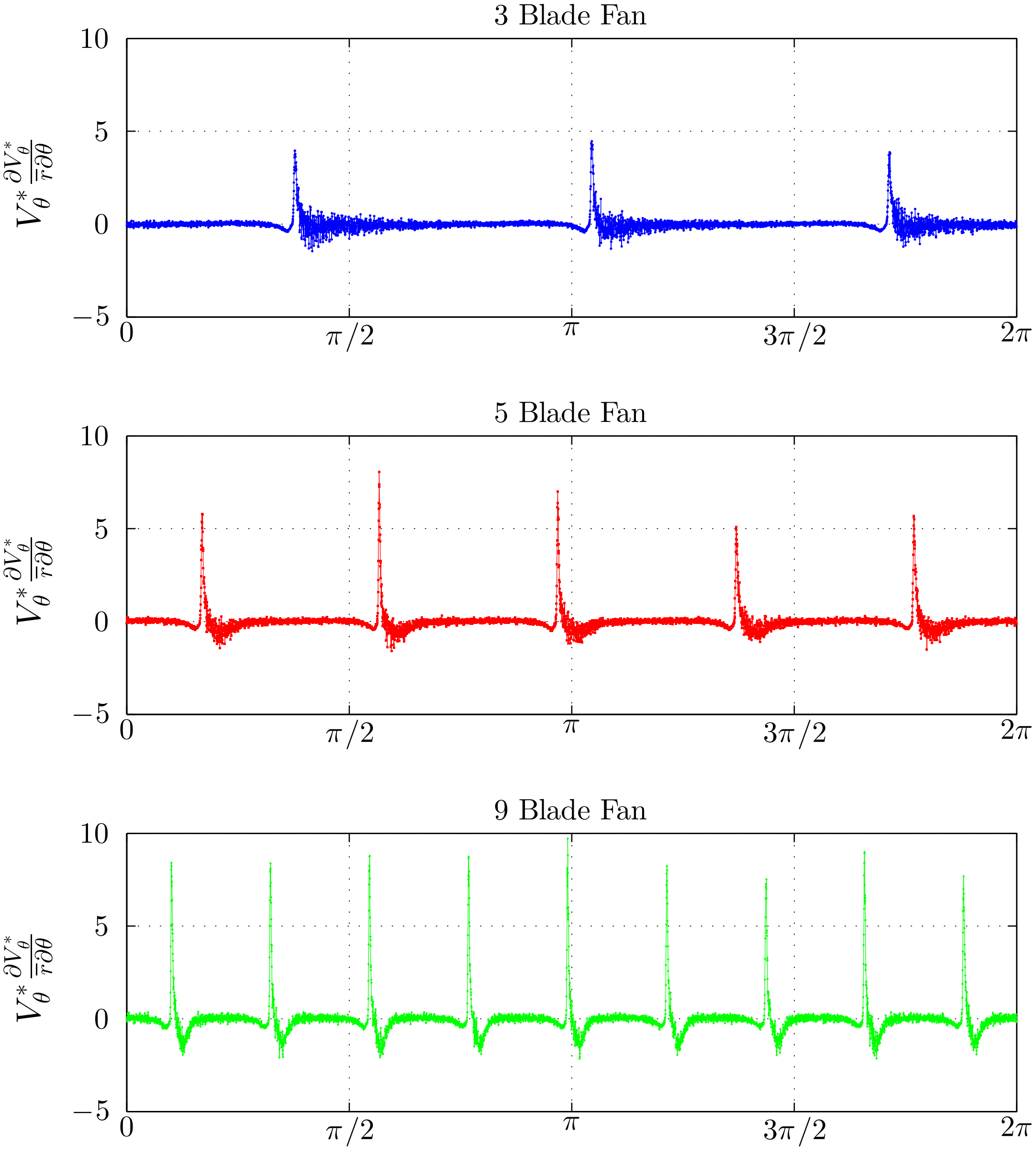

Figure 88 Case IV advection of θ–component momentum per unit mass over $0 \leq \theta \leq 2\pi$

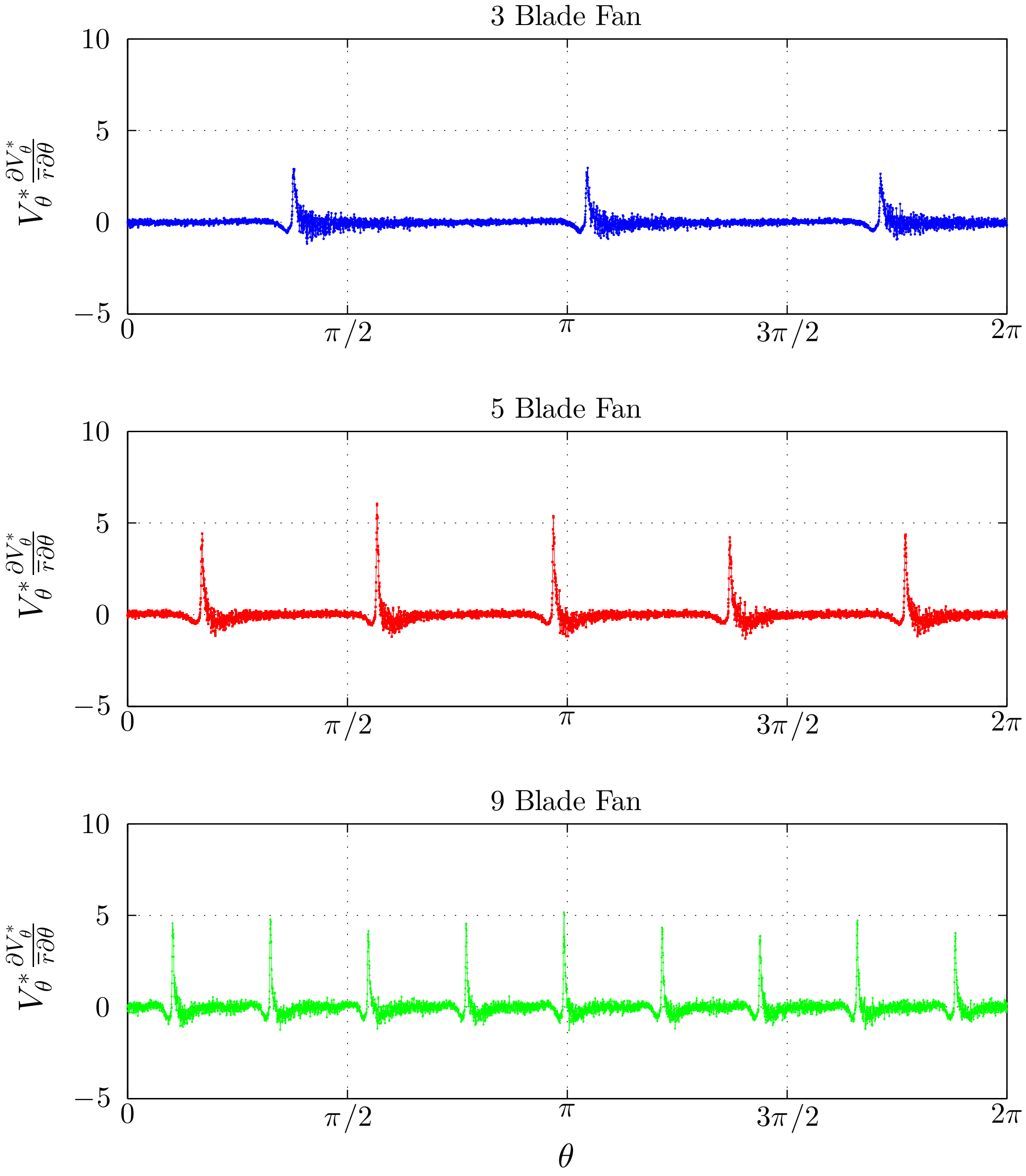

Figure 89 Case V advection of θ–component momentum per unit mass over $0 \leq \theta \leq 2\pi$

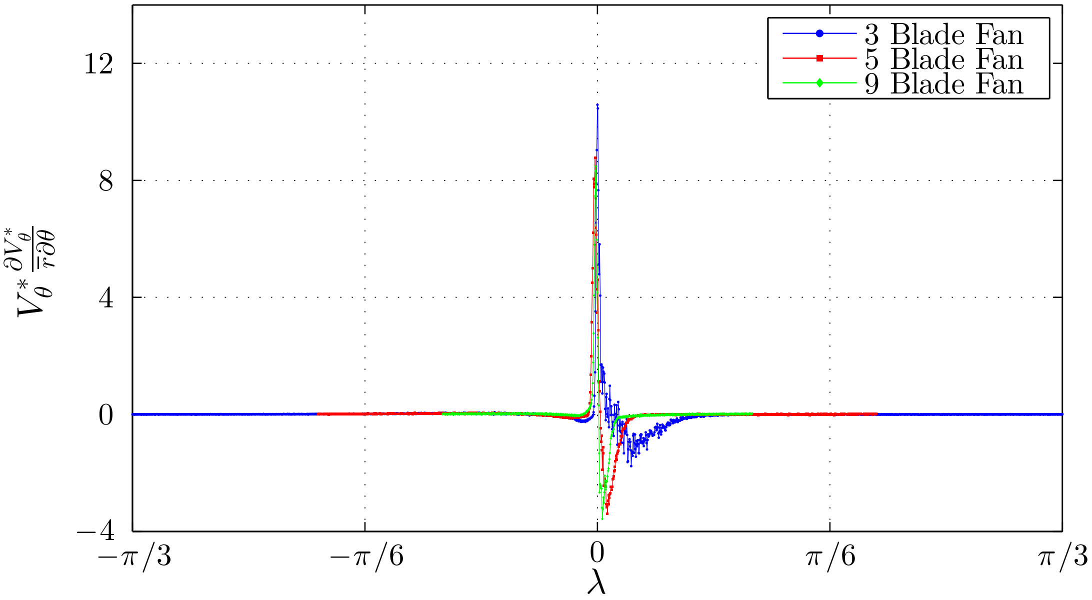

Figure 90 Case I advection of θ–component momentum per unit mass over λ_3

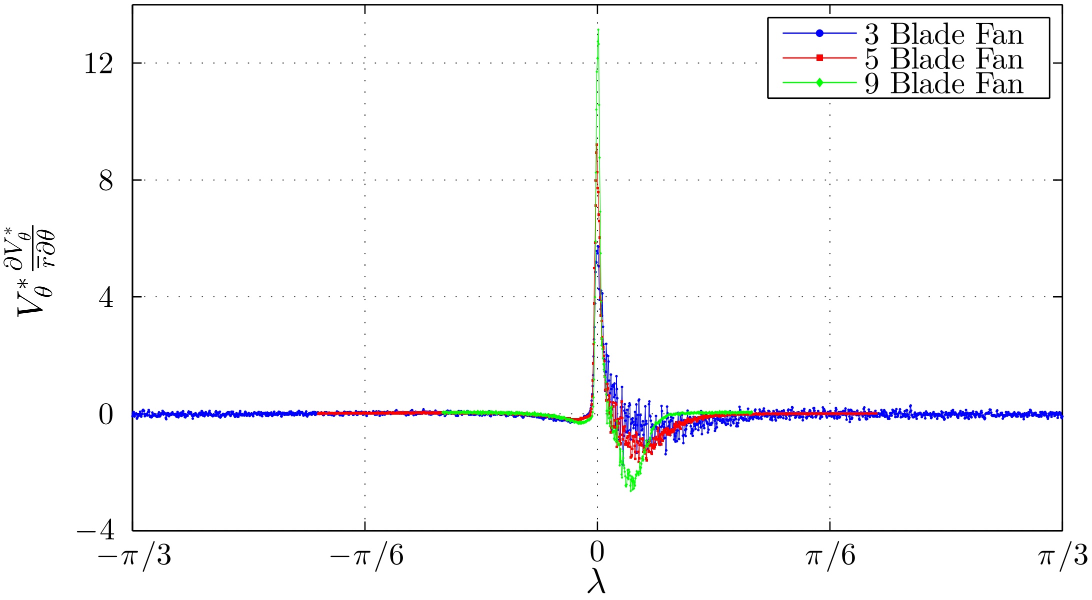

Figure 91 Case II advection of θ–component momentum per unit mass over λ_3

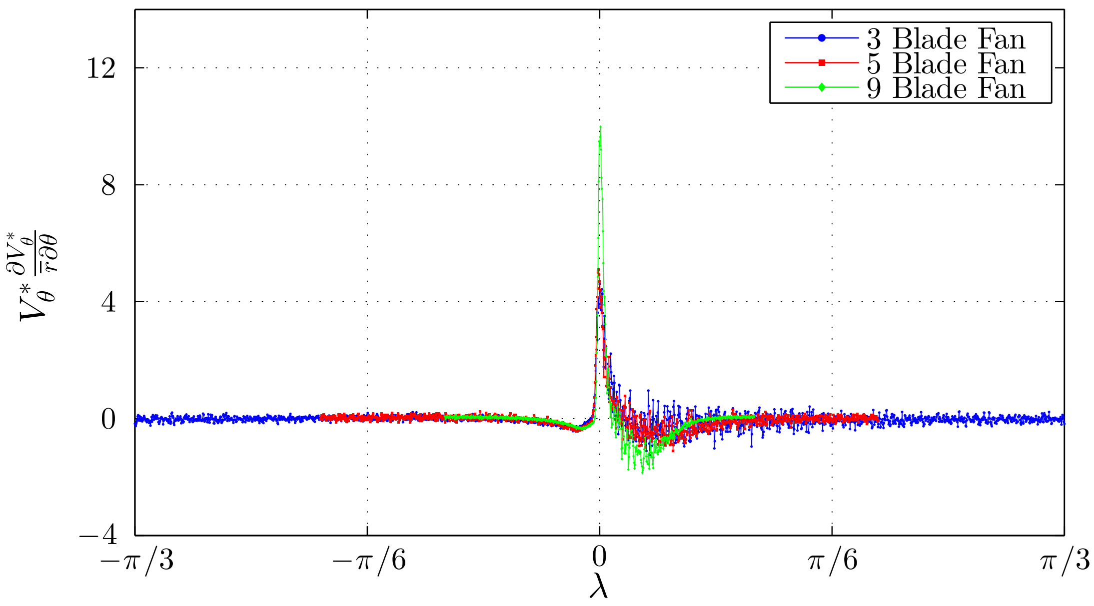

Figure 92 Case III advection of θ–component momentum per unit mass over λ_3

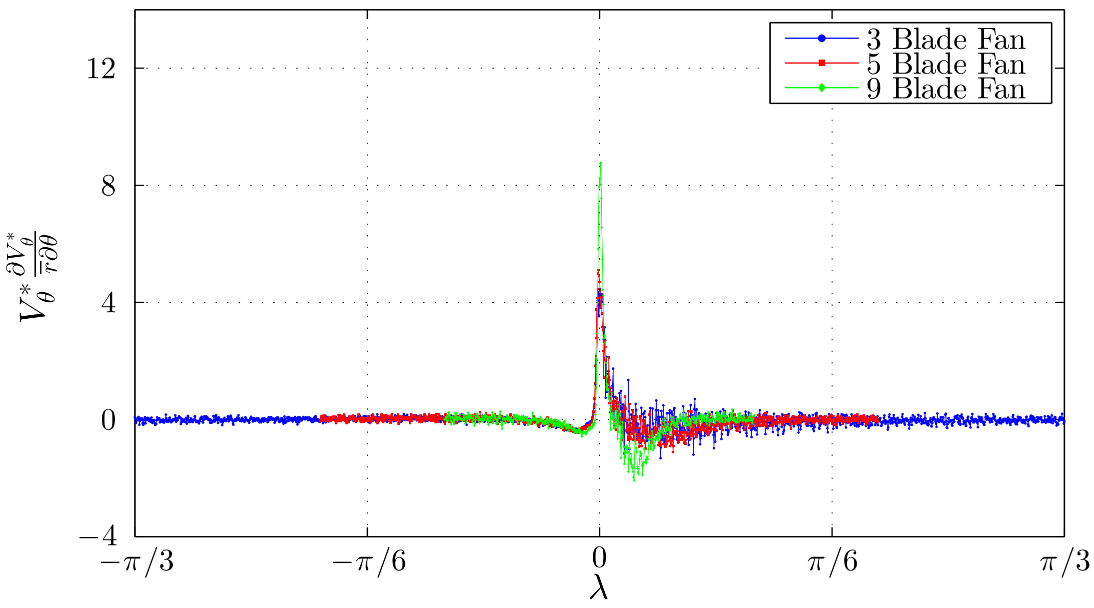

Figure 93 Case IV advection of θ–component momentum per unit mass over λ_3

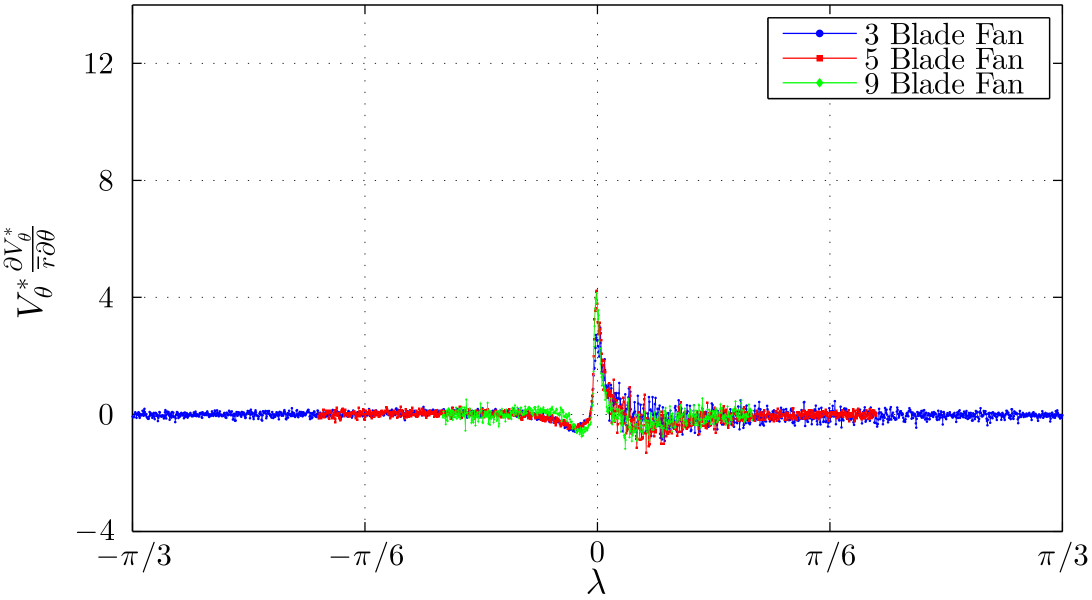

Figure 94 Case V advection of θ–component momentum per unit mass over λ_3

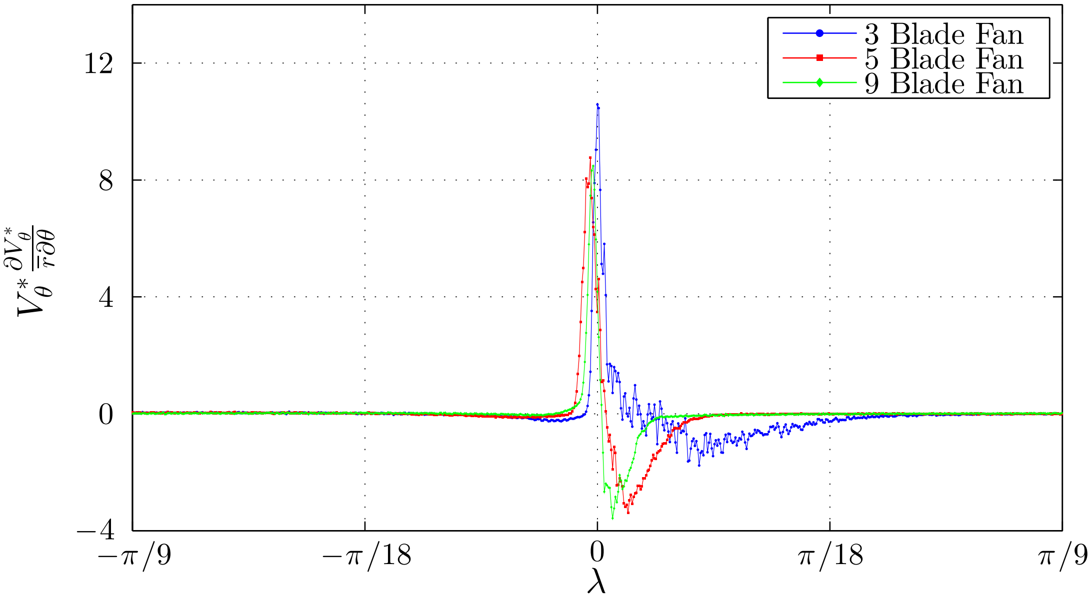

Figure 95 Case I advection of θ–component momentum per unit mass over λ_9

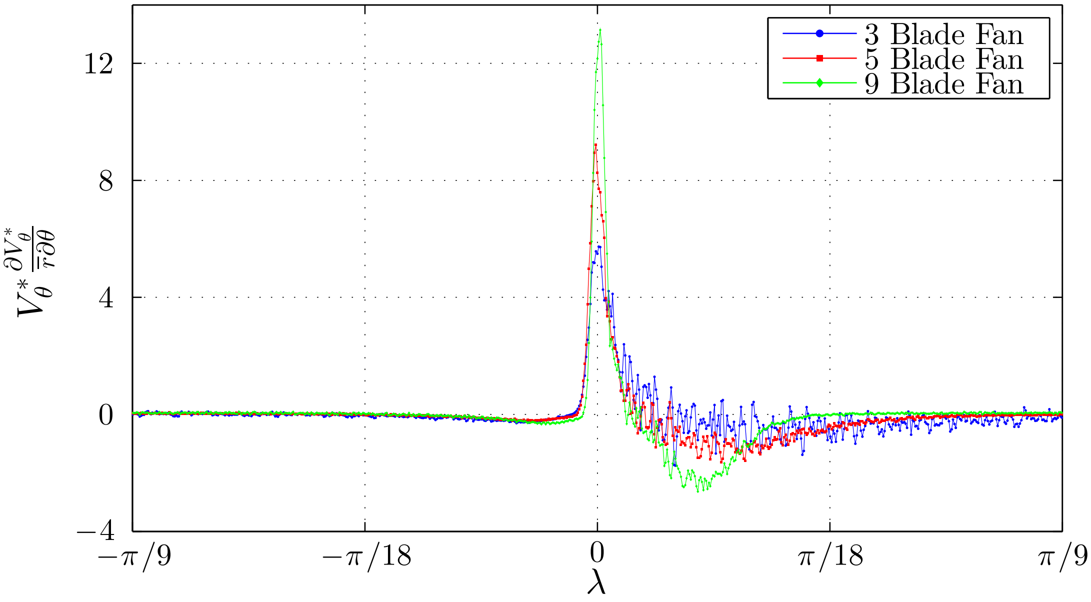

Figure 96 Case II advection of θ–component momentum per unit mass over λ_9

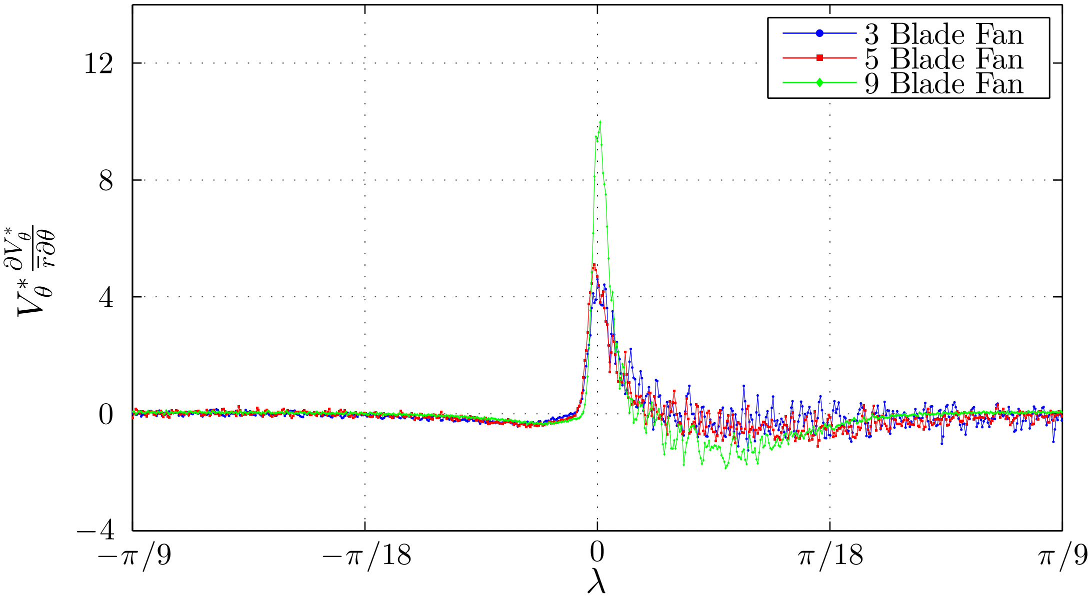

Figure 97 Case III advection of θ–component momentum per unit mass over λ_9

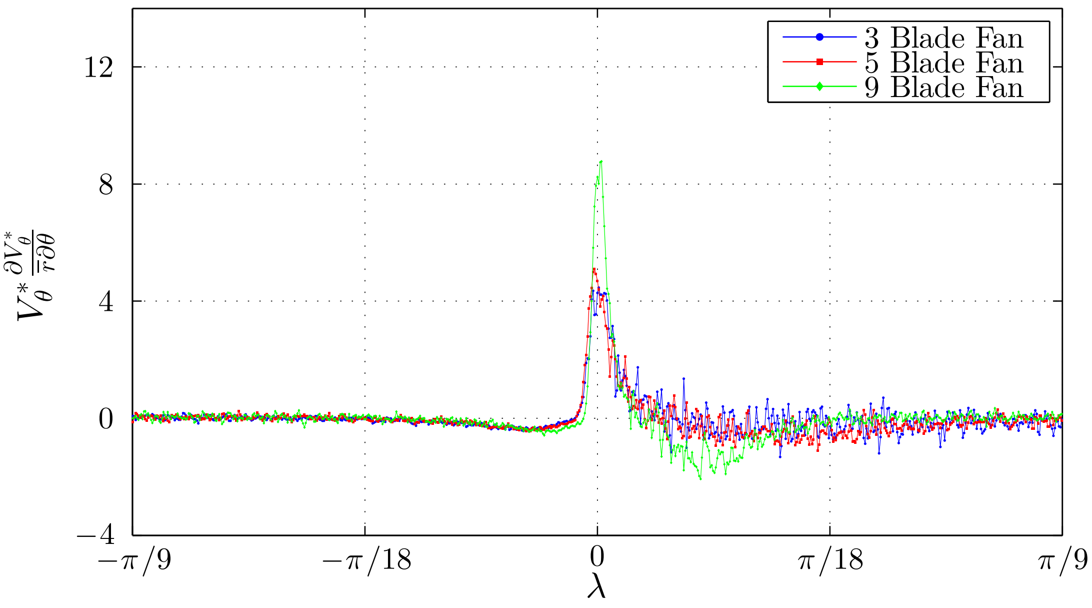

Figure 98 Case IV advection of θ–component momentum per unit mass over λ_9

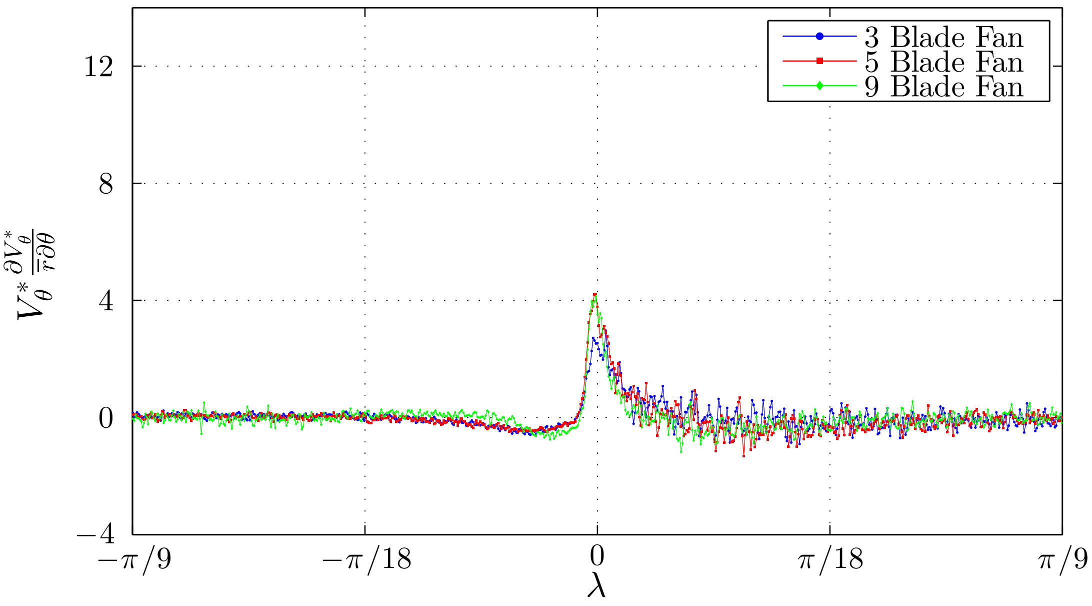

Figure 99 Case V advection of θ–component momentum per unit mass over λ_9

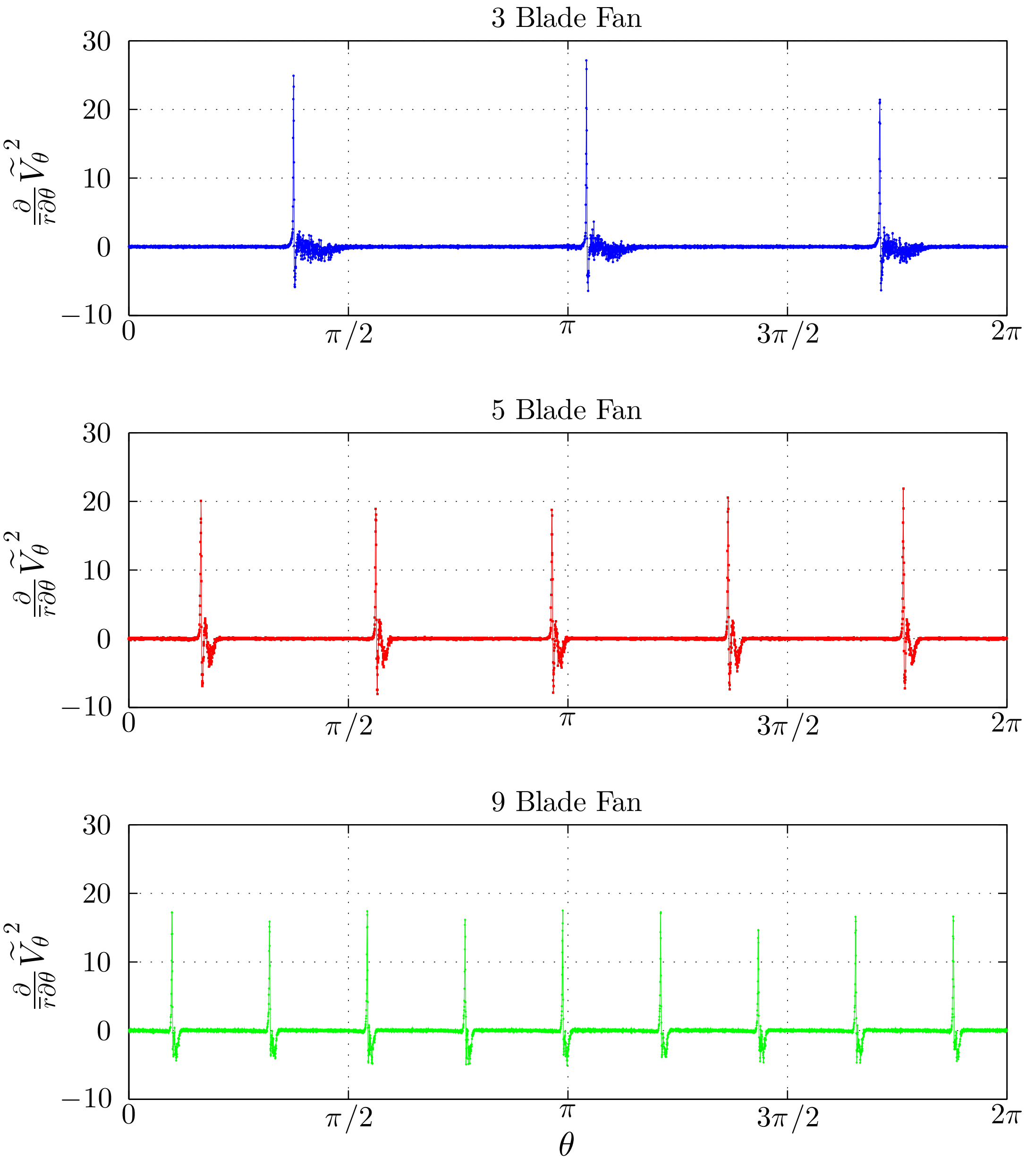

Figure 100 Case I net Reynolds normal stress in θ over $0 \leq \theta \leq 2\pi$

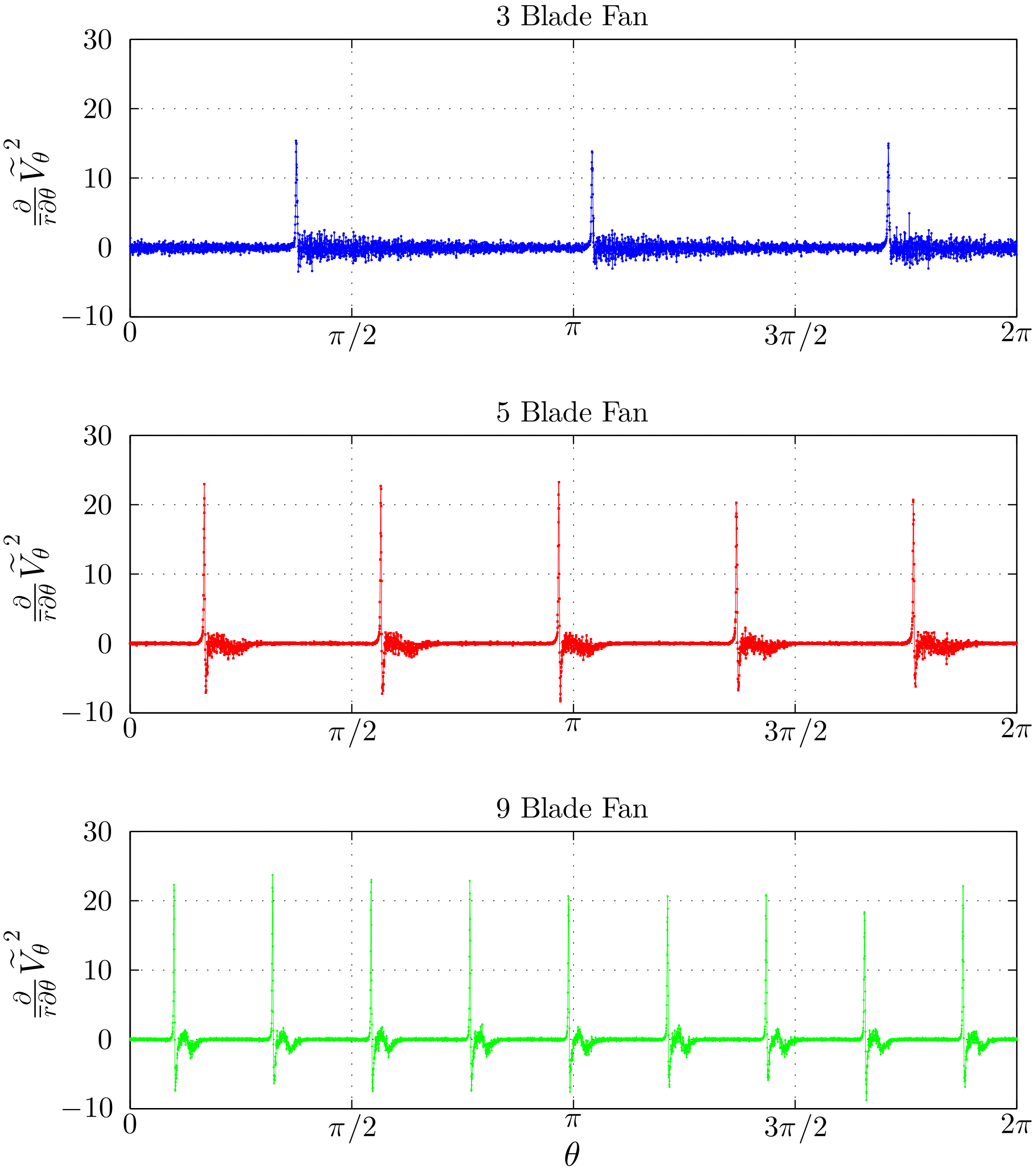

Figure 101 Case II net Reynolds normal stress in θ over $0 \leq \theta \leq 2\pi$

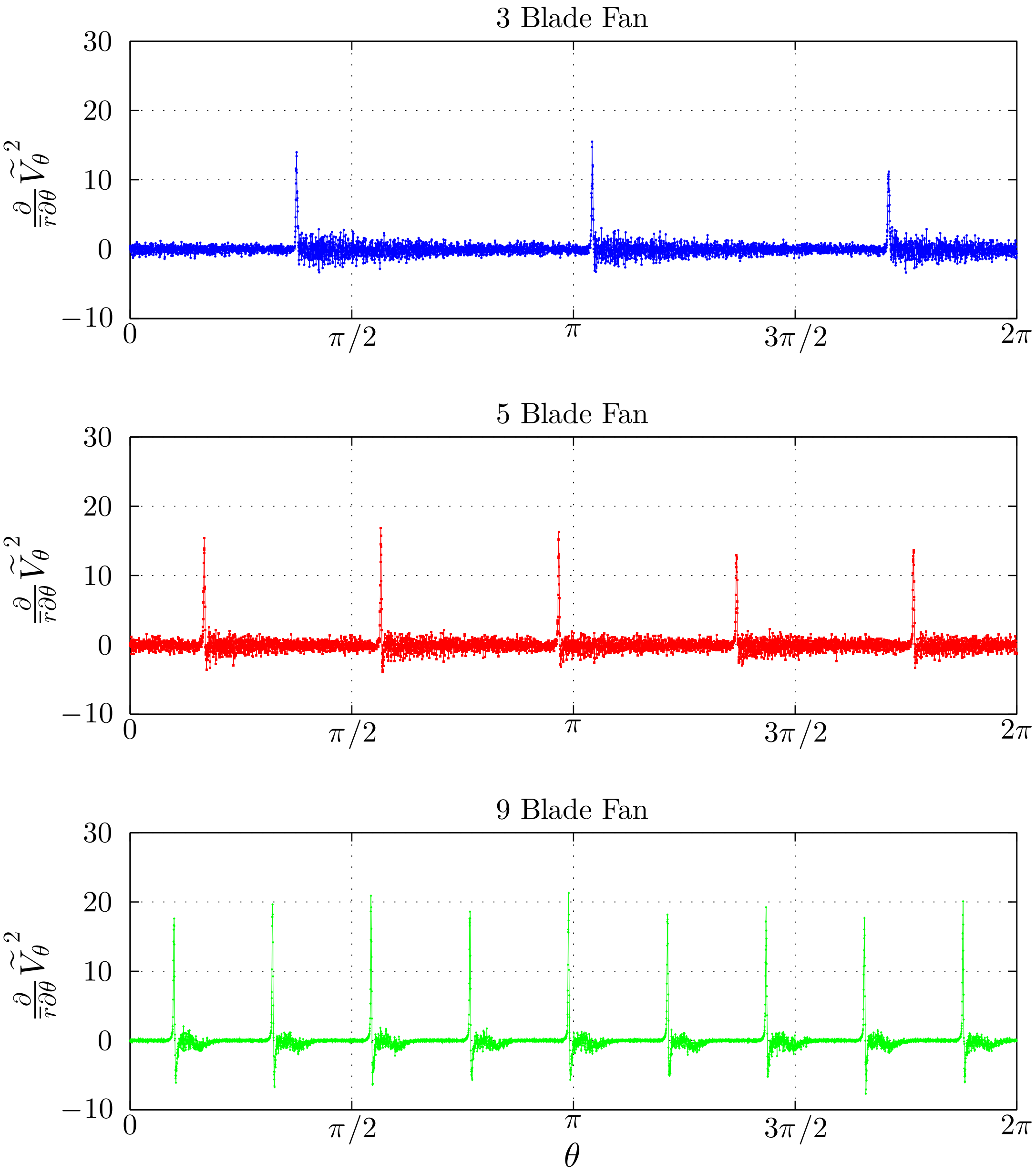

Figure 102 Case III net Reynolds normal stress in θ over $0 \leq \theta \leq 2\pi$

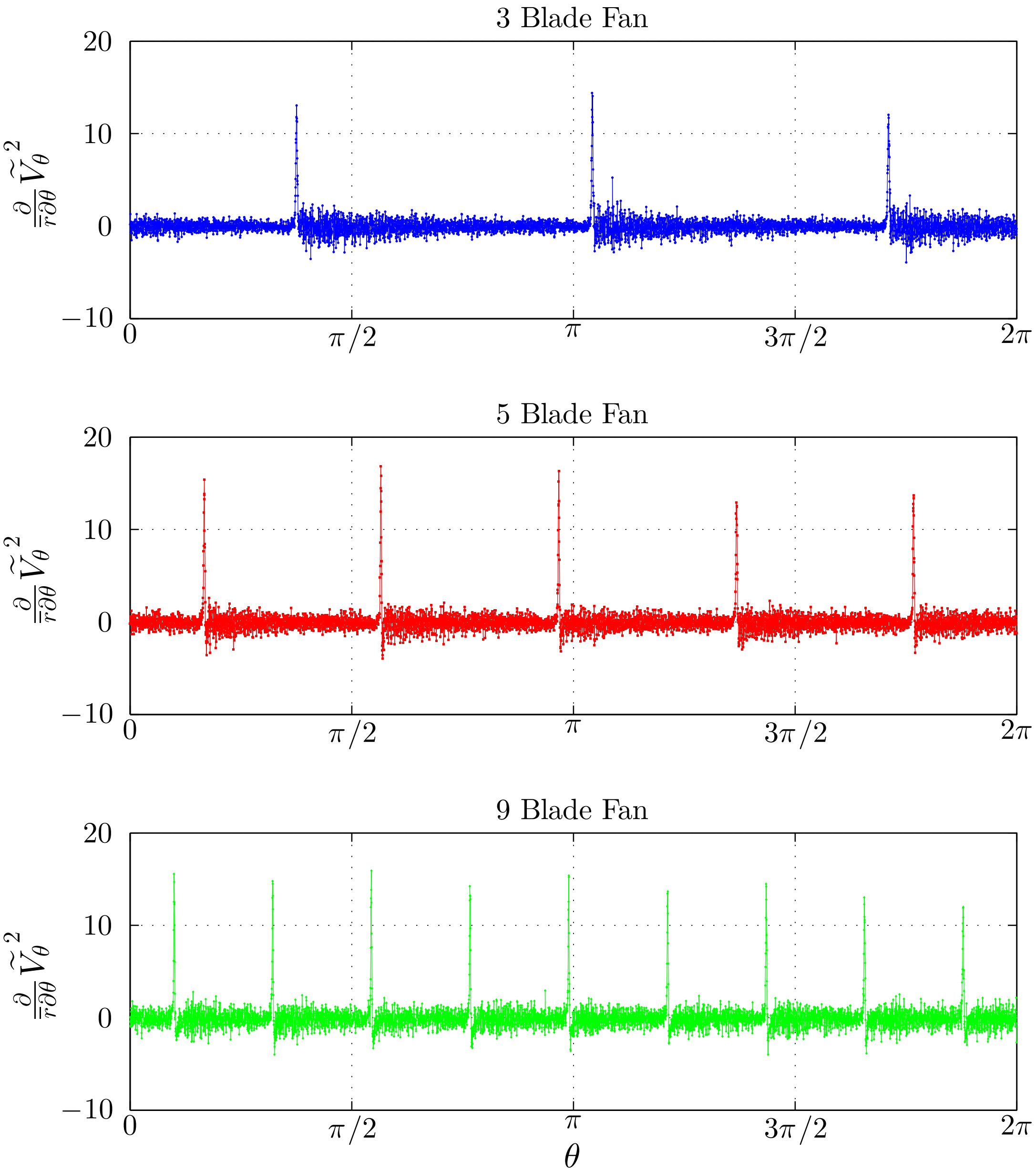

Figure 103 Case IV net Reynolds normal stress in θ over $0 \leq \theta \leq 2\pi$

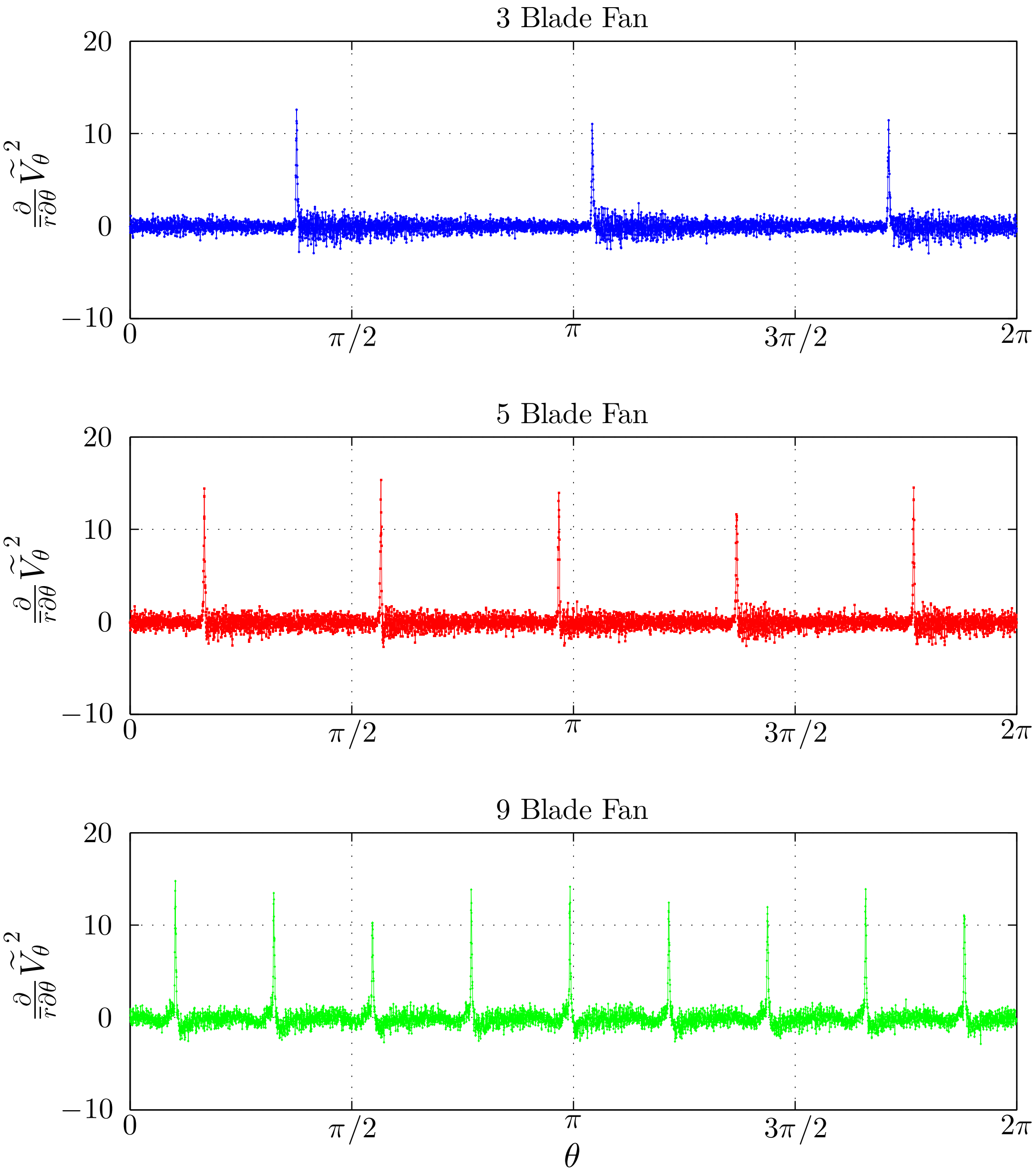
3 Blade Fan

5 Blade Fan

9 Blade Fan

Figure 104 Case V net Reynolds normal stress in θ over $0 \leq \theta \leq 2\pi$

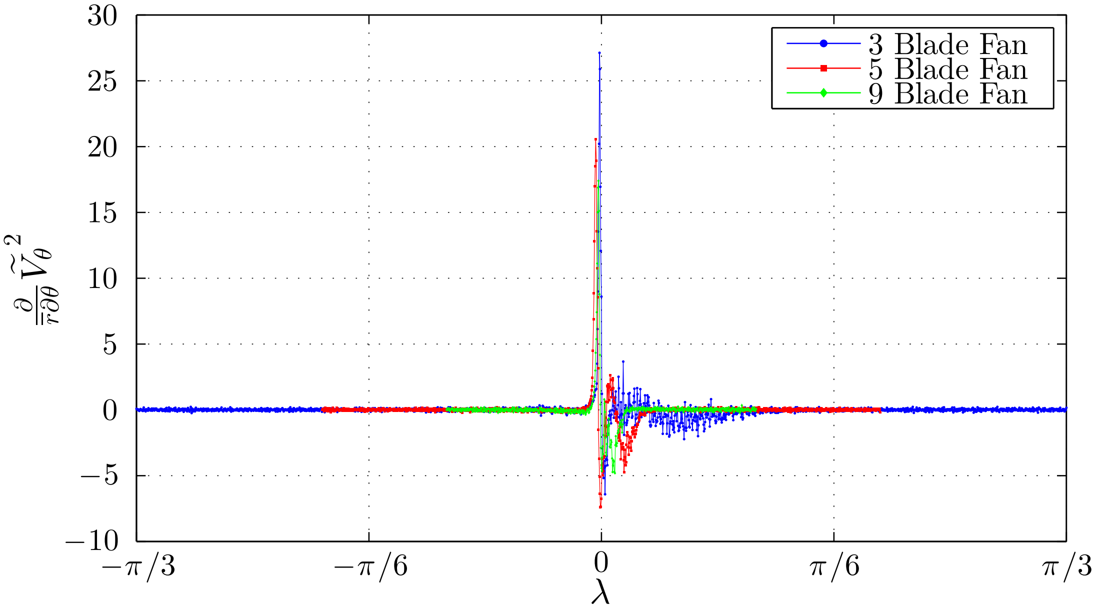

Figure 105 Case I net Reynolds normal stress in θ over λ_3

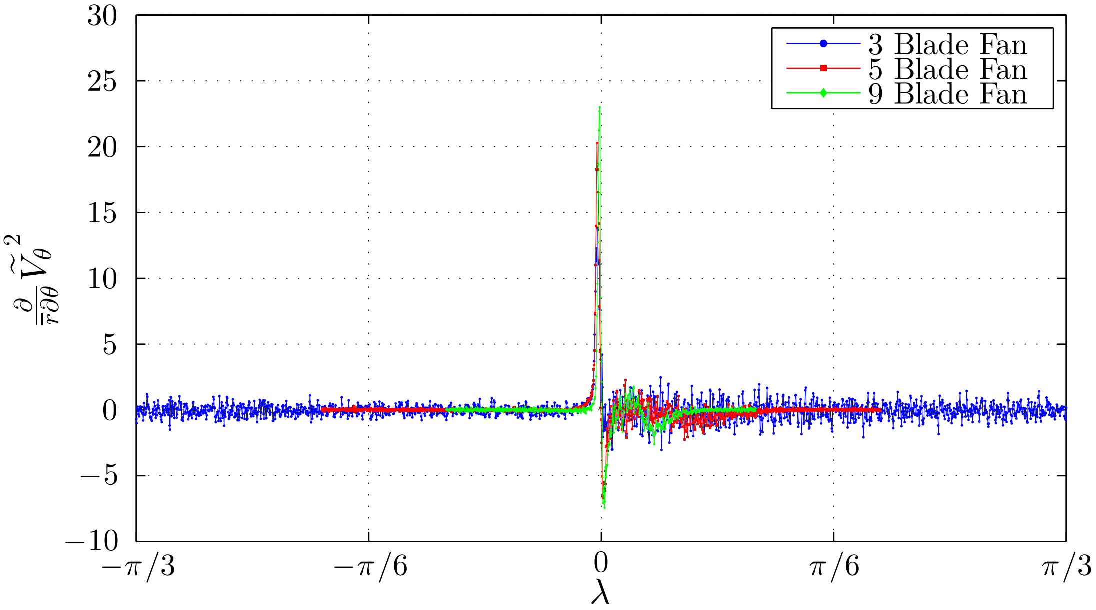

Figure 106 Case II net Reynolds normal stress in θ over λ_3

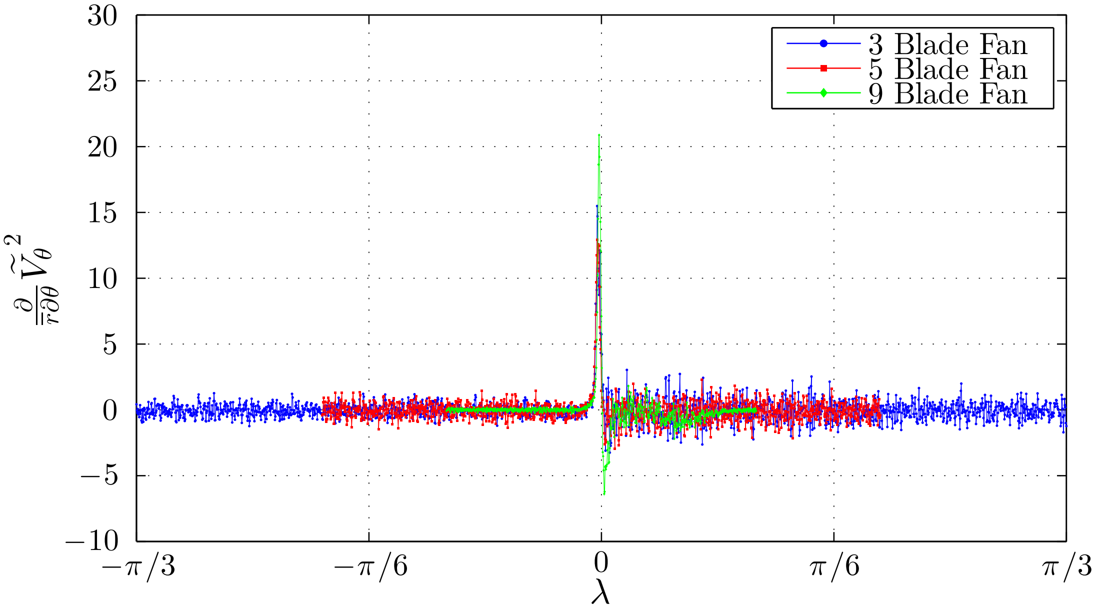

Figure 107 Case III net Reynolds normal stress in θ over λ_3

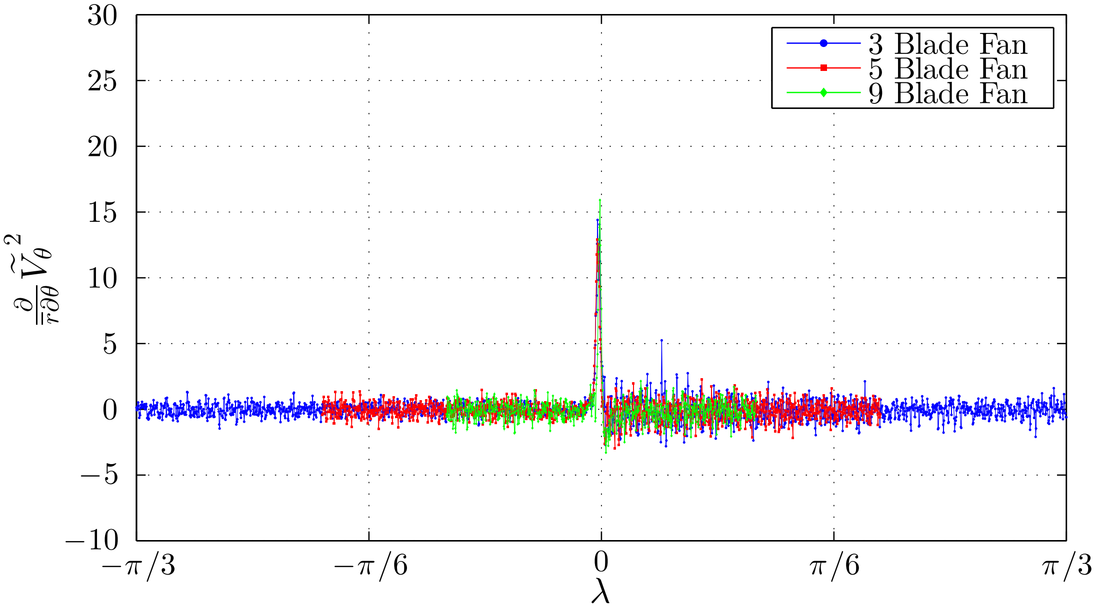

Figure 108 Case IV net Reynolds normal stress in θ over λ_3

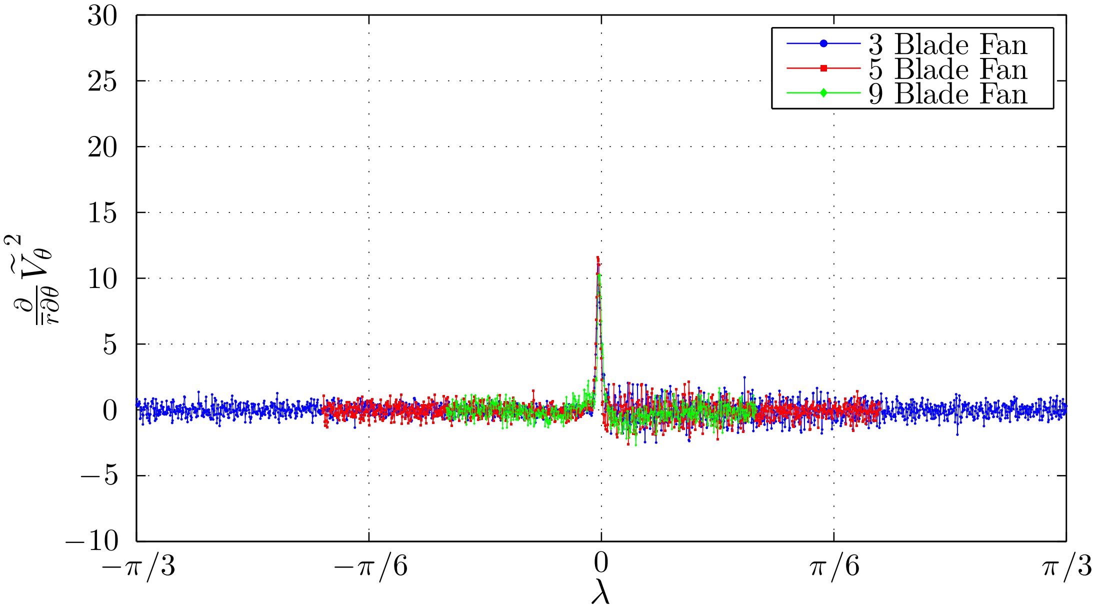

Figure 109 Case V net Reynolds normal stress in θ over λ_3

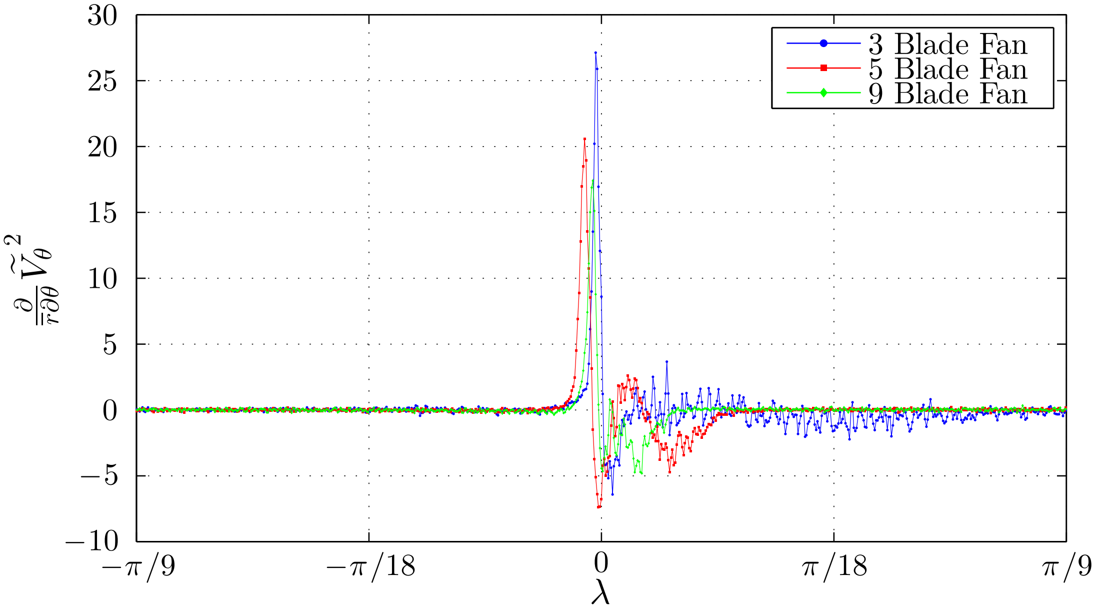

Figure 110 Case I net Reynolds normal stress in θ over λ_9

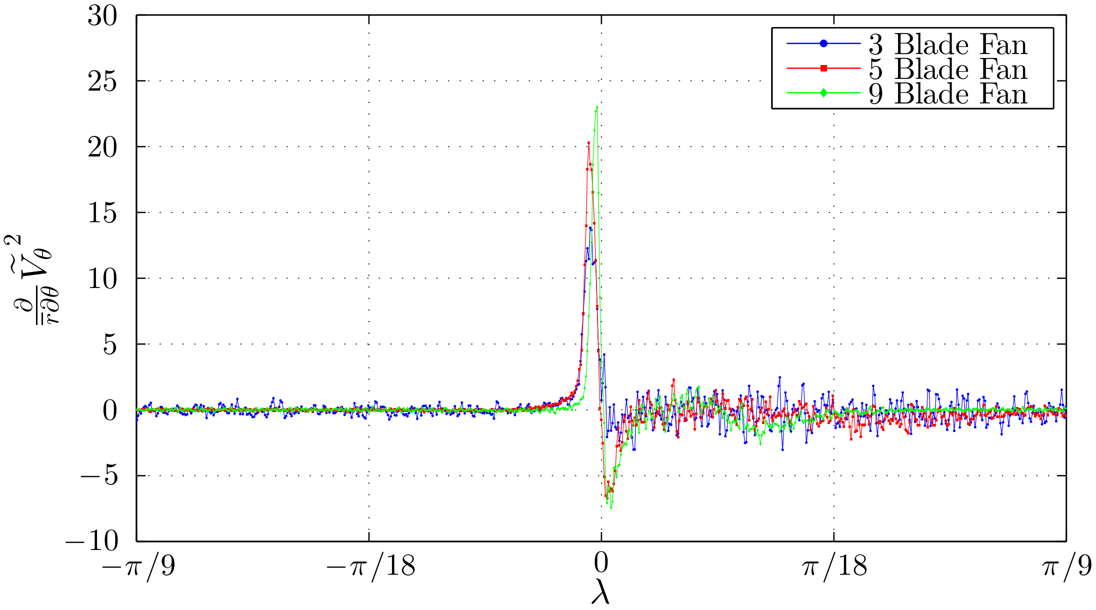

Figure 111 Case II net Reynolds normal stress in θ over λ_9

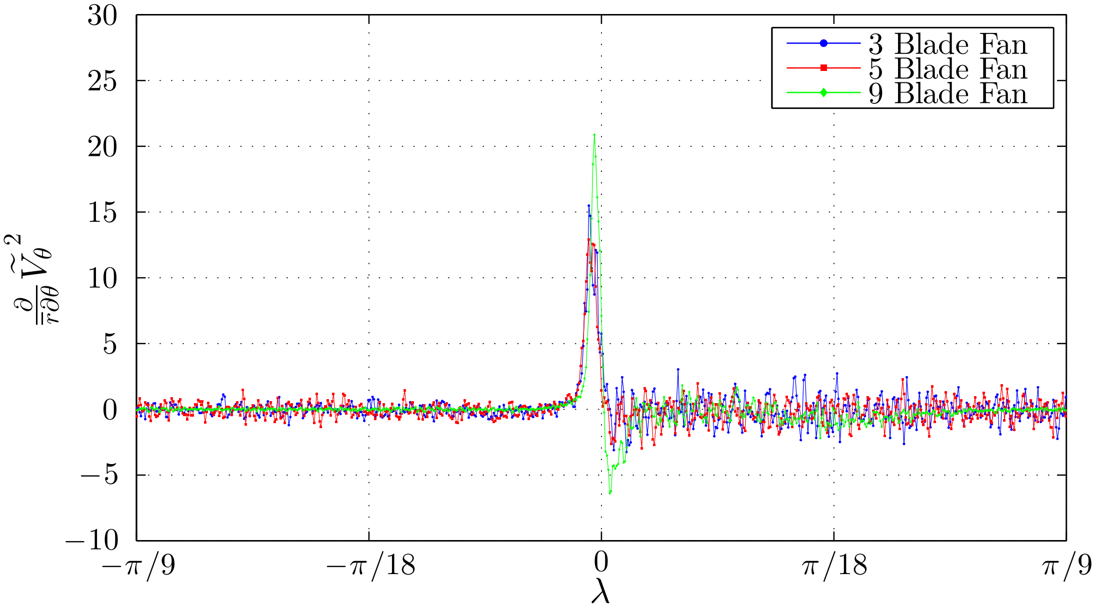

Figure 112 Case III net Reynolds normal stress in θ over λ_9

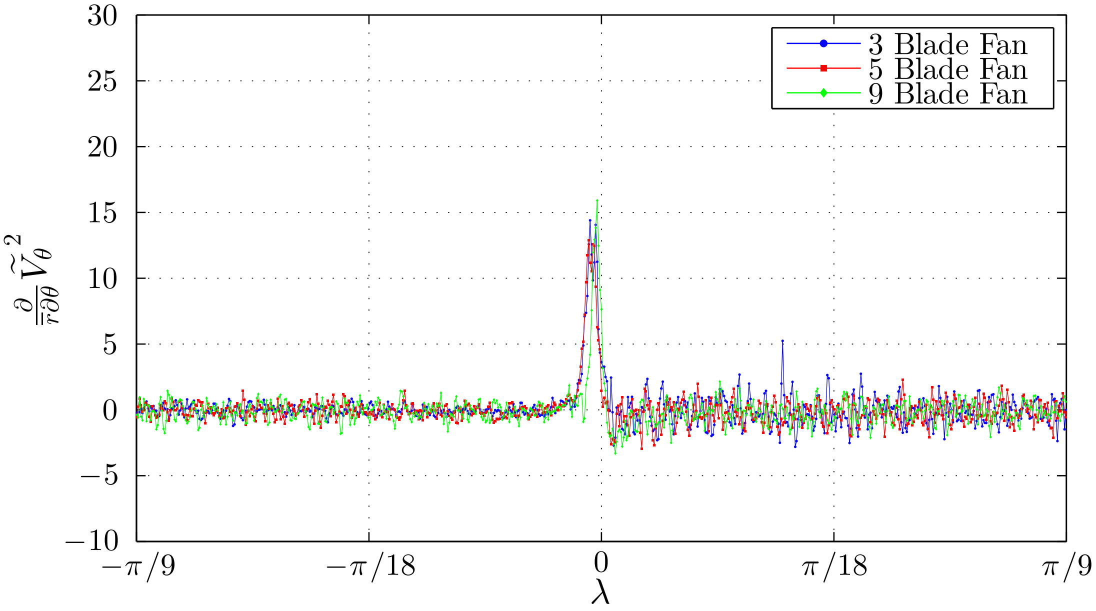

Figure 113 Case IV net Reynolds normal stress in θ over λ_9

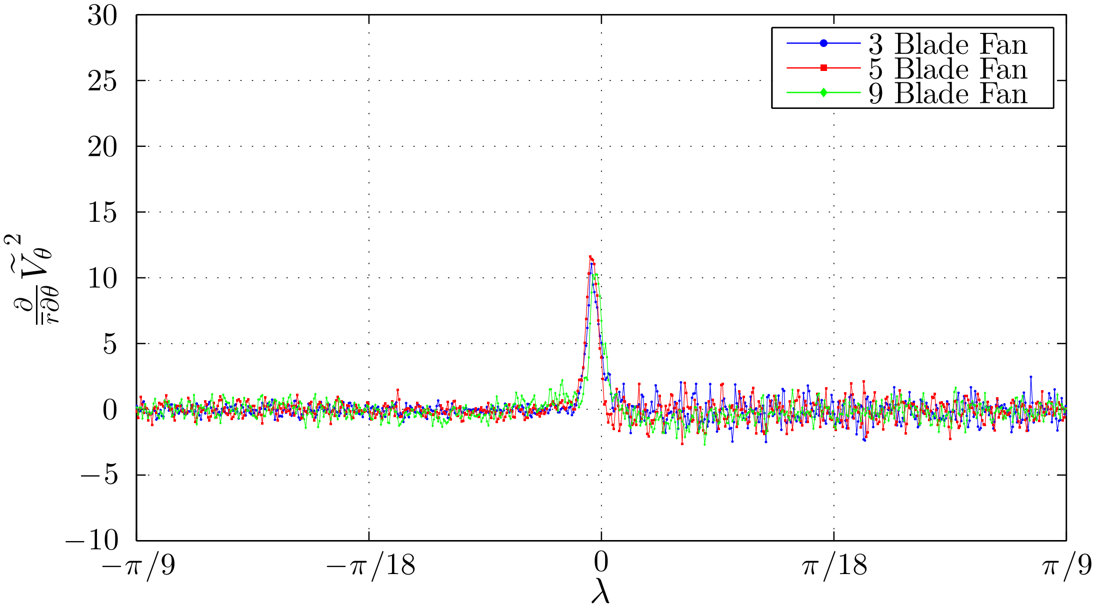

Figure 114 Case V net Reynolds normal stress in θ over λ_9

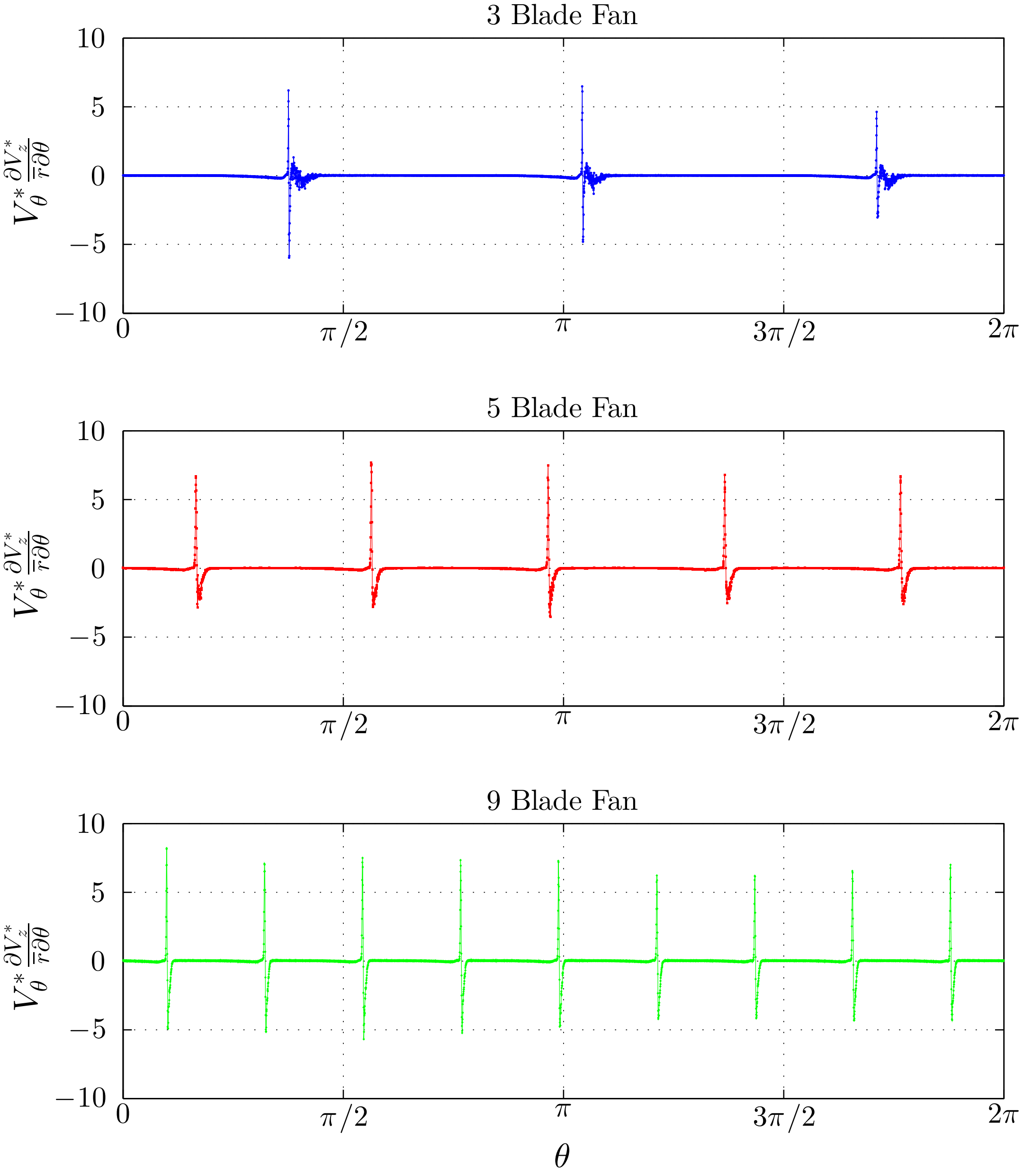

Figure 115 Case I advection of z–component momentum per unit mass over $0 \leq \theta \leq 2\pi$

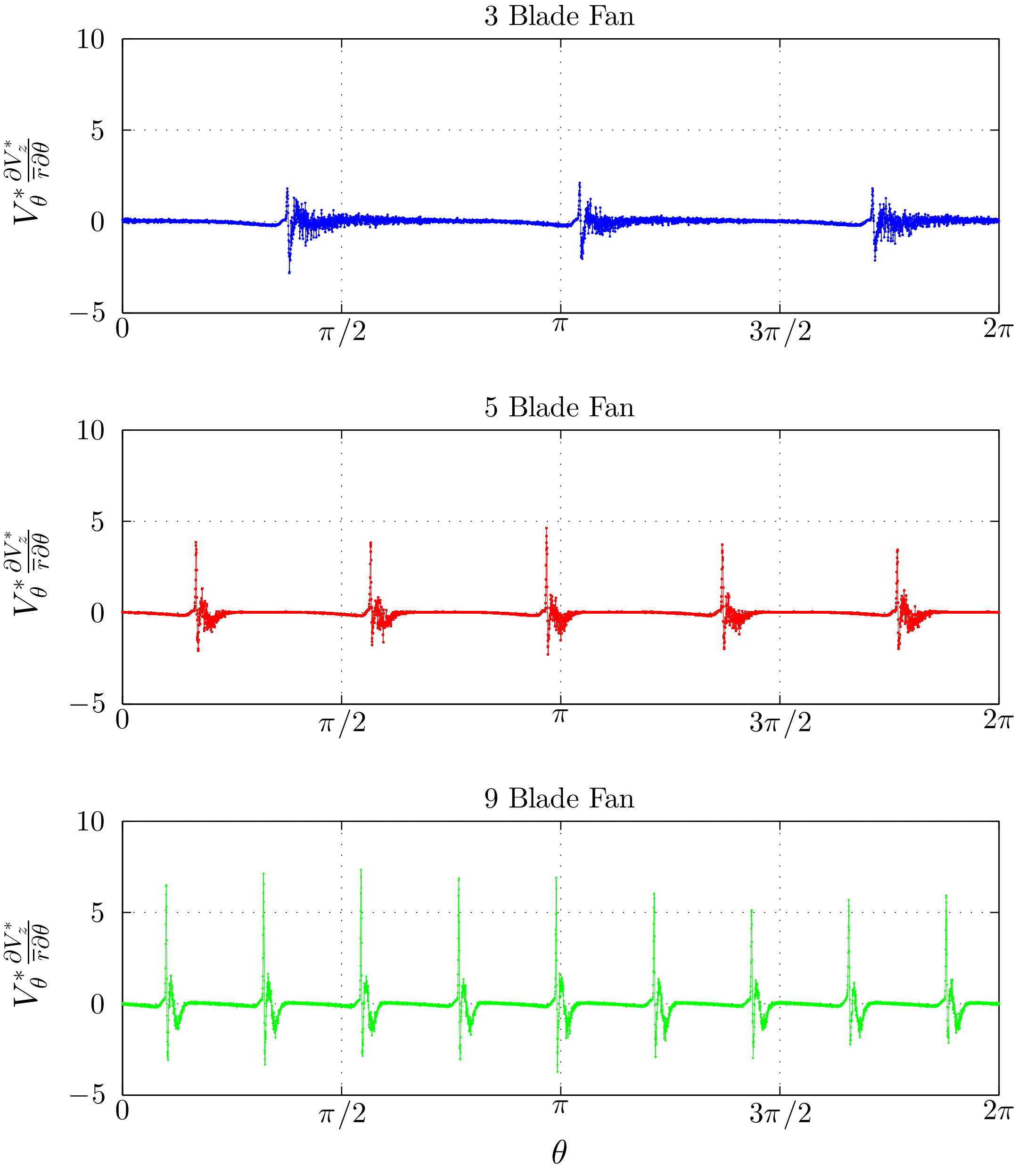

Figure 116 Case II advection of z–component momentum per unit mass over $0 \leq \theta \leq 2\pi$

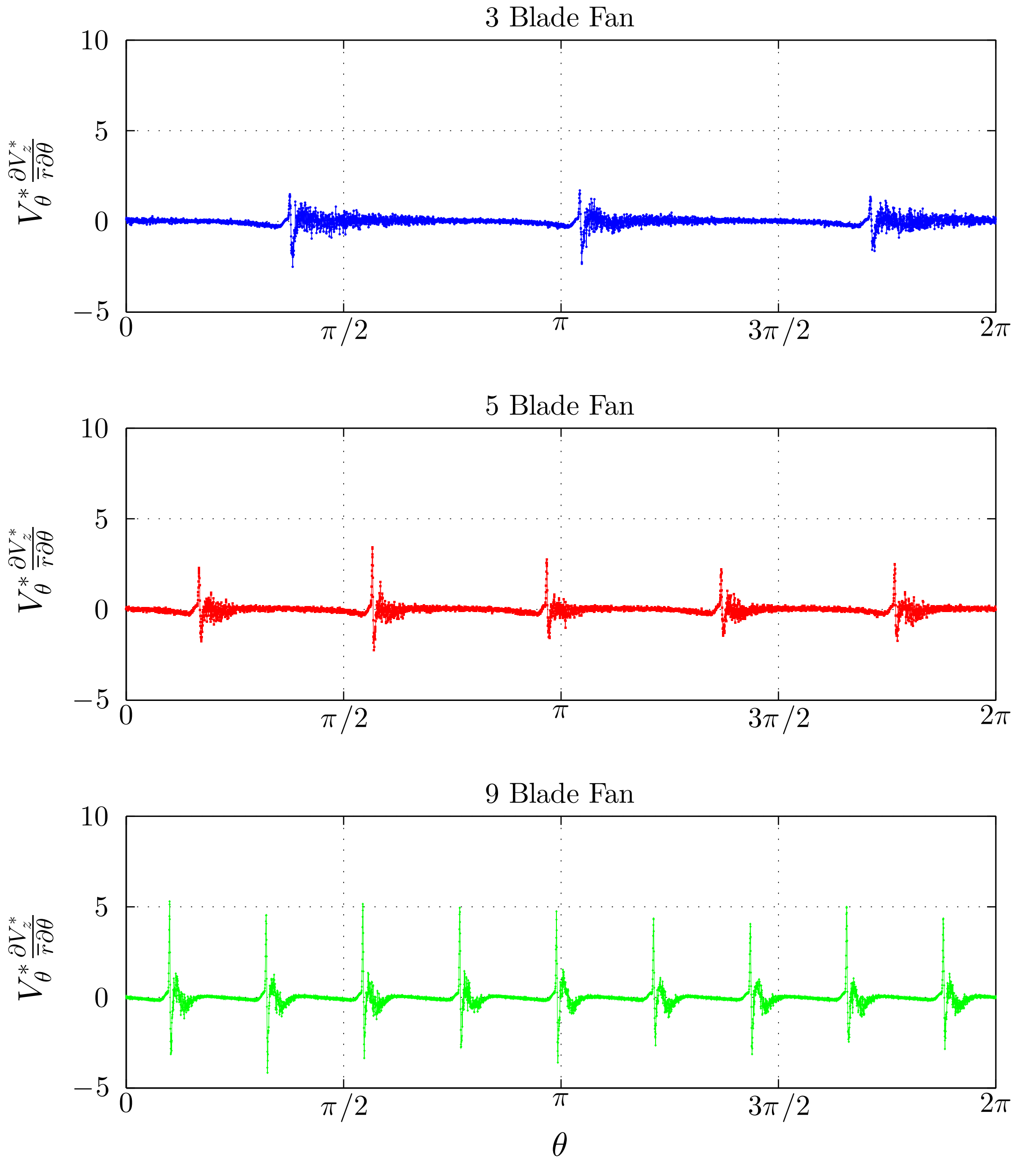
3 Blade Fan

5 Blade Fan

9 Blade Fan

Figure 117 Case III advection of z–component momentum per unit mass over $0 \leq \theta \leq 2\pi$

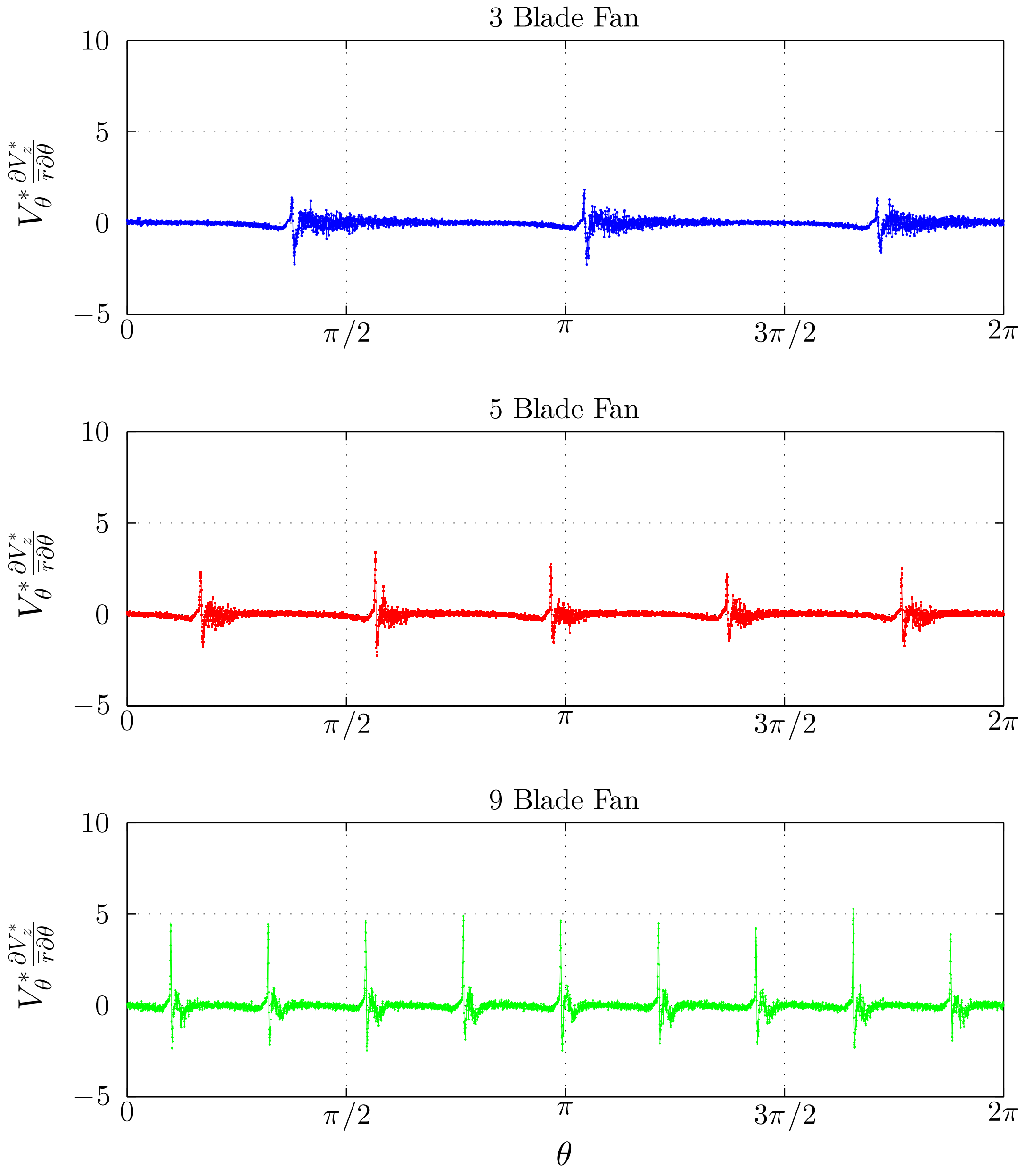

Figure 118 Case IV advection of z–component momentum per unit mass over $0 \leq \theta \leq 2\pi$

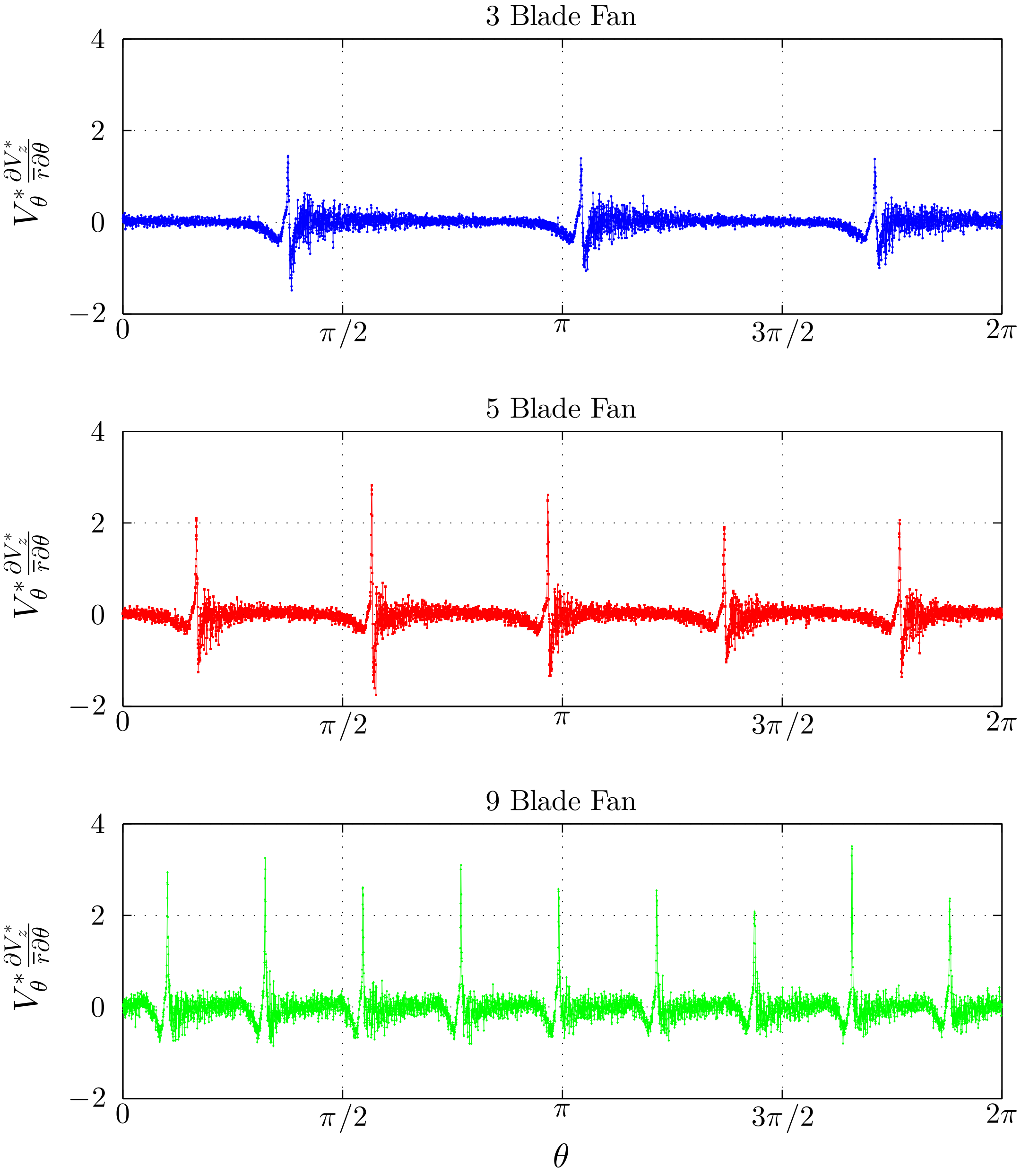

Figure 119 Case V advection of z–component momentum per unit mass over $0 \leq \theta \leq 2\pi$

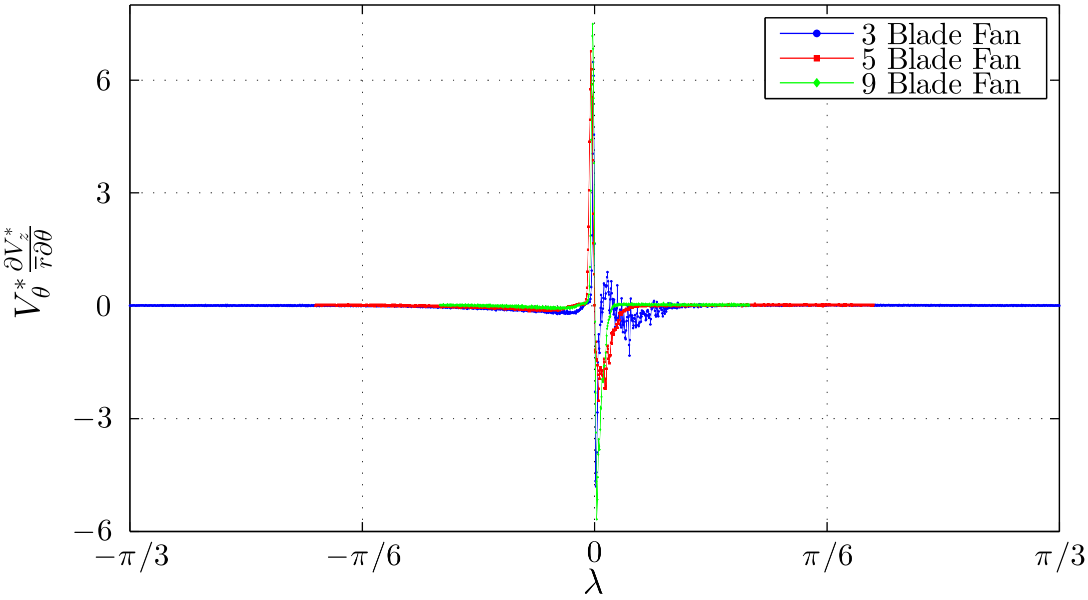

Figure 120 Case I advection of z–component momentum per unit mass over λ_3

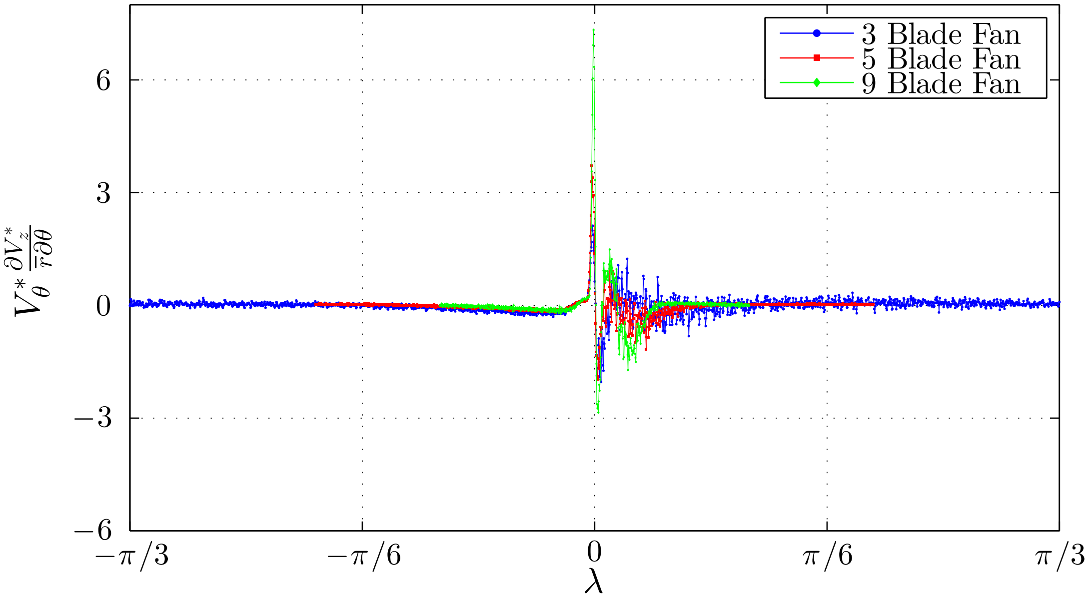

Figure 121 Case II advection of z–component momentum per unit mass over λ_3

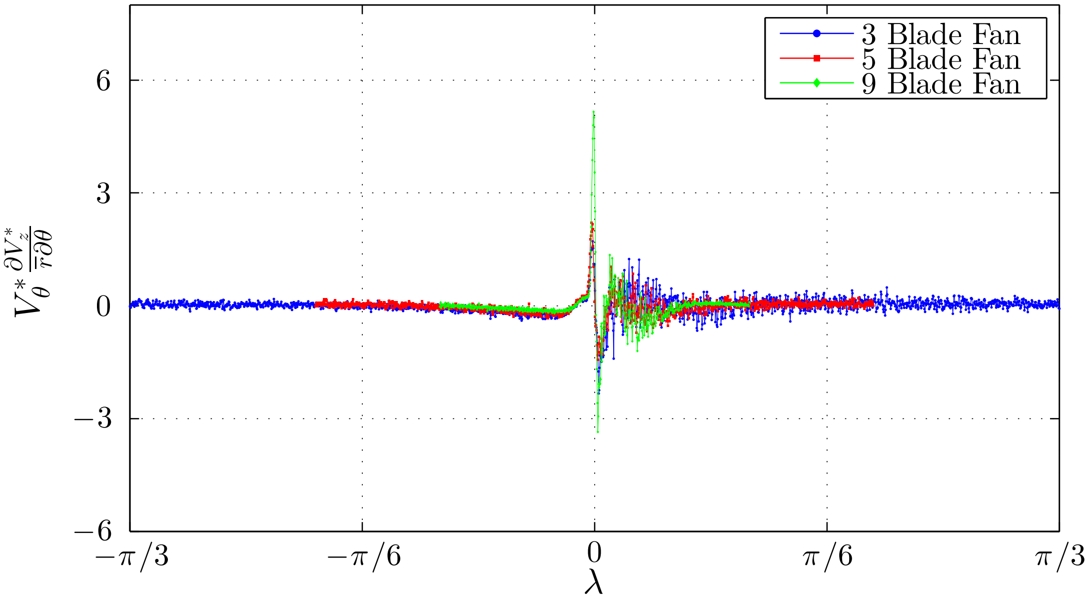

Figure 122 Case III advection of z–component momentum per unit mass over λ_3

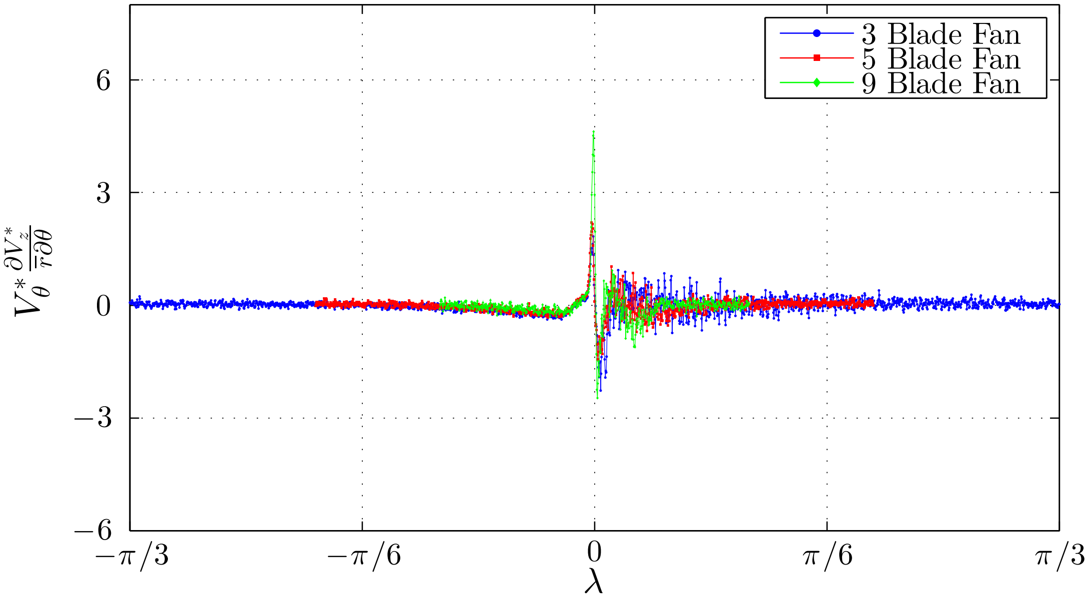

Figure 123 Case IV advection of z–component momentum per unit mass over λ_3

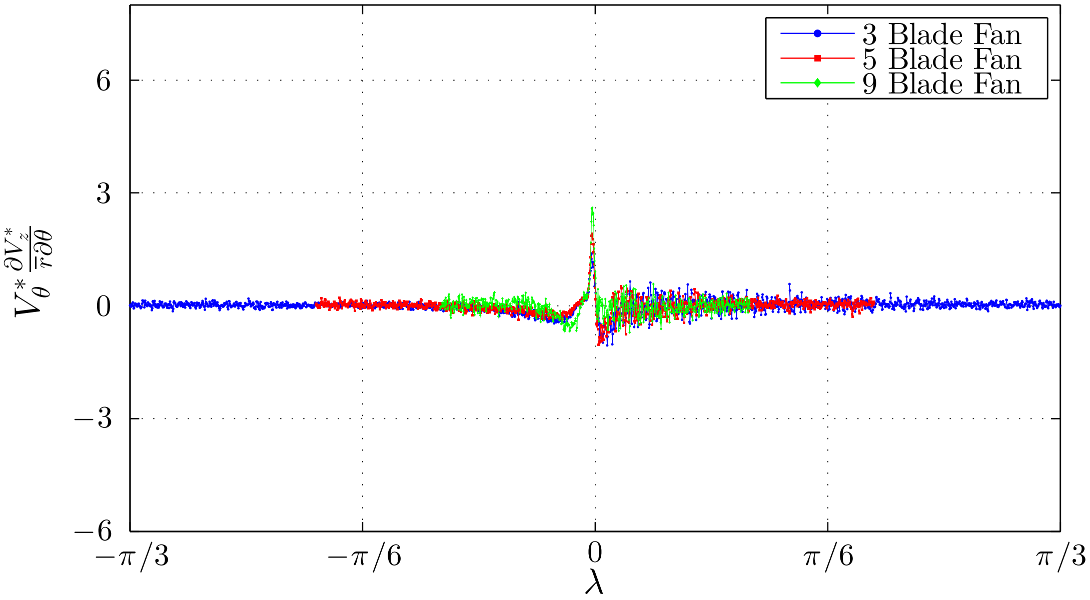

Figure 124 Case V advection of z–component momentum per unit mass over λ_3

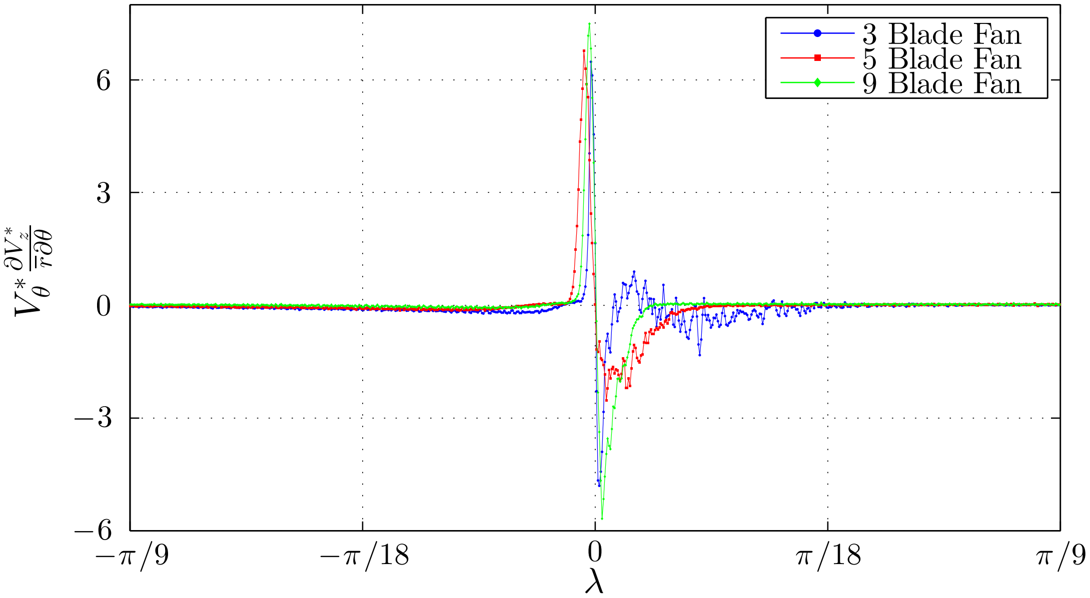

Figure 125 Case I advection of z–component momentum per unit mass over λ_9

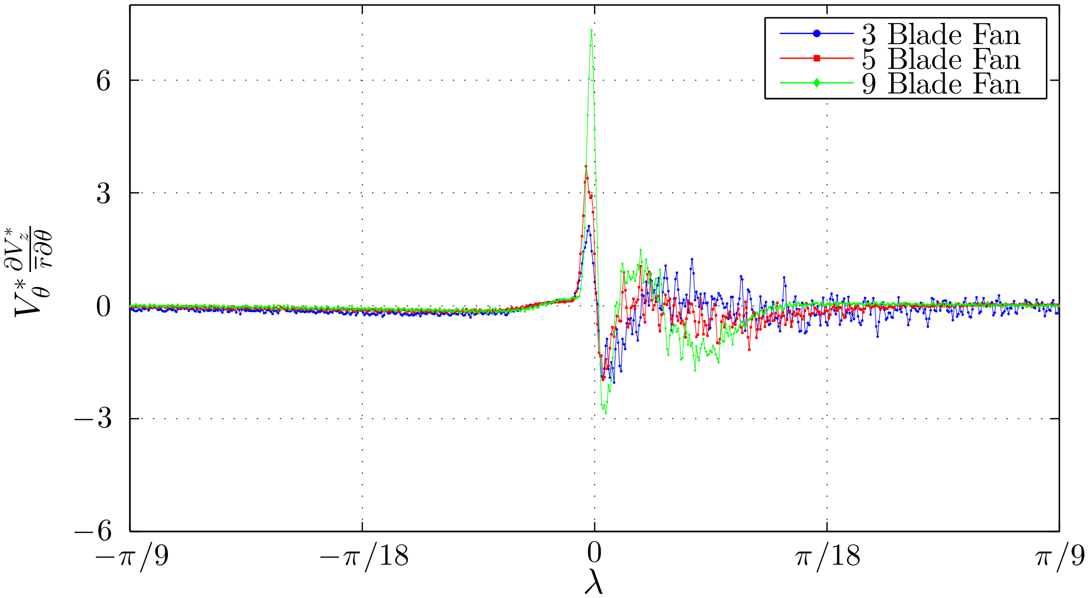

Figure 126 Case II advection of z–component momentum per unit mass over λ_9

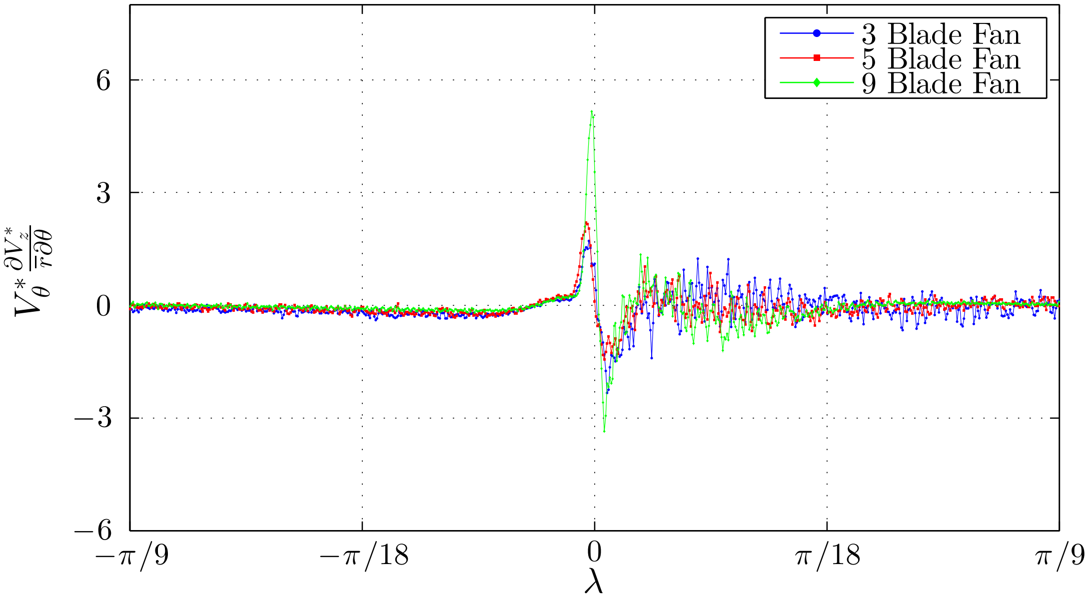

Figure 127 Case III advection of z–component momentum per unit mass over λ_9

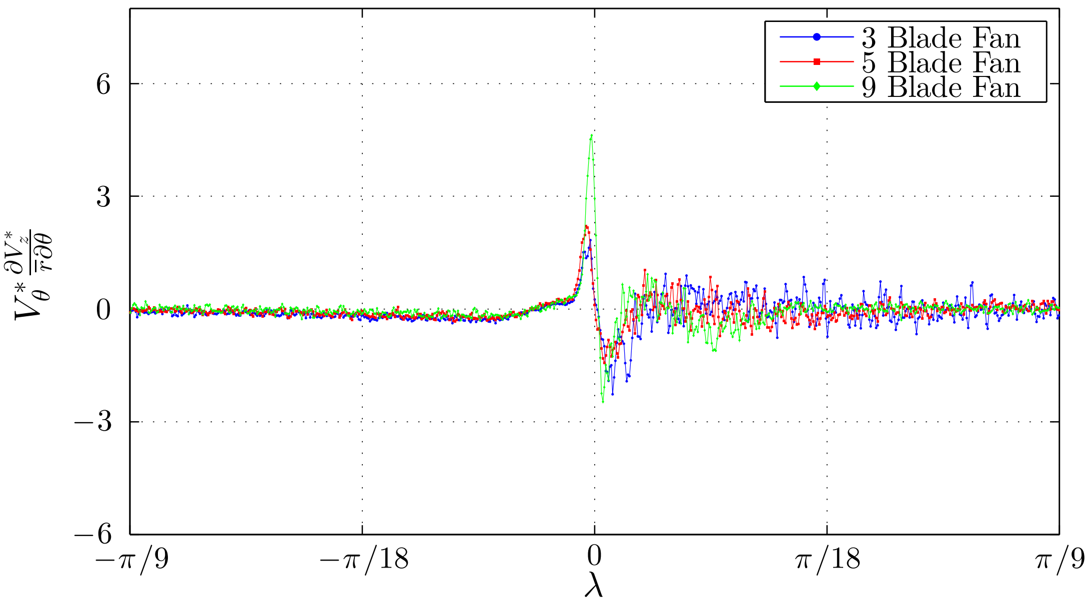

Figure 128 Case IV advection of z–component momentum per unit mass over λ_9

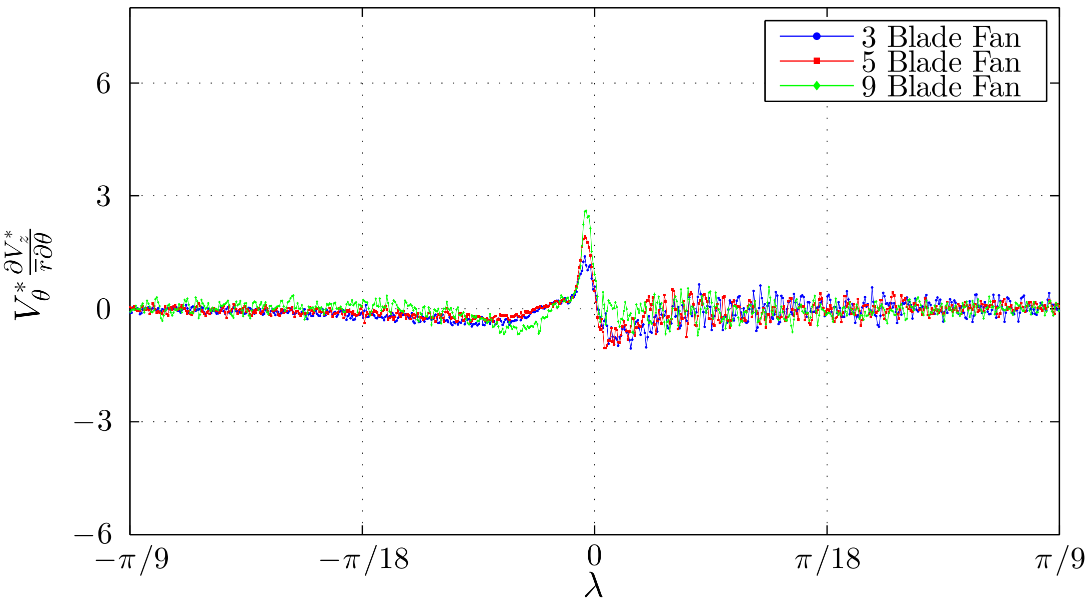

Figure 129 Case V advection of z–component momentum per unit mass over λ_9

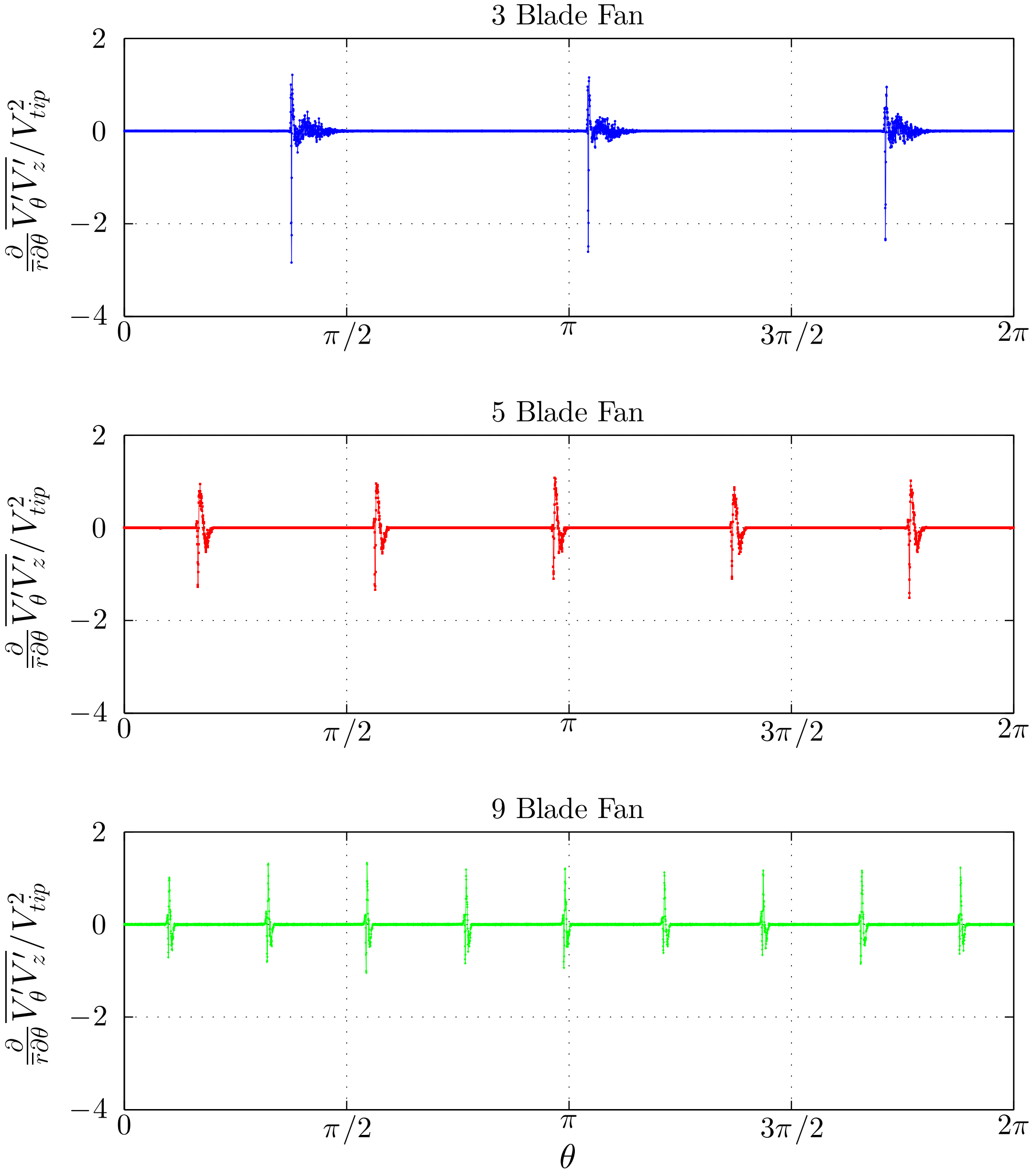

Figure 130 Case I net Reynolds shear stress in θ–z plane over $0 \leq \theta \leq 2\pi$

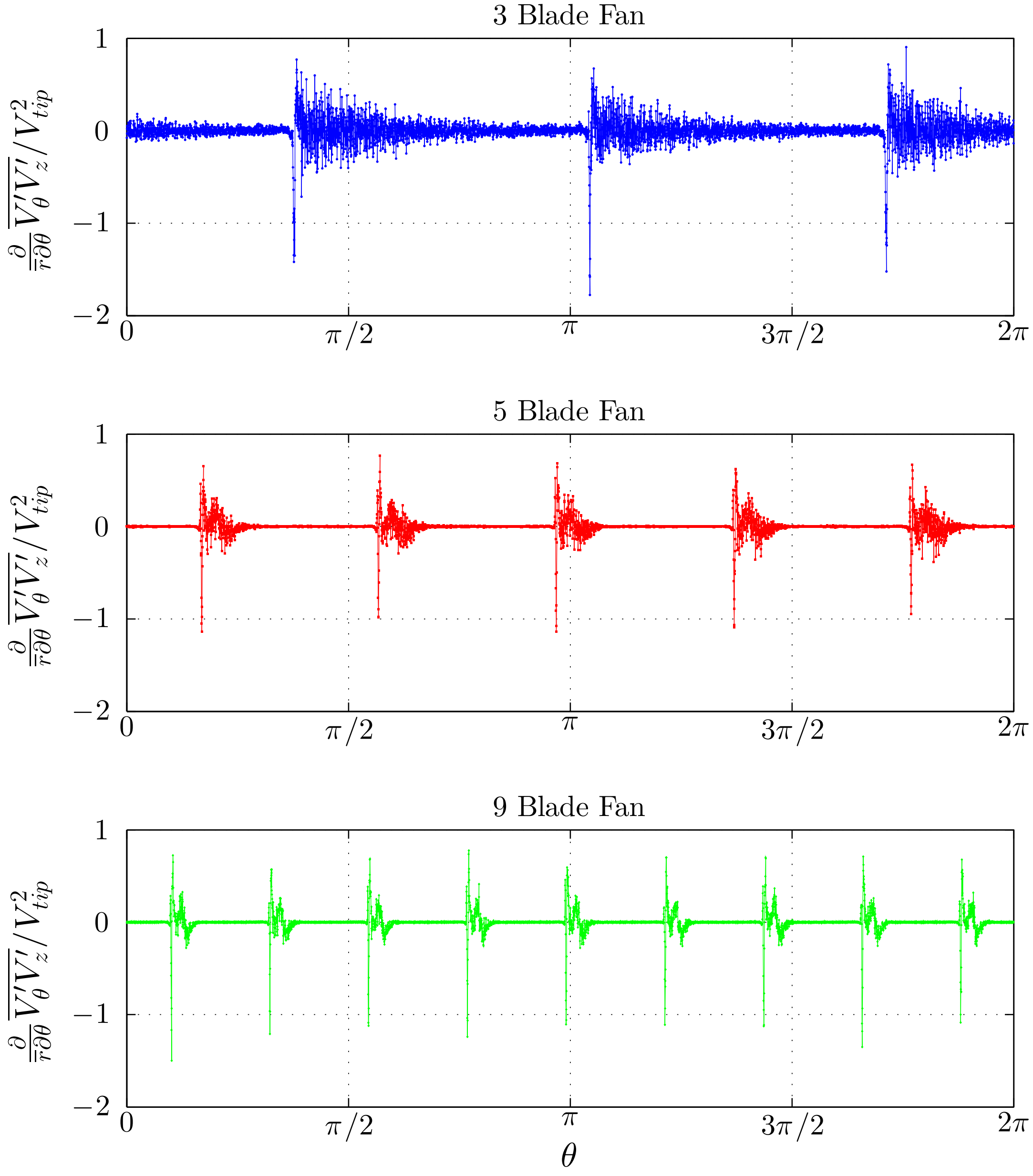

3 Blade Fan

5 Blade Fan

9 Blade Fan

Figure 131 Case II net Reynolds shear stress in θ–z plane over $0 \leq \theta \leq 2\pi$

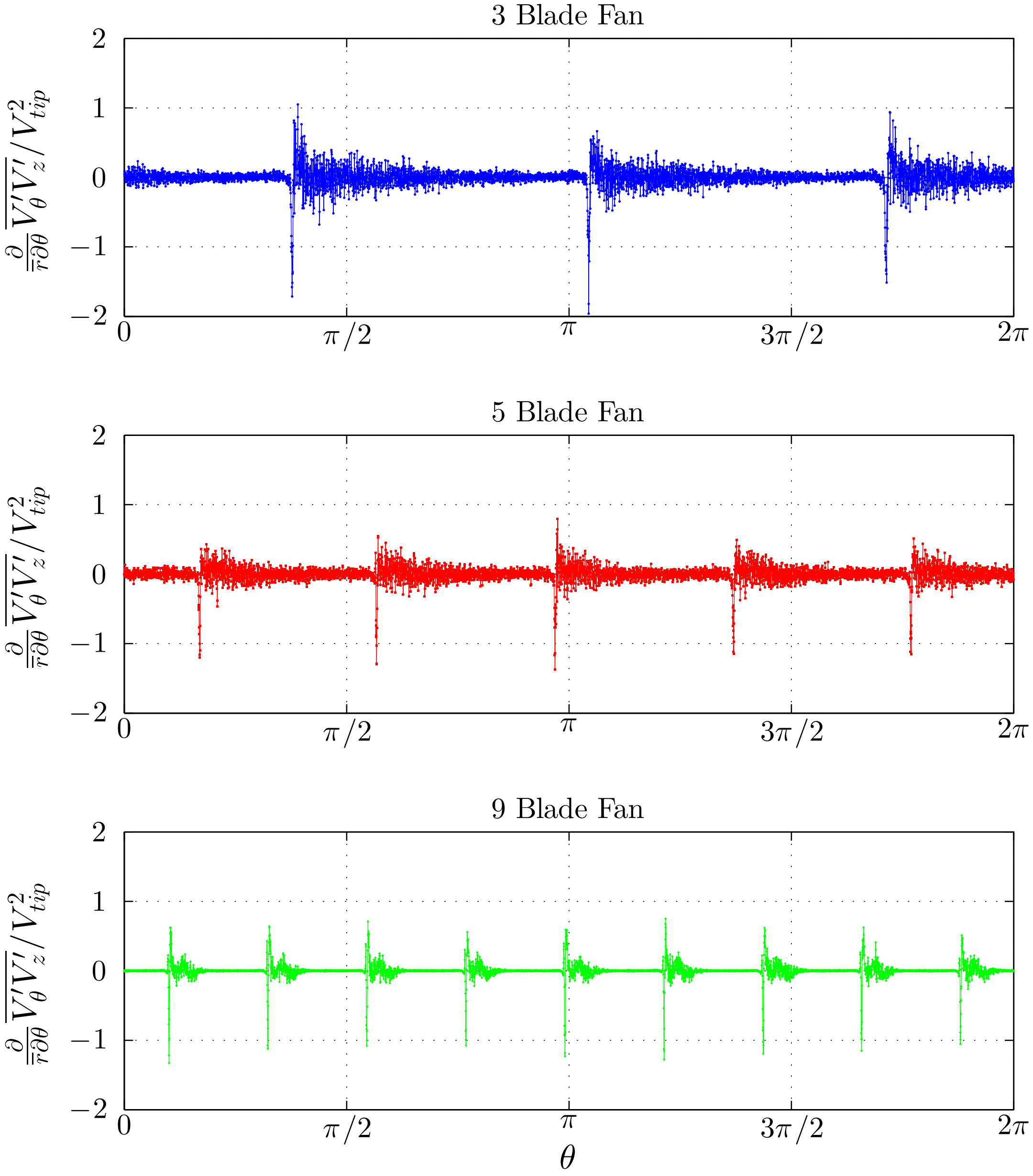

3 Blade Fan

5 Blade Fan

9 Blade Fan

Figure 132 Case III net Reynolds shear stress in θ–z plane over $0 \leq \theta \leq 2\pi$

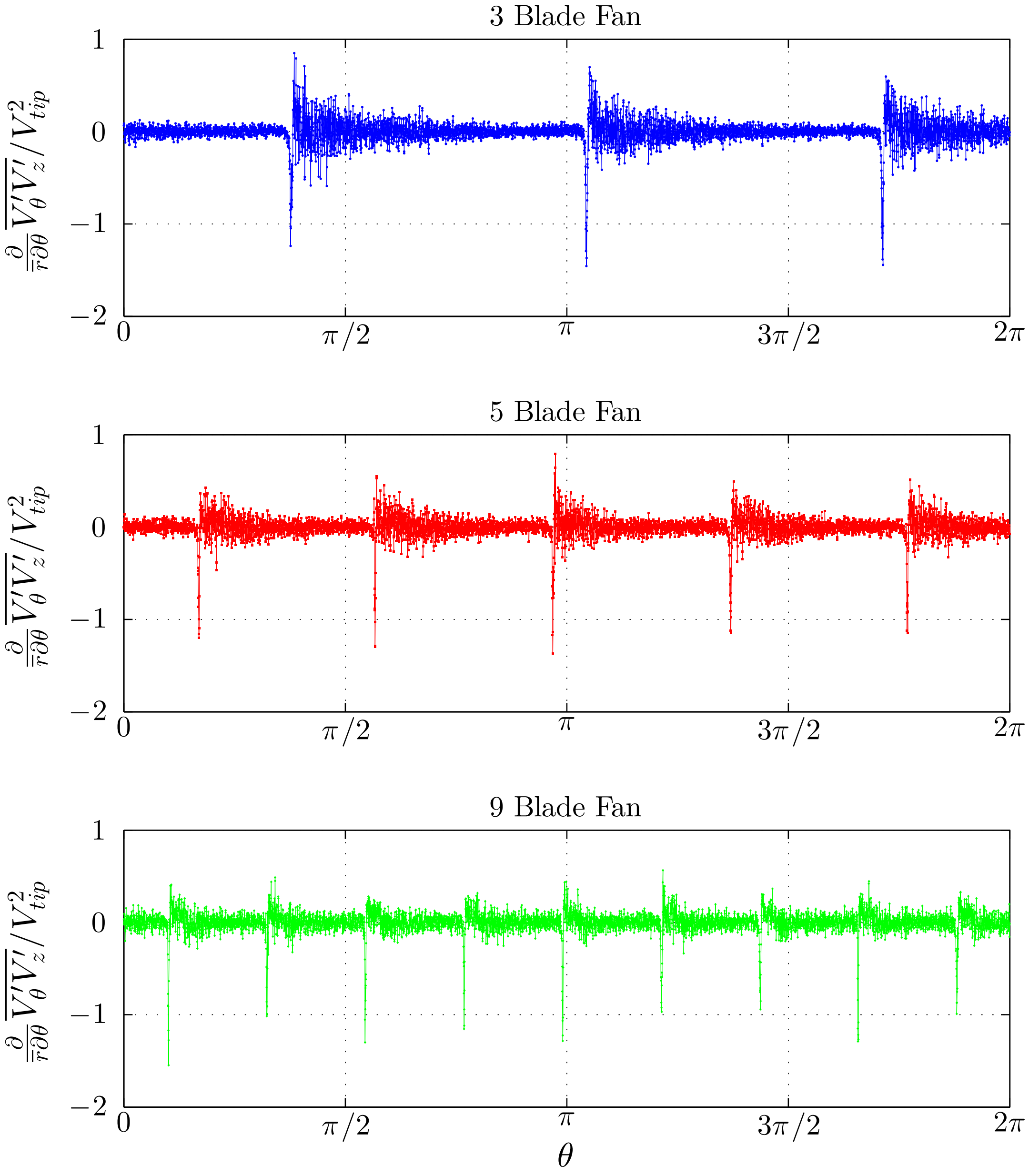

Figure 133 Case IV net Reynolds shear stress in θ–z plane over $0 \leq \theta \leq 2\pi$

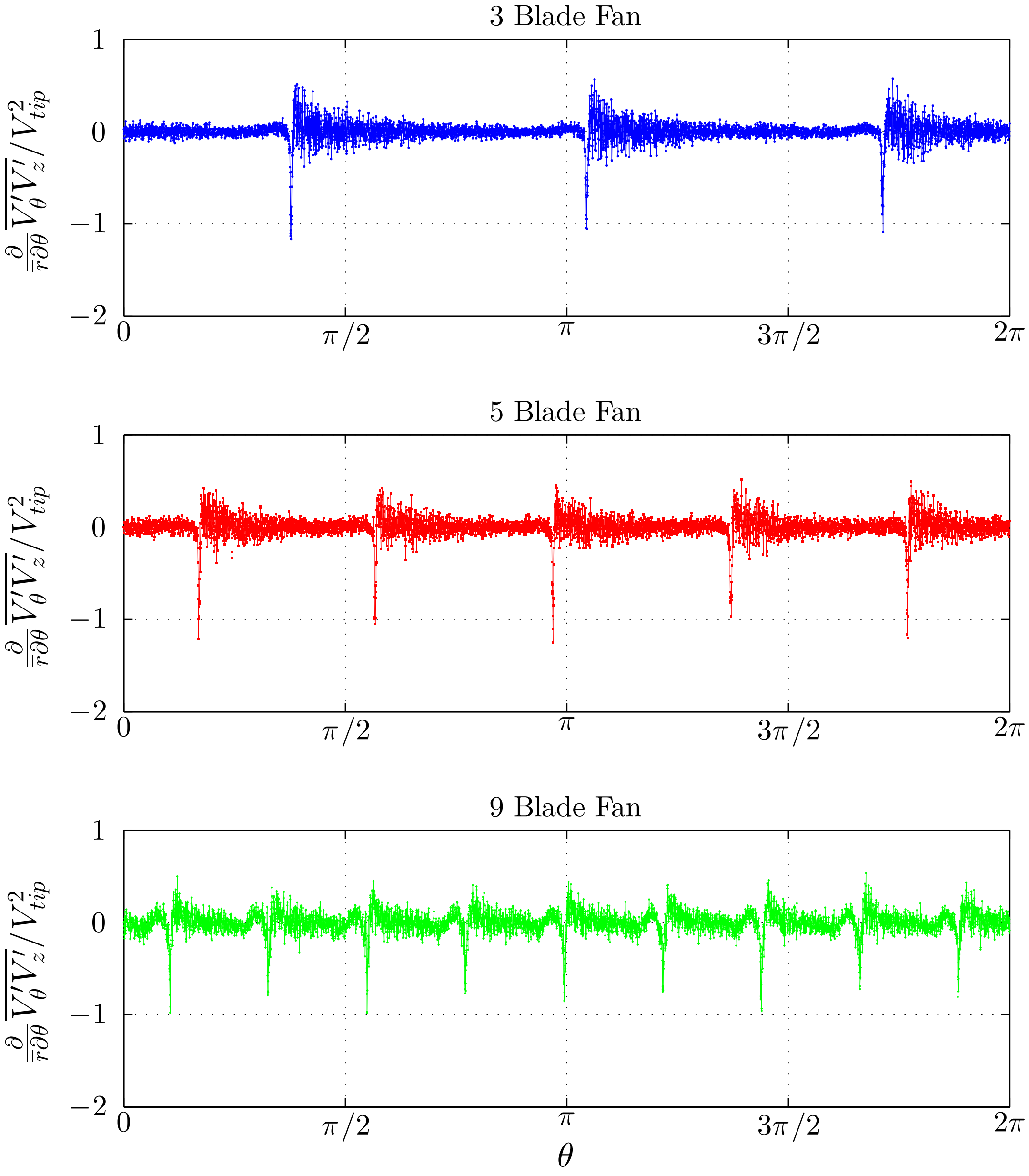

Figure 134 Case V net Reynolds shear stress in θ–z plane over $0 \leq \theta \leq 2\pi$

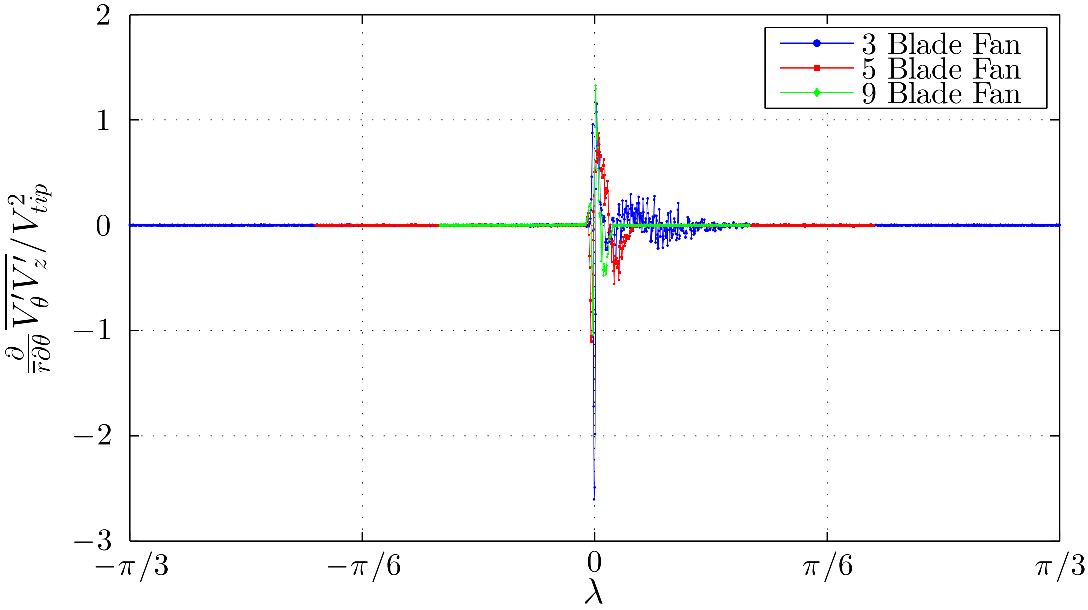

Figure 135 Case I net Reynolds shear stress in θ–z plane over λ_3

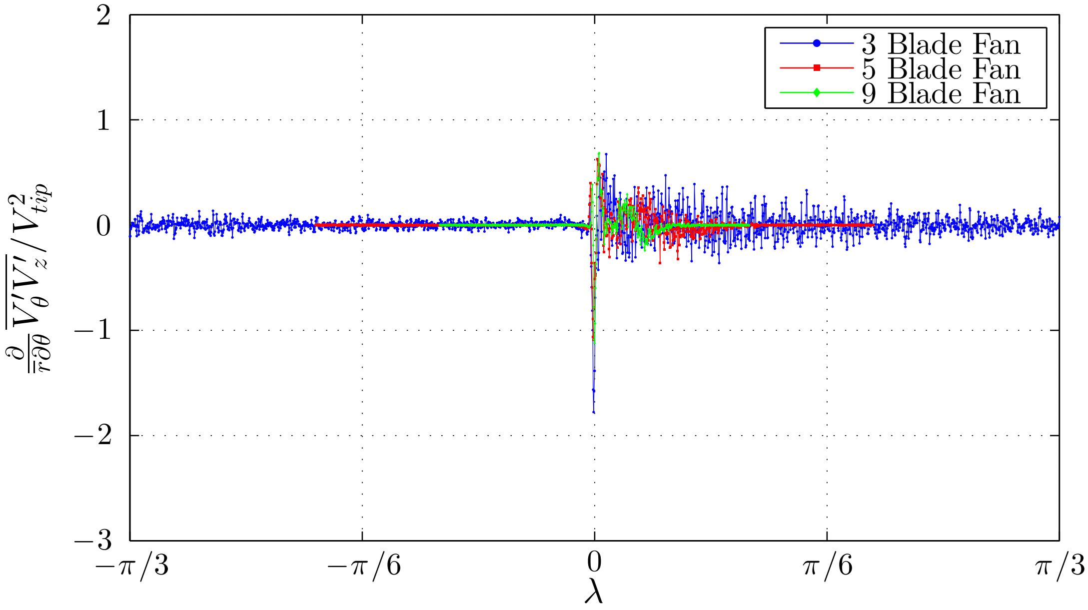

Figure 136 Case II net Reynolds shear stress in θ–z plane over λ_3

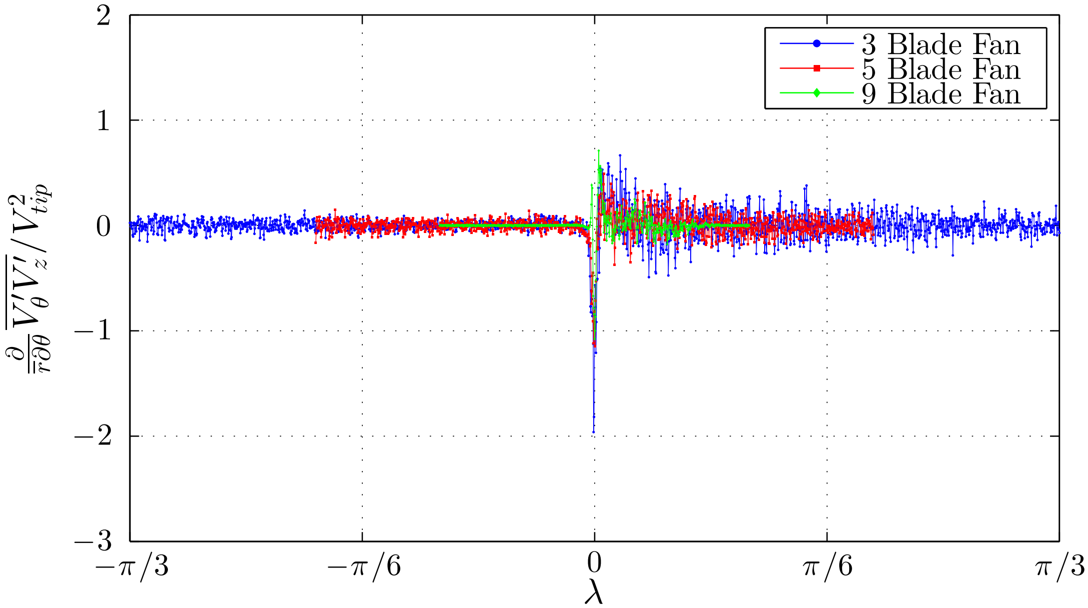

Figure 137 Case III net Reynolds shear stress in θ–z plane over λ_3

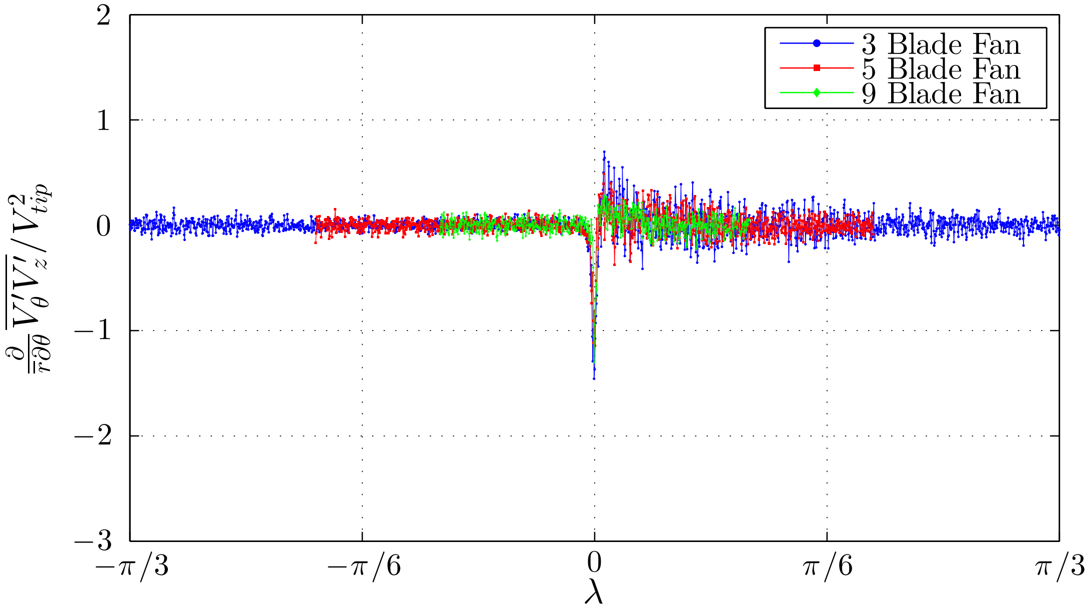

Figure 138 Case IV net Reynolds shear stress in θ–z plane over λ_3

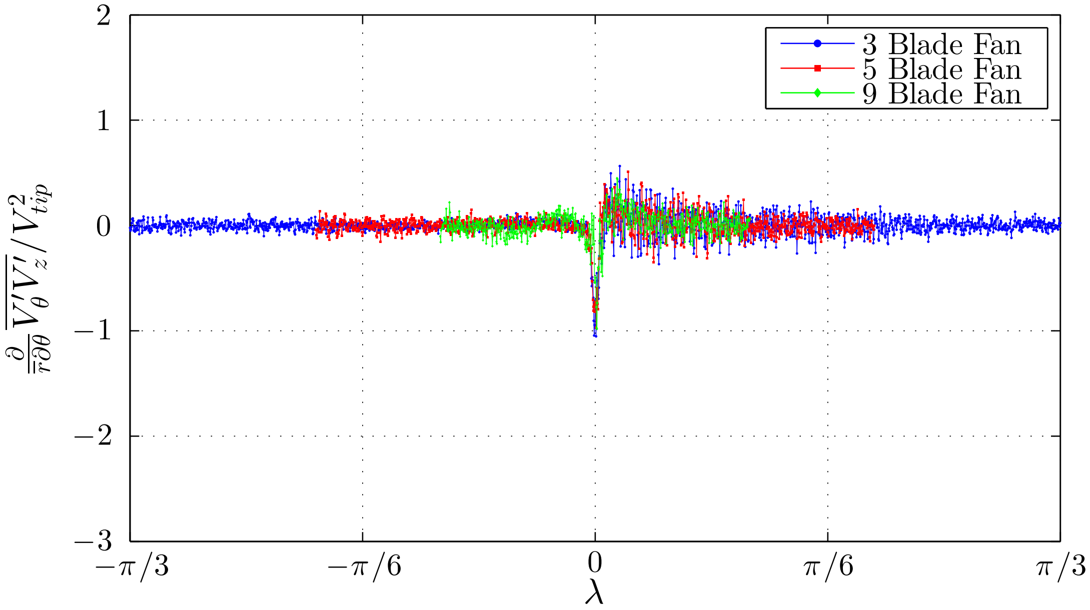

Figure 139 Case V net Reynolds shear stress in θ–z plane over λ_3

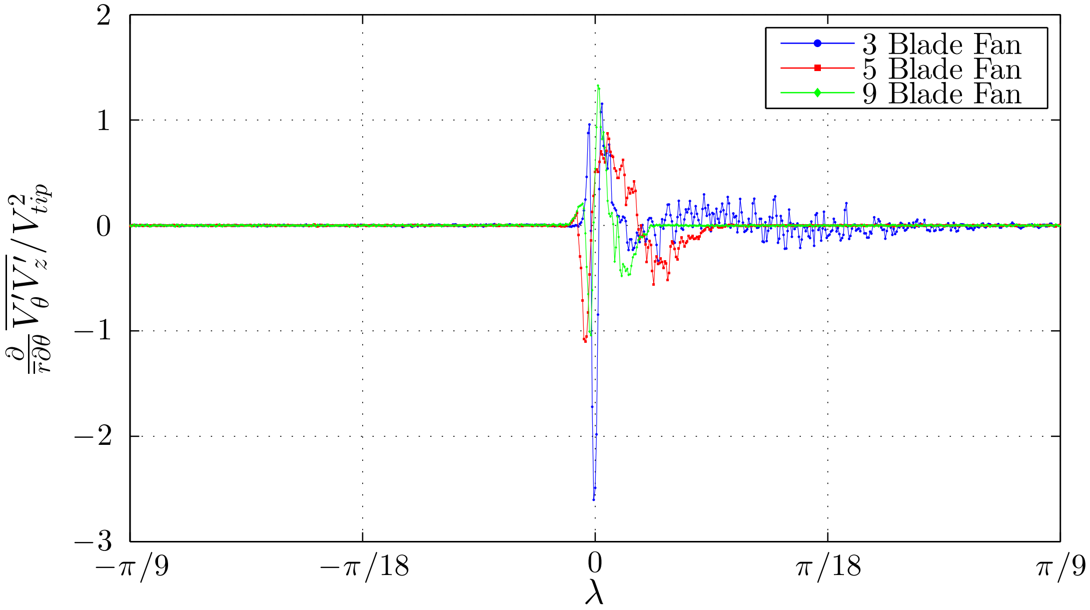

Figure 140 Case I net Reynolds shear stress in θ–z plane over λ_9

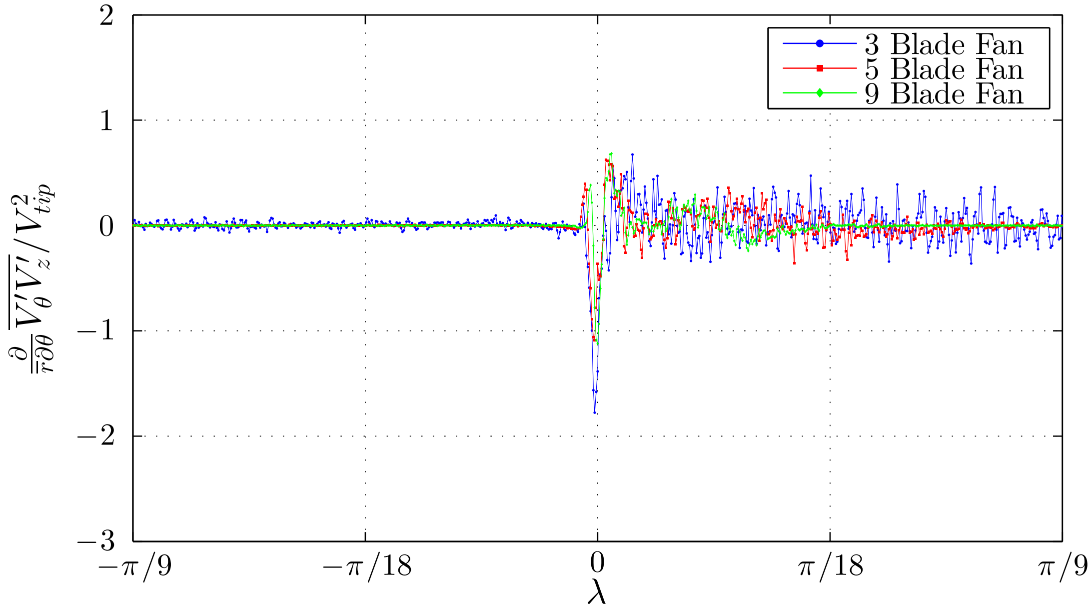

Figure 141 Case II net Reynolds shear stress in θ–z plane over λ_9

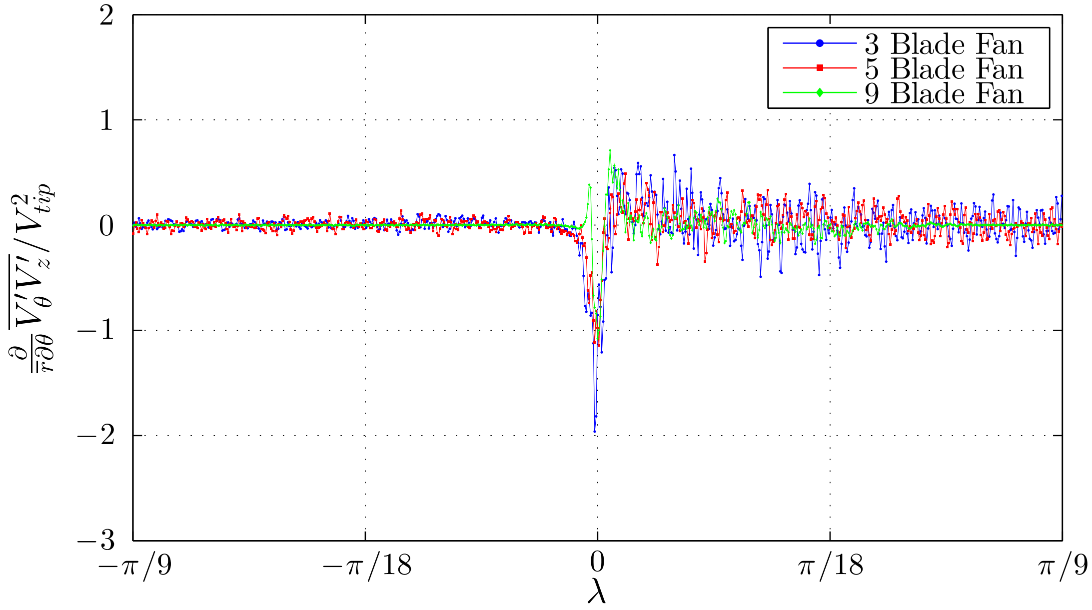

Figure 142 Case III net Reynolds shear stress in θ–z plane over λ_9

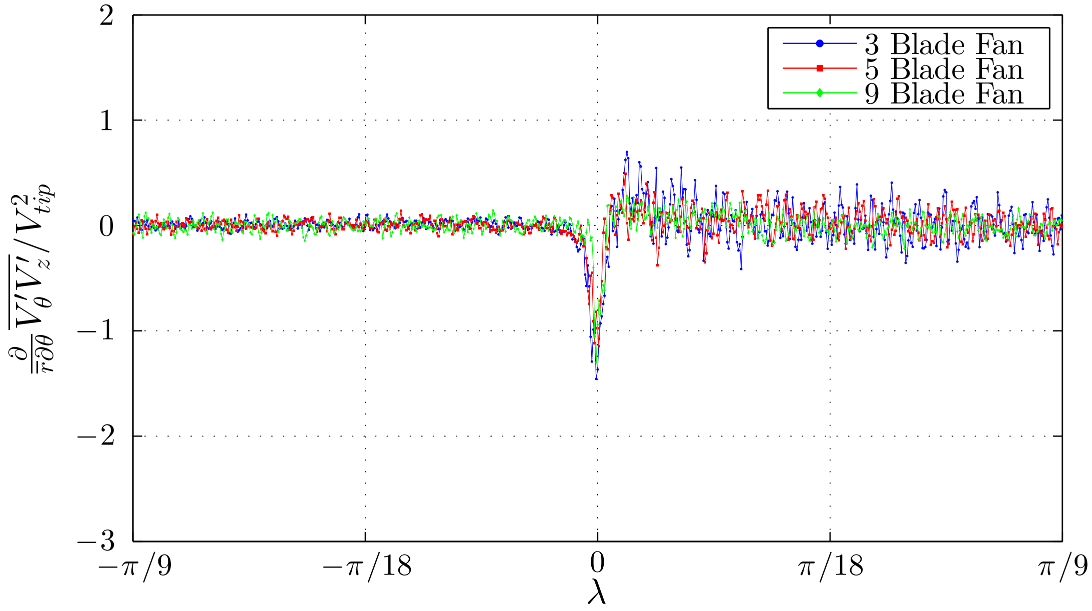

Figure 143 Case IV net Reynolds shear stress in θ–z plane over λ_9

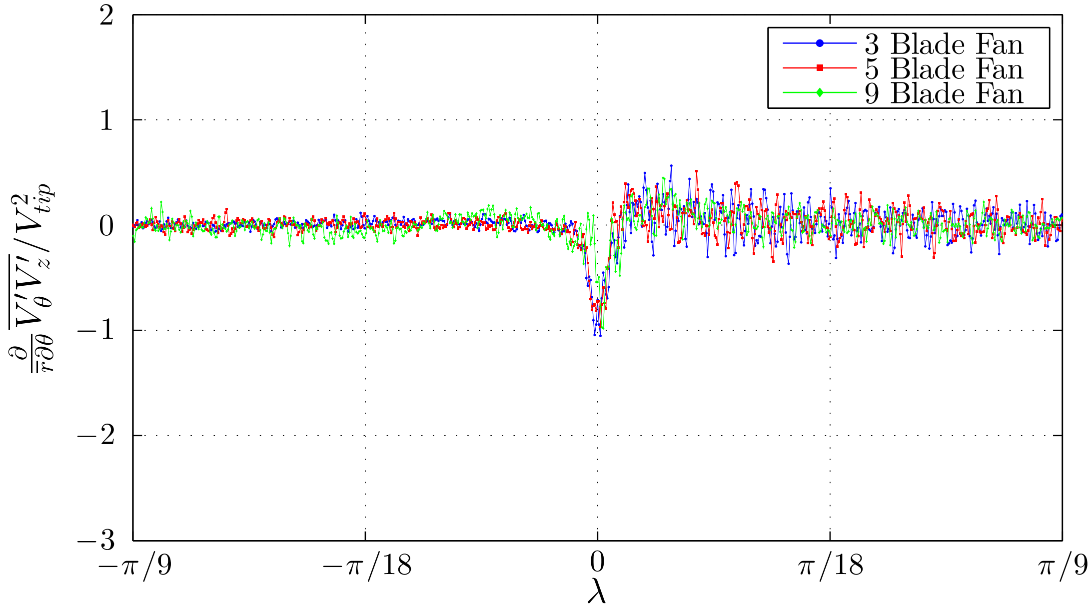

Figure 144 Case V net Reynolds shear stress in θ–z plane over λ_9

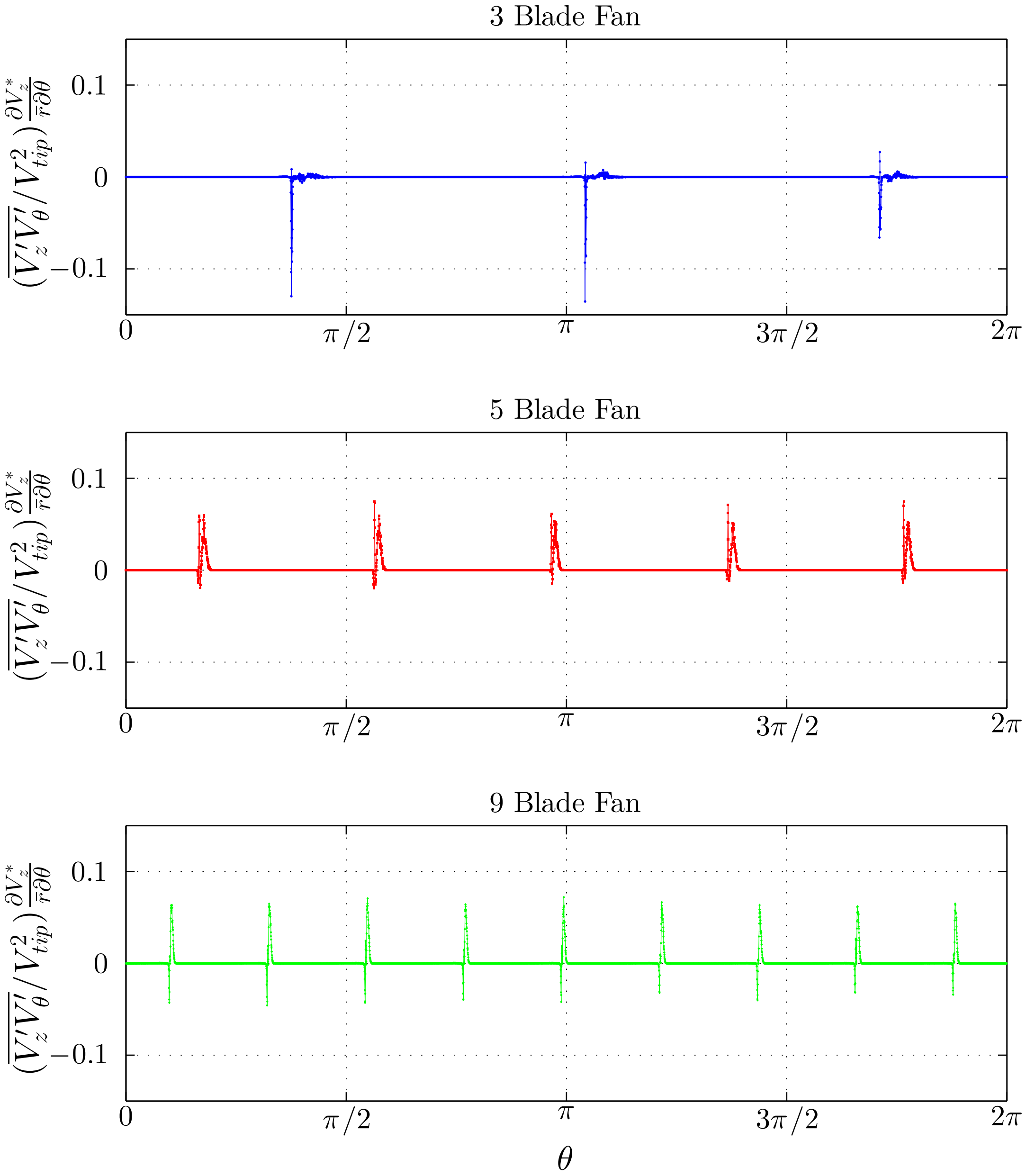

Figure 145 Case I turbulence kinetic production by Reynolds shear stress in θ–z plane over $0 \leq \theta \leq 2\pi$

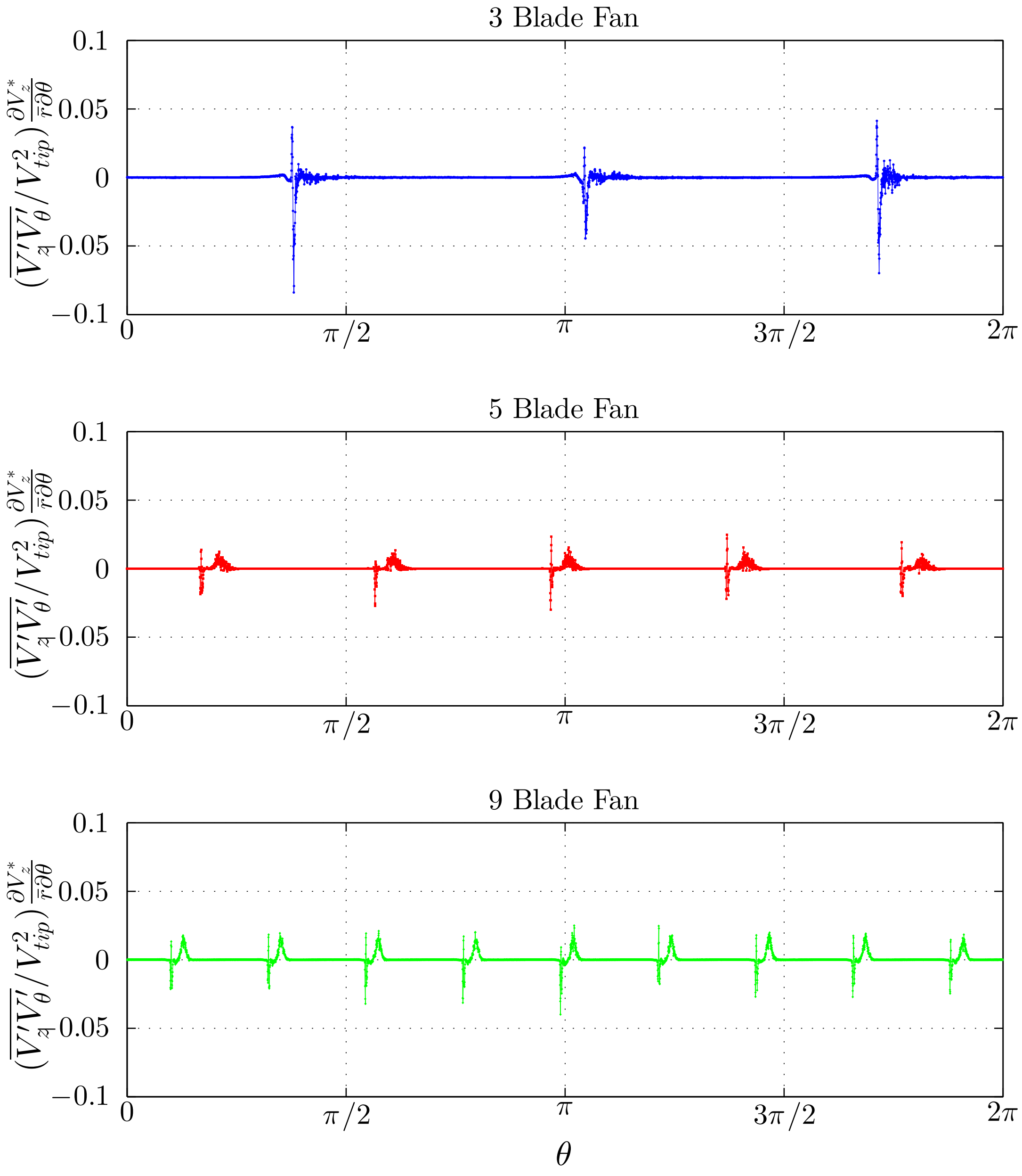

Figure 146 Case II turbulence kinetic production by Reynolds shear stress in θ–z plane over $0 \leq \theta \leq 2\pi$

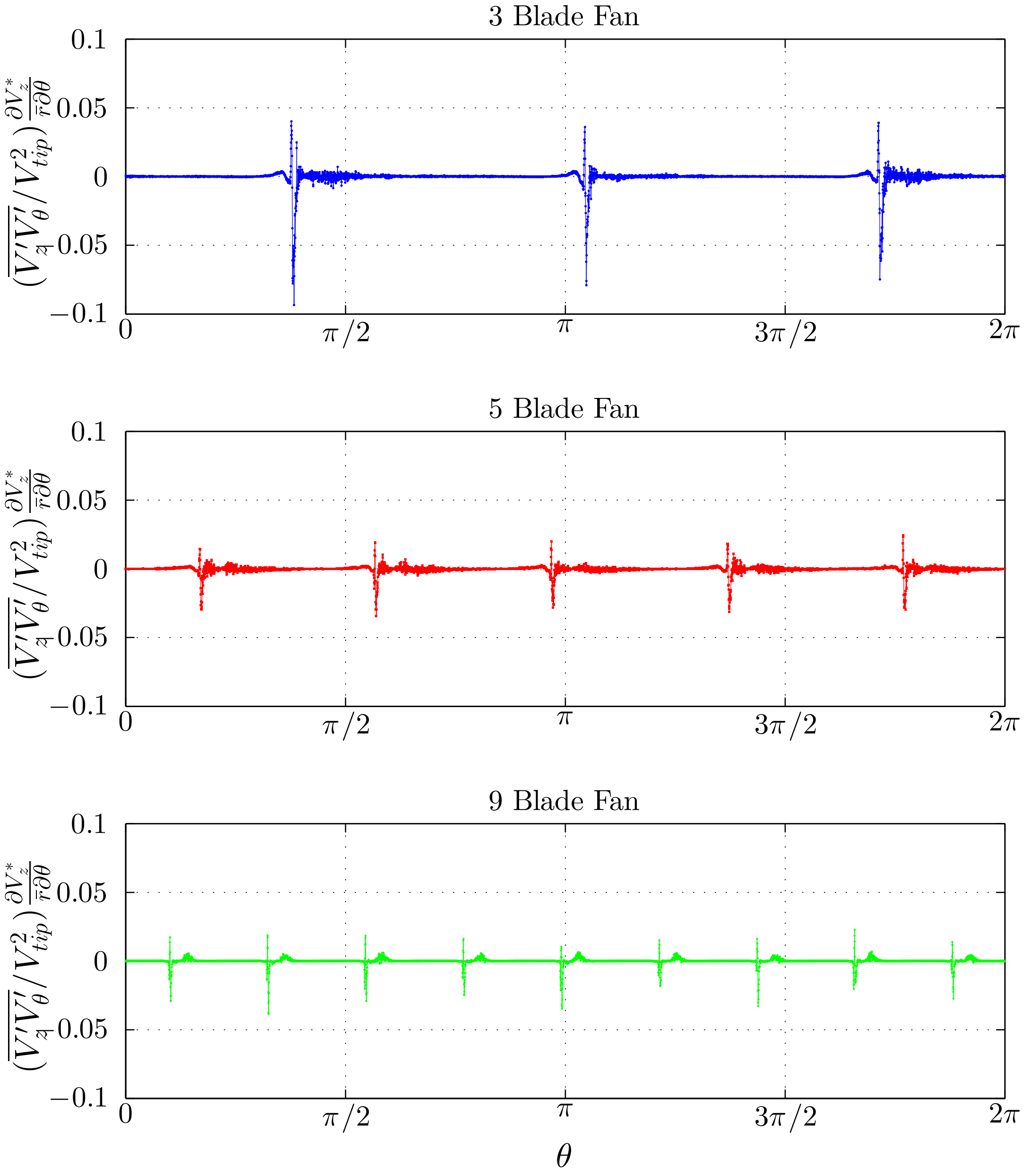

Figure 147 Case III turbulence kinetic production by Reynolds shear stress in θ–z plane over $0 \leq \theta \leq 2\pi$

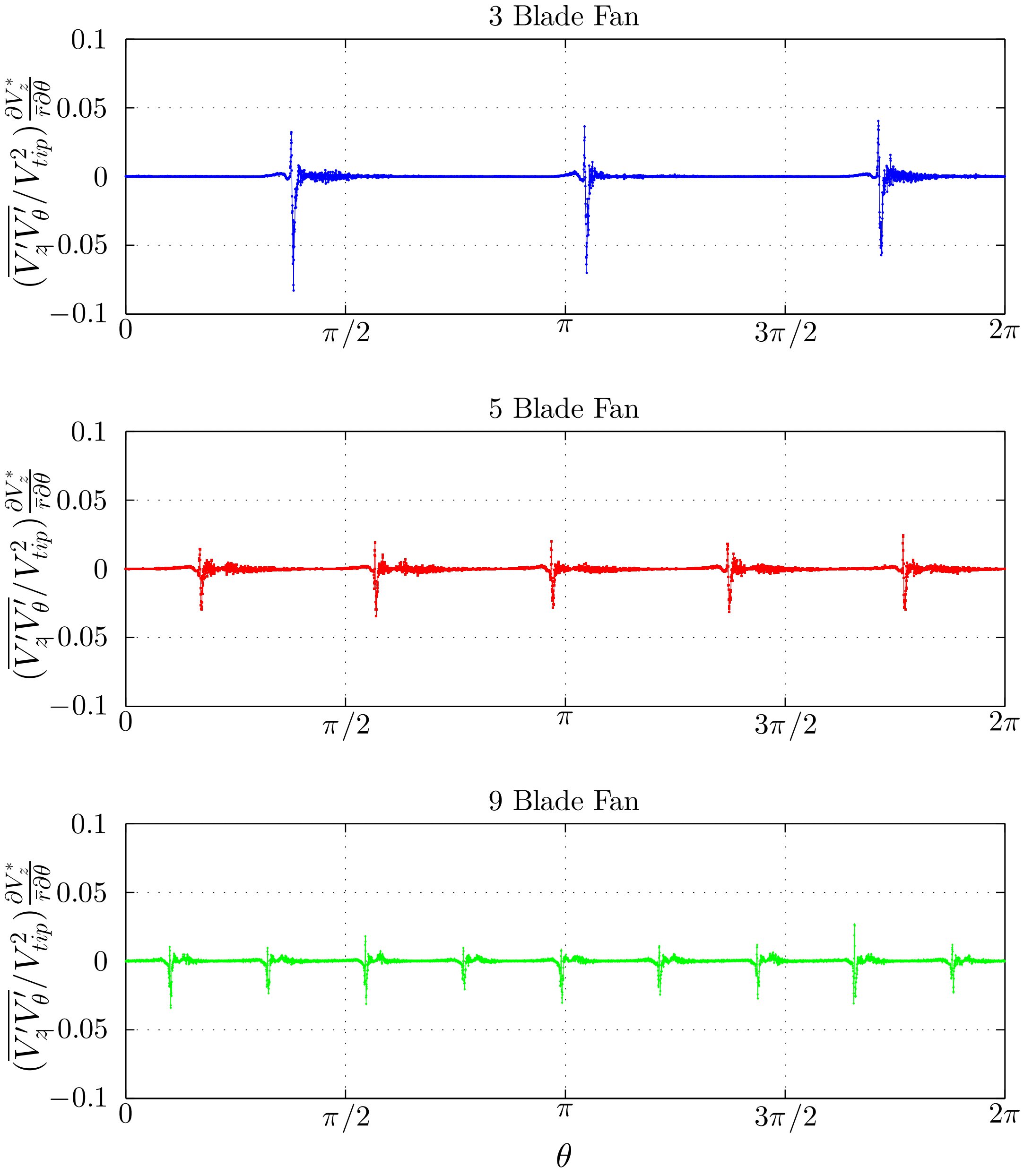

Figure 148 Case IV turbulence kinetic production by Reynolds shear stress in θ–z plane over $0 \leq \theta \leq 2\pi$

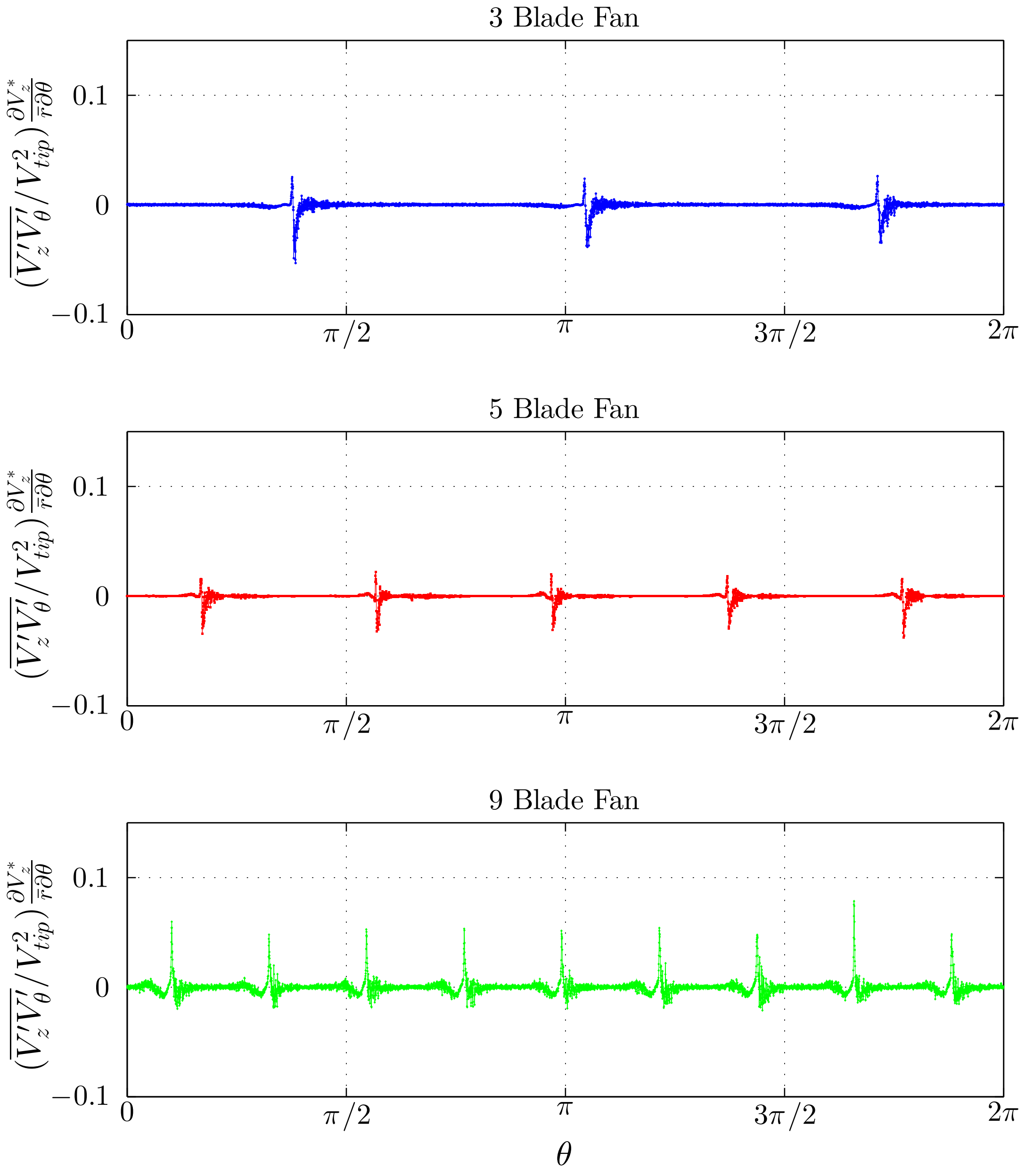

Figure 149 Case V turbulence kinetic production by Reynolds shear stress in θ–z plane over $0 \leq \theta \leq 2\pi$

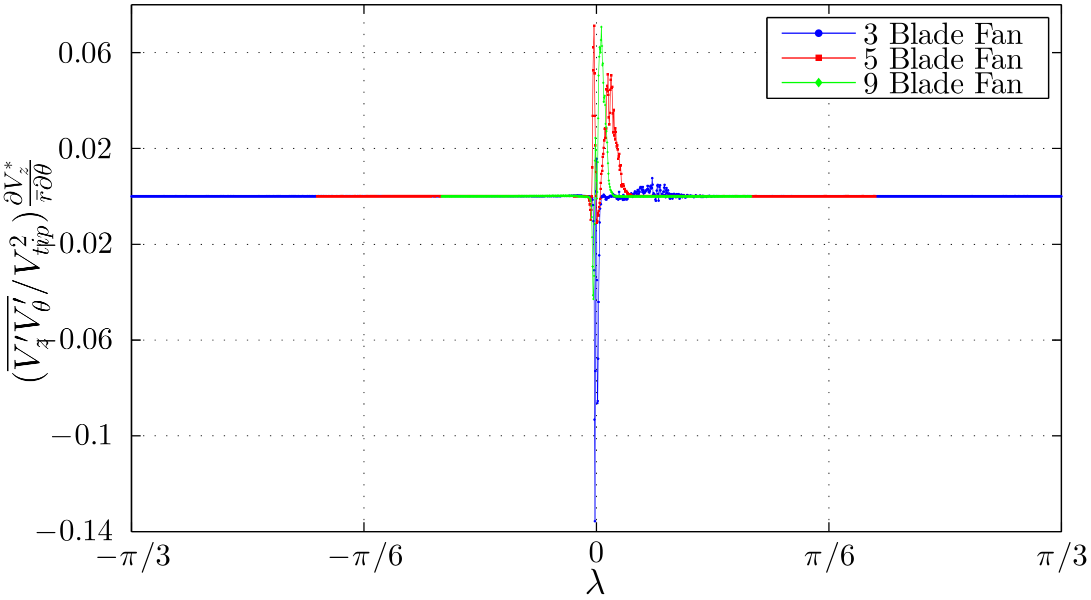

Figure 150 Case I turbulence kinetic production by Reynolds shear stress in θ–z plane over λ_3

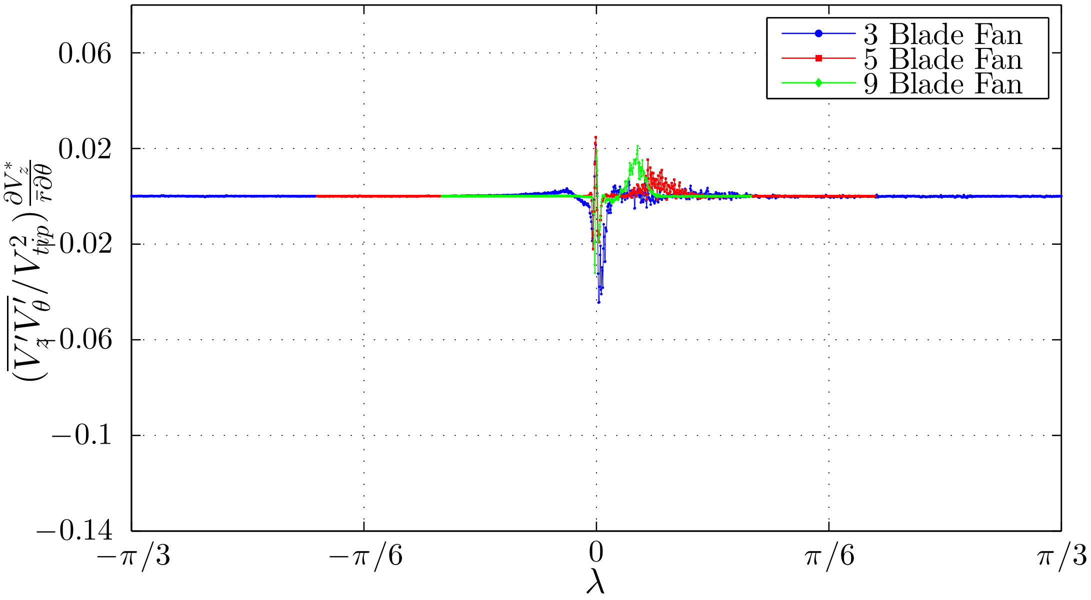

Figure 151 Case II turbulence kinetic production by Reynolds shear stress in θ–z plane over λ_3

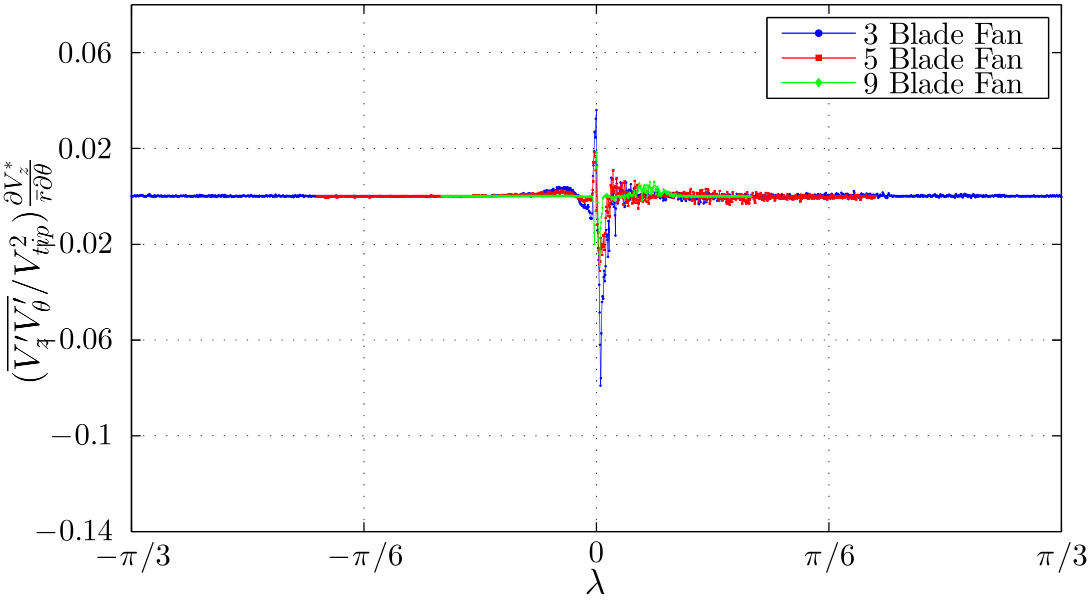

Figure 152 Case III turbulence kinetic production by Reynolds shear stress in θ–z plane over λ_3

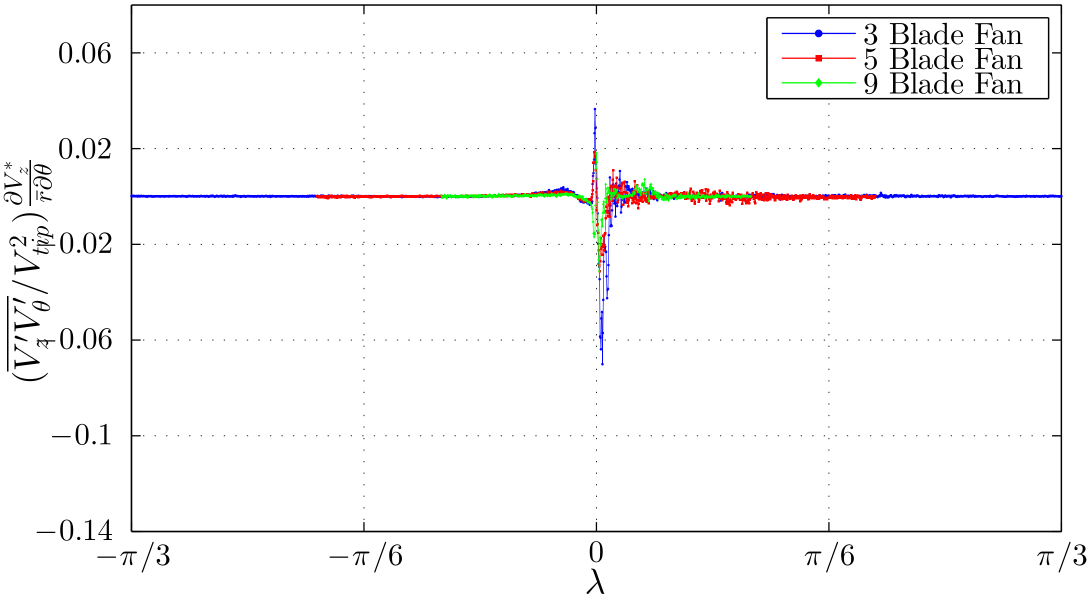

Figure 153 Case IV turbulence kinetic production by Reynolds shear stress in θ–z plane over λ_3

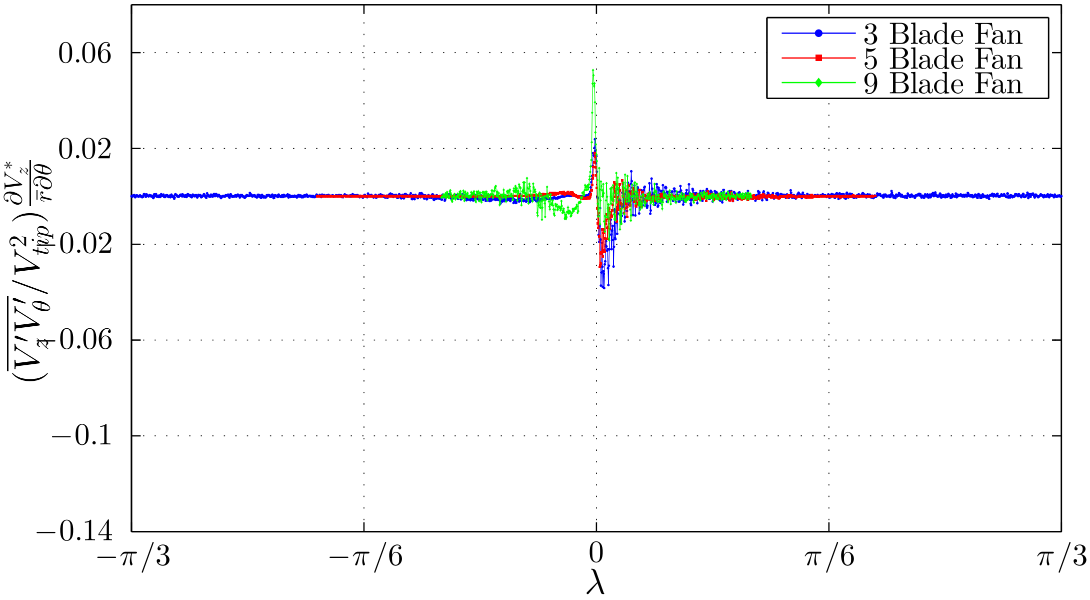

Figure 154 Case V turbulence kinetic production by Reynolds shear stress in θ–z plane over λ_3

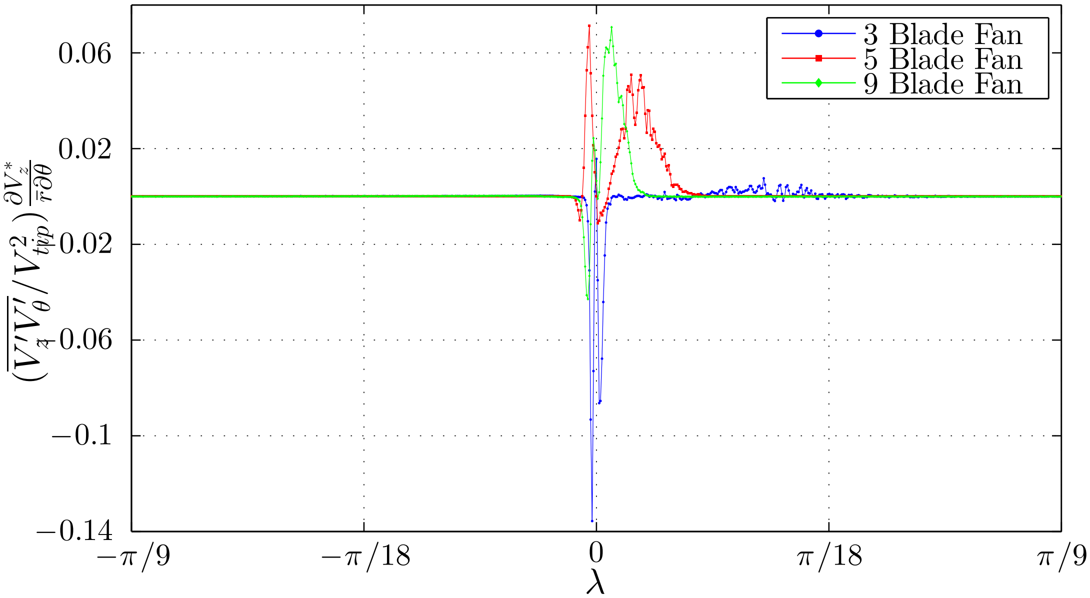

Figure 155 Case I turbulence kinetic production by Reynolds shear stress in θ–z plane over λ_9

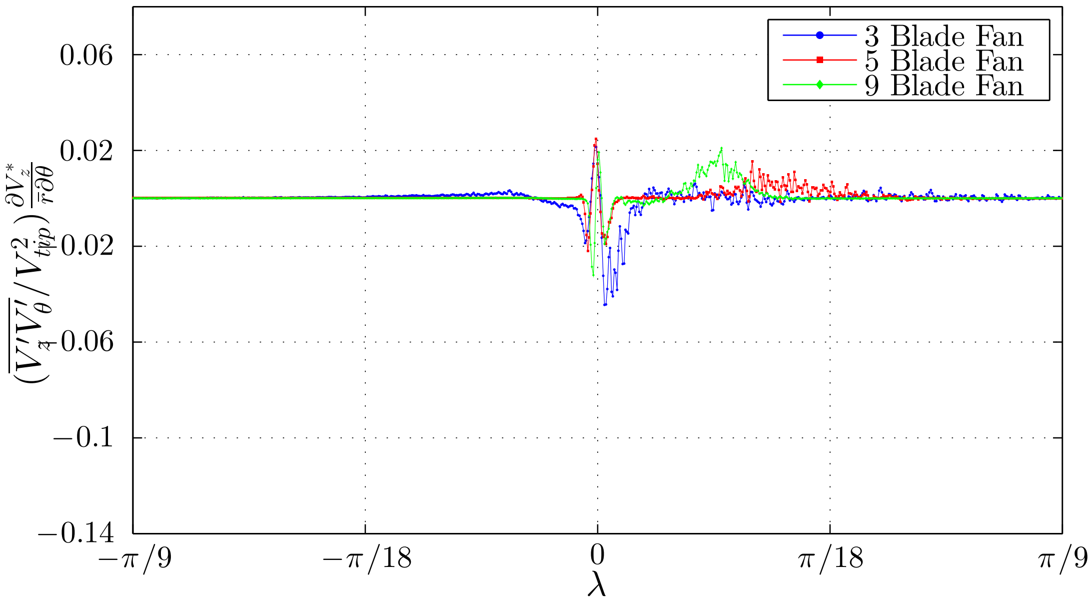

Figure 156 Case II turbulence kinetic production by Reynolds shear stress in θ–z plane over λ_9

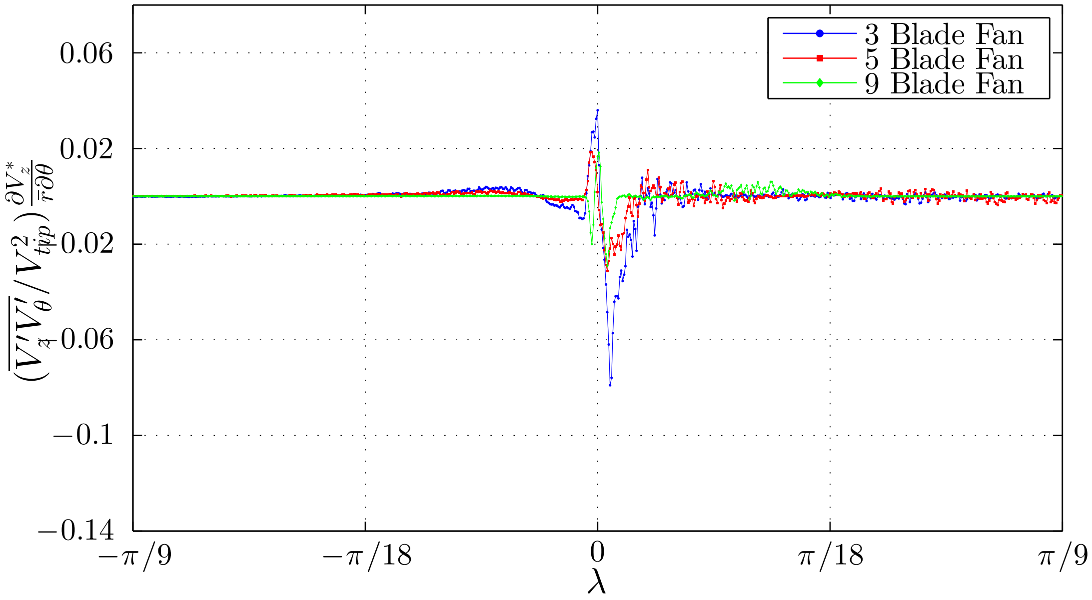

Figure 157 Case III turbulence kinetic production by Reynolds shear stress in θ–z plane over λ_9

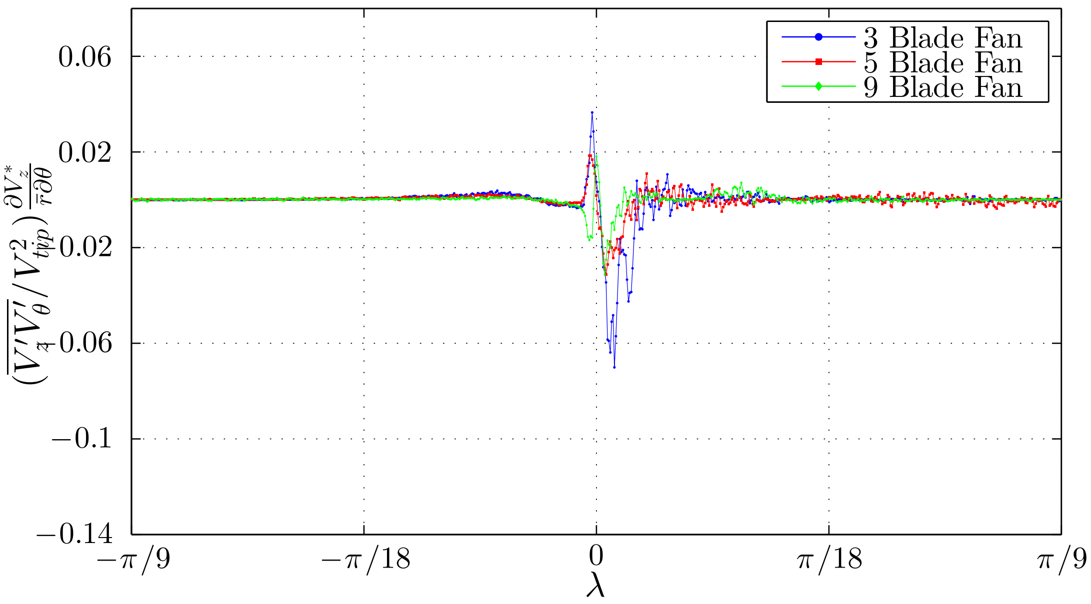

Figure 158 Case IV turbulence kinetic production by Reynolds shear stress in θ–z plane over λ_9

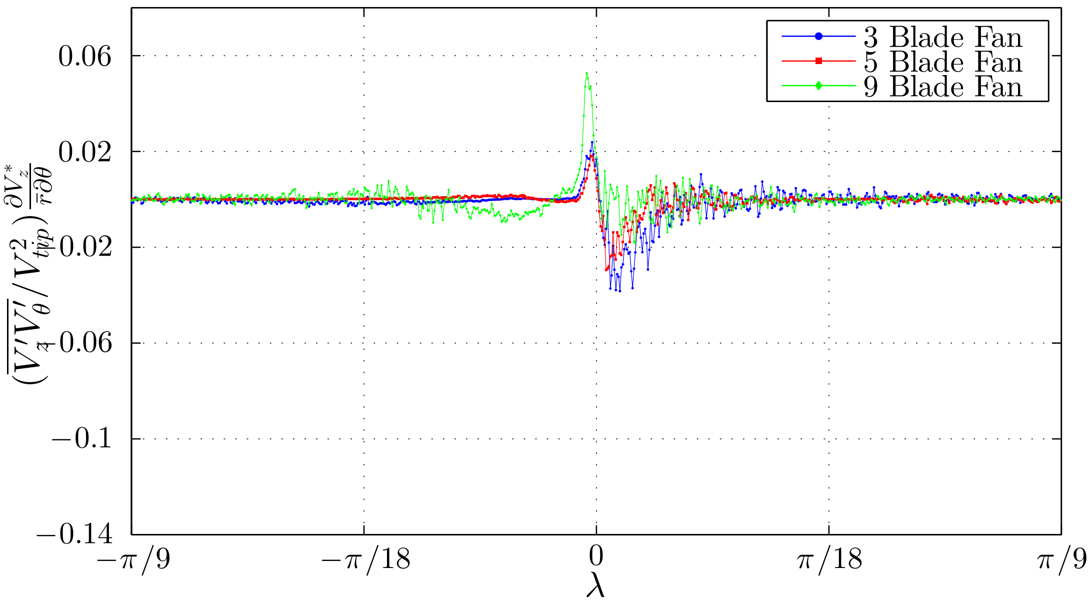

Figure 159 Case V turbulence kinetic production by Reynolds shear stress in θ–z plane over λ_9

REFERENCES

REFERENCES

Cawood, A. (2012). Surface pressure measurements on a rotating controlled diffusion blade. Master's thesis, Michigan State University.

Davoudi, B. (2014). Aeroacoustic and wake measurements on a rotating controlled diffusion blade. Master's thesis, Michigan State University.

Dusel, M. (2005). An experimental investigation of the aerodynamic shroud with an off-highway engine cooling fan. Master's thesis, Michigan State University.

Gelder, T.F. *et. al.* (1987). Design and performance of controlled-diffusion stator compared with original double-circular-arc stator. Technical report, NASA.

Hinze, J. (1975). *Turbulence.* McGraw-Hill.

Johnson, R. (1998). *The handbook of fluid dynamics.* CRC Press.

Lakshminarayana, B. (1996). *Fluid Dynamics and Heat Transfer of Turbomachinery.* John Wiley and Sons, Inc.

Morris, S.C. *et. al.* (2001). A moment-of-momentum flux mass air flow measurement device. *Measurement Science and Technology*, pages N9–N13.

Neal, D. (2010). *The effects of rotation on the flow field over a contriolled-diffusion airfoil.* PhD thesis, Michigan State University.

Neal, D.R. and Foss, J.F. (2007). The application of an aerodynamic shroud for axial ventilation fans. *Journal of Fluids Engineering*, 129(6):762–774.

Pope, S. (2000). *Turbulent Flows.* Cambridge Univeristy Press.

Tropea, C. Yarin, A. and Foss, J. (2007). *Springer Handbook of Experimental Fluid Mechanics*, volume XXVIII. Springer-Verlag.

Wallace, J.M. and Foss, J.F. (1995). The measurement of vorticity in turbulent flows. *Annual Reviews of Fluid Mechanics.*